

UILU-ENG 91-3603

Report No. 157

A FATIGUE DESIGN IN SPOT WELDS

by
Mohammed Helmi Mamoun Swellam
and
F. V. Lawrence
Civil Engineering

A Report of the
MATERIALS ENGINEERING—MECHANICAL BEHAVIOR
College of Engineering, University of Illinois at Urbana-Champaign
December 1991

ABSTRACT

The development of fatigue cracks in galvanized low carbon and high-strength-low-alloy tensile-shear-spot weldments was investigated using the AT & T Microhmmeter. The boundaries between the three stages of the fatigue life were determined based on the resistivity measurements of the Microhmmeter. Subsequently, the effects of sheet thickness, specimen width, and nugget diameter on the total fatigue life as well as its stages were studied. Sheet thickness was found to have the largest effect on fatigue life while the nugget diameter had the least. The galvanized low carbon tensile-shear specimens outperformed the corresponding high-strength-low-alloy specimens in the long life regime.

The finite element analyses together with the displacement match technique were used to determine the stress intensity factors for the tensile-shear specimen. Several geometries were analyzed and the effects of the sheet thickness, nugget diameter, specimen width and free length on the stress intensity factors were determined. The stress intensity factors determined from the linear three dimensional finite element analyses failed to correlate the fatigue data of tensile-shear specimens with different dimensions.

Consequently, an empirical K_I parameter based on the experimental fatigue data was derived. The K_I parameter collapsed the fatigue data of different spot welded specimens into a narrow band for which a best-fit was obtained. The best-fit equation help estimate the fatigue life while the K_I parameter provide the designer with a useful tool for designing the spot welds against fatigue and studying the effects of varying any of the design variables on the fatigue performance of the spot welded joint without having to resort to extensive testing.

ACKNOWLEDGEMENTS

Acknowledgement is due to all the faculty and staff members at the University of Illinois and University of Cairo for their invaluable input during the course of the author's graduate study.

The author wishes to express his deep gratitude to Prof. Frederick V. Lawrence for his fatherly guidance and broad-minded views which have been valuable inspirations during the course of this study.

The invaluable guidance and advice of Prof. Robert H. Dodds in performing the finite element analyses are sincerely acknowledged.

Acknowledgement is also due to the following people and organizations who assisted this research in various ways:

- Ms. J. Oderio, Mr. C. Kurnik, and Mr. M. Conlon for their painstaking metallography of the companion specimens.
- Dr. G. Banas for his help with experimental parts of this work.
- Ms. M. Berg, Mr. R. Hajali, Mr. M. Keppel and Mr. P. Vergas for their assistance in performing the finite element analyses.
- The National Center for Supercomputing Application (NCSA) personnel, in particular Dr. Fouad Ahmad, for providing the computing facilities.
- The Materials Engineering Research Laboratory (MERL) personnel, in particular Dr. Peter Kurath for his valuable assistance and ideas during the test program.
- The General Motors Technical Center and the Chevorlet-Pontiac-Canada Group, in particular Ms. K.W. Ewing, Dr. P.C. Wang, Dr. M.B. Motwani and Dr. S.B. Vemuri, for providing the specimens and their valuable discussions.
- The Fracture Control Program and in particular Prof. H. Sehitoglu and Prof. D. Socie for their stimulating discussions and guidance.

The author wishes to express his deepest gratitude to his mother, Bousaina; his wife, Azza; and his sister, Randa for their spiritual support and abundant encouragement.

This research project has been funded by the General Motors Technical Center, the General Motors Chevorlet-Pontiac-Canada Group, the Fracture Control Program at the University of Illinois and the National Center for Supercomputing Application.

TABLE OF CONTENTS

1. CHAPTER I: INTRODUCTION.....	1
1.1 RESEARCH DIRECTIONS IN THE FIELD OF FATIGUE OF SPOT WELDS.....	1
1.2 OBJECTIVE AND SCOPE.....	2
1.3 THESIS ORGANIZATION.....	2
2. CHAPTER II: LITERATURE REVIEW.....	4
2.1 STATIC BEHAVIOR OF SPOT WELDS.....	4
2.1.1 Types of Static Failures.....	4
2.1.2 Factors Affecting the Static Strength of Spot Welds.....	4
2.2 FATIGUE BEHAVIOR OF SPOT WELDS.....	5
2.2.1 Types of Fatigue Failures.....	5
2.2.2 Factors Affecting the Total Fatigue Life of Spot Welds.....	6
2.2.3 Models for Estimating the Fatigue Life of Spot Welds.....	7
2.2.4 Monitoring Fatigue Crack Development in Spot Welds.....	10
2.3 STRESS INTENSITY FACTORS FOR THE SPOT WELDS.....	11
2.4 FATIGUE DESIGN PARAMETERS.....	14
2.5 SUMMARY.....	16
3. CHAPTER III: EXPERIMENTAL PROCEDURES AND RESULTS.....	17
3.1 INTRODUCTION AND SYNOPSIS.....	17
3.2 EXPERIMENTAL PROCEDURES.....	18
3.2.1 Material and Specimen Preparation.....	18
3.2.2 Fatigue Testing.....	18
3.2.3 Resistivity Measurements.....	18
3.2.4 Sectioning and Crack Measurements.....	19
3.2.5 Calibration Curves.....	19
3.3 EXPERIMENTAL RESULTS.....	19
3.3.1 Observed Fatigue Crack Development	19
3.3.2 Initial Changes in Resistivity.....	20
3.3.3 Calibration and Use of the Resistivity Measurement Technique.....	20
3.3.4 Effect of Base Metal Properties on Fatigue Life Partitioning.....	22
3.3.5 Effect of Specimen Dimensions on the Fatigue Life Partitioning.....	22
3.3.6 Effect of Mean Stress on Fatigue Life Partitioning.....	23
3.3.7 Effect of Preload on Fatigue Life Partitioning.....	23
3.4 SUMMARY.....	24

4. CHAPTER IV: A SEARCH FOR A FATIGUE DESIGN PARAMETER USING THE FINITE ELEMENT.....	25
4.1 INTRODUCTION AND SYNOPSIS.....	25
4.2 FINITE ELEMENT MODEL.....	26
4.2.1 Geometry and Boundary Conditions.....	26
4.2.2 Quarter-Point-Elements and Mesh Refinement	27
4.2.3 Testing the Mesh Performance.....	27
4.3 DISPLACEMENT MATCH TECHNIQUE.....	28
4.4 DIMENSIONAL ANALYSIS OF THE TENSILE-SHEAR SPOT WELD SPECIMEN..	29
4.4.1 The Effect of the Specimen Dimensions on K_I , K_{II} and the J-Integral....	30
4.4.2 The Effect of the D/t and W/D ratios on K_I , K_{II} and the J-Integral.....	31
4.5 CORRELATING THE FATIGUE LIFE IN TERMS OF THE EQUIVALENT STRESS INTENSITY FACTOR.....	31
4.6 SUMMARY.....	32
5. CHAPTER V: THE DEVELOPMENT OF A FATIGUE DESIGN PARAMETER USING THE EXPERIMENTAL DATA.....	33
5.1 INTRODUCTION AND SYNOPSIS.....	33
5.2 THE K_i PARAMETER.....	34
5.2.1 Modelling the Effects of the Tensile-shear Specimen Dimensions.....	34
5.2.2 Correlating the Fatigue Data of Different Spot Welded Geometries.....	35
5.3 CORRELATING THE FATIGUE DATA IN TERMS OF THE K_i PARAMETER.....	37
5.4 SUMMARY.....	38
6. CHAPTER VI: DISCUSSION.....	39
6.1 INTERPRETATION OF THE RESISTIVITY CHANGES.....	39
6.2 ORIGINS OF THE DIFFERENCES BETWEEN THE BEHAVIOR OF THE LOW CARBON AND HSLA MATERIALS.....	40
6.3 A COMPARISON BETWEEN THE DIFFERENT MODELS FOR ESTIMATING THE TENSILE-SHEAR STRESS INTENSITY FACTORS.....	42
6.4 FATIGUE DESIGN PARAMETERS.....	44
6.5 THE K_i PARAMETER, ITS USE AND APPLICATION.....	45
6.6 LIMITATIONS OF THE K_i PARAMETER.....	48

7. CHAPTER VII: CONCLUSIONS, RECOMMENDATIONS AND PROPOSED FUTURE WORK.....	49
7.1 CONCLUSIONS.....	49
7.2 RECOMMENDATIONS.....	50
7.3 PROPOSED FUTURE WORK.....	51
TABLES	52
FIGURES	64
REFERENCES.....	116
Appendices	125
APPENDIX-A : POOK'S MODEL FOR THE TENSILE-SHEAR STRESS INTENSITY FACTORS	125
APPENDIX-B : INITIATION-PROPAGATION (I-P) MODEL.....	129
APPENDIX-C : RADAJ'S STRUCTURAL STRESS MODEL FOR THE STRESS INTENSITY FACTORS OF SPOT WELDED SPECIMENS.....	131
APPENDIX-D : MULTIAXIAL FATIGUE.....	133
APPENDIX-E : MIXED MODE FRACTURE MECHANICS.....	136
APPENDIX-F : RESISTIVITY RECORDS.....	137
APPENDIX-G : TOTAL FATIGUE LIFE DATA.....	216
APPENDIX-H : FATIGUE LIFE DATA FOR STAGES I, II AND III.....	228
APPENDIX-I : CRACK TIP ELEMENTS.....	238

LIST OF SYMBOLS

a	Crack depth
A	Coefficient of the best fit equation
B	Exponent of the best fit equation
c	Crack width (dimension perpendicular to crack growth)
D	Nugget diameter
e	Eccentricity of the applied load
F	Applied load
G	Geometry correction factor
K_i	Fatigue design parameter for spot welds
K_I	Mode I stress intensity factor
K_{II}	Mode II stress intensity factor
K_{Ieq}	Mode I equivalent stress intensity factor
l	Crack length
M	Applied moment
N	Number of cycles
N_I	Life devoted to stage I
N_{II}	Life devoted to stage II
N_{III}	Life devoted to stage III
N_t	Total fatigue life
P	Applied normal load
Q	Applied shear load
R	R-ratio
R_i	Current resistivity reading at nugget circumference
R_o	Original resistivity reading at nugget circumference
R_{BM}	Base metal resistivity reading
RR	Change in resistivity ratio
r	Nugget radius
r'	Correlation coefficient
t	Sheet thickness
u	Displacement along the X-axis
v	Displacement along the Y-axis
w	Displacement along the Z-axis

W	Specimen width
α	Angle between applied force and sheet normal
β	Material parameter describing sensitivity to Mode II

LIST OF ABBREVIATIONS

CP	Coach-Peel specimen
DS	Double-Shear specimen
HAZ	Heat Affected Zone
HSLA	High Strength Low Alloy steel
LC	Low Carbon steel
TS	Tensile-Shear specimen

CHAPTER I : INTRODUCTION

1.1 RESEARCH DIRECTIONS IN THE FIELD OF FATIGUE OF SPOT WELDS

Resistance spot welding has been utilized as a joining technique for many years, especially in the automotive industry. The speed of the technique and its suitability for automated assembly are the main reasons for its wide use in joining details of many different geometries. The fatigue behavior of the spot welded geometries has been studied using different laboratory specimens such as the tensile-shear, double-shear, coach-peel, and others: see Fig. 1.1. A large amount of fatigue testing has been carried out in order to study the fatigue behavior of the different spot-welded specimens. To minimize the amount of testing, several models for predicting the fatigue behavior have been developed.

The current models for estimating the fatigue life of spot welds can be classified into two major categories: i - entirely propagation based models and ii - initiation-propagation based models. Propagation models consider the total fatigue life to be devoted to propagating a single fatigue crack that exists essentially from the very first cycle of the loading. On the other hand, initiation-propagation models divide the fatigue life into three major stages: Stage I which is an initiation and early crack growth stage; Stage II in which the major crack propagates through the sheet thickness; and Stage III in which the crack propagates through the specimen width after breaking through the thickness (see Fig. 1.2).

Several researchers have tried to verify the above models experimentally by monitoring the crack development in the spot welded specimens. They developed and adopted various experimental techniques to monitor the invisible cracks during Stages I and II. Through their experiments, some of the researchers also tried to study the effect of the different design variables like the sheet thickness, number of welds and their nugget diameters on the fatigue behavior of spot welded joints. Although these joints fail by fatigue, its design was based on static considerations rather than the fatigue behavior.

Consequently, researchers tried to provide the designer with simple design load-life curves, however, basing the design on the simple applied load required testing each type of specimen for every design variable. Such design curves became extremely expensive. Therefore, the interest of researchers was then directed towards local notch root stresses and strains. However, local notch root stresses and strains did not provide useful fatigue data because the fatigue properties based on these parameters were not reproducible; the local notch root strains were found highly dependant on the strain gage dimension and the location at which they were hooked to the specimen. Recently, the interest was directed to fracture

mechanics parameters which were more successful in correlating the fatigue data of different specimens.

The search for a simple unified parameter capable of correlating the fatigue data of different specimens is still ongoing. Such a unified parameter should provide the designer with a useful tool which allows him to predict the effect of varying any of the design variables on the fatigue behavior of the different spot weldments.

1.2 OBJECTIVE AND SCOPE

The driving force of this study is the search for a simple fatigue design parameter which will correlate the fatigue data of the different spot welded geometries and allow the designer to estimate the total fatigue life as well as the number of cycles devoted to each of its three stages. The design parameter should also allow the designer to predict the consequences of variation in any of the design variables.

Thus in this study, changes in resistivity were correlated with crack depths measured during Stage II. This correlation permitted the boundaries between the three stages of fatigue life to be identified. Subsequently, the effects of base metal properties, sheet thickness, nugget diameter, specimen width, R-ratio and tensile preloads on the three Stages as well as the total fatigue were determined.

The search for the unified design parameter involved the use of the finite element technique in order to determine the stress intensity factors for the tensile-shear specimen as well as empirical methods. The finite element analyses revealed several important facts, however, the calculated K_I and K_{II} values were not as successful as the empirically derived K_I parameter in correlating the fatigue data of tensile-shear specimens with different dimensions. The K_I parameter collapsed the fatigue data of different spot welded geometries into a narrow band, allows the designer to estimate the total fatigue life as well as the number of cycles devoted to each of the three stages; and predicts the effects of the different variables on the fatigue behavior of the spot welds without having to resort to extensive test programs.

1.3 THESIS ORGANIZATION

Chapter II, Literature Review, reviews the previous work of several researchers in the field of spot welds as well as other relevant research topics. The effects of the different design variables on the static and the fatigue behavior of spot welds are summarized. Different models for estimating the fatigue life of spot welds as well as the different experimental techniques used for monitoring the crack development and subsequently verifying these models are also

presented. Finally, the parameters used in correlating the fatigue data of different spot welded specimens are reviewed.

Chapter III, Experimental Procedures and Results, presents the resistivity technique used in monitoring the crack development in tensile-shear specimens in this study. The effects of base metal properties, sheet thickness, nugget diameter, specimen width, R-ratio and tensile preloads on the total fatigue life as well as its three stages are also presented.

Chapter IV, A Search for a Fatigue Design Parameter Using the Finite Element, demonstrates the finite element capabilities in determining the stress intensity factors for the complex tensile-shear specimen subjected to a mixed mode of deformation. The effects of the sheet thickness, nugget diameter and specimen width and length on the calculated K_I and K_{II} values are presented. Finally, the equivalent stress intensity factor, K_{eq} , is used to correlate the fatigue data of the tensile-shear specimens obtained in Chapter III.

Chapter V, The Development of a Fatigue Design Parameter Using the Experimental Data, presents the K_i parameter and its derivation. This chapter also demonstrates the ability of the K_i parameter to collapse the fatigue data obtained in this study into a narrow band. Best-fit equations for determining the total fatigue life as well as the number of cycles devoted for each stage are generated.

Chapter VI, Discussion, discusses the interpretation of the resistivity changes and the origins of the differences between the behavior of the low carbon and HSLA materials. The chapter also demonstrates the superiority of the finite element in determining the stress intensity factors for the complex tensile-shear specimen. In this chapter the capabilities of the K_i in predicting the consequences caused by the variation of any of the design variables and the validity of the best-fit equations presented in Chapter V are demonstrated. Finally, the known limitations of the K_i parameter are highlighted.

Chapter VII, Conclusions, Recommendations and Future Work, presents the conclusions derived from this study and the subsequent recommendations and future work directions.

CHAPTER II : LITERATURE REVIEW

2.1 STATIC BEHAVIOR OF SPOT WELDS

2.1.1 Types of Static Failures

Two types of failures are encountered when spot welds are monotonically loaded [1]; interfacial and plug failures. In the case of the interfacial failure the nugget fails along a plane parallel to the joint sheets while in the case of plug failures the nugget fails by removing a plug from one of the joint sheets. The plug failure is usually desired in view of the larger amount of energy required for this type of failure.

It was experimentally observed that an increase in the nugget diameter to sheet thickness ratio (D/t) tends to encourage plug failures and hence, the (D/t) ratio has received a great deal of attention. Williams [2] has reviewed several relationships which determine the appropriate nugget diameter for joining two sheets of thickness (t): see Table 2.1. Most of the formulae in Table 2.1 are material independent and are confined to a certain range of thicknesses. Later, Smith [3] presented a formula which was based on fracture mechanics concepts and accounted for the base metal properties

$$D = 2.93 \left(\frac{\tau_y}{K_c} \right)^{\frac{2}{3}} (t)^{\frac{4}{3}} \quad (2.1)$$

where τ_y = yield shear strength of base metal.
 K_c = fracture toughness of base metal.

2.1.2 Factors Affecting the Static Strength of Spot Welds

Several investigators have studied the effects of sheet thickness, nugget diameter, specimen width, base metal properties on the static strength of spot welds.

The effect of the sheet thickness on the static strength was studied by Cappelli [4] Sperle [5] and Davidson [6,7]. For three sheet thicknesses (1.5, 2.0 and 2.5 mm), Cappelli observed a considerable increase in the ultimate load up to 2.0 mm thickness beyond which no noticeable increase was observed for larger thickness. Sperle presented his results in terms of the applied nominal stress, rather than applied load; and he observed no significant increase in the ultimate nominal stress with the increase of the sheet thickness. Davidson reported an

increase in ultimate load with the increase in sheet thickness and attributed this increase to the increase of the joint stiffness.

The effect of nugget diameter on the static strength of spot welds was studied by Cappelli [4] who observed an increase in the ultimate load of HSLA specimens with the increase of nugget diameter. However, the increase in the ultimate load was not directly proportional to the diameter especially when plug failures occurred. Rivet [1] and Sperle [5] reported also a markedly increase in ultimate load of tensile-shear specimens with the increase in nugget diameter.

Rivet [1] tested tensile-shear and cross-tension specimens with different widths. He measured ultimate loads, nugget rotations and energy to failure during monotonic tests. Rivet found that his measurements were dependant on the specimen width and type. In general, Rivet observed an increase in the ultimate load with the increase of specimen width. Conversely, the nugget rotation and energy to failure decreased with the increase of specimen width. The observed trends for the ultimate load, nugget rotations and energy to failure were bounded by a critical width beyond which any further increase in the specimen width had no significant effect on the measured quantity. Rivet showed also that this critical width was material independent.

Cappelli [4] tested low carbon and HSLA tensile-shear specimens. His results showed that the ultimate load of HSLA specimens was higher than that of the low carbon specimens. Davidson [7] also studied the effect of base metal mechanical properties on the static strength of tensile-shear specimens and found that the ultimate load of HSLA specimens was higher than that of low carbon steel. He also noted that the effect of the base metal properties was generally more observable in plug failures rather than in interfacial failures.

2.2 FATIGUE BEHAVIOR OF SPOT WELDS

2.2.1 Types of Fatigue Failures

When spot welds are subjected to cyclic loading, a fatigue crack initiates at the inner interface at the edge of the nugget. Later during the fatigue life, this crack propagates through the thickness of the sheet and then through the width of the specimen up to failure. Some researchers [8,9,10,11] have reported an interfacial type of failure in which the crack propagates on a plane parallel to the sheets and through the weld nugget. The later type of failure has been generally reported in cases of underwelds subjected to high load levels [8,9] and tensile-shear specimens with large stiffness [10,11].

2.2.2 Factors Affecting the Total Fatigue Life of Spot Welds

Several investigators have studied the effects of sheet thickness, nugget diameter, specimen width, base metal properties and induced compressive residual stresses on the fatigue behavior of spot welds.

Cappelli [4] did not observe a significant effect of sheet thickness on the fatigue strength of tensile-shear spot welds. Sperle [5] tested tensile-shear specimens of different thicknesses and presented his fatigue data in terms of the applied remote nominal stresses, rather than the applied load. He observed a slight increase in fatigue strength with the increase of sheet thickness, however, when he replotted the fatigue data for specimens of equal nugget diameters, he concluded that the sheet thickness had no effect on the fatigue strength (expressed in terms of remote applied stress). Conversely, Overbeeke et al. [12], Iwasaki et al. [13] Hiroshi et al. [14] and Davidson [7,10,11] reported an increase in fatigue life with the increase of sheet thickness. While Overbeeke attributed this increase to the fact that larger sheet thicknesses allowed longer propagation lives, Davidson attributed his observations to the increased joint stiffness.

The effect of nugget diameter on the fatigue behavior of spot welds was studied by several researchers. Defourny [15] observed a 50% increase in the fatigue strength of tensile-shear specimens at 10^7 cycles as a result of an increase in the electrode diameter from 5.0 to 8.0 mm. Sperle [5] found that an increase in nugget diameter yielded longer fatigue lives, however, this effect diminished in the long life regime in which he did not observe any significant effect of the nugget diameter at 10^6 cycles. Cappelli [4], Hiroshi et al. [14] and Davidson [7,10,11] reported a slight improvement in fatigue strength of tensile-shear specimens as the nugget diameter was increased for the same sheet thickness. Again Davidson attributed this slight increase in the fatigue strength to the increase in the joint stiffness, however, he stated that the diameter effect was relatively small compared to the thickness effect. Lawrence et al. [16] found no significant effect for the nugget diameter on the total fatigue life of tensile-shear specimens.

Orts [17] studied the effect of specimen width on HSLA tensile-shear specimens; he reported an increase in the fatigue strength with the increase in specimen width up to a width of 50 mm. Beyond the 50 mm limit, Orts observed no significant effect for the specimen width on the fatigue strength. Rivet [18,19] tested HSLA and low carbon tensile-shear specimens; he reported a marked improvement in fatigue performance with the increase of the specimen width. Hiroshi's [14] and Davidson's [7,10,11] results show similar trends.

Hiroshi et al. [14] tested mild steel and HSLA tensile-shear specimens and observed a significant effect for the base metal properties on the initiation stage of the fatigue life, however, they observed no effect for the base metal properties on the propagation stages of the

fatigue life. Rivet [18] reported a significant difference in the slopes of the S-N curves of low carbon and HSLA tensile-shear specimens of 2.0 mm thick sheets. He observed a transition life at 2×10^5 cycles for 20 mm wide specimens where beyond 2×10^5 cycles low carbon specimens had a greater fatigue strength than the HSLA specimens. Rivet noticed also that as the specimen width increases the transition life shifted towards longer lives.

Several researchers [20-25] studied the effect of residual stresses on the fatigue performance of weldments; they all agreed to the detrimental effect of the tensile residual stresses on the fatigue performance of weldments. Choquet et al. [24] specifically studied the effects of tensile preloads on the fatigue resistance of tensile-shear specimens. They found that a tensile preload of 75% of the ultimate static load would increase the fatigue strength at 10^7 cycles as much as 400%. Lawrence et al. [25] reported a similar trend and introduced the coining technique. Such remarkable improvement in the fatigue behavior is attributed to the compressive residual stresses created by the elastic constraint at the critical location.

2.2.3 Models for Estimating the Fatigue Life of Spot Welds

Current models for estimating the fatigue life of spot welds can be classified into two major categories: i - entirely propagation based models and ii - initiation-propagation based models. Propagation models consider the sheet interface at the nugget edge to be an intrinsic crack tip and thus the total fatigue life is devoted to propagating a single fatigue crack that exists essentially from the very first cycle of the loading. On the other hand, initiation-propagation models consider the sheet interface at the nugget edge as a sharp notch and thus the total fatigue life is composed of three major stages: Stage I which is an initiation and early crack growth stage; Stage II in which the major crack propagates through the sheet thickness; and Stage III in which the crack propagates through the specimen width after breaking through the thickness (see Fig. 1.2).

i - Propagation Models:

In these models, life devoted to initiation is neglected; and the total fatigue life is approximated by the number of cycles required to propagate a single crack up to failure. Hence, the fatigue life is estimated by integrating the Paris growth rate law, given by Eq. 2.2, as follows:

$$\frac{da}{dN} = C (\Delta K_{eff})^m \quad (2.2)$$

$$N = \frac{1}{C} \int_{a_i}^{a_f} (\Delta K_{eff})^{-m} da \quad (2.3)$$

where N = total fatigue life in cycles.
 C, m = material constants.
 ΔK_{eff} = effective stress intensity range.
 a_i = initial crack length.
 a_f = final crack length.

Several researchers supported this approximation, however they used different initial crack sizes (a_i) and ΔK formulae in their fatigue life estimates.

McMahon [26] compared the fatigue life estimates obtained from Eq. 2.3 for different values of the initial crack size (a_i): see Table 2.2. McMahon recommended the use of a_{th} because it had the advantage of accounting for changes in loading and geometry while the use of an arbitrary length can not account for such changes. He also supported his recommendation by the fact that all of the observed nonpropagating cracks were less than a_{th} in length. As for the stress intensity factor, McMahon used the solution of the semi-elliptical crack in a plate of finite width and thickness given by:

$$K_I = S \sqrt{\pi a} f(a/w) C_i M_k \quad (2.4)$$

where S = applied remote stress.
 a = crack length.
 $f(a/w)$ = correction factor for the finite width of the specimen.
 C_i = back free surface correction.
 M_k = front free surface correction factor.

Pook [27,28] provided approximate initial solutions for K_I and K_{II} in tensile-shear specimens. He obtained his solution for the tensile-shear specimen through an analogy with the strip connection in an overlap: see Appendix-A. Stress intensity factors from references [29,30,31] and dimensional analyses were used to adjust the solutions of the strip connection to the tensile-shear spot weld problem. Pook's approximate solutions were:

$$K_I = \frac{P}{r^{1.5}} [0.341 \left(\frac{2r}{t} \right)^{0.397}] \quad (2.5)$$

$$K_{II} = \frac{P}{r^{1.5}} [0.282 + 0.162 \left(\frac{2r}{t} \right)^{0.710}] \quad (2.6)$$

where P = applied load.

r = nugget radius.
 t = sheet thickness.

Pook used these expressions together with Sih's maximum tangential stress concept [32] to predict the angle at which the crack would grow. His predictions were very close to the angles observed experimentally (60° - 70°).

In another attempt for estimating the fatigue life, McMahon [26] used a two stage propagation model. In the first stage, McMahon used Pook's Mode I initial stress intensity factor up to a crack length where the K_I calculated from Eq. 2.4 was greater than Pook's initial value (Eq. 2.5). He then used Eq. 2.4 for the second stage. This two stage propagation model gave good fatigue life estimates and worked best at the short life regime. It should be noted that McMahon considered only the Mode I stress intensity factor and ignored the actual mixed mode situation.

Cooper [33,34] also used a two stage propagation model for estimating the total fatigue life. In the first stage (for $\Delta K < 6.3 \text{ MPa } \sqrt{\text{m}}$), he used an Equivalent Mode I stress intensity factor with the values $m=7$ and $C=1.92 \times 10^{-9}$ in Eq. 2.3. In the second stage (for $\Delta K > 6.3 \text{ MPa } \sqrt{\text{m}}$), he used the Mode I stress intensity factor (i.e. no further consideration for the mixed mode loading) and adopted the values of 3.4 and 2.54×10^{-9} for m and C respectively. Cooper integrated the Paris law from zero to t (sheet thickness) and reported a good agreement between his predicted crack depth versus number of cycles and the corresponding experimental data he generated in the same study.

It should be noted that the propagation models are extremely sensitive to the initial crack size (a_i) and the coupled constants C and m for which the reported values lie in the range of 2 to 7 [33].

ii - Initiation-Propagation (I-P) Model:

Wang and Lawrence [35] divided the total fatigue life into three stages; initiation and early crack growth (Stage I), crack propagation through the thickness (Stage II), and crack propagation through the width (Stage III). They considered the total fatigue life to be the sum of N_I , N_{II} and N_{III} (the number of cycles devoted to Stages I , II and III).

Wang and Lawrence combined Basquin equation [36] and the linear damage summation rule [37] to estimate the fatigue life devoted to Stage I (N_I) from Eq. 2.7. They used Peterson's equation [38,39], Neuber's formula [40] and a set up cycle analysis [41] to find the required ingredients of Eq. 2.7 : see Appendix-B.

$$\int_1^{N_I} \left[\left(\frac{\sigma_f}{\Delta\sigma/2} \right) \left(1 - \frac{\sigma_o (N)^k}{\sigma_f} \right) \right]^{\frac{1}{b}} = 1 \quad (2.7)$$

where $\Delta\sigma$ = local stress amplitude at the notch tip.

σ_f = fatigue strength coefficient.

b = fatigue strength exponent.

σ_o = local initial mean stress.

k = mean stress relaxation exponent.

As for Stage II, Wang calculated the number of cycles (N_{II}) devoted to that stage from Eq. 2.3; they adopted the values 5 and 1.0×10^{-13} for m and C respectively and used a value of 0.08 mm for a_i .

Wang and Lawrence computed the number of cycles devoted to stage III (N_{III}) by integrating the Paris law. They used the nugget diameter as an initial crack length for that stage while the end of the fatigue life was determined by the separation of the specimen: see Appendix-B

McMahon [26] compared the fatigue life estimates obtained from the I-P model with those of Table 2.2. He concluded that the I-P model gave better fatigue life estimates (within a factor of two) than the propagation models he investigated.

2.2.4 Monitoring Fatigue Crack Development in Spot Welds

There have been several experimental studies which have monitored crack propagation in spot welds and have identified the boundaries between the different stages of fatigue life.

Lawrence and Smith [42,43] studied the development of fatigue cracks by sectioning companion specimens at various stages of the fatigue life. This technique provides a clear, three-dimensional insight into the development of fatigue cracks; but it relies on more-or-less identical notch features and behavior from specimen to specimen and require a large amount of testing.

Lawrence and McMahon [43,44] developed a pre-sectioned specimen technique which enabled the development of fatigue cracks to be monitored throughout the life of a single specimen by exposing the plane of crack initiation and early growth to view. They monitored the crack growth by taking replicas at different stages during the fatigue life. Their results showed an increasing percentage of the Stage I (life up to 0.25 mm) with the fatigue life. At 10^6 cycles the ratio of initiation life to life up to a through thickness crack exceeded 50%.

Doucet [45] tested tensile-shear specimen of 8.0 mm sheet thickness. He measured the strains at the nugget edge on the outer surfaces of the specimen (back strain). He also marked the crack front at different intervals by changing the load amplitude and correlated the crack depth measured on the fracture surface with the measured back strain. Doucet used this correlation to monitor the crack growth in his tensile-shear specimens. Subsequently, he plotted crack depths versus number of cycles for each specimen and determined the initiation life by extrapolating the curve to zero cycles. Doucet concluded that the percentage of the fatigue life devoted to Stage I increased to 25% of the total life at the long life regime.

Hiroshi et al. [14] tested tensile-shear specimens of different sheet thicknesses. They measured back strains and determined the life devoted to Stage I. They defined the end of Stage I by the existence of a crack of depth equal to 0.1 mm for which they determined a corresponding characteristic strain value.

Recho and Bramat [46] performed ultrasonic measurements on tensile-shear specimens of 8.0 and 1.5 mm thick sheets. They used the marking technique of Doucet and reached the same conclusion concerning the fatigue life devoted to Stage I. They provided measurements for the crack depth (a) and crack width ($2c$) from which they calculated the aspect ratios ($a/2c$) at different stages of the fatigue life. They found that for thin specimens, the aspect ratio was around 1/10 while for the thick specimens it was around 1/5.

Smith and Cooper [33,34] used an electric potential technique to monitor through thickness crack growth. They attributed any change in the electrical potential to either crack growth or to plasticity effects for which they applied a correction. They interpreted any change in their corrected potential measurement as an extension of the intrinsic crack and concluded that the initiation stage was very small. Smith and Cooper calibrated their potential drop set up by measuring the depths of fatigue cracks appearing on the fracture surfaces of cycled specimens brittle fractured at liquid nitrogen temperatures. This technique probably revealed only the major crack and perhaps not the many secondary cracks which ultimately unite to create the major crack.

2.3 STRESS INTENSITY FACTORS FOR THE SPOT WELDS

Tada, Paris and Irwin [47] provided exact solutions for the stress intensity factors K_I , K_{II} , and K_{III} for spot welds between half spaces loaded with axial load, bending moments and torsion, respectively on the form:

$$K_{\text{axial}} = \frac{P}{2r \sqrt{\pi r}} = \frac{S \sqrt{\pi r}}{2} \quad (2.8)$$

$$K_{\text{moment}} = \frac{3}{2} \frac{M}{r^2 \sqrt{\pi r}} = \frac{3}{8} S \sqrt{\pi r} \quad (2.9)$$

$$K_{\text{shear}} = \frac{3}{4} \frac{T}{r^2 \sqrt{\pi r}} = \frac{3}{8} \tau_{\text{max}} \sqrt{\pi r} \quad (2.10)$$

Where

- P = Applied normal load
- M = Applied bending moment
- T = Applied torsional moment
- S = Resulting normal stress
- τ_{max} = Resulting maximum shear stress
- r = Nugget radius

Pook [27] presented another set of solutions for a tensile-shear load (Q) parallel to the longitudinal axis of the specimen but displaced a distance "e" normal to the specimen mid plane. The stress intensity factors were given by:

$$K_I = \frac{3e\tau}{2r} \sqrt{\pi r} = \frac{3e}{2r} \frac{Q}{r \sqrt{\pi r}} \quad (2.11)$$

$$K_{II} = \frac{\tau}{2} \sqrt{\pi r} = \frac{Q}{2r \sqrt{\pi r}} \quad (2.12)$$

Notice that if the values $M = Q * e$ and $\tau_{\text{max}} = \frac{4}{3} \frac{Q}{\pi r^2}$ are substituted in Eqs.2.9 and 2.10 respectively, they yield the same solution given by Pook in Eqs.2.11 and 2.12 .

After a series of analogics and modifications, Pook obtained a solution for the K_I and K_{II} stress intensity factors for the tensile-shear spot welds: see Appendix-A. He expressed the K_I and K_{II} in terms of the average shear stresses (τ) across the connection as follows:

$$K_I = \tau \sqrt{\pi r} \left[0.341 \left(\frac{2r}{t} \right)^{0.397} \right] = \frac{P}{r^{1.5}} \left[0.341 \left(\frac{2r}{t} \right)^{0.397} \right] \quad (2.13)$$

$$K_{II} = \tau \sqrt{\pi r} \left[0.282 + 0.162 \left(\frac{2r}{t} \right)^{0.710} \right] = \frac{P}{r^{1.5}} \left[0.282 + 0.162 \left(\frac{2r}{t} \right)^{0.710} \right] \quad (2.14)$$

Several investigators stress analyzed the tensile-shear specimen through finite element analysis, however their solutions were limited with the computers capabilities and were dependant on the type of element they used and the way they modelled the sharp notch at the sheets interface.

Wang [8] viewed the notch as a sharp notch with a finite root radius and used a 20-node-brick element in his three dimensional linear elastic analysis. He found that the stress concentration factor K_t ranged from 10 to 30 and that the largest tangential stress occurred at 70° angle with the sheets interface. He found also that the maximum stresses, in the plane of the sheet, extended over a 10° angle from the specimen longitudinal axis. Wang calculated the stress intensity factors, K_I and K_{II} , from his finite element analysis and found good agreement between his calculations and Pook's solutions.

Smith and Cooper [33,34] used the finite element technique used earlier by Yuuki [48] to determine the stress intensity factors, however, they calculated the stress intensity factors around the circumference of the nugget through the displacement match technique using the displacements of the quarter point nodes on the crack surfaces. They compared the results obtained from a two and three dimensional analyses to Pook's solution. The two dimensional finite element analysis of the plane of symmetry of the tensile-shear specimen yielded stress intensity factors which were very close to those obtained from Pook's solution, however, the three dimensional model has yielded K_I and K_{II} values which were less than Pook's solutions by almost a factor of two. Smith and Cooper presented a general plot of the parameters $\frac{K_I * r^{1.5}}{P}$ and $\frac{K_{II} * r^{1.5}}{P}$ versus $\frac{t}{2r}$. It should be emphasized that Smith's and Cooper's general curves do not consider various ratios of $\frac{t}{2r}$ where the nugget radius and the sheet thickness are (both) being varied, instead, these curves were generated for various sheet thicknesses but for the same nugget radius, specimen width and length ($D = 6.0$, $W = 50$, $L = 95$ mm).

Recently, Radaj [49,50,51] presented a model for estimating the stress intensity factors for spot welded connections from the stresses: see Appendix-C. He obtained the stresses through the boundary element analysis, however he emphasized that his general solution is not

tied to the that technique and that the structural stresses can be determined analytically by any other method or even measured experimentally. Radaj compared the results of his model to Pook's and Cooper's results; he showed that if Pook's tensile-shear specimen solution for K_I and K_{II} ($D = 5.0$ mm, $t = 1.0$ mm) are expressed in terms of the maximum nominal stresses in the sheet σ ($\sigma = 4 P / t$ per unit dimension in the specimen width direction), it yields the same results given by his approximate planar contour model for which the structural stresses are obtained by solving the planar boundary element problem (plane of symmetry of the tensile-shear specimen). On the other hand, his results based on the three dimensional boundary element analysis has yielded K_I and K_{II} values which were closer to Cooper's [33,34] three dimensional finite element results.

2.4 FATIGUE DESIGN PARAMETERS

The fatigue data of spot welded specimens have been correlated using a variety of parameters which subsequently became the design parameters used to study and design the different spot welded joints. These design parameters were:

- Remote loads and stresses
- Nugget local strains and stresses
- Fracture mechanics parameters

The remote loads and stresses were the most frequently used parameters, however, they fail to correlate the fatigue data of different geometries. Hence, basing fatigue design on these parameters requires testing each type of geometry. Nonetheless, load-life fatigue curves have helped studying and understanding the effects of several important factors that affected the total fatigue life of spot welds.

Despite the inherent problems of the back strain technique which will be discussed in Chapter III, several investigators [14,52] performed back strain measurements and correlated the fatigue data in terms of strains and stresses. Mizui et al. [52] recorded the back strain on the outer surface of several spot welded geometries: tensile-shear, double-shear, cross-tension, and coach-peel. The back strain failed to collapse the fatigue data of these geometries into a narrow band. Mizui et al. argued that the back strain measured at one location did not reflect the ratio of the bending strain to total strain and so it failed to collapse the fatigue data of the tested geometries into a narrow band. Hence, they measured the back strain at two locations on the same outer surface and classified the connections according to the ratio of the two strains. They also related the back strains to the local notch root strains at the interface of the joint sheets (through a finite element analysis) and correlated the fatigue data in terms of these local notch root strains. As a result, their data fell within a narrower band.

Several researchers used the fracture mechanics parameters to correlate the fatigue data of spot welds. Davidson [7,10,11] correlated tensile-shear fatigue data using a stiffness parameter (ES)

$$ES = \frac{P * \sqrt{\Delta\theta}}{t} \quad (2.15)$$

where P = applied load.
 $\Delta\theta$ = nugget rotation.
 t = sheet thickness.

Davidson demonstrated the importance of the joint stiffness in determining the fatigue behavior of tensile-shear spot welds by testing welded channels, instead of sheets. The channels showed longer fatigue lives for their higher rotational stiffness. Using the same argument, Davidson explained the effects of sheet thickness, nugget diameter and specimen width on the fatigue behavior of tensile-shear specimens. The usefulness of Davidson's parameter has been limited by difficulties in measuring the rotation at high load levels and inapplicability of this concept to the coach-peel and cross-tension geometries.

Mizui et al. [52] used a stress intensity factor (Eq. 2.16) for the critical plane of crack extension which they predicted through Sih's maximum tangential stress concept [32]. The fatigue data of the different geometries they tested were collapsed into a relatively narrow band as compared to other parameters.

$$\Delta K_{\theta_{\max}} = \cos \frac{\theta}{2} [\Delta K_I \cos^2 \frac{\theta}{2} - 1.5 \Delta K_{II} \sin \theta] \quad (2.16)$$

where θ = angle of maximum tangential stress.

Wang [53] used the J-integral to correlate the fatigue data of tensile-shear specimens only. The J-integral succeeded in collapsing the fatigue data of tensile-shear specimens of different thicknesses, however, in an elastic analysis, the J-integral is incapable of accounting for the effect of base metal properties on the fatigue behavior [54,55].

Recently, Radaj [49,50] has used an equivalent stress intensity factor having the form:

$$K_{eq} = (K_I^2 + K_{II}^2 + K_{III}^2)^{0.5} \quad (2.17)$$

Radaj's K_{eq} has collapsed the fatigue data of different geometries into a relatively narrow band. However, it should be noted that Radaj's K_{eq} assumes equal damage inferred by each of the different modes of deformation.

Fracture mechanics parameters were the most successful parameters to collapse the fatigue data of different specimens into a narrower band. The performance of such parameters is expected to improve if combined with the concepts of multiaxial fatigue (see Appendix-D) and mixed mode fracture mechanics (see Appendix-E).

2.5 SUMMARY

Test results have shown that the static strength of spot welds is highly dependent on the base metal properties (yield and ultimate strength), sheet thickness, nugget diameter and specimen width. The ultimate strength of the spot welded specimens increased with the increase of the pre-mentioned variables.

The fatigue behavior of the spot welded specimens was also improved with the increase of the sheet thickness and specimen width. However, unlike the static strength, the base metal properties and the nugget diameter had little or no effect on the fatigue strength of spot welded specimens. This difference in behavior is attributed to the nature and type of failures that occur in static and fatigue tests.

As for the fatigue design parameters, fracture mechanics parameters were the most successful parameters to collapse the fatigue data of different specimens into a narrower band. The performance of such parameters is expected to improve if combined with the concepts of multiaxial fatigue and mixed mode fracture mechanics .

CHAPTER III : EXPERIMENTAL PROCEDURES AND RESULTS

3.1 INTRODUCTION AND SYNOPSIS

Several investigators have tried to monitor the fatigue crack development in the tensile-shear specimens as mentioned in Chapter II. Lawrence and Smith [42] used the sectioning technique which provided a clear, three-dimensional insight into the development of fatigue cracks; but it relied on more-or-less identical notch features and behavior from specimen to specimen. Lawrence and McMahon [43] developed a pre-sectioned specimen technique which enabled the development of fatigue cracks to be monitored throughout the life of a single specimen by exposing the plane of crack initiation and early growth to view. However, they had to introduce a correction factor in the expressions of the stress intensity factors in order to account for the effect of the free surface on the crack growth rate.

Doucet [45], Recho and Bramat [46], Hiroshi et al. [14] and Mizui et al. [52] measured strains and correlated them with the crack depth. The strains of interest are those at the interface of the joint sheets while those measured are usually at the nugget edge on the specimen outer surface (back strains). This location at which the strains are measured is still an area of high stress concentration and thus the recorded back strains are highly dependant on the size and location of the strain gauges. Moreover, the back strain reflects two strain components: the first is a bending component due to nugget rotation which is highly dependant on the sheet thickness; and the second is a stretching component due to the crack extension. These inherent difficulties have limited the reproducibility of the experimental results and hence the generation of fatigue design characteristics in terms of the back strains.

Smith and Cooper [34] used an electric potential technique to monitor through thickness crack growth. They hypothesized that any change in their corrected potential measurement reflected the extension of the intrinsic crack (created by the welding process) and consequently concluded that the initiation stage was very small. Their calibration technique probably revealed only the major crack and perhaps not the many secondary cracks which ultimately unite to create the major crack.

In this study, the AT&T microhmeter (Metal Inspector Model 100), which measured the resistivity, was used to monitor the fatigue crack development at the critical locations on HSLA and Low Carbon tensile-shear specimens. The microhmeter was first calibrated by generating curves relating the changes in resistivity to the corresponding maximum crack depths which were determined by the sectioning technique. These calibration curves provided

the characteristic values of resistivity which define the boundaries between the three stages of the fatigue life. Later, changes in the resistivity were recorded throughout the fatigue life; and based on the characteristic values of the calibration curves, the number of cycles devoted to each stage was determined. Subsequently, load-life curves, up to the different stages of the fatigue life, were generated. From these load-life curves, the effects of the considered variables on the fatigue behavior of tensile-shear specimens were determined: see the complete test matrix in Table 3.1.

3.2 EXPERIMENTAL PROCEDURES

3.2.1 Material and Specimen Preparation

Tables 3.2 and 3.3 list the chemical compositions and mechanical properties for the galvanized low carbon (LC) and galvanized high-strength-low-alloy (HSLA) steel sheets studied. Both sheet materials were galvanized on two sides with 0.025 mm thickness zinc coatings. Specimens were made by welding two coupons; each coupon (38 mm width x 127 mm length) was cut from the main sheet with its length along the rolling direction. The tested sheet thicknesses were 0.9, 1.40 and 2.7 mm (including the two galvanized layers). The total length of the tensile-shear specimen was 216 mm with a 38 mm overlap: see Fig 3.1.

A Sciaky single-phase, microprocessor-controlled A-C electrical resistance spot welder was used to weld the specimens. Peel tests were performed after welding every seventh specimen to check the maintenance of the desired nugget diameter. Nugget diameters of 4.8, 6.1, 7.6 and 8.64 mm were produced by the welding schedules shown in Table 3.4.

3.2.2 Fatigue Testing

Specimens were fatigue loaded using a 3 kip M.T.S. servo-hydraulic test frame and a constant amplitude sinusoidal load history with various mean loads ($R = 0, -0.2, \text{ and } 0.5$). The test frequency was 15 Hz. All tests were conducted under ambient laboratory conditions (22 °C, 50% R.H.). The complete separation of the specimen into two parts defined the total fatigue life (N_f). Except for few cases where resistivity measurements were performed, "run-out" tests were terminated at 3×10^6 cycles.

3.2.3 Resistivity Measurements

An A.T.&T. Microhmeter (Metal Inspector Model 100) was used to manually measure the resistivity at the critical location on each side of the tensile-shear specimens: see Fig. 3.2. This device automatically makes two measurements of resistivity using direct current but reverses the sense of the current through the probes for each measurement after which it

computes an average value and displays the result. The resistivity measurements were performed while the fatigue test was instantaneously halted and while the specimen was loaded with a static load equal to 50% of the maximum applied fatigue load.

3.2.4 Sectioning and Crack Measurements

Typical depths of polish (thickness of removed layer) ranged from 0.13 to 0.3 mm with the smaller values being used near the center-line of the specimen. Silicon carbide grinding paper of grits ranging from 120 to 600 were first used for thick layer removal. This Stage was then followed by a finer polish using 0.3 and 0.05 micron Aluminum Oxide powder successively. Following the mechanical polishing, a chemical mill (85 c.c of H_2O_2 of 30% concentration + 15 cc of H_2O + 5 cc of HF acid 48% concentration) was used in order to remove any smearing imparted by polishing.

Microscopic examination of each section was carried out in a Leitz hardness tester and crack depths were measured at 400 X magnification. The processes of polishing and crack depth measurement were repeated through out the nugget zone in order to determine the maximum crack depth on each side of the specimen.

3.2.5 Calibration Curves

Companion specimens (almost identical specimens) were loaded with the same load for different number of cycles after which the difference between the original and current resistivity ($R_i - R_o$) were determined on both sides of each specimen. Specimens were then sectioned and the corresponding maximum crack depth on each side of every specimen was also determined. Calibration curves relating the change in resistivity ($R_i - R_o$) to the measured (maximum) crack depth (a) were generated for the different tested thicknesses and materials as shown in Fig. 3.3. Figure 3.4 represents the same data of Fig. 3.3 in a normalized form where the crack depth was normalized by the sheet thickness and the change of resistivity was normalized by the base resistivity reading.

3.3 EXPERIMENTAL RESULTS

3.3.1 Observed Fatigue Crack Development

Figure 3.5 is a representation of the different sections observed while polishing one companion specimen. The number at the top of each sketch indicates the sequence in which the polished sections were observed. The crack depths (a) and nugget chord observed at each section are indicated. Figure 3.5 shows that more than one crack initiated at the circumferential notch as suggested by the results of finite element studies which showed that notch-root

stresses remain maximum at angles as large as 10 degrees on either side of the centerline of the specimen [8]. These cracks grow through the thickness as well as away from the nugget periphery, and they ultimately coalesce into a major elliptical crack which then propagates through the thickness. A typical fatigue crack as observed on a polished section is shown in Fig. 3.6.

Sketch 20 of Fig. 3.5 also shows how the elliptical crack extended (in the direction of the specimen width) beyond the nugget diameter although it had not broken through the thickness. This observation confirms that major cracks possess small aspect ratios ($l/2c$) and that by the time the major elliptical crack breaks through the thickness, it is as wide as the nugget diameter. Such small aspect ratios have been reported by Smith and Cooper [34] and Recho and Bramat [46]; they are attributed, in this study, to the linking process of the secondary cracks mentioned earlier.

3.3.2 Initial Changes in Resistivity

Figure 3.3 is a plot of the change in resistivity ($R_i - R_0$) as a function of measured crack depth (a) for the conditions and materials studied. There was a lot of scatter in the data for crack lengths less than 0.25 mm. This scatter is attributed to events other than crack growth and in particular to the breaking of contacts between the two sheets which formed during the welding processes by the natural points of contact and by the vaporized or expelled material. During the initial cycles, it is thought that these contacts break and cause the observed early resistivity changes (and scatter): see Fig. 3.6. This belief was reinforced by sectioning several 1.4 mm thick specimens which had changes in resistivity less than $2 \mu\Omega\text{cm}$; no cracks were found upon sectioning these specimens. Polish depths during sectioning of such specimens were of the order 0.13 mm. Thus, if a crack were missed, then its width and length would have been less than 0.13 and 0.03 mm, respectively (for an aspect ratio $l/2c=0.25$). Thus, the changes in resistivity for crack lengths less than 0.25 mm were ignored and not included in the determination of the relationship between change in resistivity and crack depth.

3.3.3 Calibration and Use of the Resistivity Measurement Technique

The calibration curve is shown in Fig. 3.4 in which the effects of material and sheet thickness were eliminated by plotting the data in terms of the change of resistivity ratio (RR) and the ratio of the crack depth to the plate thickness (a/t). The resistivity ratio (RR) is the ratio of the change in resistivity to the base resistivity of the sheet (R_{BM}):

$$RR = \frac{R_i - R_0}{R_{BM}} \quad (3.1)$$

A best fit for all the obtained data is shown in Fig. 3.4. Note that the minimum reliable limits for the 0.9 and 1.4 mm thick plates are at an a/t ratio of ≈ 0.18 . This minimum detectable crack depth corresponded to a change in resistivity ratio (RR) of 0.12. This value is arbitrarily defined herein as the end of Stage I and corresponded to crack depths (a) between ≈ 0.16 to 0.48 mm depending upon the plate thickness (t): see Fig 3.4. The conclusion of Stage II or penetration of the propagating fatigue crack to the outer surface of the specimen was taken as an a/t ratio of 0.92 which corresponded to a relative change in resistivity ratio (RR) of 0.65: see Fig 3.4. Thus, these two resistivity ratios were taken as the boundaries between the three stages of the fatigue life. Table 3.5 lists the values of base resistivities as well as changes in resistivity used in this study to define the boundaries between the three Stages of fatigue life.

Resistivity measurements were performed on four specimens of each test series. Figure 3.7 gives a typical record for LC and HSLA specimens. In all cases, the life devoted to each Stage was determined by the lives at which the data exceeded the resistivity ratios of 0.12 and 0.65. Complete records of the resistivity measurements are included in Appendix-F.

Based on the resistivity measurements, S-N plots were developed for the duration of each of the three Stages (I, II, and III) as will be shown later in Figs. 3.9-3.11, 3.14-3.16 and 3.19-3.21. These curves allowed reliable interpolation of the data and were used as the basis of the comparisons below (for the complete set of data refer to Appendices G and H). Best-fit regression curves were fitted to the data, and the correlation coefficient (r') of the fit was calculated:

$$\Delta P = A N^B \quad (3.2)$$

where:

ΔP	=	Load range in Newtons
N	=	N_I, N_{II}, N_{III} , or N_t
A, B	=	Regression analyses constants

The values of A , B and r' for the best fit curves to all data obtained using the D-C resistivity measurement technique are listed in Table 3.6. It should be noted that the regression analyses are for data between 10^4 and 10^7 cycles and the best fit curves should not be used to estimate results outside this life region. Secondly, due to statistical averaging through the regression analyses, values of N_I , N_{II} and N_{III} calculated from the regression curves to the measured data will not sum exactly to the regression curve for N_t . Thus in using these data in Table 3.6 to create Figs 3.12, 3.17, 3.22 and 3.27, calculated values of N_I , N_{II} and N_{III} were

proportionately increased or decreased so that the sum of N_I , N_{II} and N_{III} equalled the calculated value of N_t .

3.3.4 Effect of Base Metal Properties on Fatigue Life Partitioning

The fatigue behavior of the LC and HSLA specimens was quite similar when compared on a total life basis as is shown in Fig. 3.8. The HSLA specimens gave a slightly lower fatigue strength at long lives.

The resistivity measurements permitted the fatigue lives of the two materials to be decomposed into life spent in each of the three Stages. Figures 3.9-3.11 presents the load-life plots for the experimental data. In general, the low carbon specimens show longer lives at Stage I, however, the two materials show no significant differences during Stages II and III. This observation agrees with Hiroshi's results [14].

Figure 3.12 presents a bar chart generated from the best-fits of Table 3.6. The bar chart shows the duration of Stages I, II, and III for LC and HSLA specimens of identical geometry loaded with 4000 and 2000 Newton load ranges ($R = 0$); short and long life regime respectively. Both materials gave about the same N_t when cycled at $\Delta P = 4000$ N because the life devoted to Stages II and III were about the same while the life devoted to Stage I was very small in the case of the HSLA specimen and less than that of Stages II and III in the case of the LC specimen and hence unimportant in both materials.

At long lives ($\Delta P = 2000$ N), it is apparent that Stage I increases in importance for both materials. In the case of the HSLA specimens, Stage I nearly equals the duration of Stages II and III; while for the LC specimens Stage I dominates and controls the fatigue life at 10^7 cycles. Thus, the difference between the LC and HSLA specimens is ascribed to a greater period spent in Stage I (crack initiation and early growth) in the LC material.

3.3.5 Effects of Specimen Dimensions on the Fatigue Life Partitioning

Figures 3.13-3.16 show the effects of the different specimen dimensions on the total fatigue life data as well as data for the three stages. In general, durations of all three stages increased with the increase in sheet thickness and specimen width. On the other hand, an increase in the nugget diameter (for the same sheet thickness and specimen width) resulted in slightly longer Stage I durations; and possessed a varying effect on Stage II depending on the sheet thickness and the considered life regime. Stage III durations were almost insensitive to the nugget diameter variations.

Figure 3.17 presents a bar chart which is generated from the best-fit equations of Table 3.6. The bar chart compares the duration of Stages I, II, and III and N_t for LC specimens loaded with a 2000 N load range; it helps view the effect of the specimen dimensions at that

load level. As shown in Figs. 3.13 and 3.17, the sheet thickness (t) had the largest effect on the total fatigue life, N_t . The reason for this large effect is ascribed to the increase in the durations of all three stages with the increase of the sheet thickness: see Fig. 3.17.

Specimen width (W) had a moderate effect on N_t , especially at the long life regime ($\Delta P = 2000$ N). As seen in Fig. 3.17, an increase in specimen width had a moderately beneficial effect on all three Stages of the fatigue life and hence an increase in the specimen width resulted in a moderate increase in the total life (N_t).

An increase in nugget diameter (D) caused only a modest increase in N_t of LC specimens as is seen in Fig. 3.13. The reasons for this insensitivity are apparent in the data plots (Figs 3.14-3.16) as well as in Fig. 3.17 which shows that an increase in nugget diameter increased the duration of Stage I, especially at the long Life regime (as predicted by TSIP model of Lawrence and Wang [8,9]). However, Stage II was either insensitive or adversely affected by the increase in the nugget diameter (see Fig. 3.15) with a consequent very small gain in N_t . Stage III is almost unaffected. The conflicting observations regarding the nugget diameter influence on the total fatigue in Chapter 2, is ascribed to the off-setting effects of the nugget diameter on the three stages. Figure 3.17 shows also that the total fatigue life of low carbon specimens is mainly dominated by Stage I. This dominance is quite obvious at the long life regime ($N_t > 10^5$ cycles) and is less pronounced at the short life regime.

3.3.6 Effect of Mean Stress on Fatigue Life Partitioning

Figures 3.18-3.21 show the R-ratio effect on the total fatigue life and its stages; in general, Stages II and III are less sensitive to the variations in the R-ratio than Stage I. The data shows that the $R = 0.5$ had the most detrimental effect while the $R = 0$ and $R = -0.2$ showed no significant difference. One can also observe a larger scatter in the HSLA Stage I data (Fig. 3.19) which may be attributed to slower mean stress relaxation rate.

The bar chart in Fig. 3.22 shows the same trends observed in Figs. 3.18-3.21. Moreover, one can also observe that specimens tested at $R = -0.2$ show slightly longer Stage I durations than those tested at $R = 0$. In addition, Fig. 3.22 shows that, except for $R = 0.5$, at $\Delta P = 3000$ N the total fatigue life of low carbon specimens is still dominated by Stage I.

3.3.7 Effect of Preload on Fatigue Life Partitioning

The preload effect on HSLA specimens (with a higher yield stress and a slower mean stress relaxation rate) has been also studied. Figure 3.23-3.26 show the total fatigue life data as well as its stages for an as-welded and preloaded HSLA specimens. The total fatigue life and all its stages have been improved by orders of magnitude, specially Stage I. This improvement is attributed to the compressive residual stresses created by the elastically loaded

material surrounding the plastic zone at the notch tip. Figure 3.27 shows the bar chart generated from the best-fit equations; similar magnitudes of improvement are also observed.

3.4 SUMMARY

Changes in resistivity were correlated with crack depths measured during Stage II during which changes in resistivity were caused by the growth of a major crack. This correlation permitted the boundaries between the three stages of fatigue life to be identified. Consequently, the effect of base metal properties, sheet thickness, nugget diameter, specimen width, R-ratio and tensile preloads on the three stages as well as the total fatigue were determined.

Tensile-shear spot welds of galvanized low carbon steel performed better than the galvanized HSLA during Stage I, hence the galvanized low carbon specimens showed slightly longer total fatigue lives than the HSLA specimens.

As for the different specimen dimensions, the sheet thickness had the largest effect on the total fatigue life while the nugget diameter had the least. The sustained fatigue load at 10^5 cycles increased linearly with the sheet thickness and was proportional to the square root of the specimen width as shown in Figs. 3.28 and 3.29.

While the $R = 0.5$ had the largest detrimental effect on the fatigue life compared to $R = 0$ and $R = -0.2$, the tensile overloads increased the fatigue lives of HSLA specimens by orders of magnitude mainly due to the generated compressive residual stresses.

CHAPTER IV : A SEARCH FOR A FATIGUE DESIGN PARAMETER USING THE FINITE ELEMENT

4.1 INTRODUCTION AND SYNOPSIS

Several models for designing and studying the fatigue behavior of spot welds are based on the fracture mechanics parameters like the crack opening displacement in Davidson's [7,10,11] nugget rotation model; the stress intensity factors in Lawrence's [25,35], Yuuki's [48] and Cooper's [34] models; the J-integral in Wang's model [53]; and the equivalent stress intensity factor in Radaj's [49,50] recent model. Except for Davidson who measured the nugget rotation experimentally and Lawrence who used Pook's expressions, all other researchers used numerical methods such as the finite element and the boundary element techniques to estimate the fracture mechanics parameters necessary for their models. The parameters obtained from the finite element analysis were dependant on the advances in the computational fracture mechanics field and subsequently the type of element used.

Both, Cooper [34] and Wang [53], used a 20-node-brick element in their three dimensional linear elastic analysis. Cooper modelled the sharp notch as a crack; hence, he calculated the stress intensity factors from the displacements of the quarter-point-nodes of the first ring of elements. Wang also used the quarter-point-node element, however he computed the J-integral and used it to correlate the fatigue data of tensile-shear and sheet to tube specimens with different dimensions (sheet thickness and nugget diameter and shape). Limited by the computers capabilities, neither Cooper nor Wang presented the effect of the mesh size on their results, thus, their results were questioned by Radaj [49,50] who presented expressions for the stress intensity factors (which are the components of the equivalent stress intensity factor in Eq. 2.17) in terms of the local structural stresses which he obtained through the boundary element technique. Radaj [49] analyzed a spot weld subjected to different loading conditions which he superposed to obtain the stress intensity factors for the different commonly observed geometries like the tensile-shear, cross-tension and others.

In this chapter, the tensile-shear specimen will be analyzed through a three dimensional linear elastic finite element model with a quarter-point 20-node-brick elements at the circumferential crack tip. The J-integral will be computed as well as the stress intensity factors, K_I and K_{II} , which are specifically computed from the displacements of the nodes on the crack faces through the displacement match technique. The dependency of the results on the mesh size and confidence in the used technique will be first addressed in order to determine the appropriate mesh for the analysis. The appropriate mesh will then be used in a dimensional

study for the tensile-shear spot welded specimen to determine the effects of the different specimen dimensions on the stress intensity factors. Hence, the existence of a numerically determined fatigue design parameter will be investigated by correlating the fatigue data of tensile-shear specimens (with different dimensions) in terms of the stress intensity factors; the success or failure of the determined stress intensity factors in correlating the fatigue data will determine their success as design parameters.

The PATRAN software was used to generate the finite element mesh and the ABAQUS code was used for the analyses on the CRAY YMP and the CRAY 2 computers.

4.2 FINITE ELEMENT MODEL

4.2.1 Geometry and Boundary Conditions

The tensile-shear specimen is shown in Fig. 4.1. The specimen has a plane of symmetry, the X-Z plane, and an axis of axial symmetry, the Y axis. Hence, using the appropriate boundary conditions reflecting the symmetry conditions, only one quarter of the specimen was analyzed as shown in Fig. 4.1.

Nodes on the X-Z plane (plane of symmetry) were restrained in the direction perpendicular to that plane, i.e. $v = 0$ on the plane $Y = 0$. For nodes on the Y-Z plane, the displacement components of the nodes with positive Z-coordinate were tied to those with negative Z-coordinate through the following constraints:

$$u^+ = -u^- \quad , \quad v^+ = v^- \quad , \quad w^+ = -w^- \quad (4.1)$$

Where u , v and w are the three displacement components at each node in the X, Y and Z directions respectively and the superscript + designate the nodes with positive Z-coordinate while the - designate the nodes with negative Z-coordinate. It should be noted that, for the same Y-Z plane, the above constraints apply also to the nodes on the sheets interface ($Z = 0$), however, since a row of single nodes exist along the line of the sheets interface inside the nugget area, these constraints become:

$$u = 0 \quad , \quad w = 0 \quad (4.2)$$

Nodes at the grip end were only allowed to displace in the X-direction while both v and w were restrained.

4.2.2 Quarter-Point-Elements and Mesh Refinement

The sharp notch created by the welding process was modelled as a circumferential crack at the tip of which the familiar fan-shape mesh was constructed: see Fig. 4.2. Barsoum [76] and Banks-Sills [77] recommend the use of quarter-point-node elements as the first ring of elements in order to model the stress singularity at the crack tip for elastic analyses; the rest of the model may be meshed with regular 20-node-brick elements. The quarter-point-node element was created by collapsing the nodes on one of the faces of a regular 20-node-brick element to the line of the crack front and subsequently moving the midside nodes to the quarter point positions. Hence, clusters of nodes were formed along the crack front (see Appendix-I). The nodes at each cluster are either tied together or free to move independently; the elastic solution of the crack problem is insensitive to these two kinematic conditions.

Common practice in the field of the Computational Fracture Mechanics [78,79] recommends an element size for the quarter-point crack-tip element within 1 to 5% of the crack length or the remaining ligament. The quarter-point-node elements must also have straight sides in the fan plane [80], otherwise the induced singularity is destroyed. Along the radial direction of the fan, the size of the successive rings of regular 20-node-brick elements may be sequentially doubled without affecting the accuracy of the solution.

4.2.3 Testing the Mesh Performance

Initially, a cracked problem similar to the spot weld geometry (for which a solution for the stress intensity factor exists) was analyzed using the above mentioned recommendations in order to test the performance of the possible finite element meshes. An axially loaded cylinder with a circumferential crack was used at this test stage. The convergence to the solution in the case of the cylinder justifies the use of the same crack tip model with the similar spot weld geometry. Hence, a 3-D finite element mesh of a circumferentially cracked cylinder has been analyzed. The stress intensity factors calculated from the displacement match technique (as will be shown in the following section) for the circumferentially cracked cylinder were within 2.3 to 3.2 % of the known solution as shown in Table 4.1. It should be noted that reducing the radial size of the first ring of elements from 0.17 to 0.03 mm did not affect the results significantly.

Cooper's tensile-shear specimen dimensions were duplicated, modelled with different finite element meshes and analyzed. The calculated stress intensity factors (as will be shown in the following section) for Cooper's geometry agreed well with his results. Table 4.2 shows the results obtained from the different models which were used in meshing Cooper's geometry. Reducing the radial size of the first ring of elements from 0.21 to 0.05 mm resulted in a slight increase in the K_I and K_{II} values, however, the element size in the circumferential direction had

no significant effect on the results; models with four and eight elements along the circumference have yielded almost the same results.

4.3 DISPLACEMENT MATCH TECHNIQUE

The displacement match technique is one of the techniques which allows us to calculate the stress intensity factors from the output of a finite element analysis. The technique depends mainly on equating the fracture mechanics solution for the displacements fields around the crack tip to the displacements obtained from the finite element analysis, hence, the stress intensity factors (the only unknown in the equations) can be determined as follows:

the displacement fields are given by:

$$u = \frac{K_I}{4\mu} \sqrt{\frac{\xi}{2\pi}} \left[(2\kappa-1) \cos\left(\frac{\theta}{2}\right) - \cos\left(\frac{3\theta}{2}\right) \right] - \frac{K_{II}}{4\mu} \sqrt{\frac{\xi}{2\pi}} \left[(2\kappa+3) \sin\left(\frac{\theta}{2}\right) - \sin\left(\frac{3\theta}{2}\right) \right] \quad (4.3)$$

$$w = \frac{K_I}{4\mu} \sqrt{\frac{\xi}{2\pi}} \left[(2\kappa+1) \sin\left(\frac{\theta}{2}\right) - \sin\left(\frac{3\theta}{2}\right) \right] - \frac{K_{II}}{4\mu} \sqrt{\frac{\xi}{2\pi}} \left[(2\kappa-3) \cos\left(\frac{\theta}{2}\right) - \cos\left(\frac{3\theta}{2}\right) \right] \quad (4.4)$$

where

u and w	=	displacement components in the X and Z directions respectively.
ξ and θ	=	polar coordinates with the origin at the crack tip.
κ	=	$3 - 4\nu$, for plane strain.
κ	=	$\frac{(3 - \nu)}{(1 + \nu)}$, for plane stress.
ν	=	Poisson's ratio.

Thus, the relative displacements between the sheets interface (for $\theta = 180^\circ$ and $\theta = -180^\circ$) are given by :

$$u_{-180} - u_{+180} = \frac{K_{II}}{\mu} \sqrt{\frac{\xi}{2\pi}} (\kappa + 1) \quad (4.5)$$

$$w_{+180} - w_{-180} = \frac{K_I}{\mu} \sqrt{\frac{\xi}{2\pi}} (\kappa + 1) \quad (4.6)$$

where for plane strain $\kappa = 3 - 4\nu$ and for plane stress $\kappa = \frac{(3 - \nu)}{(1 + \nu)}$, ν is Poisson's ratio.

The relative displacements can also be expressed in terms of the nodal displacements along the interfacial edges of the quarter-node elements (see Appendix-I) by :

$$u_{1-9-2} - u_{5-13-6} = (2 u_1 - 4 u_9 + 2 u_2 - 2 u_5 + 4 u_{13} - 2 u_6) \frac{x}{L} + (4 u_9 - u_1 - 3 u_2 - 4 u_{13} + u_5 + 3 u_6) \sqrt{\frac{x}{L}} + (u_2 - u_6) \quad (4.7)$$

$$w_{5-13-6} - w_{1-9-2} = (2 w_5 - 4 w_{13} + 2 w_6 - 2 w_1 + 4 w_9 - 2 w_2) \frac{x}{L} + (4 w_{13} - w_5 - 3 w_6 - 4 w_9 + w_1 + 3 w_2) \sqrt{\frac{x}{L}} + (w_2 - w_6) \quad (4.8)$$

Equating the square root terms in Eqs. 4.5 and 4.6 to those of Eqs. 4.7 and 4.8, we get:

$$K_{II} = \frac{\mu}{(\kappa + 1)} \sqrt{\frac{2\pi}{L}} (4 u_9 - u_1 - 3 u_2 - 4 u_{13} + u_5 + 3 u_6) \quad (4.9)$$

$$K_I = \frac{\mu}{(\kappa + 1)} \sqrt{\frac{2\pi}{L}} (4 w_{13} - w_5 - 3 w_6 - 4 w_9 + w_1 + 3 w_2) \quad (4.10)$$

4.4 DIMENSIONAL ANALYSIS OF THE TENSILE-SHEAR SPOT WELD SPECIMEN

Several tensile-shear specimen dimensions were studied; the applied load (P) was kept equal to 2000 N. for all of the analyzed cases. The different finite element models (for the different dimensions) had the radial size of the first ring of elements equal to 0.05 mm and spanned the 90° circumferential crack tip with six elements. Table 4.3 includes the stress intensity factors, K_I and K_{II} , as well as the averaged J-integral (over contours 2-5) for different sheet thicknesses, nugget diameters and specimen widths. The table also include the plane strain energy release rate, G, calculated from:

$$G = \frac{(1 - \nu^2)}{E} [K_I^2 + K_{II}^2] \quad (4.11)$$

Table 4.3 also shows the percentage of the range of the J-integral over the contours 2 - 5 as well as the percentage of the difference between the J-integral and the calculated plane strain energy release rate G. The J-integral over the contours 2 - 5 varies by 0.3 % at most; this low

percentage establishes more confidence in the results. The percentage of the difference between the J-integral and the calculated plane strain energy release rate G is below 3.2 %; thus the analyzed cases are probably closer to the plane strain situation rather than the plane stress which is about 11 % higher than the plane strain case (for $\nu = 0.33$).

4.4.1 The effect of the Specimen Dimensions on K_I , K_{II} and the J-integral

Figure 4.3 shows the effect of the sheet thickness on K_I , K_{II} and subsequently the J-integral. The dependance of the three values on the sheet thickness can be represented by power functions as shown in Fig. 4.3. The exponents for the best-fit power functions were -0.72, -0.43 and -1.01 for K_I , K_{II} and J-integral respectively. An increase in the sheet thickness from 0.9 to 2.7 mm (for the same nugget diameter, specimen width and specimen length) resulted in a decrease in the K_I , K_{II} and the J-integral by factors of 2.2, 1.6 and 3.0 respectively; it thus appears that the sheet thickness effect on K_I is larger than its effect on K_{II} .

As shown in Fig. 4.4 the nugget diameter had a large effect on K_{II} where an increase in the nugget diameter from 4.8 to 10.0 has decreased the K_{II} value by a factor of 2.1. On the other hand, the K_I barely changed. The exponents for the best-fit power functions were -0.07, -0.99 and -1.46 for K_I , K_{II} and J-integral respectively. It thus appears that the change in the nugget diameter mainly affects the K_{II} and subsequently the J-integral.

As for the specimen width, Fig. 4.5 shows how K_I , K_{II} and the J-integral decreased as the specimen width was increased. K_I showed the highest sensitivity to the specimen width while K_{II} showed the least; increasing the specimen width from 22 mm to 100 mm reduced the K_I , K_{II} , and the J-integral by factors of 3.1, 1.1 and 1.9 respectively. The exponents for the best-fit power functions were -0.74, -0.06 and -0.42 for K_I , K_{II} and J-integral respectively. It should be noted that the effect of the specimen width on K_{II} tends to fade as the specimen width exceeds 50 mm. It thus appears that the change in the specimen width mainly affects the K_I (and subsequently the J-integral) specially for specimens of widths larger than 50 mm.

A specimen with an overlap equal to 50 mm rather than 38 mm was also analyzed in order to determine the effect of the overlap size on the results: see Table 4.3. The effect was insignificant when the results of the 50 mm overlap specimen was compared to the corresponding 38 mm overlap specimen (all other specimen dimensions were identical: $t = 1.4$, $D = 6.1$ and $W = 50$ mm).

As depicted in Fig. 4.6, the specimen length also affected the K_I , K_{II} and the J-integral, however, the length effect was minor when compared to the effects of the sheet thickness, nugget diameter and specimen width. When the specimen free length was increased from 95 mm to 292 mm the K_I , K_{II} , and the J-integral were barely increased by factors of 1.09, 1.02 and 1.07 respectively; the power exponents are thus all positive and less than 0.1.

The effect of the sheet cross-sectional area is also shown in Figs. 4.7-4.9. In Fig. 4.7 the K_I decreases steadily as the sheet cross sectional area is increased, however, the K_{II} and the J-integral does not show a stable trend. In Figs. 4.8 and 4.9 a distinction has been made between two cases; in the first case the specimen width was held constant while the sheet thickness was varied; conversely, in the second case the sheet thickness was held constant while the specimen width was varied. Holding the specimen width constant and increasing the sheet thickness (Fig. 4.8) decreased all three quantities for an increasing cross sectional area. The same trend has been observed in Fig. 4.9, however, in the former case the K_I , K_{II} and the J-integral showed steeper slopes and subsequently larger changes than the case in which the sheet thickness was held constant.

4.4.2 The Effect of the D/t and W/D ratios on K_I , K_{II} and the J-integral

Figure 4.10 shows the variation of K_I , K_{II} and the J-integral with the nugget diameter to sheet thickness ratio (D/t). As shown in Fig. 4.10, the results did not show a steady trend. However, when a distinction was made between the case of constant nugget diameter and varying sheet thickness and that of constant sheet thickness and varying nugget diameter, two different steady trends were observed as shown in Figs. 4.11 and 4.12. For the case where the nugget diameter is held constant, all three parameters increase with the increase of the D/t ratio. Conversely, for the case where the sheet thickness is held constant, the K_{II} and the J-integral decrease with the increase of D/t ratio while K_I remains almost unchanged. The ratios $\frac{K_I * r^{1.5}}{P}$ and $\frac{K_{II} * r^{1.5}}{P}$ have also been plotted versus the D/t ratio in Fig. 4.13. Unlike Cooper's similar curves, Fig. 4.13 showed an unsteady trend especially for the $\frac{K_I * r^{1.5}}{P}$ curve.

A behavior similar to that observed for the sheet cross sectional area and D/t ratio has been also observed for the W/D ratio as shown in Fig. 4.14. Consequently, it appears that one should not consider these factors uniquely, instead, it is preferable to consider each of the sheet thickness, nugget diameter and specimen width individually as independent parameters.

4.5 CORRELATING THE FATIGUE LIFE IN TERMS OF THE EQUIVALENT STRESS INTENSITY FACTOR

Through the finite element analyses of the specimen dimensions of tasks 24, 9, 16 and 13 the corresponding K_I and K_{II} were determined. An equivalent stress intensity factor was calculated from the K_I and K_{II} values as follows:

$$K_{eq} = (K_I^2 + K_{II}^2)^{0.5} \quad (4.12)$$

Figure 4.15 presents the total fatigue life data of tasks 24, 9, 16 and 13 in terms of the K_{eq} (solid symbols) as well as the maximum applied load (opened symbols). As shown in Fig. 4.15 the K_{eq} was not able to collapse the fatigue data of the different tasks; the scatter in the K_{eq} data was as large as that of the maximum applied load. Moreover, the solid triangles data were slightly elevated above the diamonds which means that the smaller the nugget diameter the longer the fatigue life; this strange diameter effect depicted in the K_{eq} data presentation does not show in the load-life presentation.

4.6 SUMMARY

The finite element technique was successful in determining the stress intensity factors for the complex tensile-shear specimen subjected to a mixed mode of deformation. The effects of the different specimen dimensions were determined. While both the K_I and K_{II} values decreased with the increase of the sheet thickness and the specimen width, the nugget diameter had almost no effect on K_I , however K_{II} increased with the increase of the nugget diameter. Among the studied specimen dimensions, the specimen free length was found to possess the least effect on the stress intensity factors.

The parametric study has also demonstrated the inadequacy of the sheet cross sectional area, the D/t ratio and W/D ratio as unique parameters influencing the K_I and K_{II} values; thus it is advisable to consider each of the sheet thickness, nugget diameter and specimen width individually as independent parameters.

Although the calculated stress intensity factors are extremely useful for studying the static behavior of tensile-shear specimens, the equivalent stress intensity factor has failed to correlate the fatigue data of tensile-shear specimens with different dimensions. This can be attributed to the fact that the functional dependance of the finite element K_I and K_{II} values on the different specimen dimensions is different from that sensed in the load-life presentation; compare Figs. 3.28 and 3.29 to Figs. 4.3 to 4.6.

CHAPTER V : THE DEVELOPMENT OF A FATIGUE DESIGN PARAMETER USING THE EXPERIMENTAL DATA

5.1 INTRODUCTION AND SYNOPSIS

Several parameters have been used to correlate the fatigue data of spot welds: remote loads and stresses, nugget notch root local strains and stresses and fracture mechanics parameters. Among these parameters, the fracture mechanics parameters were the most successful in correlating the fatigue data for different spot welded specimens. However, it is preferable to fit the analytical solutions of the fracture mechanics parameters to experimental fatigue data in order to account for the multiaxial fatigue and mixed mode material behavior and to avoid the inevitable differences between the static and the fatigue behavior of spot welds as will be discussed in Chapter VI.

Early research work in the high cycle multiaxial fatigue field (see Appendix-D) indicate the importance of the shear and normal stresses as the main components of the fatigue damage parameters. Guest [59], Findely [60] Stulon and Cummings [61] all realized that fatigue failures initially started on the planes of maximum shear and thus their damage parameters had two main components: the first component reflected the effect of the maximum shear stress; the second component, which was usually multiplied by a material constant, reflected the effect of the normal stress component on the plane of maximum shear. The above mentioned forms of the damage parameters were extended to the low cycle regime through the use of strains rather than stresses. Miller et al. [63-65], Lohr and Ellison [66] and Socie et al. [67-70] combined the shear and normal strains on the critical plane in their damage parameters. In both regimes, high and low cycle regimes, the damage parameters include material constants that reflects the material response to the shear components.

Similarly, several investigators [72-74] in the field of fracture mechanics (see Appendix-E) have shown that possible mixed mode fracture criteria possess an elliptical shape which is function of the different stress intensity factors and material constants. On the other hand, Tanaka [75] showed that the threshold stress intensities, $K_{I\text{ th}}$ and $K_{II\text{ th}}$, are also related through an elliptical functional form; this time the ingredients of the functional were the threshold stress intensities and material constants which are different from those of the fracture criteria. Tanaka has also shown that crack growth data show better correlation in terms of an equivalent stress intensity factor rather than in terms of the stress intensity factors K_I , K_{II} or K_{III} individually.

The failure of the stress intensity factors to correlate the fatigue data of tensile-shear specimens in Chapter IV is attributed to the fact that the functional dependence of the K_I and K_{II} values on the different specimen dimensions is different from that encountered in fatigue. Moreover, the initial stress intensity factors reflect notch root strains and not crack development. Consequently, empiricism together with the above mentioned multiaxial fatigue and mixed mode fracture mechanics concepts will be used to derive a fatigue design parameter K_i which is basically a Mode I equivalent stress intensity factor modified empirically to account for the effects of the different specimen dimensions on the fatigue behavior of spot welds. The K_i parameter will also consider the different responses of the low carbon and the HSLA materials to Mode II stress intensity factor and it will be used in correlating the total fatigue life data for coach-peel, tensile-shear and double-shear spot welded specimens. The K_i parameter will also be used in correlating the fatigue data of Stages I, II and III of the tensile-shear specimens tested in this study.

5.2 THE K_i PARAMETER

5.2.1 Modelling the Effects of the Tensile-Shear Specimen Dimensions

Figure 4.15 demonstrated the inadequacy of the equivalent stress intensity factor calculated from the finite element K_I and K_{II} values in correlating the fatigue data of tensile-shear specimens with different dimensions. The reason for this failure is believed to be related to the difference between the static and the fatigue behavior of spot welds; while the static behavior may be related to the initial stress intensity factors, the same parameters are not as useful in studying the crack development and the fatigue behavior of spot welds.

As shown in Fig. 3.28, the fatigue strength (at 10^5 cycles) changes linearly with the sheet thickness; the (0.0, 0.0) data point is a fictitious point which has to be satisfied by the linear relation as much as possible. Two of the data points in Fig. 3.28 were obtained in this study from Tasks 9 and 16. The other two data points were obtained from Hiroshi's data [14]; the width of Hiroshi's specimens were equal to 40 mm (as close as possible to the specimen width used in this study, 38 mm). Similarly, the effect of the specimen width is determined from Fig. 3.29; the relation between the fatigue strength and the specimen width can be represented by a power function whose exponent is equal to 0.4866. Two data points were obtained from Tasks 24 and 9 of this study while the other two data points were obtained from Hiroshi's [14] and Cooper's [33] data. Hiroshi's sheet thickness and nugget diameter were equal to 1.4 and 6.0 mm respectively while Cooper's sheet thickness and nugget diameter were equal to 1.5 and 6.0 mm.

Based upon the above two functional forms and the weak dependence of the fatigue life on the nugget diameter, the fatigue data of Tasks 24, 9, 16 and 13 are plotted in Fig. 5.1 in terms of the maximum applied load P as well as the factor $\frac{P}{t \sqrt{W}}$ which collapses the data into a narrow band and incidentally possesses the same dimensions as the stress intensity factors.

5.2.2 Correlating the Fatigue Data of Different Spot Welded Geometries

Figure 5.2 compares the fatigue performance of several tensile-shear and coach-peel joints of low carbon and HSLA steels [81]. The relatively poor performance of the coach-peel specimens is attributed to a difference in the nature of the applied loads and subsequently the local parameters at the edge of the spot welds. While the coach-peel joint is subjected to bending moments and axial loads, the tensile-shear is mainly subjected to shear and bending moments. Moreover, Fig. 5.2 also shows that 0% off edge coach-peel specimens (i.e the nugget is located at the edge of the coach-peel flange and thus a larger eccentricity is created) possess lower fatigue strengths than coach-peel specimens with weld nuggets located at the center of the flange. In this study, the nugget location is always at the center of the coach-peel flange or the tensile-shear overlap unless otherwise specified. As shown in Fig. 5.2, the applied load fails to correlate the fatigue data of tensile-shear and coach-peel specimens with different nugget locations.

Figure 5.3 shows one-half of a spot weld subjected to arbitrary load (F) at and an angle (α) to the sheet normal. Because of the eccentricity of the loading (e), the nugget experiences a normal force (P) a shearing force (Q) and an applied moment ($M = F * e$). When $\alpha = 90$ degrees, the loading condition is that of the coach-peel spot welded specimens. When α approaches 0 degrees, the loading condition is that of the tensile-shear. In general, a spot weld nugget could be subjected to a combination of shearing loads (Q), axial loads (P) and bending moments (M), that is a combination of Mode I and Mode II loadings.

A local parameter (K_i) which describes the notch root stresses (and thus the incidence of fatigue there) was developed by superposing the stress intensity factors for two sheets joined by a circular region. The stress intensity factors for two half-spaces joined by a circular region subjected to an axial load (P), moment (M) and shear load (Q) are given by [47]:

$$K_{\text{axial}} = \frac{P}{2r\sqrt{\pi r}} \quad (5.1)$$

$$K_{\text{moment}} = \frac{3M}{2r^2\sqrt{\pi r}} \quad (5.2)$$

$$K_{\text{shear}} = \frac{Q}{2r\sqrt{\pi r}} \quad (5.3)$$

where:

- r = Nugget radius,
- P = Normal component of the applied load: see Fig. 5.3
- Q = Shearing component of the applied load
- M = $F \cdot e$
- e = Eccentricity of loading

Linear superposition at the edge of the spot weld leads to:

$$K_I = K_{\text{axial}} + K_{\text{moment}} \quad (5.4)$$

$$K_{II} = K_{\text{shear}} \quad (5.5)$$

Through a simplified form of Broek's Mode I equivalent stress intensity factor [74], the initial, equivalent Mode I stress intensity factor of a spot weld is:

$$K_{I_{\text{eq}}} = \sqrt{K_I^2 + \beta K_{II}^2} \quad (5.6)$$

where β is a material constant which reflects the material response to Mode II. The material constant β was obtained by collapsing two sets of total fatigue life data for specimens with the same sheet thickness, nugget diameter and specimen width. The first set of data was for coach-peel specimens (Mode I only) while the second was for tensile-shear specimens (Modes I and II). Values of β obtained in this study from data in reference [81] were 2 and 3 for the LC and HSLA specimens respectively as shown in Figs. 5.4 and 5.5.

The $K_{I_{\text{eq}}}$ can collapse the fatigue data of tensile-shear and coach-peel specimens of the same sheet thickness, nugget diameter and specimen width. However, when the $K_{I_{\text{eq}}}$ was used to correlate the fatigue data of tensile-shear specimens with different dimensions, a wider scatter (relative to the applied load-life data presentation) was observed: see Fig. 5.6. The $K_{I_{\text{eq}}}$ exaggerates the effect of the nugget diameter and fails to account for the variation in the sheet thickness and specimen width. Consequently, the $K_{I_{\text{eq}}}$ (Eq. 5.6) was divided by a geometrical correction factor (G) (Eq. 5.7) to obtain the $K_{I \text{ max}}$ parameter (Eq. 5.8) which reflects differences in loading condition (Mode I and II), material response to Mode II and differences in nugget diameter (D), sheet thickness (t) and specimen width (W). The geometrical

correction factor (G) was obtained by collapsing the total fatigue life data of tasks 24, 9, 16 and 13 (of Table 3.1) into a narrow band as shown in Fig 5.7. The key points in deriving the G factor were to account for the different modes of deformation and at the same time maintain the $\frac{P}{t \sqrt{W}}$ form in the case of tensile-shear specimens.

$$G = \sqrt{\frac{t^2 W}{r^3} \left(\frac{9t^2}{4r^2} + 1 \right)} \quad (5.7)$$

$$K_{i \max} = \frac{K_{Ieq}}{G} = \sqrt{\frac{K_{I \max}^2 + \beta K_{II \max}^2}{\frac{t^2 W}{r^3} \left(\frac{9t^2}{4r^2} + 1 \right)}} \quad (5.8)$$

Furthermore, three sets of tensile-shear specimens loaded with $R = -0.2$, $R = 0$ and $R = 0.5$ (tasks 5, 4 and 6 of Table 3.1) were used to determine the R-ratio effect. Four different parameters ($K_{i \max}$, $\Delta K_i = K_{i \max} * (1 - R)$, $(\Delta K_i * K_{i \max})^{0.5}$ and $K_{i \max} * (1 - R)^{0.85}$) were used to correlate the total fatigue life data of the considered load sets. The least scatter in the data was observed in the case of $K_{i \max} * (1 - R)^{0.85}$; see Fig 5.8. Hence, the final form for the K_i parameter is as follows:

$$K_i = \sqrt{\frac{K_{I \max}^2 + \beta K_{II \max}^2}{\frac{t^2 W}{r^3} \left(\frac{9t^2}{4r^2} + 1 \right)}} * (1-R)^{0.85} \quad (5.9)$$

5.3 CORRELATING THE FATIGUE DATA IN TERMS OF THE K_i PARAMETER

Figure 5.9 presents the total fatigue life data of the coach-peel and tensile-shear specimens of Fig. 5.2 in terms of the K_i . The K_i collapsed the data into a narrow band despite the differences in specimen type and weld nugget location. It should be noted that coach-peel specimens are subjected to Mode I only; and that unlike the tensile-shear specimens, the coach-peel are insensitive to the base metal. HSLA and low carbon coach-peel specimens behave similarly in the long life regime; see Fig. 5.2.

K_i and load-life fatigue data of coach-peel and double-shear specimens from reference [25] are presented in Fig. 5.10. The load-life presentation shows that while the low carbon and HSLA coach-peel specimens behave similarly at the long life regime, the double-shear specimens which are subjected to a Mode II only [49,50] show longer fatigue lives than the corresponding HSLA specimens. This difference in behavior is accounted for in the K_i parameter through the β constant and is mainly attributed to the residual stress state and its effect on the initial crack development as will be discussed in Chapter VI. Figure 5.10 also shows how the wide scatter in the load-life data has been eliminated by the use of the K_i parameter.

HSLA and low carbon coach-peel, double-shear and tensile-shear total fatigue life data (about 400 data points obtained in this study as well as those of references 25 and 81) are correlated in terms of the K_i in Fig. 5.11. Three best-fit equations are generated; one for the HSLA data, the second for the low carbon data and the third for the combined HSLA and low carbon data. As shown in Fig 5.11, the best-fit lines lie close to each other.

Figure 5.12 presents the Stage I fatigue data for all the tensile-shear specimens monitored by the potential drop technique. Similarly, three best-fit equations were generated for the HSLA and the low carbon data separately and combined; the best-fit lines lie close to each other especially in the long life regime where most of the data points fall. Similar plots and best-fit equations for Stages II and III are shown in Figs. 5.13 and 5.14.

5.4 SUMMARY

The K_i parameter collapsed the total fatigue life data of coach-peel, double-shear and tensile-shear specimens into a narrow band; it considered the different modes (Mode I and II) at the edge of the spot weld, the difference in the fatigue response of HSLA and low carbon specimens and the different geometrical dimensions.

The K_i parameter should provide the designer with a useful tool for determining the fatigue life of different spot-welded joints. Moreover, the K_i parameter should help the designer determine and compare the effects of several variables on the fatigue performance of the joints without having to resort to extensive testing as will be shown in Chapter VI.

CHAPTER VI : DISCUSSION

6.1 INTERPRETATION OF THE RESISTIVITY CHANGES

The measured changes in resistivity during the fatigue life of a spot weld are attributed to several causes and can be broken into three periods: see Figs. 6.1, 3.3 and 3.7. The first period (1) is characterized by a rapid rate of change in resistivity and occurs during the first few cycles. This first period is then followed by a second period (2) during which the resistivity changes at a slower rate. Finally, there is a third period (3) during which the rate of change of the resistivity increases once more. These three periods are believed to coincide with the following events: Period 1 - breaking of contacts between sheets; Period 2 - multiple microcrack initiation and early crack growth; and Period 3 - the formation of a major macrocrack and its propagation through the thickness and then through the width of the specimen. These events have been confirmed through the optical examination of sectioned specimens: see Figs. 3.5 and 3.6.

Thus the early change in resistivity during Stage I (Periods 1 and 2) is mainly dominated by the changes in resistivity due to the breaking of contacts between the sheets. This dominance has been supported by the microscopic observation of cracks after sectioning several 1.4 mm thick specimens which had changes in resistivity less than $2 \mu\Omega\text{cm}$; no cracks were observed (at 800X) while sectioning these specimens. The argument that cracks might have been completely removed within one polished layer infers that these missed cracks were 0.03 mm in depth and 0.13 mm in width (see section 2.5). Such microcracks are still too small to cause major changes in resistivity that can be sensed by the Microhmeter.

Later, the microcracks grow and link together forming the major crack as shown in Fig. 3.7. The onset of the major crack formation ($RR \approx 0.12$) begins Stage II during which the changes in resistivity increases steadily and reflects mainly the growth of the major crack. The rate of change in resistivity, or the crack growth rate, over Stage II is not constant as shown in Fig. 6.1 where it reaches its maximum at the end of Stage II. It should be emphasized that changes in resistivity during Stage III can not be correlated to the crack length because at that stage the crack is growing through the width of the specimen in an unsymmetrical fashion (with respect to the axis of loading).

Figure 6.1 also shows how the failure side might change during the fatigue life. In the case of the low carbon specimen the microcracks initiated and linked faster on one of the sides, however, for an unknown reason the major crack slowed down while that of the other side

(eventually the failure side) grew, broke through the thickness and through the specimen width. This behavior did not appear consistently; it may be related to the crack closure phenomenon and the critical notch root radius.

The above observations contradict the work of Smith and Cooper [33,34]. Smith and Cooper assumed that the early changes in potential is solely caused by crack growth and consequently concluded that the total fatigue life of spot welds is exclusively devoted to the propagation of a single fatigue crack. They also concluded that the single fatigue crack propagates at a constant growth rate during most of the fatigue life of their tensile-shear mild steel specimens. The HSLA and low carbon tensile-shear specimens tested in this study behaved differently as shown in Fig. 6.1; both showed a typical cumulative damage curve where the growth rate varies during the fatigue life. Probably, the reported constant growth rate is due to the misinterpretation of the early change in the measured potential as to be caused by the growth of a single crack.

6.2 ORIGINS OF THE DIFFERENCES BETWEEN THE BEHAVIOR OF THE LOW CARBON AND HSLA MATERIALS

The low carbon (LC) specimens experienced longer Stage I lives than the corresponding HSLA; this difference resulted in a slightly longer fatigue life for LC material in the long life regime. Several arguments may be used to explain the longer Stage I duration of the LC tensile-shear specimens. Such arguments are mainly based on residual stresses, fatigue notch factor, threshold stress intensity, local stress strain hysteresis and the material response to Mode II stress intensity factor as will be discussed hereafter.

The (as-welded) residual stresses at the periphery of the nugget where crack initiation and early growth take place are believed to be tensile and limited only by the yield point of the material in that locality (the heat-affected-zone, HAZ). While it is difficult to measure the yield strength of these HAZ materials, the yield point can be correlated with the micro-hardness of those regions [82]. Hardness measurements in the HAZ for both materials are listed in Table 6.1. The HSLA HAZ has a higher hardness which indicates a greater capability of sustaining higher residual stresses than the low carbon HAZ. The existence of higher residual stresses explains the relatively poor fatigue performance of the tensile-shear HSLA specimens in Stage I. Preloaded HSLA tensile-shear spot welds showed a marked improvement in the Stage I duration presumably due to induced compressive residual stresses in the region of crack initiation and early crack growth: see Figs. 3.24 to 3.27. Low carbon tensile-shear specimens are expected to behave similarly but to a lesser extent since the HSLA material can sustain much higher levels of compressive residual stress than the low carbon.

The insensitivity of coach-peel specimens to base metal (as compared to tensile-shear and double-shear specimens) is probably due to the initial crack development. While cracks initially extend parallel to the sheets interface in coach-peel specimens, cracks initiate and extends at 60° or more with the sheets interface in tensile-shear and double-shear specimens. The cracking direction in tensile-shear specimens is probably more affected by the residual stresses which were found to be radial and circumferential tensions at the surface of the specimen [83].

Not only does the higher hardness of the HSLA indicate a higher residual stress, but also it indicates a higher fatigue notch factor. McMahon [82] related the fatigue properties and Peterson's constant (through the ultimate strength) to the hardness measurements as follows:

$$a = 25.4 * 10^{-3} \left(\frac{600}{\text{BHN}} \right)^{1.8} \quad (a \text{ in mm, BHN} = \text{Brinell hardness number}) \quad (6.1)$$

It follows from the hardness measurements in Table 6.1 that Peterson's constant (a) for the HSLA and low carbon coarse grain regions are 0.058 and 0.122 mm respectively and that K_{fmax} for the HSLA and low carbon tensile-shear specimens ($t = 1.4$, $D = 6.1$ and $W = 38$ mm) are equal to 15 and 10 according to Eqs. B-7 and B-8. Despite the fact that the K_{fmax} for the HSLA is almost 1.5 times that of the low carbon, the roughly estimated fatigue limit which is obtained by dividing the ultimate strength (Table 6.1) by $2 K_{fmax}$, is almost equal in both cases: 40 and 39 MPa for the considered HSLA and low carbon tensile-shear specimens respectively. With almost no difference in the fatigue limits of the considered tensile-shear specimens, it is difficult to explain the difference in the behavior of these two materials in terms of the estimated fatigue limit. The same fatigue limit argument explains the controversial conclusions [4,14,54] regarding the effects of the base metal properties on the fatigue strength of spot welds since the hardness of the HAZ are sensitive to several variables that might produce different HAZ properties from steel sheets of the same classification.

Unlike the K_{Ic} , ΔK_{th} for high strength steels are generally less than those of the lower strength steels. Based on the hardness measurements, the HSLA HAZ threshold stress intensity factor is expected to be lower than that of the low carbon specimens and consequently, the sharp notch which is almost as sharp as a crack, will propagate faster in the HSLA specimens resulting in a shorter Stage I fatigue life. Although this threshold argument may appear logical, it is incapable of explaining why the HSLA and low carbon coach-peel specimens behaved similarly.

Kan [84] found that the stable local hysteresis loop of tensile-shear HSLA specimen has larger stress amplitude than that of the low carbon specimens (for the same strain

amplitude). For a 0.01 strain amplitude, the stress amplitude of the HSLA and low carbon tensile-shear specimens were 550 and 248 MPa respectively. Thus, the HSLA tensile-shear specimens experience higher local stresses than the corresponding low carbon specimens; this higher local stresses may be the cause of the poor performance of the HSLA tensile-shear specimens during Stage I.

The load-life representations of the fatigue data in Figs. 5.2 and 5.10 show that the low carbon tensile-shear and double-shear specimens outperform the corresponding HSLA specimens. On the other hand, the HSLA and low carbon coach-peel specimens at the long life regime behave similarly. This difference in behavior, which seems to be specimen dependant, can be explained in terms of the applied modes of deformation; the tensile-shear specimen is subjected to a mixed mode of deformation (Mode I and II at the specimen centerline), the double-shear specimen is subjected to Mode II only and the coach-peel specimen is subjected to Mode I only. Therefore, it appears that the two materials respond to Mode I equally while Mode II is more detrimental in the case of the HSLA specimens.

6.3 A COMPARISON BETWEEN THE DIFFERENT MODELS FOR ESTIMATING THE TENSILE-SHEAR STRESS INTENSITY FACTORS

Since the finite element stress intensity factors were not able to correlate the fatigue data of tensile-shear specimens with different dimensions, it is necessary to demonstrate that this inability was not due to the finite element method adopted in this study. Such a demonstration justifies the resort to empiricism in deriving the K_I parameter and can be achieved by comparing the current methods for estimating the stress intensity factors to that used in this study.

As mentioned in Chapter II, Pook's stress intensity factors agreed well with the results obtained from Cooper's two dimensional finite element analysis and Radaj's two dimensional boundary element solution. Despite this agreement, the models are conceptually different; while Pook's expressions imply that the stress intensity factors are solely dependant on the average shear stresses conveyed by the nugget (see Appendix-A), Radaj's plane contour model [49] implies that the stress intensity factor are mainly dependant on the structural normal stresses on the sheet cross section (also see Appendix-C). In addition, Pook has used Chang's lap bonded results [29]; the use of the lap bonded results have obscured the effect of the nugget diameter on the stress intensity factors.

Contrary to the two dimensional analysis, Cooper's and Radaj's reported results obtained from the three dimensional analysis were less than Pook's stress intensity factors by almost a factor of two probably because they account for the geometry effects in the specimen

width direction. Subsequently, the K_I and K_{II} values obtained in Chapter IV will be compared to the corresponding results obtained from Cooper's and Radaj's three dimensional analyses. While Cooper's corresponding K_I and K_{II} values were obtained by graphical interpolation from his curves, stresses obtained from the finite element solutions in this study were used to evaluate the corresponding Radaj's K_I and K_{II} values.

Figures 6.2 and 6.3 show Radaj's K_I and K_{II} values calculated from stresses at different locations behind the crack-like notch tip for tensile-shear specimens with variable specimen width (W) and the same sheet thickness, nugget diameter and specimen length ($t = 1.4$, $D = 6.1$ and $L = 140$ mm). As shown in Figs. 6.2 and 6.3, Radaj's solution is highly dependant upon the location at which the stresses are calculated or measured; more than 200% increase in the K_I and K_{II} values occurred over 5 mm distance. A second degree best-fit polynomial was used to extrapolate the results to the crack tip ($X = 0$). Table 6.2 compares the K_I and K_{II} values obtained in this study to Radaj's extrapolated values; the K_{II} values are in very good agreement, however, Radaj's K_I values are about 25% less than those obtained in this study.

Cooper's corresponding values are 86 and 176 MPa $\sqrt{\text{mm}}$ for K_I and K_{II} respectively. Note that Cooper's curves do not consider the effect of the specimen width since they were generated for 50 mm wide and 95 mm long specimens which are closest to the dimensions of the third specimen in table 6.2. Despite the difference in specimen length and the relative coarseness of Cooper's mesh, a good agreement between Cooper's results and the third value in Table 6.2 still exist; the difference is within the length effect shown in Fig. 4.6. However, it should be emphasized that the use of Cooper's curves will lead to erroneous results if the nugget diameter of the considered specimen is different from that which Cooper analyzed (Cooper obtained his curves for variable sheet thickness but for the same nugget diameter, 6.0 mm). The reason for the erroneous results is clear in Figs. 4.13 and 4.10 to 4.12. The figures show that a distinction has to be made between two cases: case 1, where the sheet thickness is varied while the nugget diameter is held constant; and case 2, where the nugget diameter is varied while the sheet thickness is held constant. Such a distinction is missed in Cooper's curves as well as in Pook's solution.

The above comparison demonstrates the superiority of the finite element K_I and K_{II} values obtained in this study among other solutions. The superiority of the finite element method is attributed to three main reasons: the agreement between the calculated energy release rate (G) and the J-integral (see Chapter IV); the independence of the finite element K_I and K_{II} values on the location as compared to Radaj's solution; and unlike Pook's solution, the finite element method considers the nugget diameter and the sheet thickness independently.

6.4 FATIGUE DESIGN PARAMETERS

The fatigue design parameters can be categorized into three main groups: remote loads and stresses, nugget local strains and stresses and fracture mechanics parameters. The remote loads and stresses failed to correlate the fatigue data for specimens with different dimensions and of different geometries. Hence, basing fatigue design on these parameters requires testing each type of geometry. Nonetheless, load-life fatigue curves have helped studying and understanding the effects of several important factors that affected the total fatigue life of spot welds and thus they are indispensable.

The nugget notch root local strains and stresses collapsed the fatigue data of similar geometries into a narrow band regardless of the specimen dimensions, however, these parameters are difficult to measure or estimate; the strains of interest are those at the interface of the joint sheets while those measured are usually at the nugget edge on the specimen outer surface (back strains) which is an area of high stress concentration. This high stress concentration causes the technique to be highly dependant on the size and exact location of the strain gauges which is the same problem encountered with Radaj's model for the stress intensity factors. Limited with these difficulties, the nugget notch root local strains and stresses failed to collapse the fatigue data of different geometries into a narrow band and also failed to provide the designer with reproducible fatigue properties.

The fracture mechanics parameters were more successful in correlating the fatigue data for specimens with different dimensions as well as those of different geometries. Within this group of parameters, two subgroups may be identified according to the nature of these parameters: analytical or empirical parameters. The analytical parameters have a sound theoretical basis, however, this group of parameters can not account for the differences between the static and the fatigue behavior of spot welds. Base metal properties and the nugget diameter effects are examples of such differences. While higher base metal ultimate strength yielded higher static strengths for the tensile-shear and cross-tension specimens [1,7], the effect of the base metal properties on the fatigue strength was different. The low carbon tensile-shear specimens yielded slightly higher fatigue strengths than the corresponding HSLA specimens while low carbon and HSLA coach-peel specimens showed almost the same fatigue strengths. As for the nugget diameter effect on the static and fatigue strengths of tensile-shear specimens, the static strength was found to be highly dependant on the nugget diameter [1,4,5] while the overall fatigue strength (over the three stages of the fatigue life) was found almost independent of the nugget diameter [10,11,16, 54].

Consequently, the main reason for the superiority of the K_i parameter over the finite element stress intensity factors in correlating the fatigue data is attributed to the fact that the K_i has been derived to reflect the effects of the sheet thickness (t), specimen width (W) and nugget diameter on the fatigue behavior of the spot welded specimens ($1/t$, $1/\sqrt{W}$ and no dependance on nugget diameter as shown in Figs. 3.28, 3.29 and 3. 13). On the other hand, the finite element stress intensity factors show different dependancy on the specimen dimensions especially the nugget diameter as shown in Figs 4.3 to 4.5. The dependancy of the stress intensity factors on D seems to agree with the static behavior of spot welds rather than the fatigue behavior; the stress intensity factors reflect notch root strains rather than crack development.

Compared to Davidson [7,10,11] and Hiroshi's [14] empirical parameters, the K_i is applicable to specimens other than the tensile-shear specimen to which these parameters are limited. In addition, the K_i parameter does not require any experimental measurement and considers the mixed mode of deformation at the edge of the spot weld along the specimen centerline.

The K_i parameter allows the designer to study the effects of different variables relating to the fatigue problem of spot welds and estimate the total fatigue life as well as its stages as will be shown in the next section.

6.5 THE K_i PARAMETER, ITS USE AND APPLICATION

The main driving force for this study was to provide the designer with a simple and useful design tool which allows him to predict the effects of the different variables on the fatigue behavior of the spot welds without having to resort to extensive test programs. The ability of the K_i parameter to satisfy the designer needs will be demonstrated hereafter.

As shown in Chapter V, the general form of the K_i parameter is given by

$$K_i = \sqrt{\frac{K_{I \max}^2 + \beta K_{II \max}^2}{\frac{t^2 W}{r^3} \left(\frac{9t^2}{4r^2} + 1 \right)}} * (1-R)^{0.85} \quad (6.2)$$

According to Eqs. 5.1 and 5.2 the K_I for the coach-peel specimen with an applied force (F) and an eccentricity (e) is given by:

$$K_I = \frac{F}{2r\sqrt{\pi r}} + \frac{3\Gamma^*e}{2r^2\sqrt{\pi r}} = \frac{F}{2r\sqrt{\pi r}} * \left(1 + \frac{3e}{r}\right) \quad (6.3)$$

therefore for $R = 0$, Eq. 6.2 can be expressed as:

$$K_i = \frac{F}{2t\sqrt{\pi W}} * \left(1 + \frac{3e}{r}\right) * \left(\frac{9t^2}{4r^2} + 1\right)^{-0.5} \quad (6.4)$$

Equation 6.4 reflects the importance of the eccentricity (e) in determining the fatigue life of tensile-shear specimens and allows the designer to quantify the effect of offsets in the nugget location. The effect of the flange angle of coach-peel specimen can also be studied through the K_i parameter. For a θ° flange angle (with the vertical), Eq. 6.2 can be expressed as:

$$K_i = \frac{F}{2t\sqrt{\pi W}} * \left\{ \left(1 + \frac{3e}{r}\right)^2 * \sin^2\theta + \beta * \cos^2\theta \right\}^{0.5} * \left(\frac{9t^2}{4r^2} + 1\right)^{-0.5} \quad (6.5)$$

Now consider a defective coach-peel specimen where the nugget radius was equal to 2.4 mm (specimen with defect) instead of 2.9 (intended specimen) and the weld nugget was offset by 11 mm such that the eccentricity of the load " e " is equal to 31 mm instead of 20. For an equal fatigue life (i.e equal K_i) Eq 6.4 predicts a reduction in the sustained fatigue load to about 0.58 that of the intended joint. A practical remedy for this defective joint is simply the reduction of its flange angle. Equation 6.5 predicts an improvement in the sustained fatigue load to about 0.78 that which was intended as a consequence of reducing the flange angle to about 48° . Figure 6.4 shows the experimental results for the considered cases; at 10^6 cycles, the sustained fatigue load of the defective and the 48° joint are 0.56 and 0.88 that of the intended specimen respectively.

Similarly, for a tensile-shear specimen Eq. 6.2 reduces to:

$$K_i = \frac{F}{2t\sqrt{\pi W}} * \left(\frac{9t^2}{4r^2} + \beta\right)^{0.5} * \left(\frac{9t^2}{4r^2} + 1\right)^{-0.5} \quad (6.6)$$

Equation 6.6 can be used to clarify the effect of using HSLA instead of low carbon steel sheets on the fatigue behavior of the corresponding tensile-shear spot welds. According to yield stresses (see Table 3.3), a 2.7 mm thick low carbon steel sheet can be replaced by a 1.4 mm HSLA sheet. Subsequently, the nugget radius is decreased from 4.30 to 3.03 mm. For an equal fatigue life (i.e equal K_i) Eq. 6.6 predicts that the sustained fatigue load for the HSLA

tensile-shear specimen is about 0.42 that sustained by the low carbon specimen. Table 3.6 provides the best-fits for the load-life data. At 10^6 cycles (for $R = 0$) the sustained fatigue load for the HSLA and low carbon specimens are 2280 and 4146 N respectively; the ratio of the sustained loads is 0.55. It should be noted that the reduction in the fatigue load is mainly due to the reduction in sheet thickness and not because of superiority of the low carbon steel sheets.

Apart from studying the effects of the different variables on the fatigue performance of spot welded joints, the K_i parameter can be used to correlate and predict the fatigue life of spot welds. Figure 6.5 and 6.6 show how the K_i parameter collapses the fatigue data of different spot welded geometries in the literature into a narrow band. In addition, Figure 6.5 and 6.6 show also the agreement between the best-fit equation obtained in this study and the recent fatigue data of reference [85] as well as Stanford's (sheet to channel specimen) [86] and Davidson's (channel to channel specimens) [10,11].

Rivet's [18] tensile-shear data were also correlated in terms of the K_i parameter in Fig. 6.7; the figure shows how the K_i parameter collapses the fatigue data of specimens with different sheet thicknesses, nugget diameters and widths. Figure 6.7 shows also a slight deviation of Rivets long life data ($N > 10^6$ cycles) from the best-fit equation obtained in this study. This slight deviation is attributed to two main reasons: the runout cutoff used in this study and Rivet's definition of failure. The runout cutoff used in this study was 3×10^6 cycles and consequently the extrapolation of the best-fit equation beyond that limit may be questionable. Rivet's definition of failure where fatigue tests were halted when a visible crack of 15 mm length was observed on the surface of the specimen deprived the specimens from completing the Stage III fatigue life as defined in this study. It should be noted that the importance of Stage III increases for wider specimens and that crack arrest during that stage may sometimes occur [25] at low remote stress levels.

As for fatigue life estimates, Figs. 6.8 to 6.11 show the estimated fatigue life versus the experimental life. While the majority of the points lie between the two dashed lines representing a factor of two between the estimated and the experimental life, a few points fell outside the two dotted lines which represent a factor of three between the estimated and the experimental life. It should be noted that the estimated life for Hiroshi's data [14] was limited to the sum of Stages I and II since the failure was defined by the first appearance of a visible crack on the specimen surface. Calculated values of N_I and N_{II} were proportionately increased or decreased so that the sum of N_I , N_{II} and N_{III} equalled the calculated value of N_t .

6.6 LIMITATIONS OF THE K_i PARAMETER

It should be noted that the K_i parameter with its current form does not account for the tail effect (contact area behind the nugget) which highly affects the fatigue life of the coach-peel specimens. The K_i parameter is also unable to account for the effect of initial overloads. Moreover, the K_i does not consider any redundancy in the original structure which may result in a redistribution of stresses and subsequent changes in the fatigue behavior.

It should be also noted that the best-fit equations were obtained for fatigue data with total fatigue lives within the range of 10^4 to 3×10^6 cycles. The extrapolation of the best-fit equations to the low cycle regime ($N_t < 10^3$ cycles) might overestimate the fatigue life. The fatigue behavior of spot welds in the low cycle regime is mainly governed by the propagation stages during which the fatigue cracks are subjected to almost Mode I only and behaves as central cracks in a uniaxially loaded plates. This explains why the Stage I data show a better correlation in terms of K_i than Stages II and III where cracks are less affected by the residual stresses as is the case with the coach-peel specimens.

On the other hand, the extrapolation of the best-fit equations beyond 3×10^6 cycles can not account for the situations where the cracks growing through the specimen width may halt and thus the complete separation may never occur.

Fortunately, the last two limitations for the extrapolation of the best-fit equations are not frequently encountered in the fatigue analysis of spot welds. The low cycle regime is seldom encountered because the static considerations controls the design at such high load levels while the crack arrest phenomenon usually occurs in specimens with widths larger than the values specified by the specifications.

It should be emphasized that the calculated values of N_I , N_{II} and N_{III} have to be proportionately increased or decreased so that the sum of N_I , N_{II} and N_{III} is equal to the calculated value of N_t .

CHAPTER VII : CONCLUSIONS, RECOMMENDATIONS AND PROPOSED FUTURE WORK

7.1 CONCLUSIONS

1. Changes in resistivity were correlated with crack depths measured during Stage II during which changes in resistivity were caused by the growth of a major crack. This correlation permitted the boundaries between the three stages of fatigue life to be identified based solely on the measured resistivity.
2. A poor correlation between the resistivity changes and measured crack depth was observed during Stage I. This poor correlation was attributed to the breaking of the contacts between the two sheets of the weldment and to multiple crack initiation around the periphery of the weld nugget.
3. Tensile-shear spot welds of galvanized low carbon steel performed better than the galvanized HSLA during Stage I. Both materials gave about the same total fatigue life, but the low carbon material performed better in the long-life region. The notch-root residual stresses (based on higher values of hardness) in the HSLA spot weld HAZ is believed to be the main cause for the difference in the fatigue behavior of the HSLA and low carbon tensile-shear specimens.
4. Sheet thickness had the largest effect on the total fatigue life while the nugget diameter had the least.
5. Stage I constituted more than 40% of the total life of low carbon specimens within the life range 10^5 to 10^7 cycles. This percentage increases at longer lives.
6. Load ratio had an influence on the total fatigue lives of both low carbon and HSLA spot welds. For both materials, there was virtually no difference between tests run at $R = 0$ and $R = -0.2$, but both materials gave shorter lives when tested under $R = 0.5$ load conditions.

7. Tensile overloads increased the fatigue lives of HSLA specimens by orders of magnitude; the coining technique should be considered as an important phase in the welding cycle.
8. The finite element technique provide an accurate method for determining the stress intensity factors for the complex tensile-shear specimen subjected to a mixed mode of deformation. The results demonstrated the inadequacy of the sheet cross sectional area, the D/t ratio and W/D ratio as unique parameters determining the K_I and K_{II} values; thus it is advisable to consider each of the sheet thickness, nugget diameter and specimen width individually as independent parameters.
9. The K_i parameter collapsed the total fatigue life data of several spot welded geometries into a narrow band. The K_i parameter provides the designer with a useful tool for determining the fatigue life of different spot-welded joints. Moreover, it helps the designer determine and compare the effects of several parameters on the fatigue performance of the joints without having to resort to extensive testing.

7.2 RECOMMENDATIONS

1. Unlike the static performance, the total fatigue life of spot welds shows slight dependance on the nugget diameter within the investigated life range (10^4 to 3×10^6 cycles). Thus, the concern with the nugget diameter tolerance may be considered insignificant from the fatigue point of view within the considered life range.
2. HSLA and LC specimens of the same thickness gave about the same total fatigue life. However, the use of the HSLA yields thinner sheet thickness than the LC (at least by a factor of two if design is based on the static yield stress of the base metal). This reduction in thickness results in a remarkable decrease in fatigue life which can not be compensated for by increasing the nugget diameter only. A more effective way to compensate for this decrease in fatigue life would be through incorporating the coining technique in the weld cycle.
3. The use of the D/t ratio as a unique variable for determining the stress intensity factors and the static strength of spot welds should be considered carefully. Based upon the

finite element results it is recommendable to consider the sheet thickness and nugget diameter as independent variables.

4. The use of the K_I parameter as a design parameter is highly recommended. Its use will reduce the number of tests in the future since it accounts for a large number of variables.

7.3 PROPOSED FUTURE WORK

1. Confidence in the resistivity measurements has been established in this study. The use of the AT&T equipment has been valuable in partitioning the fatigue life of tensile-shear specimens. The equipment can be used in monitoring the crack growth in other geometries like coach-peel, sheet to tube specimens and others.
2. Concepts of multiaxial fatigue and mixed mode fracture mechanics provided the basis for the K_I parameter. Thus the extension of the K_I parameter to handle multiaxial loadings is highly recommended where spot welds are usually subjected to multiaxial loads in practice.
3. Residual stresses remarkably affect the fatigue performance of spot welds. The knowledge of the residual stress state at the notch zone provides a pertinent information for reliable fatigue life predictions especially if the coining technique is incorporated in the weld cycle. Due to the nature of the geometry, neutron diffraction method which is capable of measuring residual stresses at relatively larger depths (compared to other techniques), is recommended.
4. In view of the available fatigue data and the different parameters, the statistical analysis as well as the establishment of a fatigue data bank for spot welds is highly recommended.
5. The nonlinear finite element analyses of coach-peel and cross-tension specimens are highly recommended for a better understanding of the behavior of such flexible joints.

TABLES

Table 2.1

DIFFERENT D - T RELATIONS AS SUMMARIZED BY WILLIAMS [2]

Formula	Units of D and t	Applicable Thickness Range
$D = 1.6 * t + 0.1$	inches	0.1 - 0.3
$D = 5 * t^{0.5}$	mm	up to 12.7
$D = k * t$, $k = 3.6 - 4.0$	mm	0.5 - 2.5
$D = \frac{5}{3} * t + 7.0$	mm	5.0 - 25.0

Table 2.2

DIFFERENT ASSUMPTIONS FOR THE INITIAL CRACK SIZE AND THE SUBSEQUENT NATURE OF THE FATIGUE LIFE ESTIMATE OBTAINED FROM THE PROPAGATION MODEL [26]

Initial Crack Size (mm)	Nature of a_i	Nature of the fatigue life estimate
$a_i = 0.05$	arbitrarily	Nonconservative
$a_i = 0.25$	arbitrarily	Conservative
$a_i = a_{th}$	$a_{th} = (\Delta K_{th} / s_e)^2 / \pi$	Conservative at long lives
$a_i = a_{pl}$	a_{pl} is the plastic zone size	Nonconservative at long lives

Table 3.1
Test Matrix

Task	Material	Sheet Thickness mm	Nugget Diameter mm	Specimen Width mm	R-Ratio	Potential Drop Measurements	Specimen Condition
1	Gal. HSLA	1.4	6.1	38	0	Stage II	As Welded
2	Gal. HSLA	1.4	6.1	38	-0.2	Stage II	As Welded
3	Gal. HSLA	1.4	6.1	38	0.5	Stage II	As Welded
4	Gal. L.C.	1.4	6.1	38	0	Stage II	As Welded
5	Gal. L.C.	1.4	6.1	38	-0.2	Stage II	As Welded
6	Gal. L.C.	1.4	6.1	38	0.5	Stage II	As Welded
7	Gal. LC	1.4	4.8	38	0	Stage II	As Welded
8	Gal. LC	1.4	4.8	38	-0.2	Stage II	As Welded
9	Gal. LC	1.4	4.8	38	0.5	Stage II	As Welded
10	Gal. HSLA	1.4	4.8	38	0	Stage II	As Welded
11	Gal. HSLA	1.4	4.8	38	-0.2	none	As Welded
12	Gal. HSLA	1.4	4.8	38	0.5	none	As Welded
13	Gal. LC	0.9	6.1	38	0	Stage II	As Welded
14	Gal. LC	0.9	6.1	38	-0.2	Stage II	As Welded
15	Gal. LC	0.9	6.1	38	0.5	Stage II	As Welded
16	Gal. LC	0.9	4.8	38	0	Stage II	As Welded
17	Gal. LC	2.7	8.6	38	0	Stage II	As Welded
18	Gal. LC	2.7	8.6	38	-0.2	Stage II	As Welded
19	Gal. LC	2.7	8.6	38	0.5	Stage II	As Welded
20	Gal. LC	2.7	7.6	38	0	none	As Welded
21	Gal. LC	2.7	7.6	38	-0.2	none	As Welded
22	Gal. LC	2.7	7.6	38	0.5	none	As Welded
23	Gal. HSLA	1.4	4.8	22	0	stage II	As Welded
24	Gal. LC	1.4	4.8	22	0	stage II	As Welded
25	Gal. HSLA	1.4	6.1	38	0	stage II	Overloaded

Table 3.2
CHEMICAL COMPOSITION IN WEIGHT PERCENTAGE

Material	C	Mn	P	S	Si	Al	N	Nb	Ce
Galv. Low Carbon	0.024	0.24	0.009	0.017	0.026	0.041	0.007	-	-
Galv. HSLA	0.07	0.06	0.11	0.016	0.02	0.08	-	0.029	0.026

Table 3.3
MECHANICAL PROPERTIES IN THE LONGITUDINAL DIRECTION

Material	0.2% Offset Yield Strength (MPa)	Ultimate Tensile Strength (MPa)	% Elongation in 50.8 mm
Galvanized Low Carbon	212	298	37.5
Galvanized HSLA	420	501	27.0

Table 3.4
Welding Schedules and the Corresponding Nugget Diameters

Material	Sheet Thickness (mm)	Weld Current (Kamps)	Electrode Force (N)	Hold Time (Cycles)	Weld Time (Cycles)	Nugget Diameter *
HSLA	1.4	12	3700	30	18	6.1
HSLA	1.4	12	3700	30	14	4.8
LC	0.9	10	2000	30	14	6.1
LC	0.9	10	2000	30	12	4.8
LC	1.4	10	3000	30	16	6.1
LC	1.4	10	3000	30	14	4.8
LC	2.7	16	7000	30	24	8.6
LC	2.7	16	7000	30	18	7.6

* Except for the 2.7 mm thick sheets, electrodes used in welding the specimens had tip diameters equal to 6.35 mm. The 2.7 mm thick sheets were welded with special electrodes of 8.5 mm tip diameter.

Table 3.5
GEOMETRICAL DIMENSIONS AND CHARACTERISTIC RESISTIVITY VALUES

Material	<u>Dimensions</u> (mm)			Average Base Resistivity $\mu\Omega\text{cm}$	Resistivity Change at Boundary Between Stages I and II $\mu\Omega\text{cm}$	Resistivity Change at Boundary Between Stages II and III $\mu\Omega\text{cm}$
	t	D	W			
HSLA	1.4	6.1	38	15.2	2.0	10.0
	1.4	4.8	38			
	1.4	4.8	22			
LC	1.4	6.1	38	14.8	2.0	10.0
	1.4	4.8	38			
	1.4	4.8	22			
LC	0.9	6.1	38	9.5	1.2	6.0
	0.9	4.8	38			
LC	2.7	8.6	38	13.7	1.6	9.0

Table 3.6
CONSTANTS OF REGRESSION ANALYSIS CURVES TO THE MEASURED FATIGUE LIFE DATA

Material	Dimensions (mm)			R	Stage I			Stage II			Stage III			Total Life		
	t	D	W		A	B	r'	A	B	r'	A	B	r'	A	B	r'
LC	0.9	4.8	38	0.0	8,606	-0.1371	0.96	14,906	-0.1725	0.99	8630	-0.1459	0.93	18,213	-0.1831	0.97
	0.9	6.1	38	0.0	27,591	-0.2203	0.96	7,063	-0.1309	0.60	18,705	-0.2162	0.98	19,475	-0.1878	0.94
	0.9	6.1	38	-0.2	9,191	-0.1315	0.96	33,150	-0.2657	0.93	17,764	-0.2074	0.96	21,118	-0.1941	0.97
	0.9	6.1	38	0.5	5,883	-0.1092	0.94	26,091	-0.2381	0.93	4,491	-0.1063	0.90	8,650	-0.1373	0.83
LC	1.4	4.8	38	0.0	10,322	-0.1032	0.98	119,760	-0.3127	0.95	16,228	-0.1488	0.95	22,162	-0.1562	0.96
	1.4	4.8	38	-0.2	16,537	-0.1349	0.96	32,609	-0.1927	0.87	45,900	-0.2386	0.99	40,351	-0.1955	0.94
	1.4	4.8	38	0.5	4,819	-0.0594	0.99	18,256	-0.1623	0.93	8,279	-0.1115	0.99	11,826	-0.1198	0.95
LC	1.4	4.8	22	0.0	25,539	-0.1954	0.99	21,493	-0.1931	0.98	12,057	-0.1529	0.97	26,551	-0.1904	0.99
LC	1.4	6.1	38	0	14,433	-0.1265	0.98	9,798	-0.0962	0.67	13,849	-0.1346	0.95	26,338	-0.1618	0.96
	1.4	6.1	38	-0.2	103,030	-0.2832	0.99	25,269	-0.1793	0.88	26,019	-0.1900	0.95	30,135	-0.1723	0.96
	1.4	6.1	38	0.5	5,460	-0.0570	0.97	10,679	-0.1106	0.74	7,680	-0.0928	0.69	14,095	-0.1268	0.91
LC	2.7	7.6	38	0.0	---	---	---	---	---	---	---	---	---	114,010	-0.22437	0.93
	2.7	7.6	38	-0.2	---	---	---	---	---	---	---	---	---	98,801	-0.2305	0.95
	2.7	7.6	38	0.5	---	---	---	---	---	---	---	---	---	44,312	-0.1799	0.96
LC	2.7	8.6	38	0.0	42,403	-0.1739	0.98	41,789	-0.1840	0.99	82,699	-0.2484	0.99	78,312	-0.2127	0.98
	2.7	8.6	38	-0.2	307,470	-0.3351	0.99	79,425	-0.2363	0.99	125,000	-0.2795	0.99	121,900	-0.2465	0.99
	2.7	8.6	38	0.5	174,510	-0.2947	0.99	60,567	-0.2186	0.99	23,519	-0.1565	0.99	121,690	-0.2525	0.99

Table 3.6 (Continued)

CONSTANTS OF REGRESSION ANALYSIS CURVES TO THE MEASURED FATIGUE LIFE DATA

Material	Dimensions (mm)		R	Stage I			Stage II			Stage III			Total Life		
	t	D W		A	B	r'	A	B	r'	A	B	r'	A	B	r'
HSLA	1.4	4.8 38	0.0	11,699	-0.1416	0.98	343,760	-0.3913	0.96	54,626	-0.2540	0.99	44,969	-0.2191	0.97
	1.4	4.8 38	-0.2	---	---	---	---	---	---	---	---	---	28,194	-0.1787	0.93
	1.4	4.8 38	0.5	---	---	---	---	---	---	---	---	---	22,672	-0.1773	0.99
HSLA	1.4	4.8 22	0.0	9,167	-0.1266	0.96	32,435	-0.2193	0.91	28,663	-0.2361	0.97	33,784	-0.2140	0.97
HSLA	1.4	6.1 38	0.0	3,934	-0.0400	0.51	47,600	-0.2301	0.96	39,553	-0.2312	0.97	25,241	-0.1740	0.88
	1.4	6.1 38	-0.2	7,155	-0.1046	0.87	57,271	-0.2414	0.99	38,529	-0.2203	0.99	81,186	-0.2621	0.96
	1.4	6.1 38	0.5	3,218	-0.0473	0.99	16,396	-0.1530	0.98	19,509	-0.1855	0.94	25,848	-0.1867	0.95
HSLA*	1.4	6.1 38	0.0	20,102	-0.1254	0.99	9,183	-0.0708	0.69	16,510	-0.1261	0.92	19,488	-0.1188	0.96

* Preloaded group of specimens

Table 4.1
STRESS INTENSITY FACTORS FOR A CIRCUMFERENTIAL CRACKED CYLINDER
CALCULATED FROM THE DISPLACEMENT MATCH TECHNIQUE
 $K_I = 15.51 \text{ MPa}\sqrt{\text{mm}}$, ACCURACY = 1%

Radial Size of Crack Tip Element (mm)	0.17	0.09	0.05	0.03
$K_I \text{ (MPa}\sqrt{\text{mm}})$	16.00	15.91	15.90	15.87
Error %	3.2	2.6	2.5	2.3

Table 4.2

STRESS INTENSITY FACTORS FOR COOPER'S TENSILE-SHEAR SPECIMEN DIMENSIONS
CALCULATED FROM THE DISPLACEMENT MATCH TECHNIQUE

Tip Elements Description			Results from the Finite Element Analyses			G
size (mm)	#/90° Hz.	#/90° Vl.	K_I (MPa√mm)	K_{II} (MPa√mm)	J (N/mm)	(N/mm)
0.21	4	4	78.3	183.9	0.187	0.182
0.05	4	4	83.0	187.4	0.188	0.191
0.05	8	4	84.3	186.2	0.185	0.190

Table 4.3

RESULTS OF THE FINITE ELEMENT ANALYSES

Varied Dimension	Specimen Dimensions (mm)				K_I (MPa√mm)	K_{II} (MPa√mm)	$J_{av.}$ (N/mm)	G (N/mm)	$\frac{J_{max} - J_{min}}{J_{av}}$ % over contours 2 - 5	$\frac{J_{av.} - G}{J_{av}}$ %
	t	D = 2r	W	L						
Sheet Thickness (t)	0.9	6.1	38	140	136.7	229.8	0.3290	0.3185	0.21	3.19
	1.4	6.1	38	140	105.1	188.5	0.2115	0.2075	0.19	1.89
	2.0	6.1	38	140	81.4	161.7	0.1473	0.1461	0.13	0.81
	2.7	6.1	38	140	61.5	143.4	0.1081	0.1085	0.18	0.37
Nugget Diameter (D)	1.4	4.8	38	140	103.5	241.7	0.3113	0.3080	0.26	1.06
	1.4	8.6	38	140	102.0	134.3	0.1298	0.1266	0.15	2.46
	1.4	10.0	38	140	98.2	116.5	0.1065	0.1034	0.09	2.91
Specimen Width (W)	1.4	6.1	22	140	170.1	202.7	0.3170	0.3120	0.19	1.58
	1.4	6.1	50	140	90.9	186.6	0.1952	0.1920	0.20	1.64
	1.4	6.1	100	140	54.3	183.1	0.1640	0.1626	0.24	0.85
*Overlap = 50	1.4	6.1	50	140	90.0	187.2	0.1949	0.1922	0.15	1.38
Specimen Free Length (L)	1.4	6.1	38	95	102.3	187.2	0.2046	0.2028	0.19	0.88
	1.4	6.1	38	216	110.5	189.8	0.2176	0.2149	0.23	1.24
	1.4	6.1	38	292	112.4	190.2	0.2207	0.2175	0.18	1.45

* All specimens had an overlap equal to 38 mm except this specimen which was used to examine the overlap effect .

Table 6.1
HARDNESS MEASUREMENTS AND ESTIMATED STRENGTH

Zone	Low Carbon			HSLA		
	Average Vickers Hardness	Equivalent Brinell Hardness	Strength (MPa)	Average Vickers Hardness	Equivalent Brinell Hardness	Strength (MPa)
Base Metal	131	130	413	179	179	503
Base Metal Close to HAZ	146	147	482	195	195	586
Spherodized	196	196	620	233	233	710
Intercritical Zone	210	210	655	254	243	786
Refined Grain	221	220	689	362	342	1124
Coarse Grain	265	251	827	394	373	1241
Weld Metal	281	266	868	384	364	1220

Table 6.2

A COMPARISON BETWEEN THE STRESS INTENSITY FACTORS OBTAINED IN THIS STUDY
AND THOSE OBTAINED FROM RADAJ'S STRUCTURAL STRESS MODEL

Specimen Dimensions (mm)				Current Study		Radaj's Model	
t	D	W	L	K _I (MPa $\sqrt{\text{mm}}$)	K _{II} (MPa $\sqrt{\text{mm}}$)	K _I (MPa $\sqrt{\text{mm}}$)	K _{II} (MPa $\sqrt{\text{mm}}$)
1.4	6.1	22	140	170.1	202.7	132.4	202.6
1.4	6.1	38	140	105.1	188.5	83.9	188.4
1.4	6.1	50	140	90.9	186.6	73.1	186.5
1.4	6.1	100	140	54.3	183.1	44.8	183.1

FIGURES

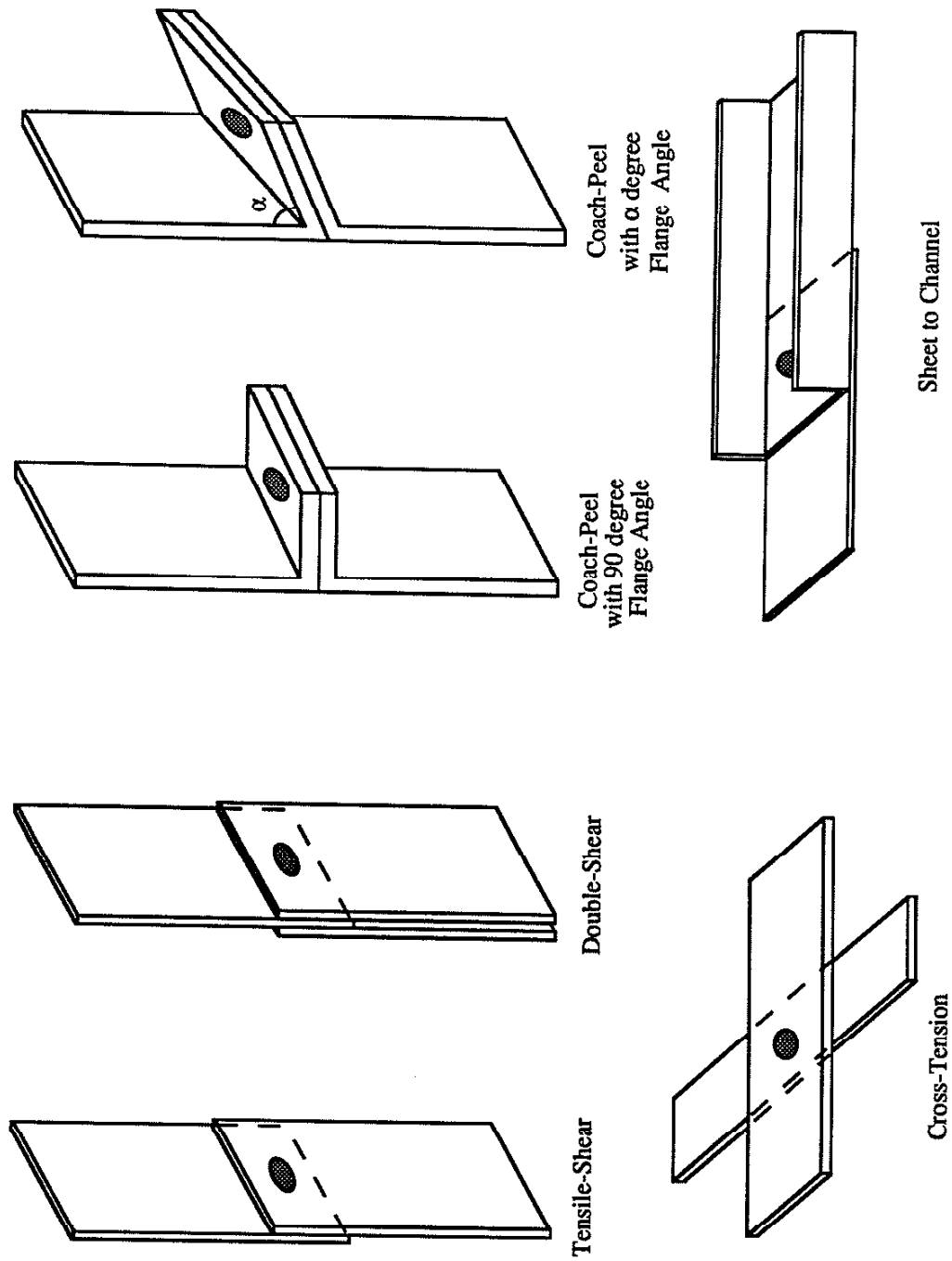


Fig. 1.1 Various spot welded specimens

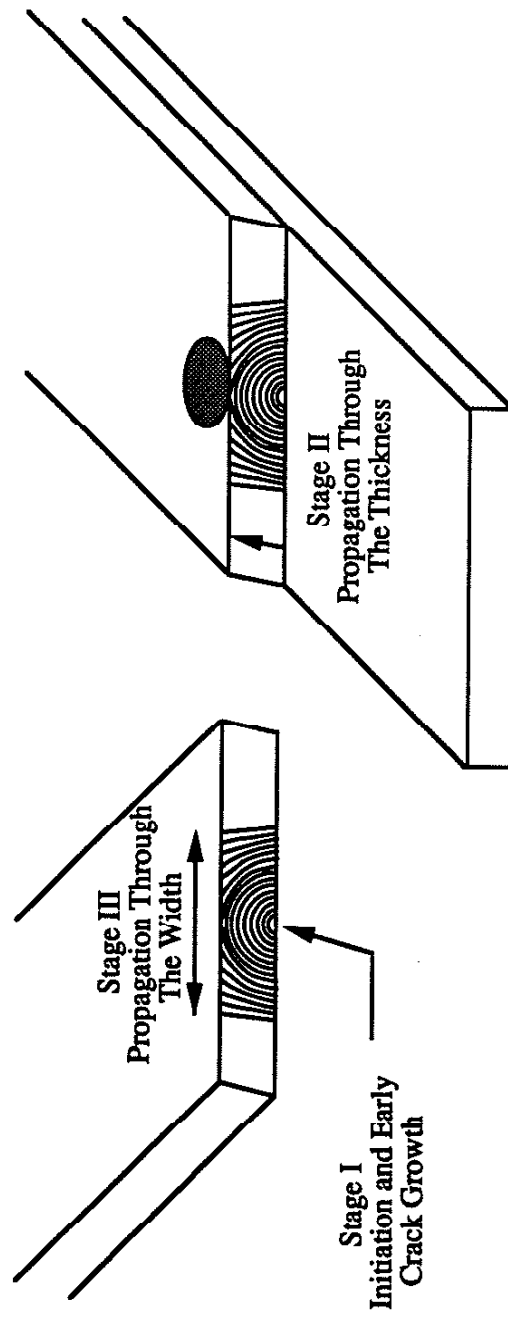


Fig. 1.2 The Different Stages of the Fatigue Life

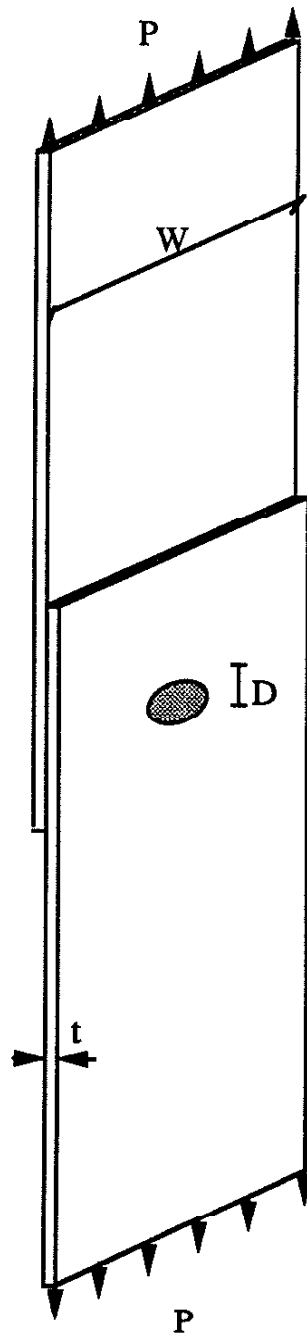


Fig. 3.1 Basic dimensions for the tensile-shear specimen

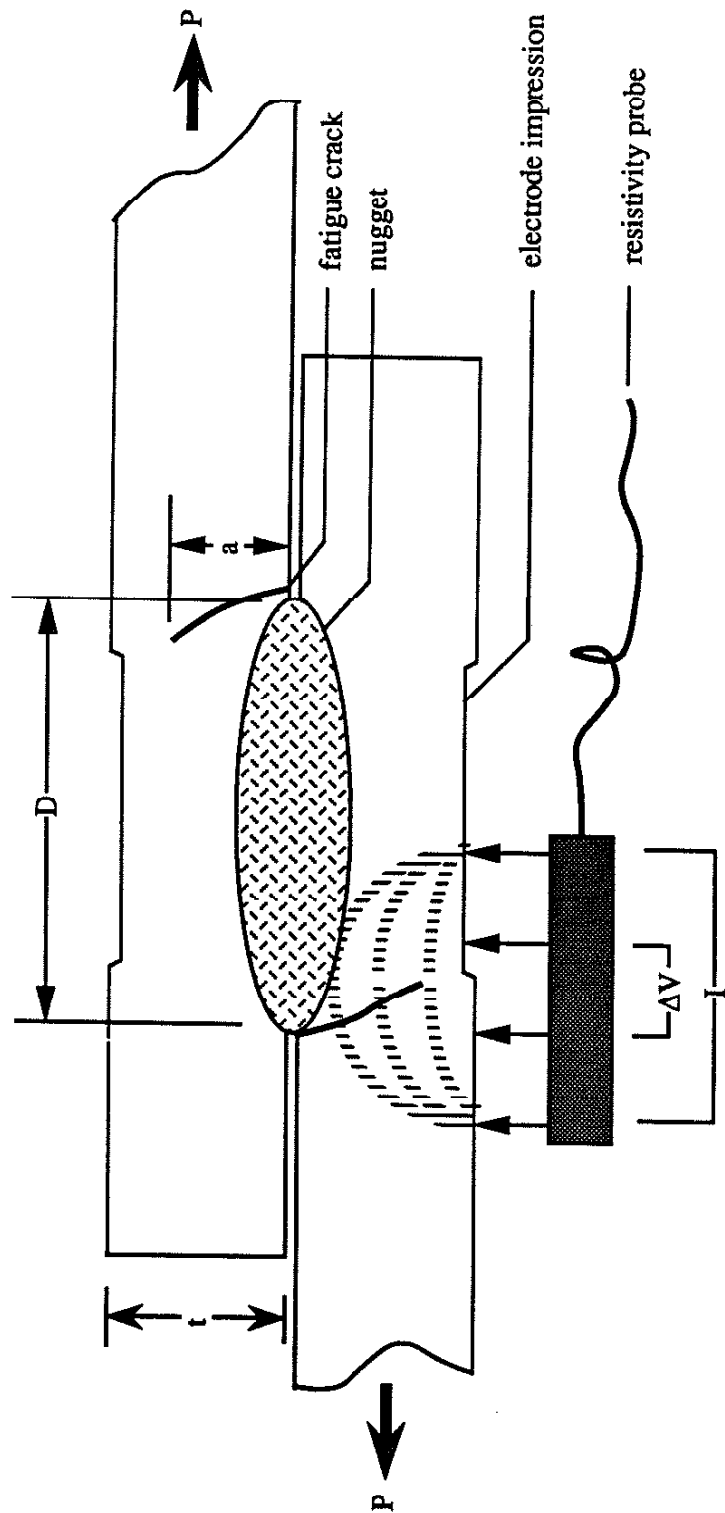


Fig. 3.2 Sketch showing the location of fatigue crack development in a tensile-shear specimen and the use of the resistivity measurement probe to sense the fatigue crack development

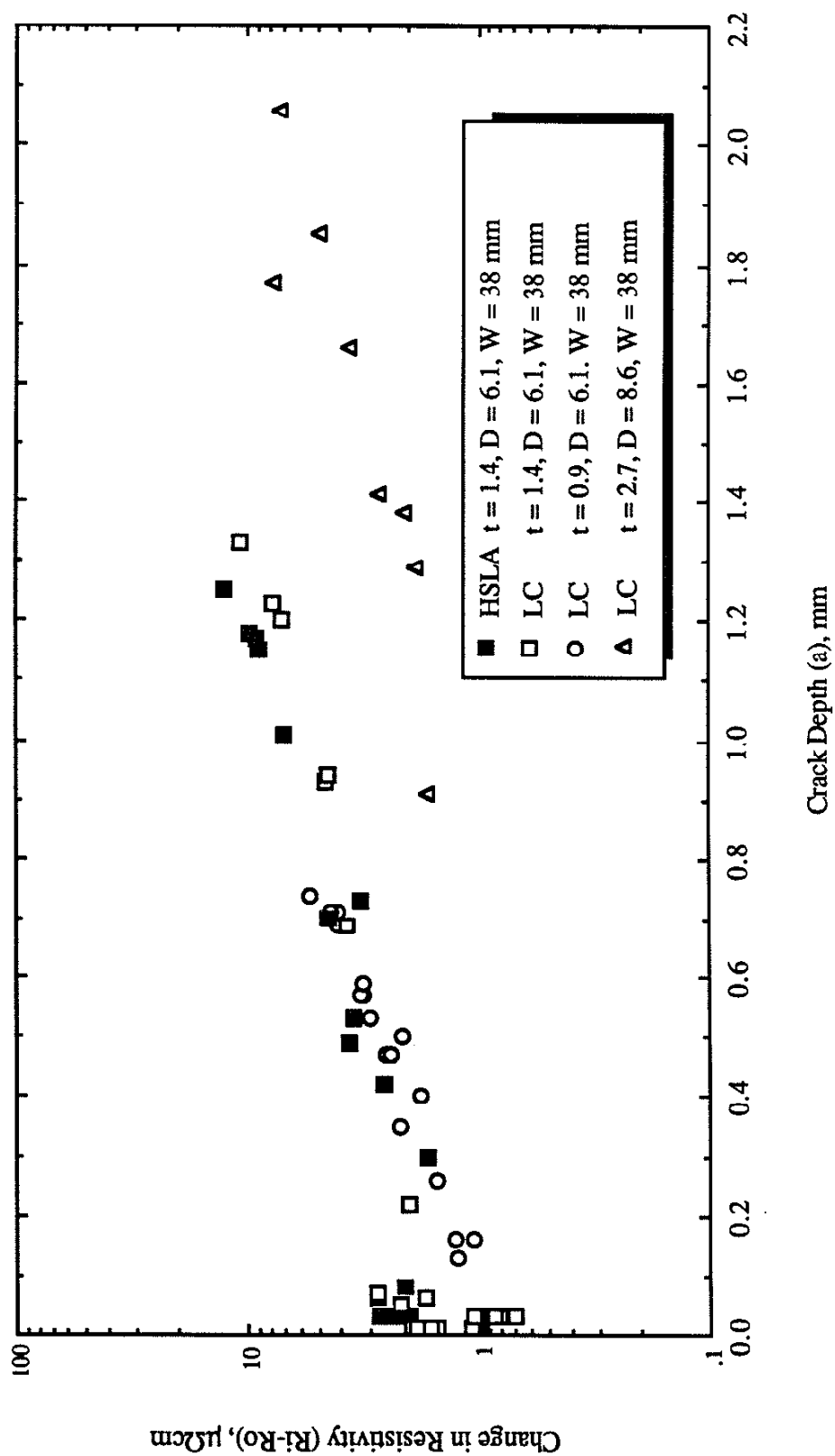


Fig. 3.3 Measured Change in resistivity as a function of crack depth.

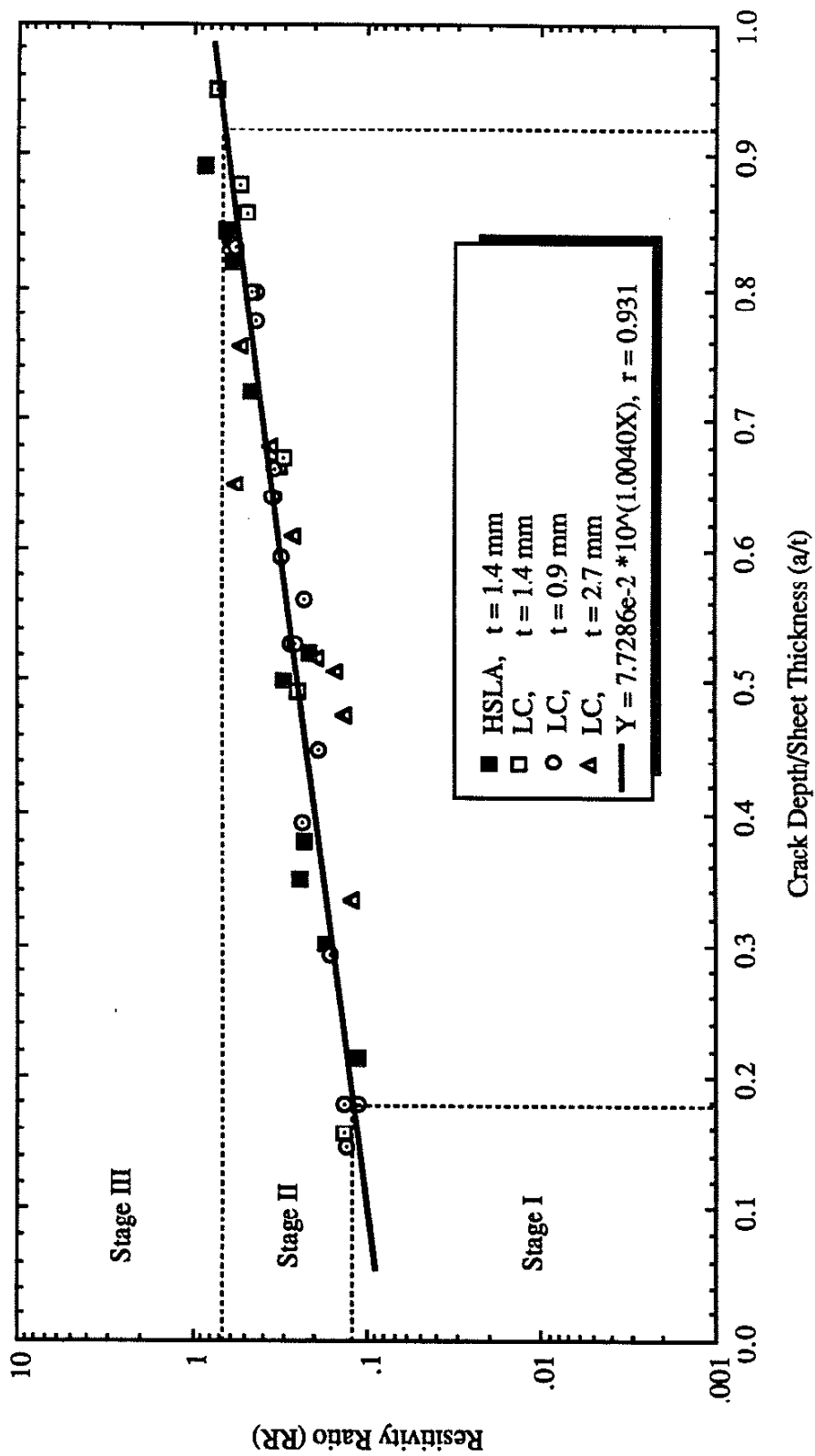


Fig. 3.4 Resistivity ratio versus the ratio of crack depth to sheet thickness. The boundaries between Stages I and II and Stages II and III are indicated.

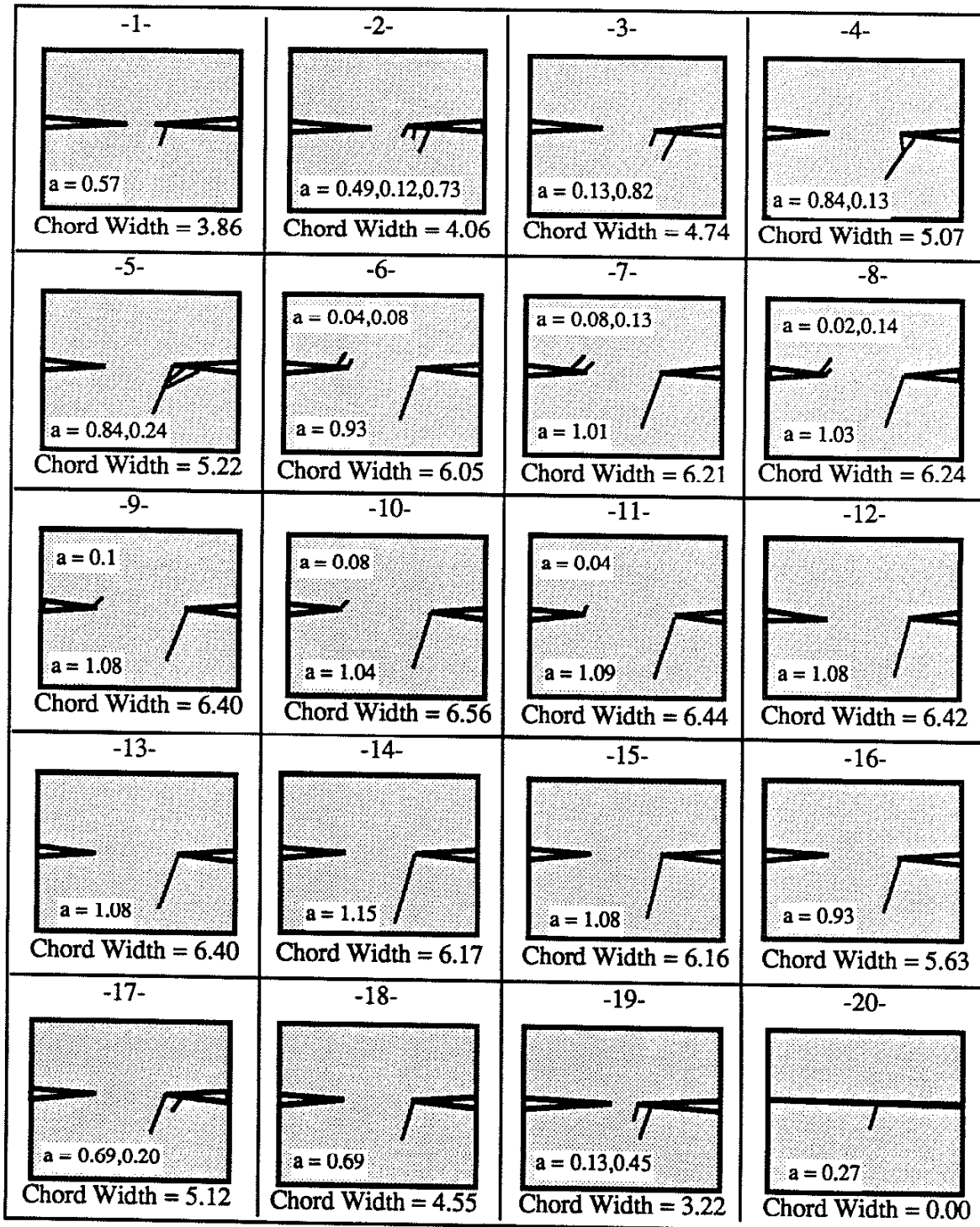
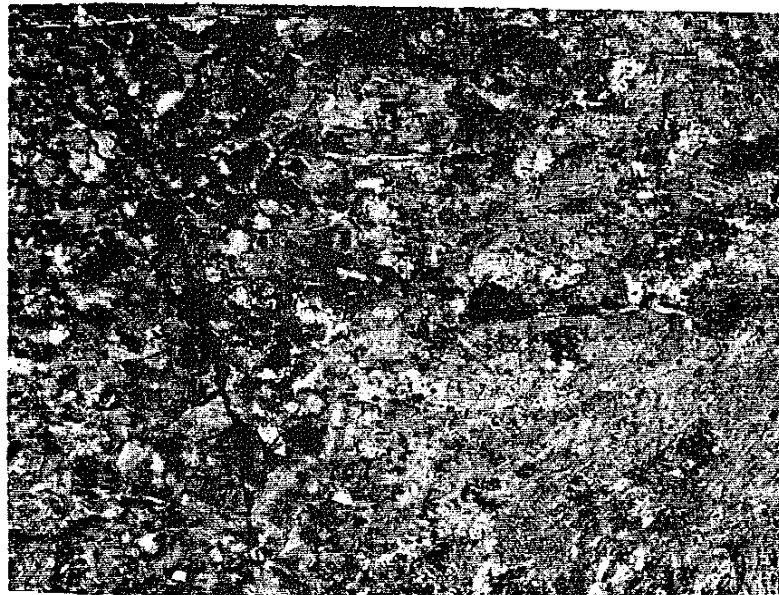
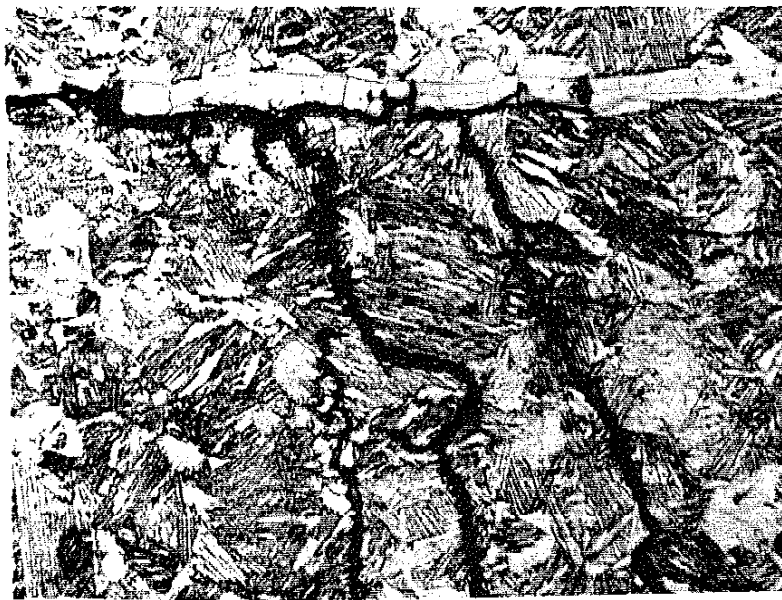


Fig. 3.5 A log for the Different Sections Observed During Polishing



100 μm



10 μm

Fig. 3.6 (top) Polished section of specimen cycled for 250,000 cycles at $\Delta P = 2000$ N. Fatigue cracks begin near periphery of nugget. Several independent cracks are apparent. (below) Higher magnification view of seam between two sheets and the origin of fatigue cracks at nugget periphery. White material at interface between two sheets is zinc from galvanized coating.

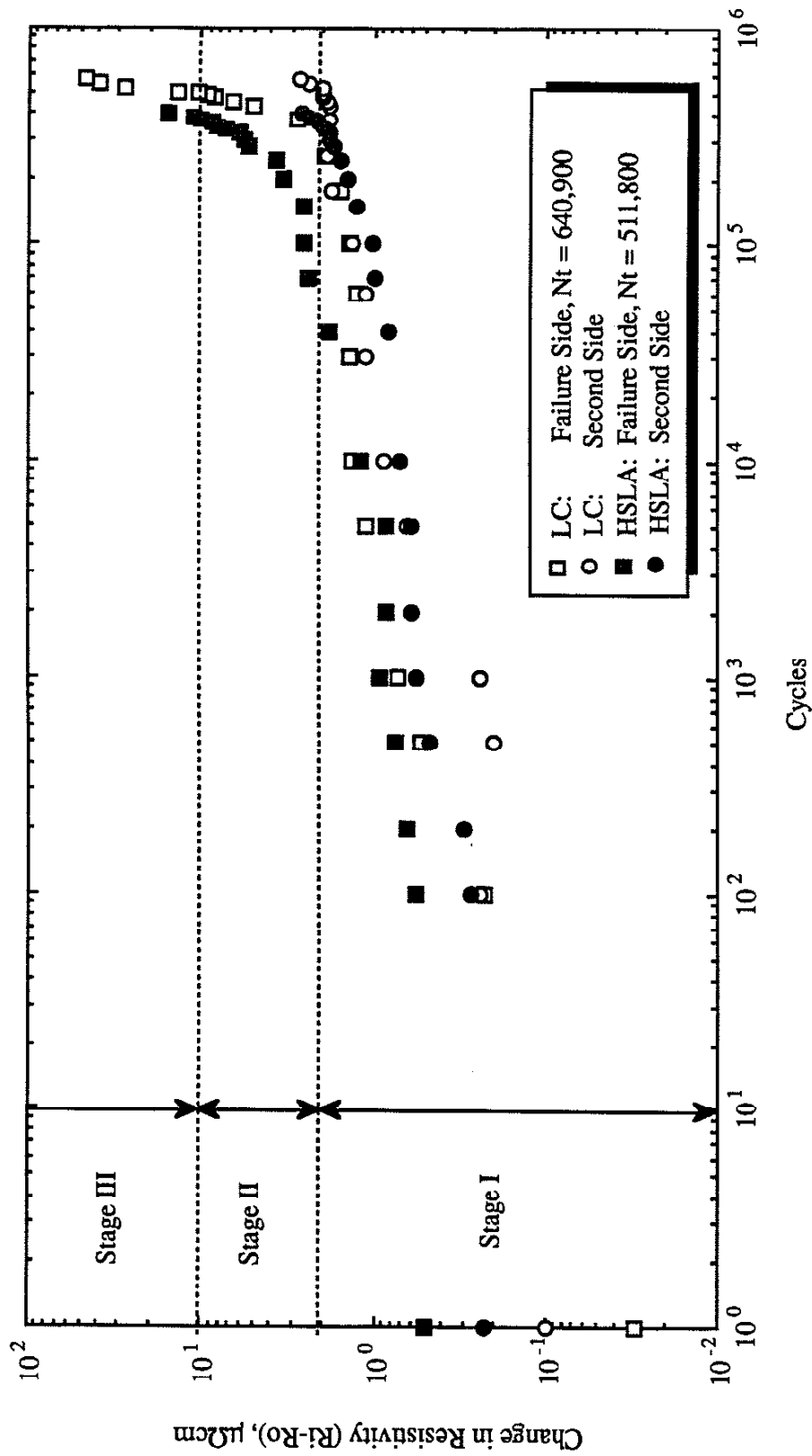
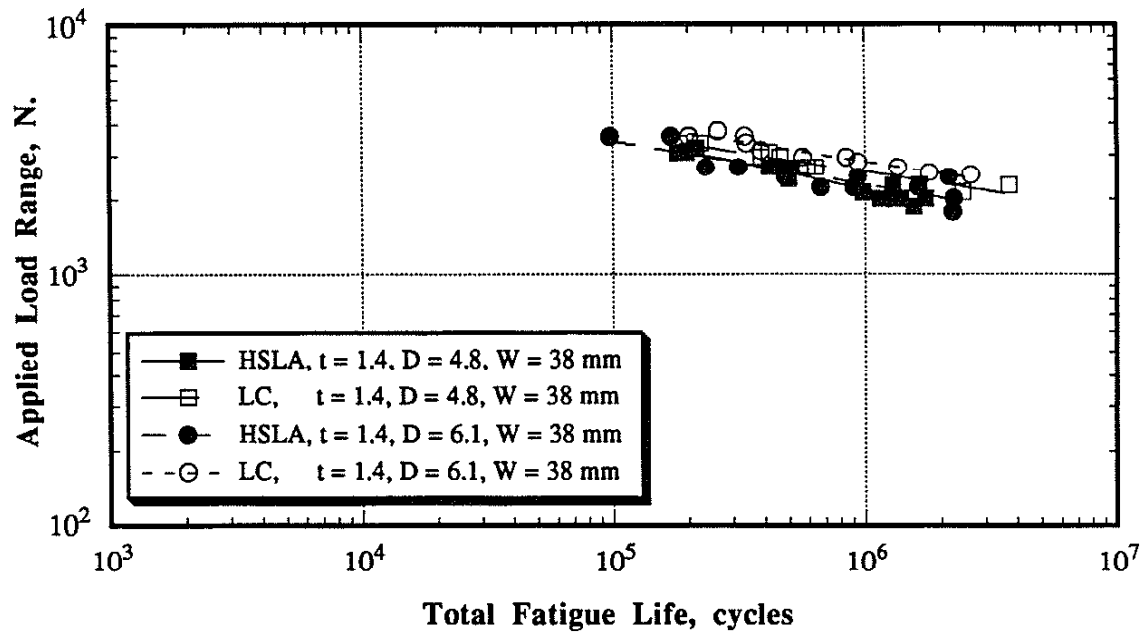
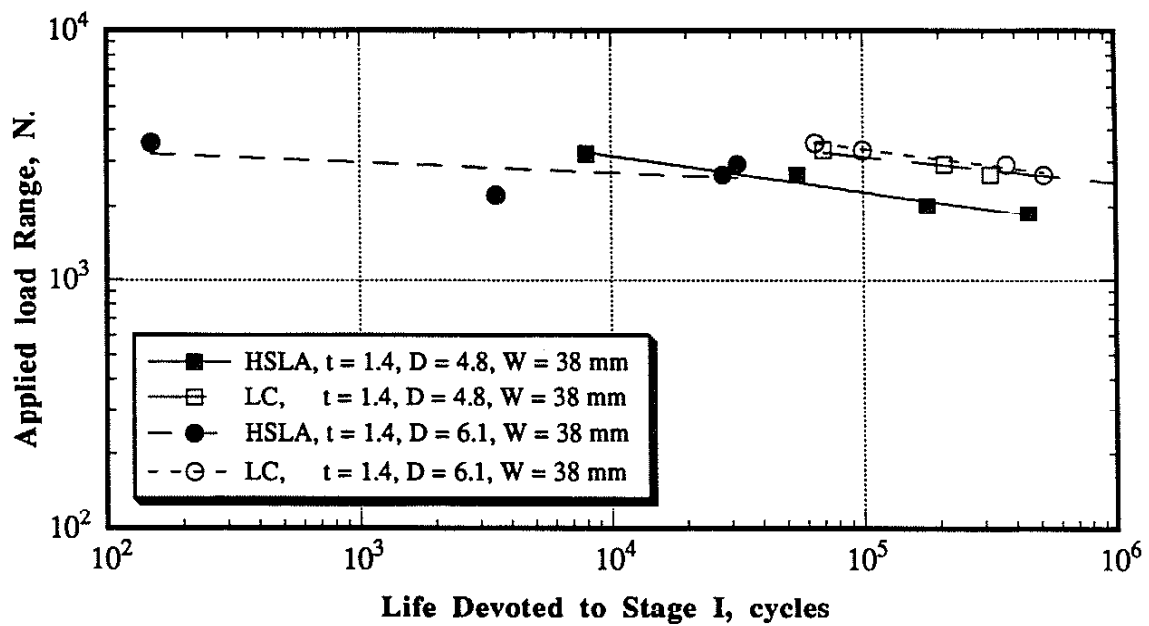
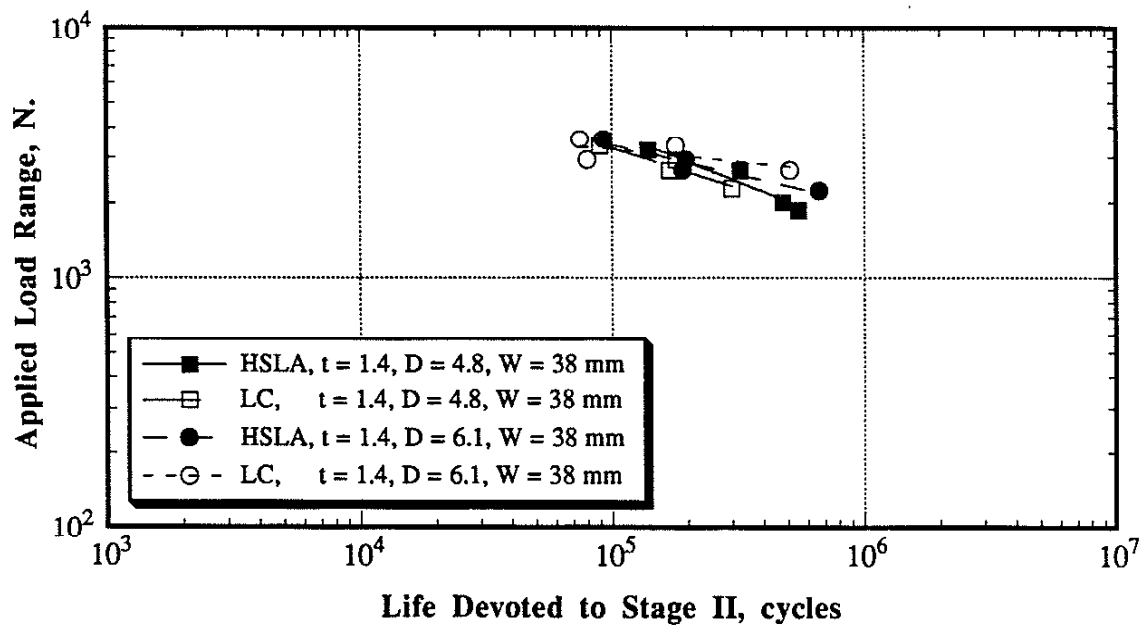
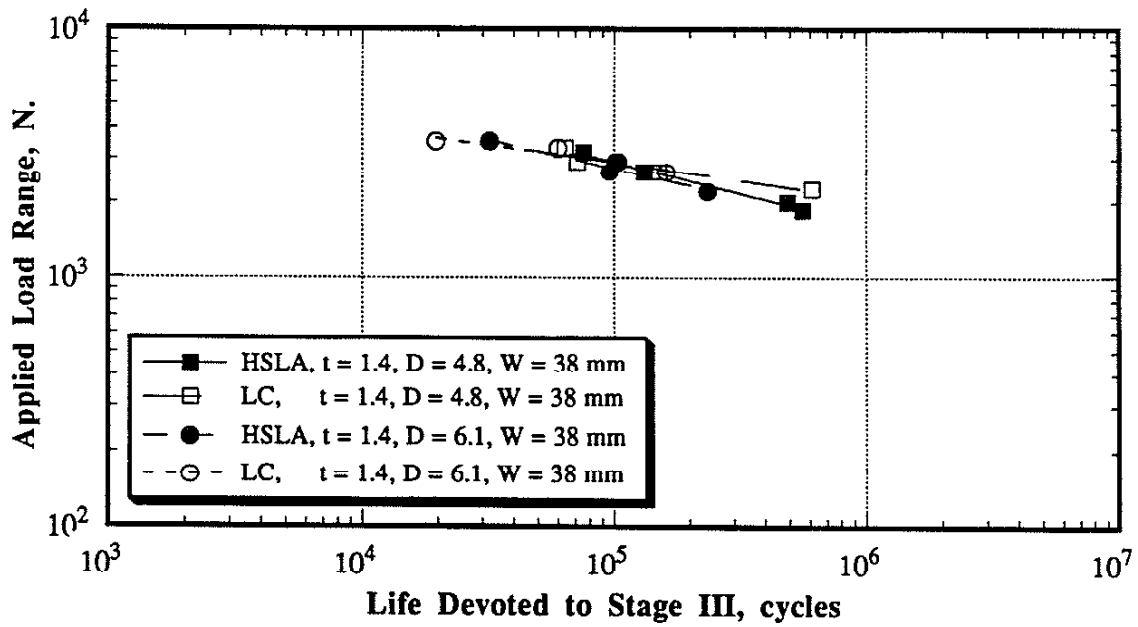


Fig. 3.7 Change in resistivity as a function of cycles for typical LC and HSLA specimens

Fig. 3.8 Material effect on the total fatigue life, $R = 0$ Fig. 3.9 Material effect on Stage I, $R = 0$

Fig. 3.10 Material effect on Stage II, $R = 0$ Fig. 3.11 Material effect on Stage III, $R = 0$

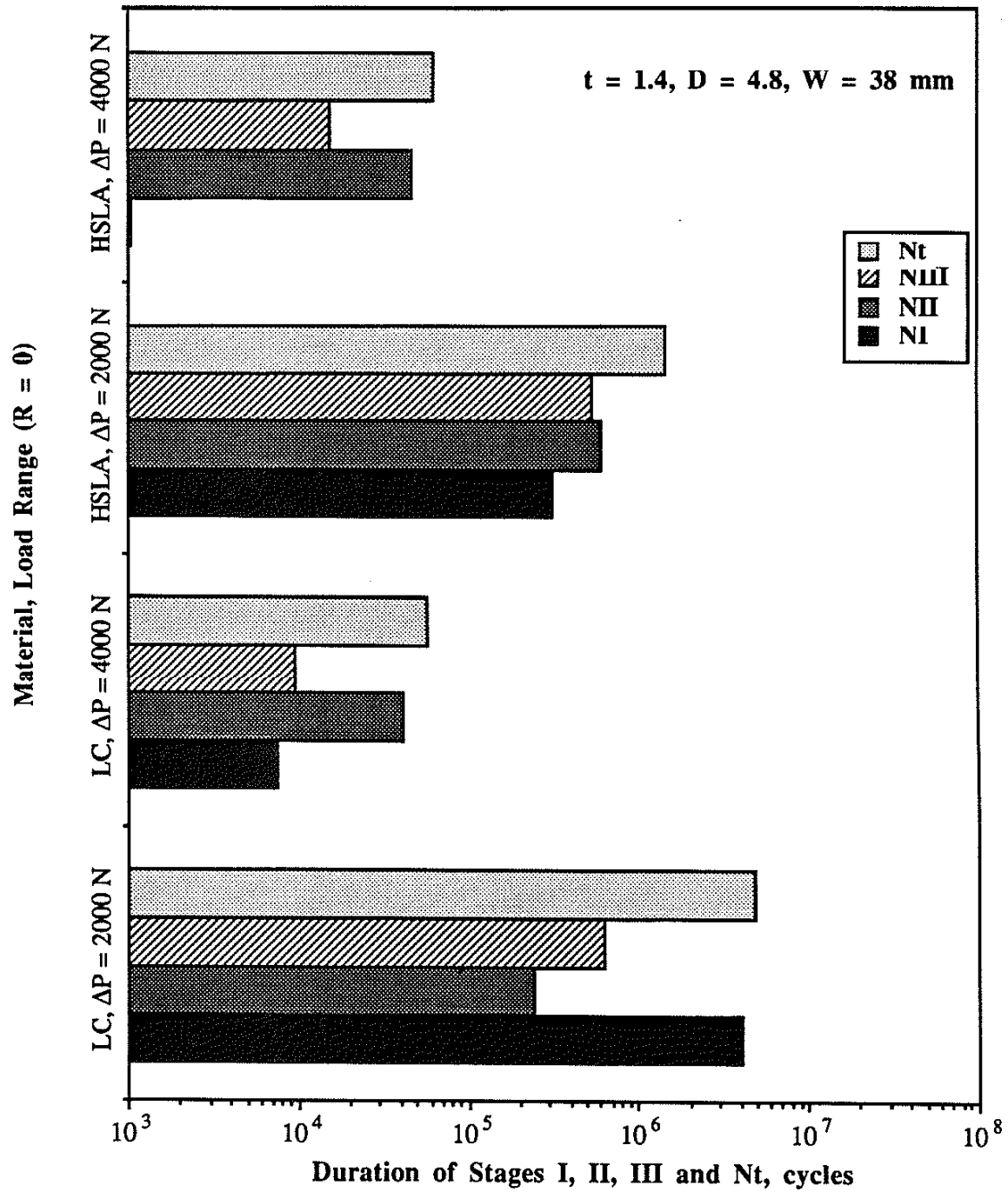


Fig. 3.12 Comparison of the effect of base metal properties on the total fatigue life and its three stages

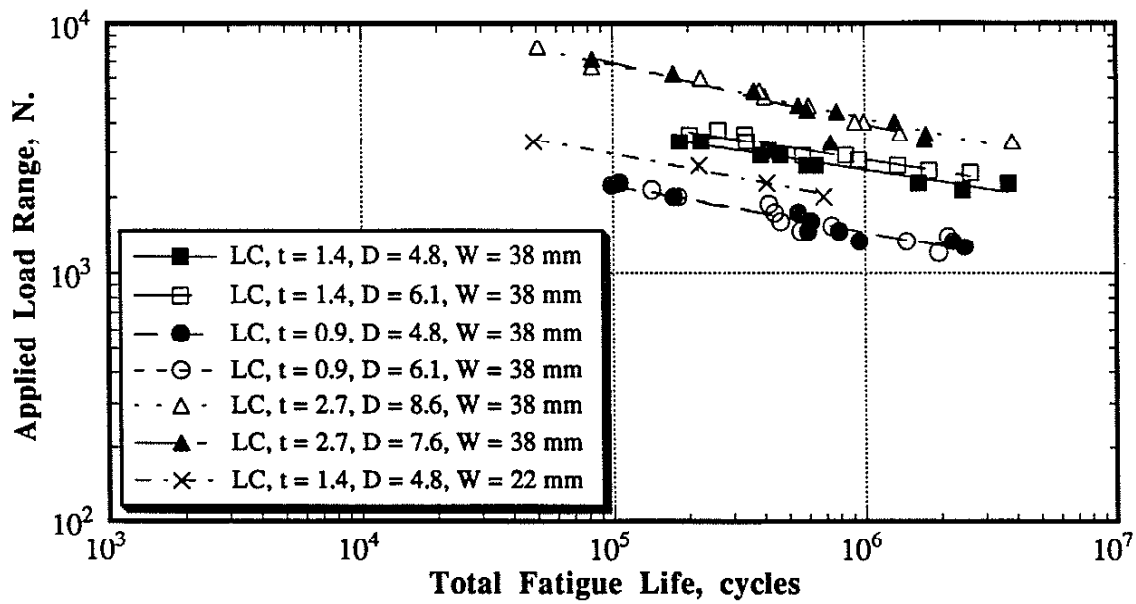


Fig. 3.13 Effects of specimen dimensions the total fatigue life, $R = 0$

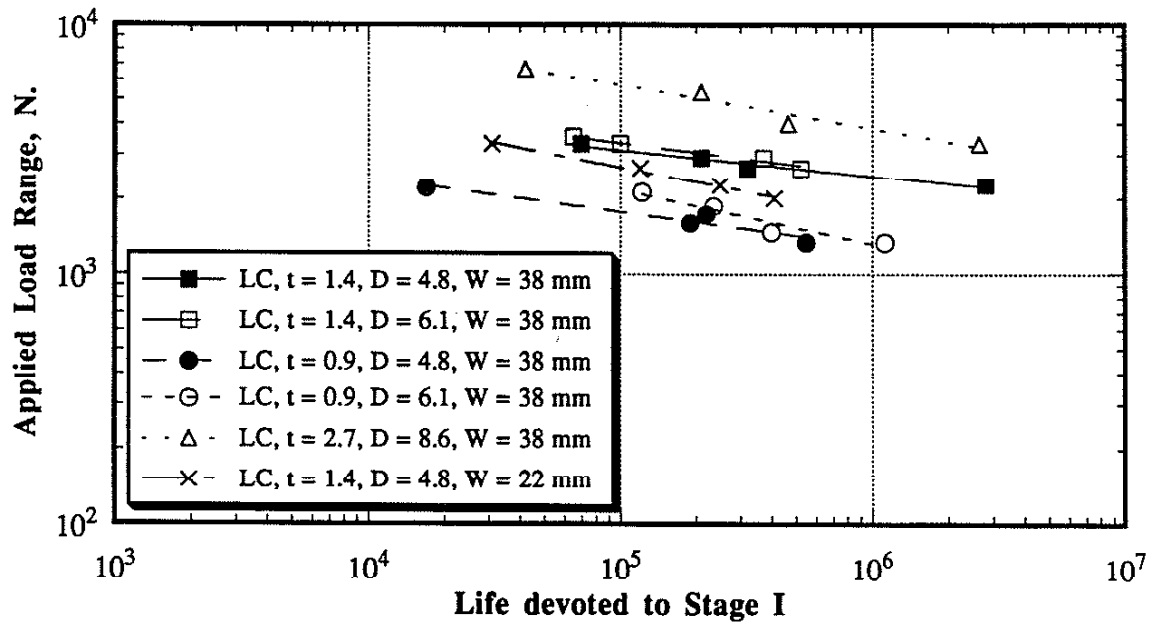
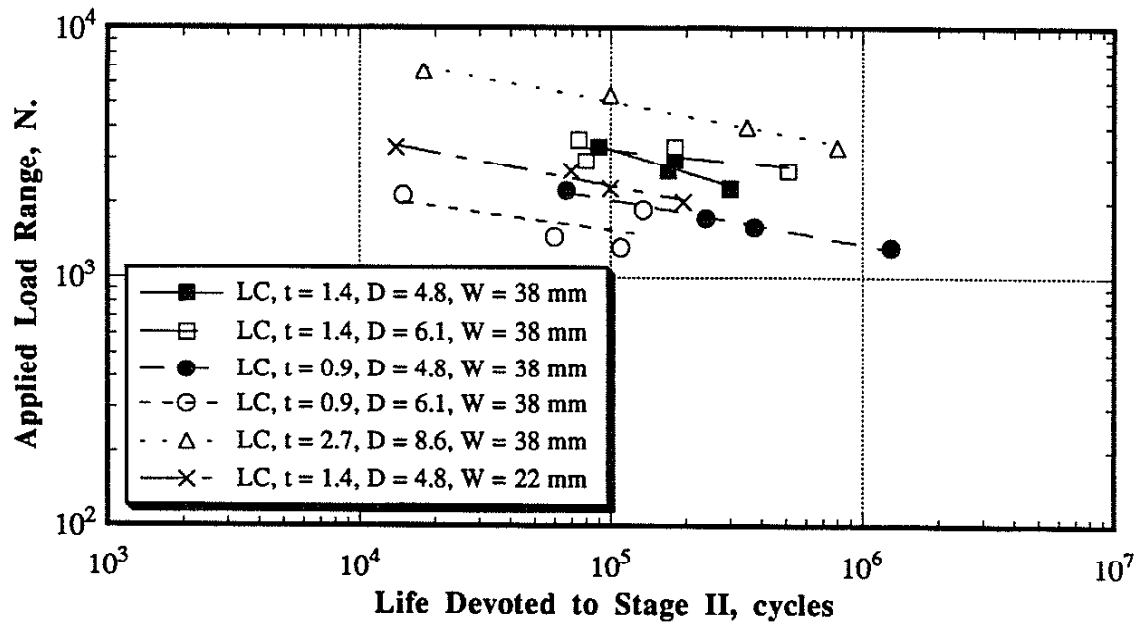
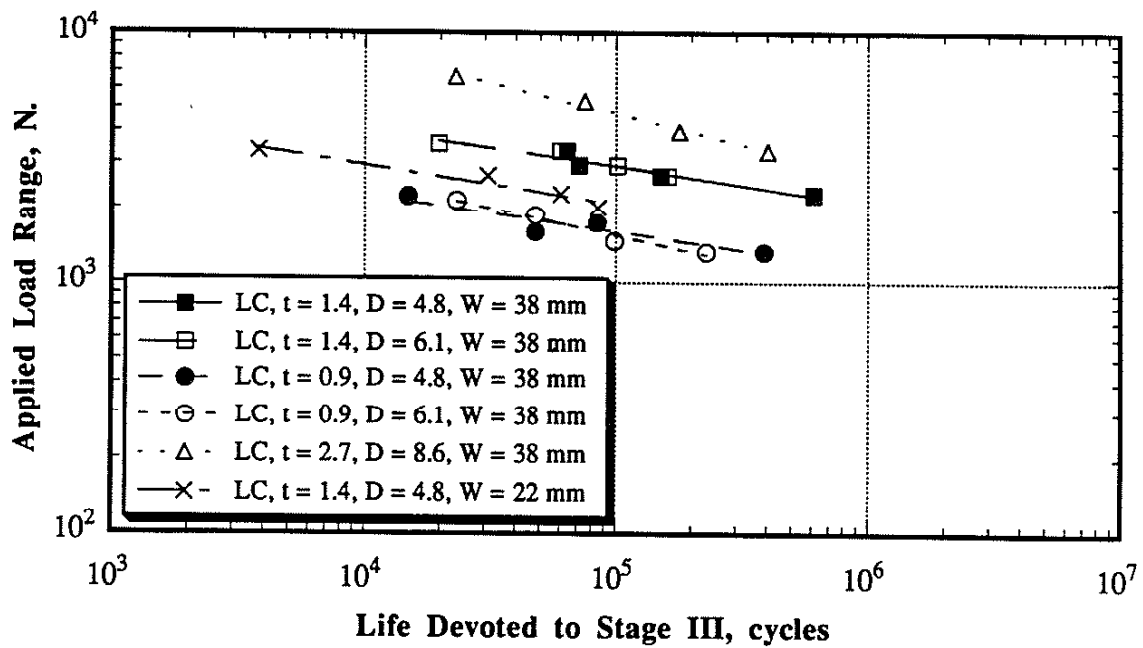


Fig. 3.14 Effects of specimen dimensions on Stage I, $R = 0$

Fig. 3.15 Effects of specimen dimensions on Stage II, $R = 0$ Fig. 3.16 Effects of specimen dimensions on Stage III, $R = 0$

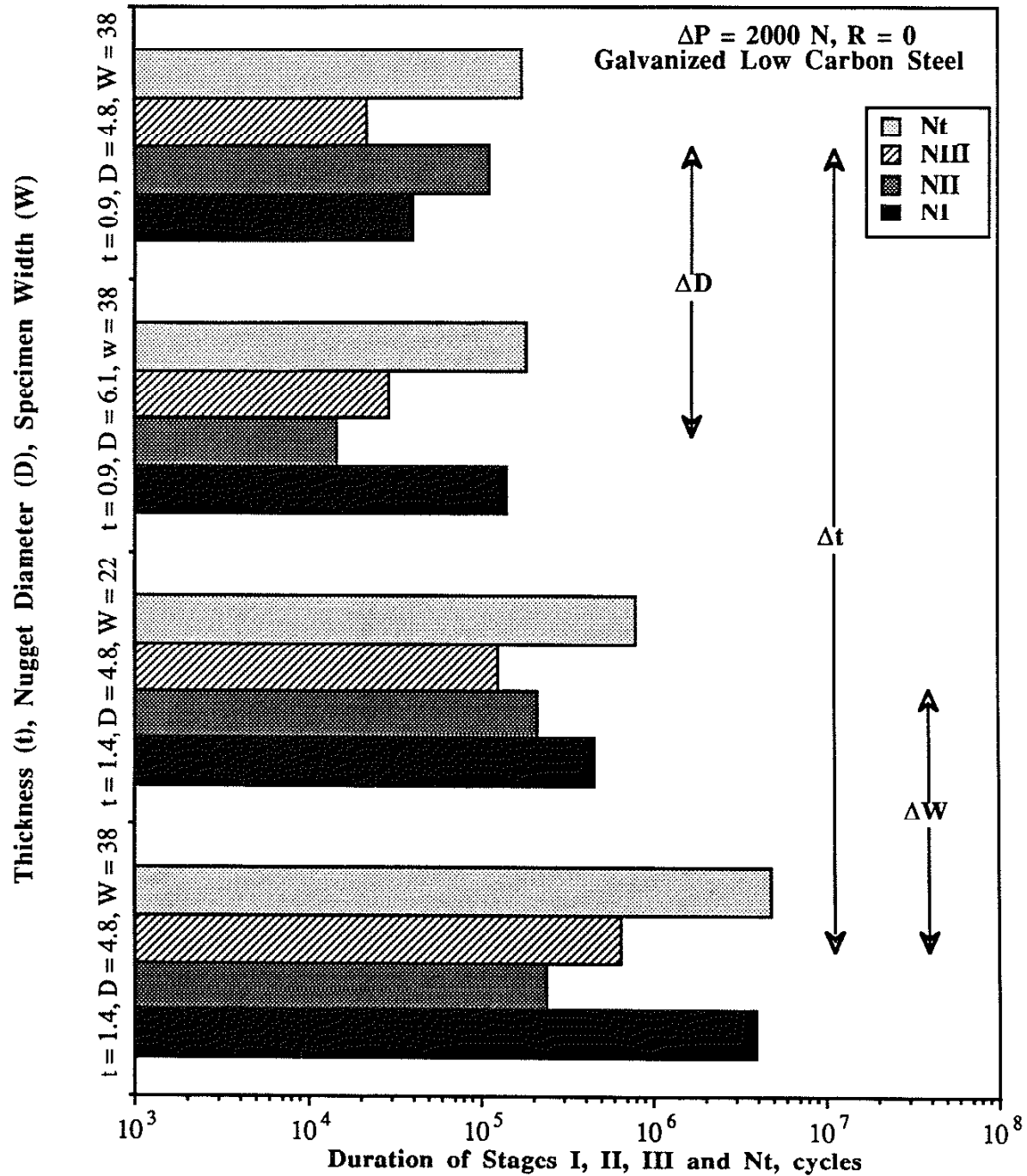


Fig. 3.17 Comparison of the effect of weld geometry on the total fatigue life and its three stages for Galvanized low carbon specimens

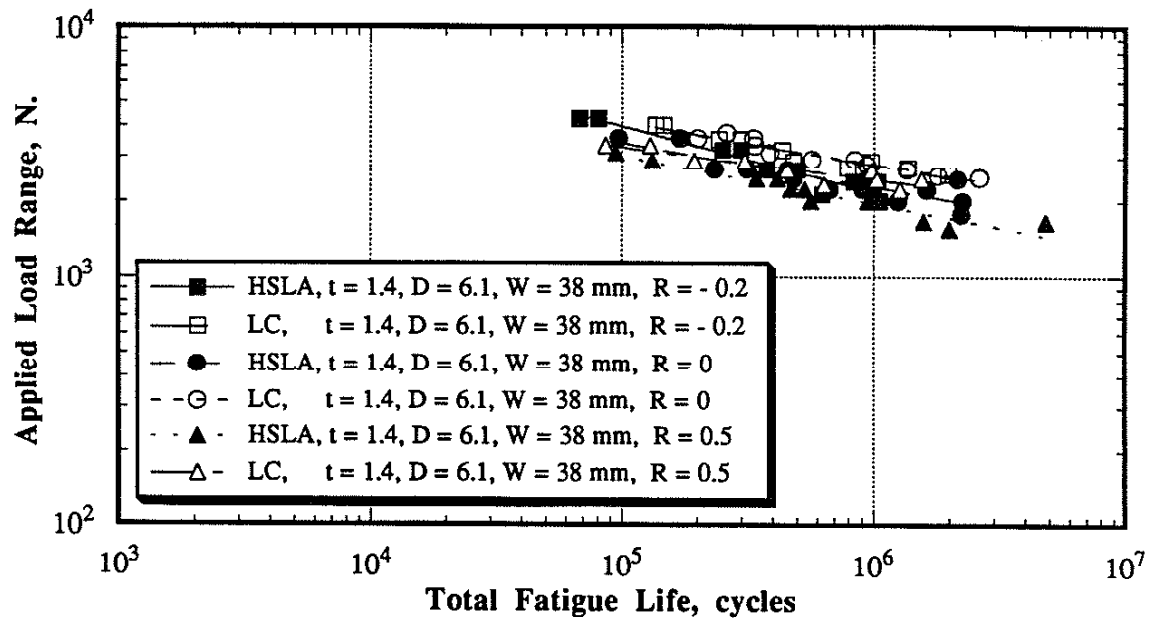


Fig. 3.18 Effect of the R-ratio on the total fatigue life

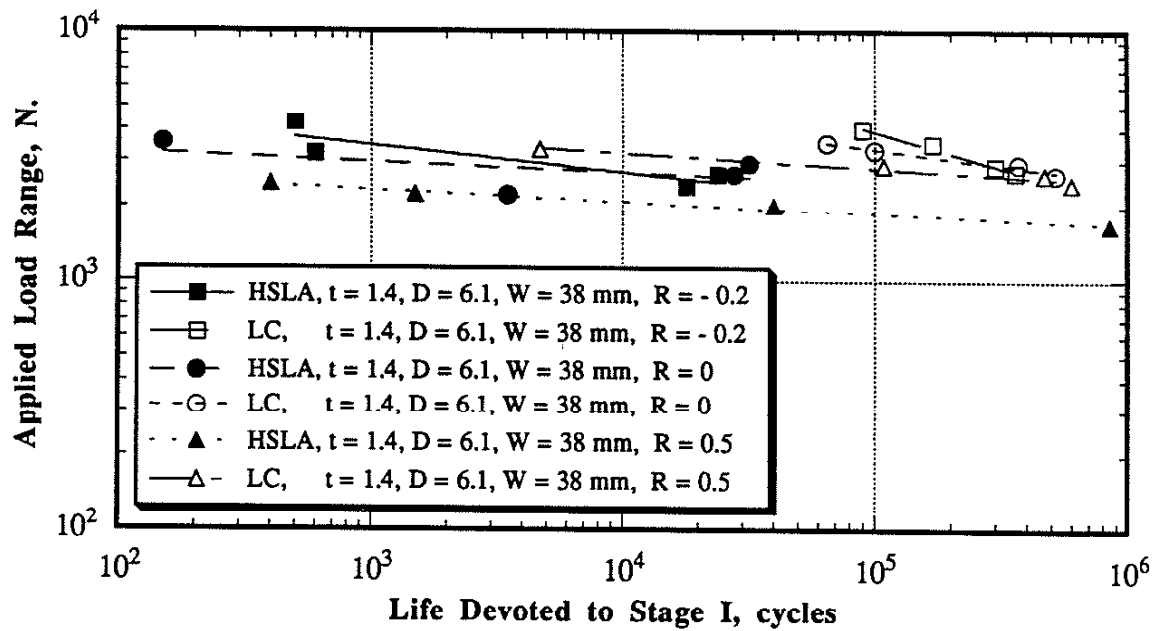


Fig. 3.19 Effect of the R-ratio on Stage I

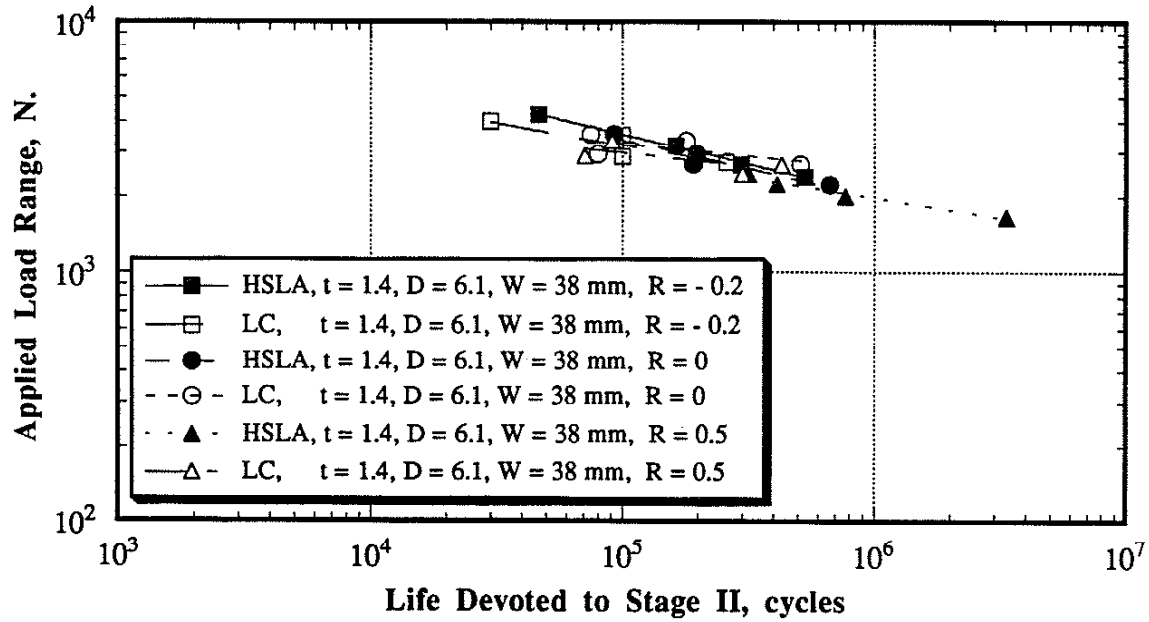


Fig. 3.20 Effects of the R-ratio on Stage II

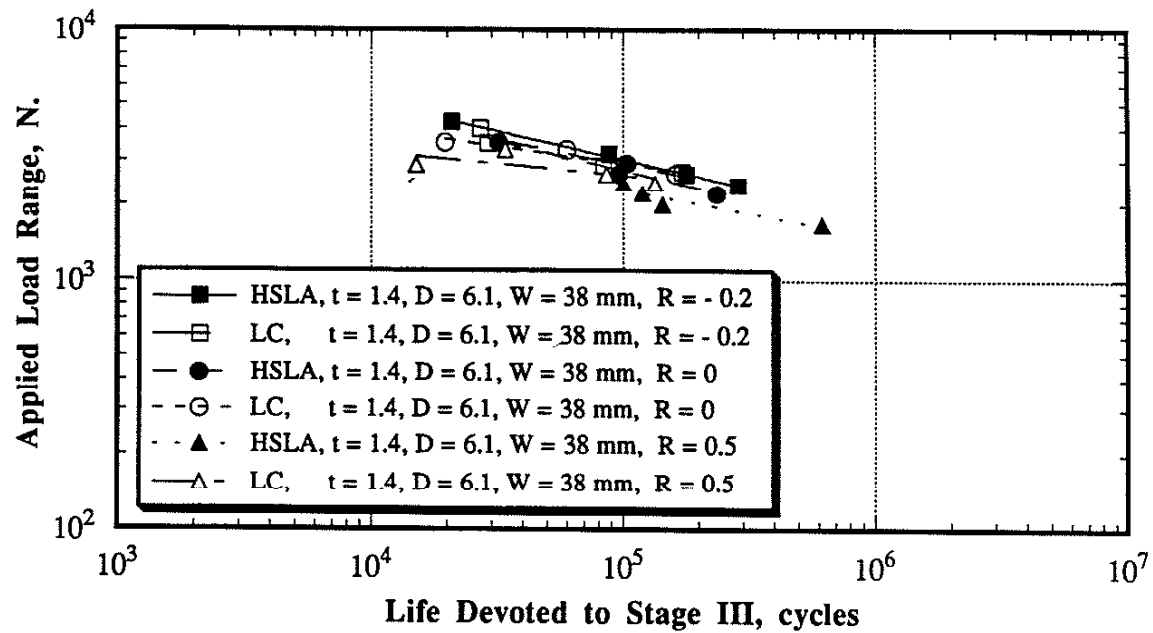


Fig. 3.21 Effect of the R-ratio on Stage III

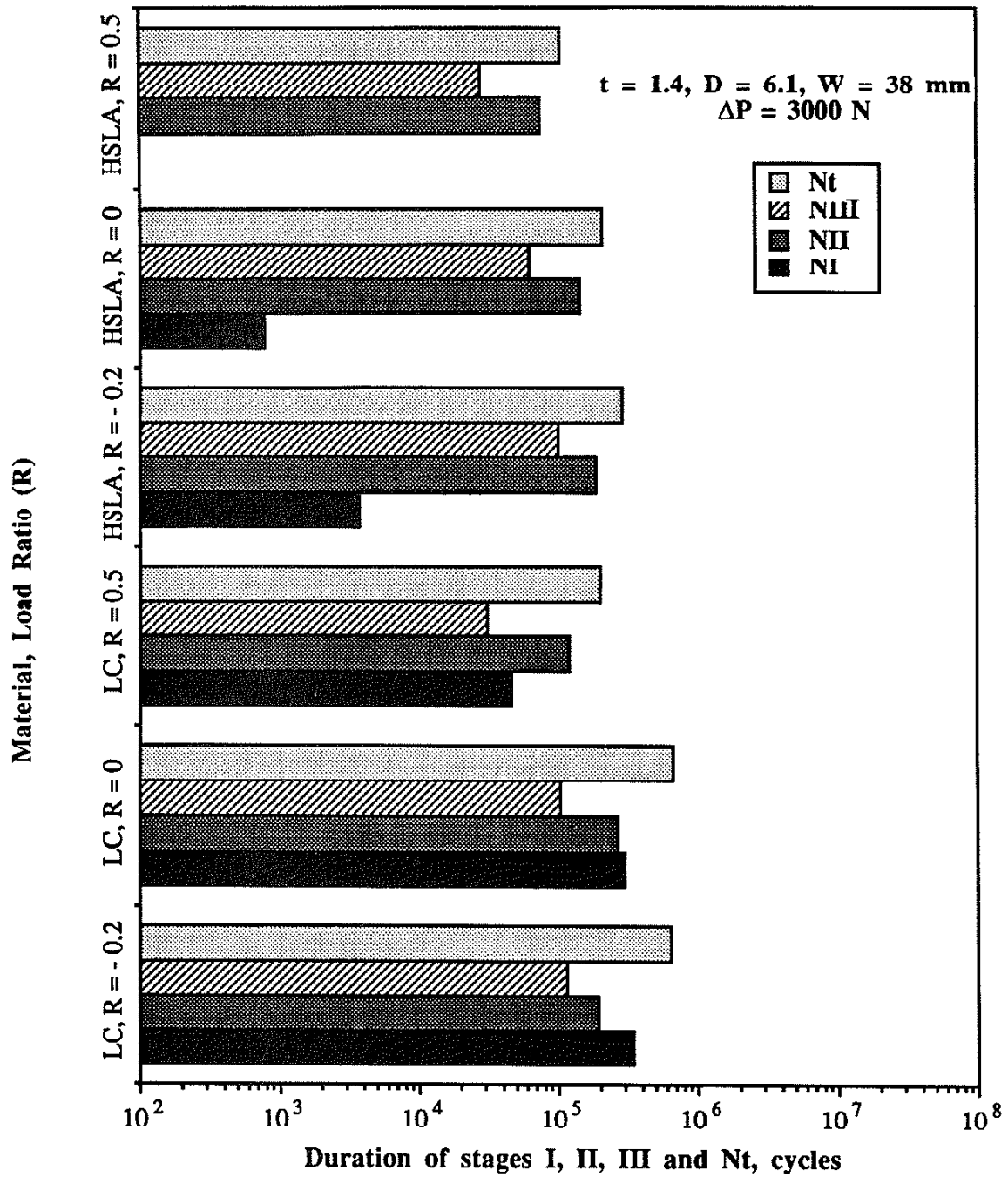


Fig. 3.22 Comparison of the effect of R ratio on the total fatigue life and its three stages

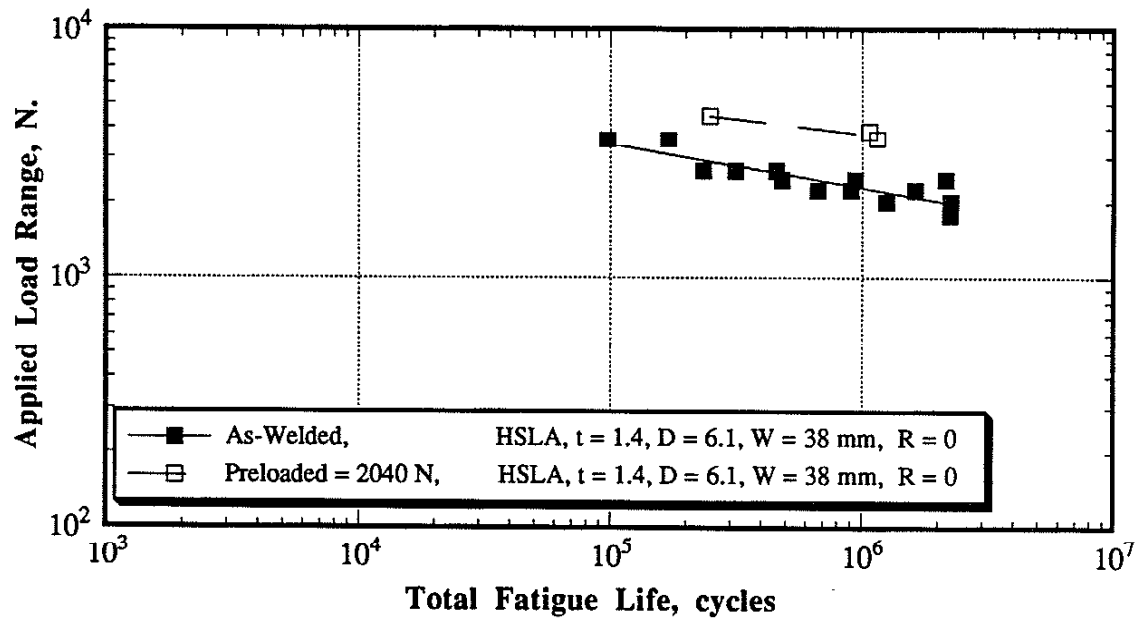


Fig. 3.23 Preload effect on the total fatigue life

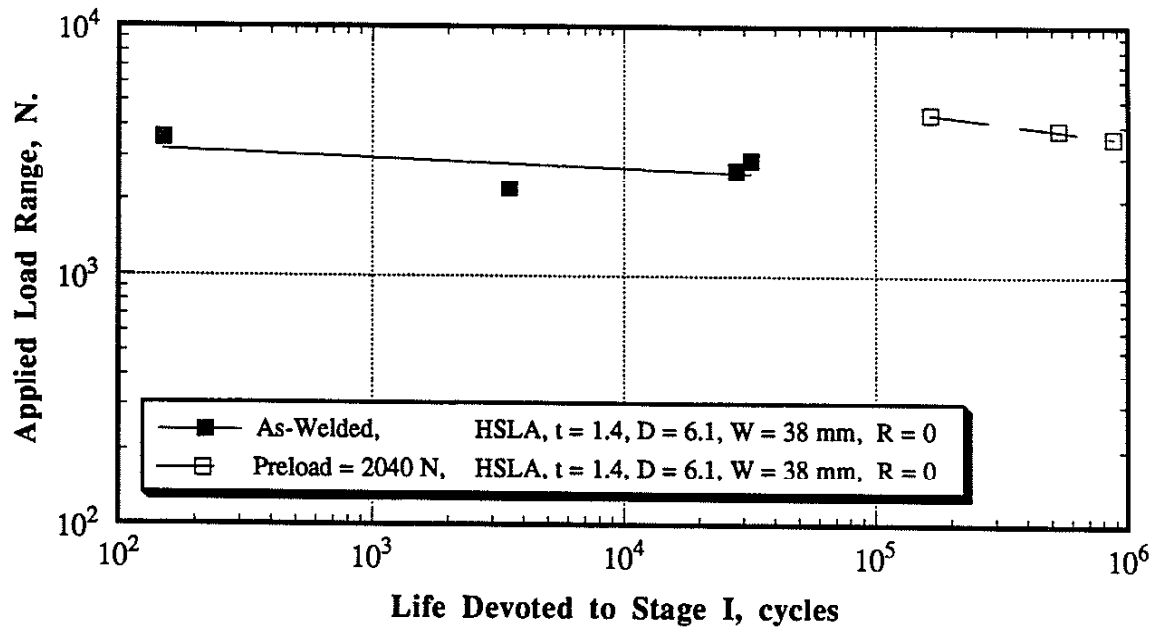


Fig. 3.24 Preload effect on Stage I

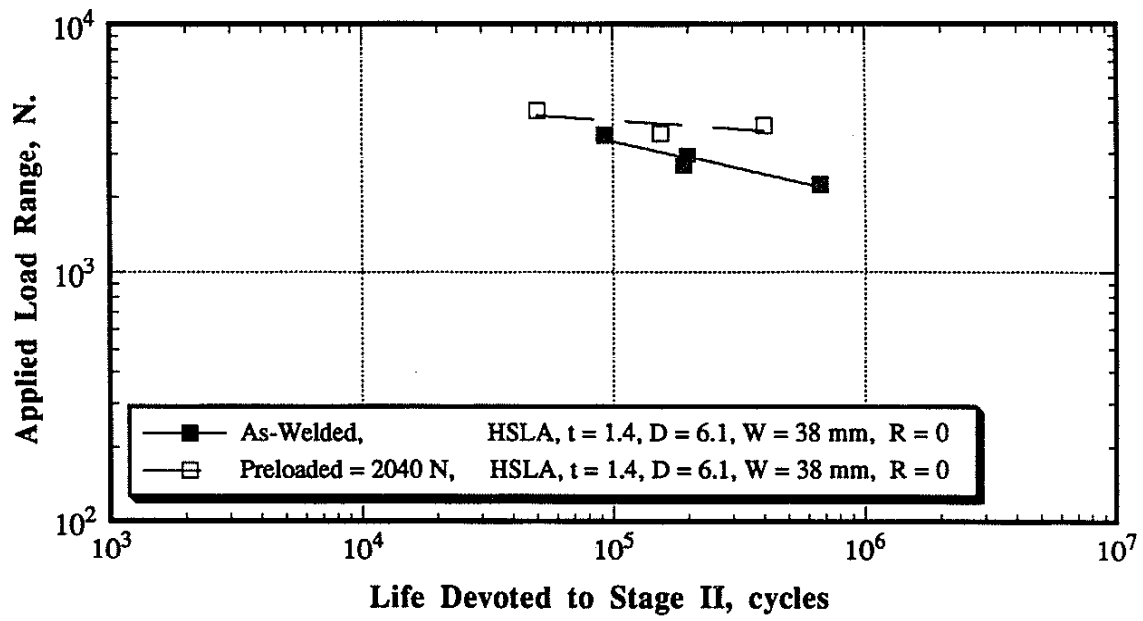


Fig. 3.25 Preload effect on Stage II

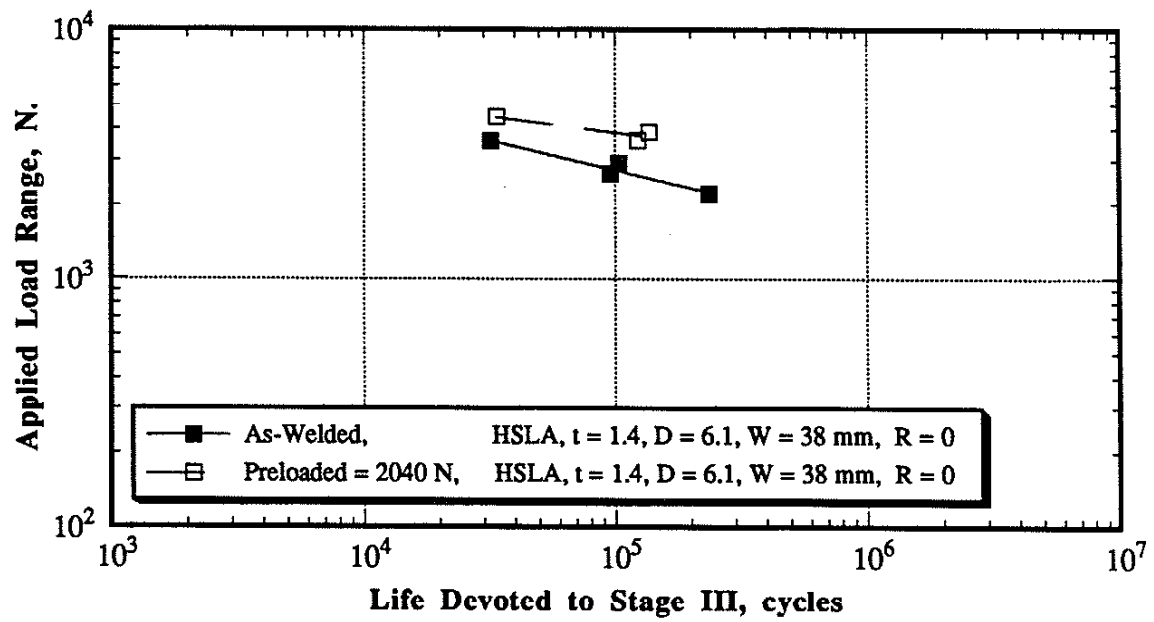


Fig. 3.26 Preload effect on Stage III

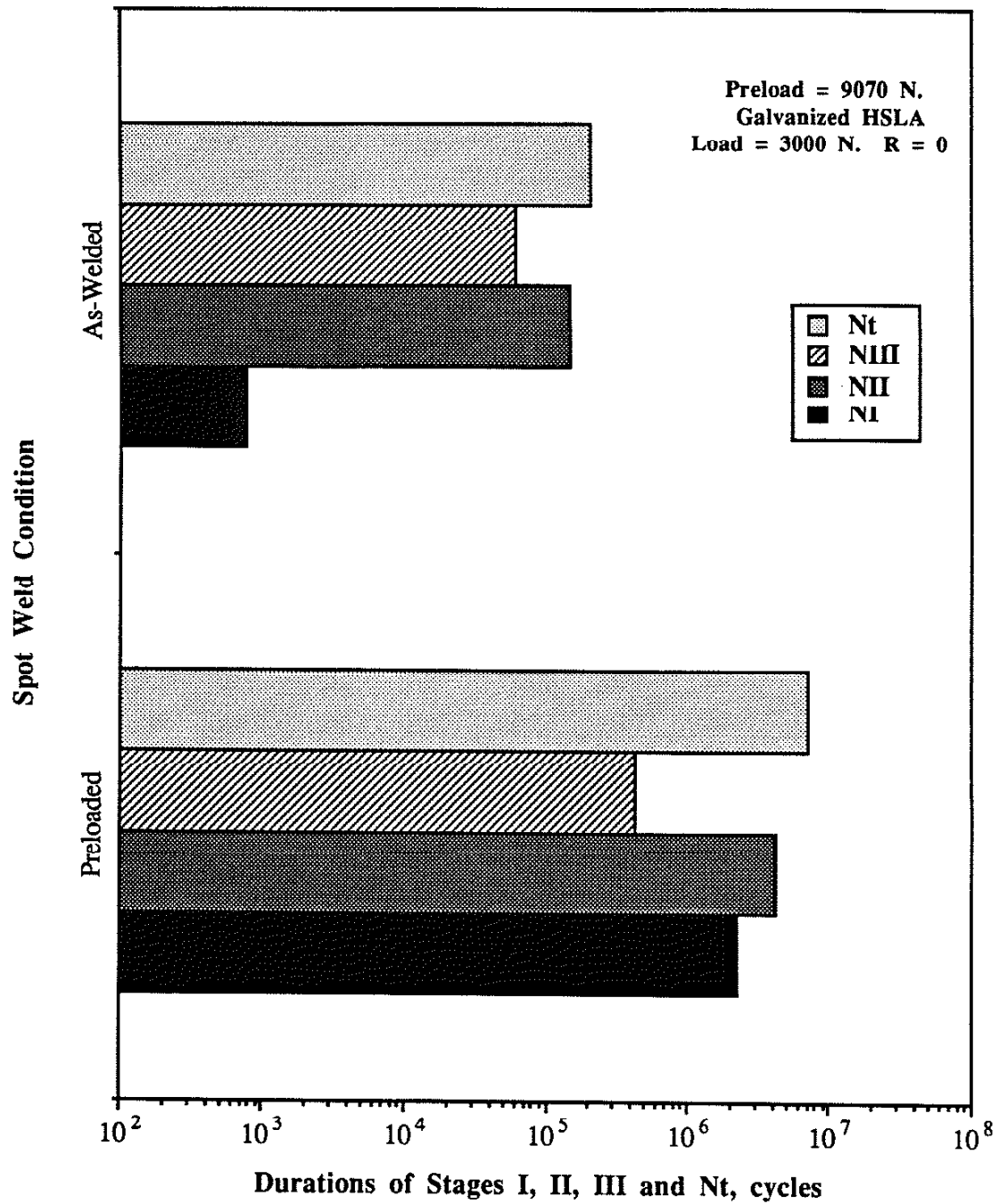


Fig. 3.27 Comparison of the effect of the preload on the total fatigue life and its stages

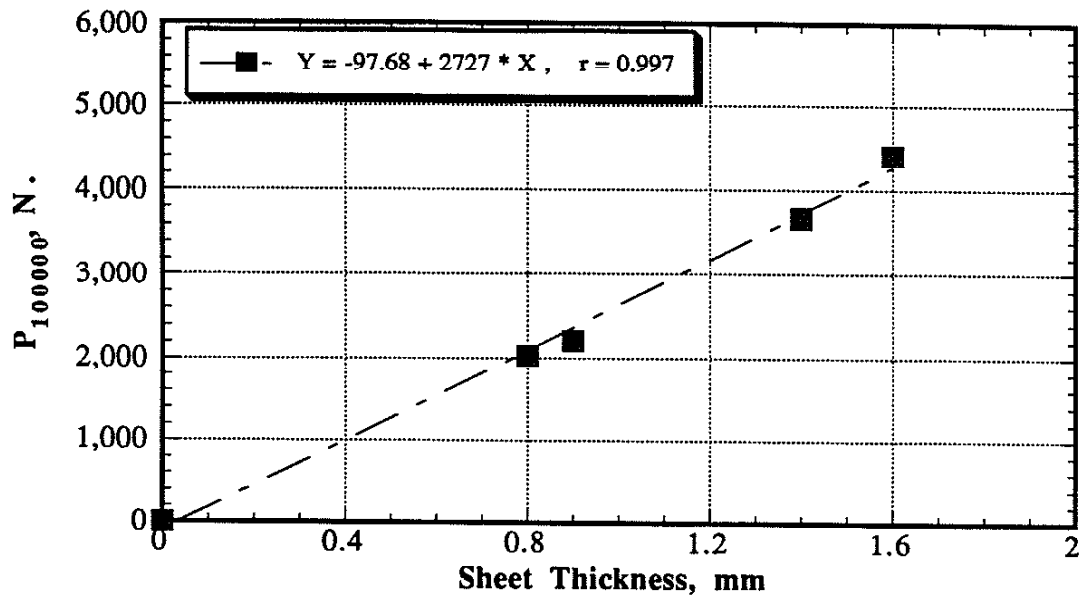


Fig. 3.28 Sheet thickness effect on the fatigue strength at 10^5 cycles

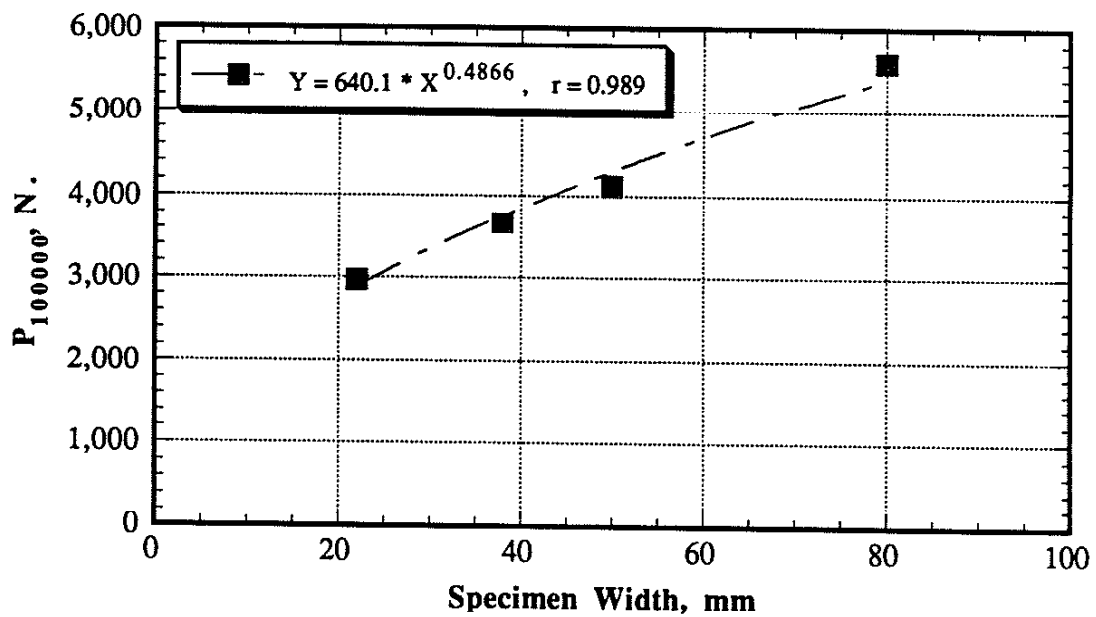


Fig. 3.29 Specimen width effect on the fatigue strength at 10^5 cycles

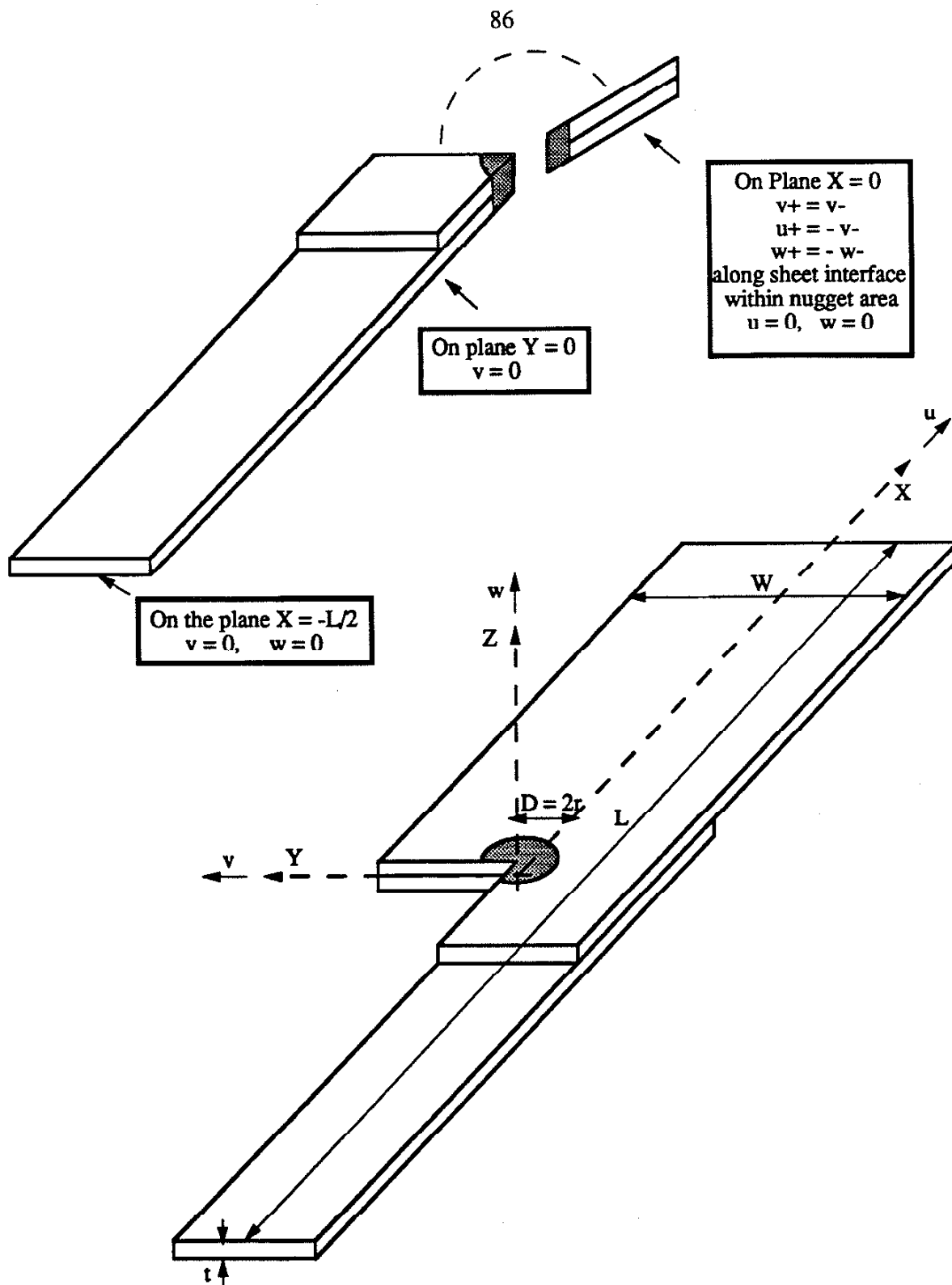


Fig. 4.1 Dimensions of tensile-shear specimen and the boundary conditions for the finite element model

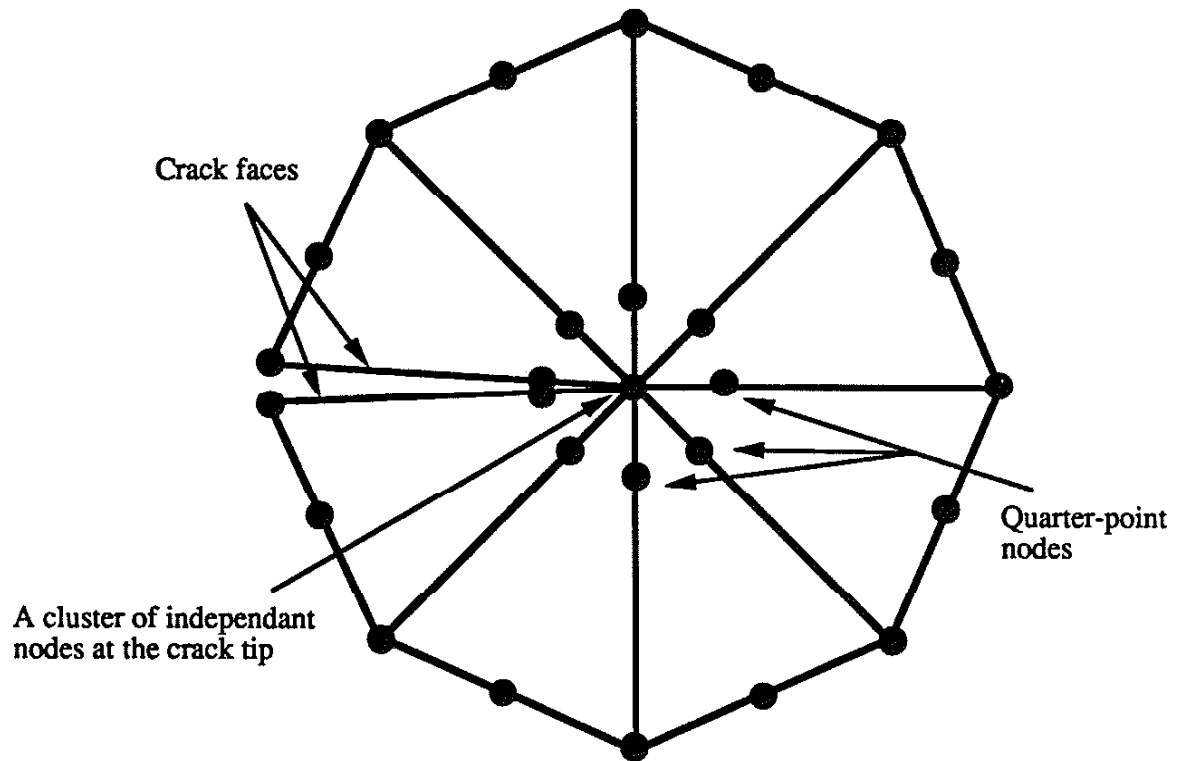


Fig. 4.2 The fan shape first ring of elements with quarter-point nodes

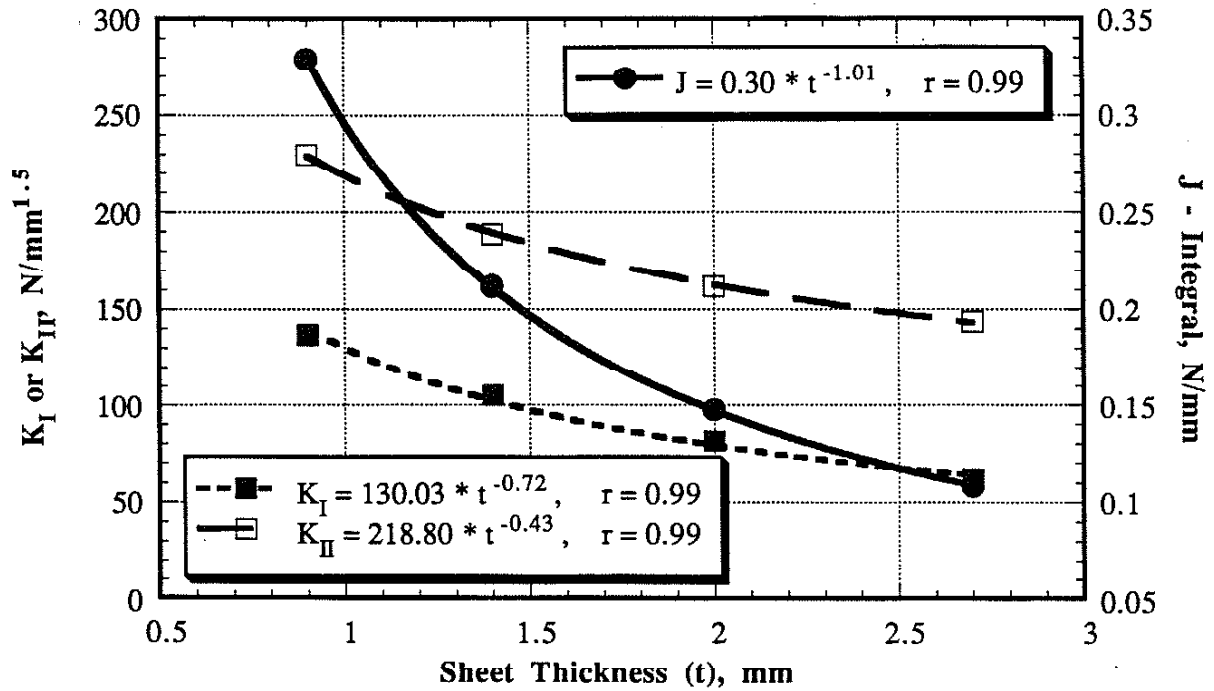


Fig. 4.3 Sheet thickness effect on the K_I , K_{II} and J-integral at the centerline of the tensile-shear specimen, $D = 6.1$, $W = 38$, $L = 140$ mm

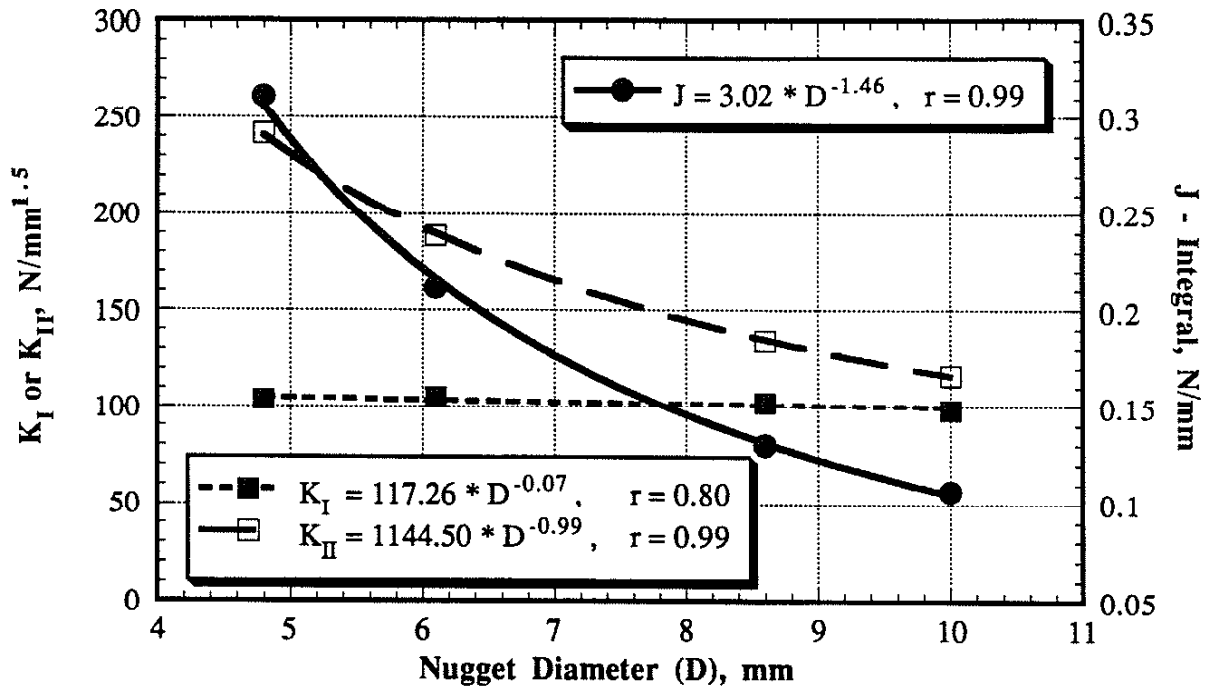


Fig. 4.4 Nugget diameter effect on the K_I , K_{II} and J-integral at the centerline of the tensile-shear specimen, $t = 1.4$, $W = 38$, $L = 140$ mm

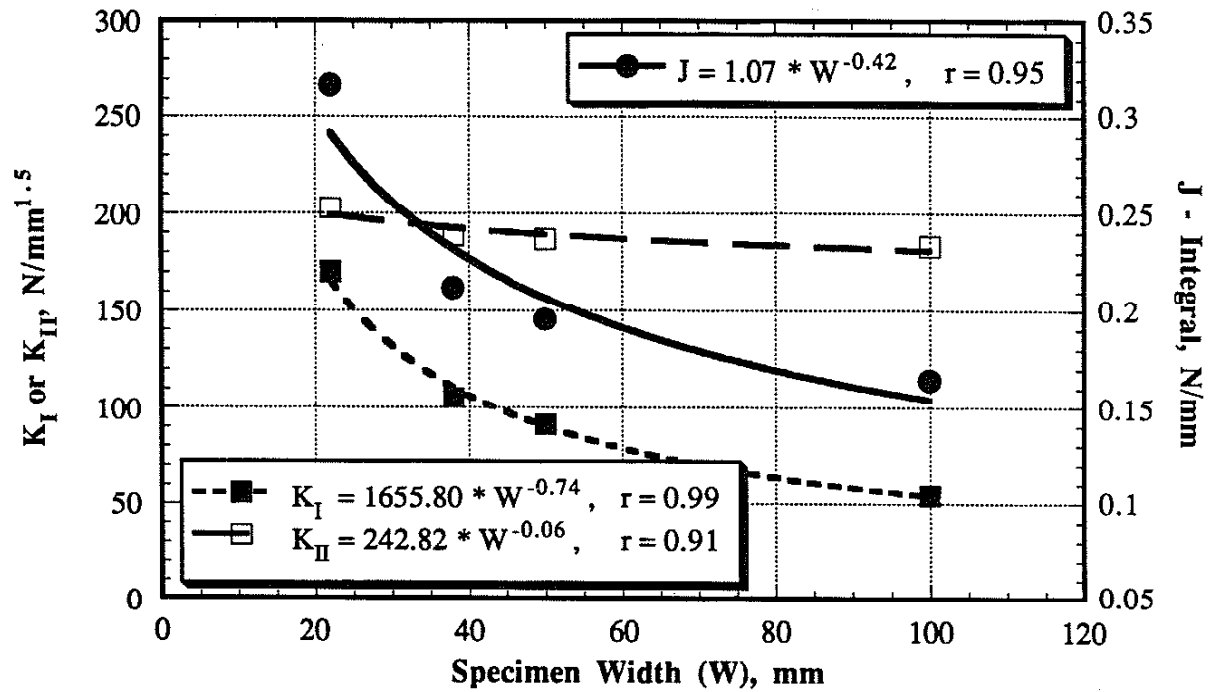


Fig. 4.5 Specimen width effect on the K_I , K_{II} and J-integral at the centerline of the tensile-shear specimen, $t = 1.4$, $D = 6.1$, $L = 140$ mm

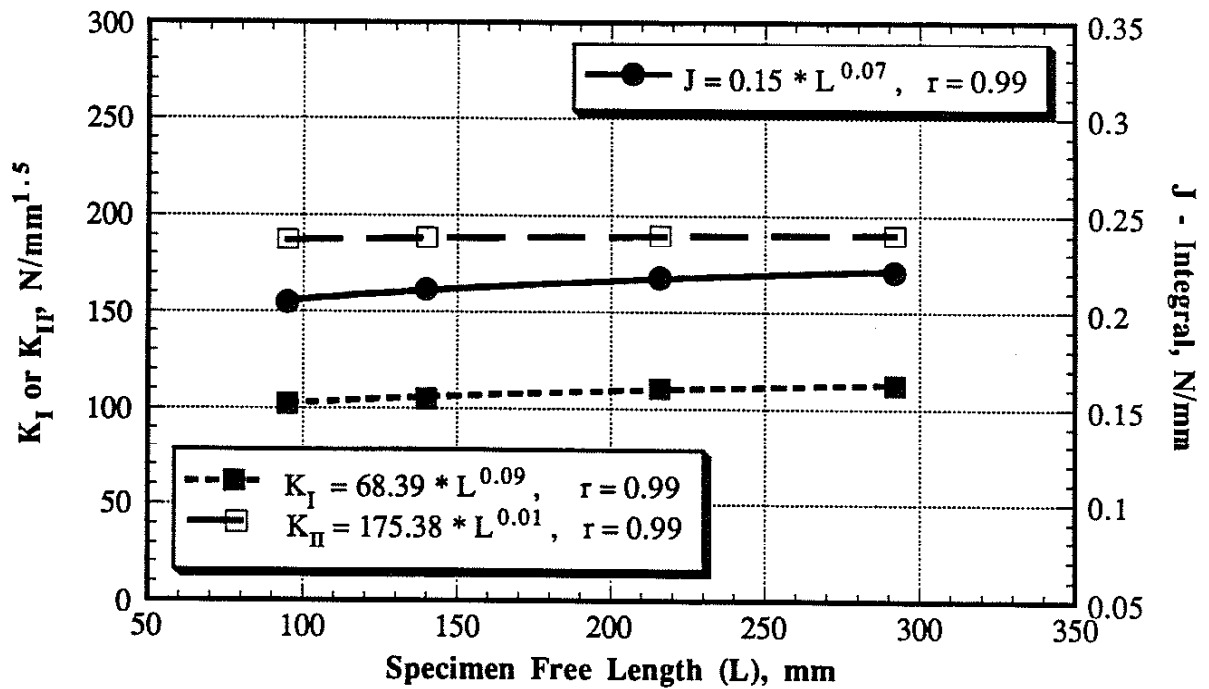


Fig. 4.6 Specimen free length effect on the K_I , K_{II} and J-integral at the centerline of the tensile-shear specimen, $t = 1.4$, $D = 6.1$, $W = 38$ mm

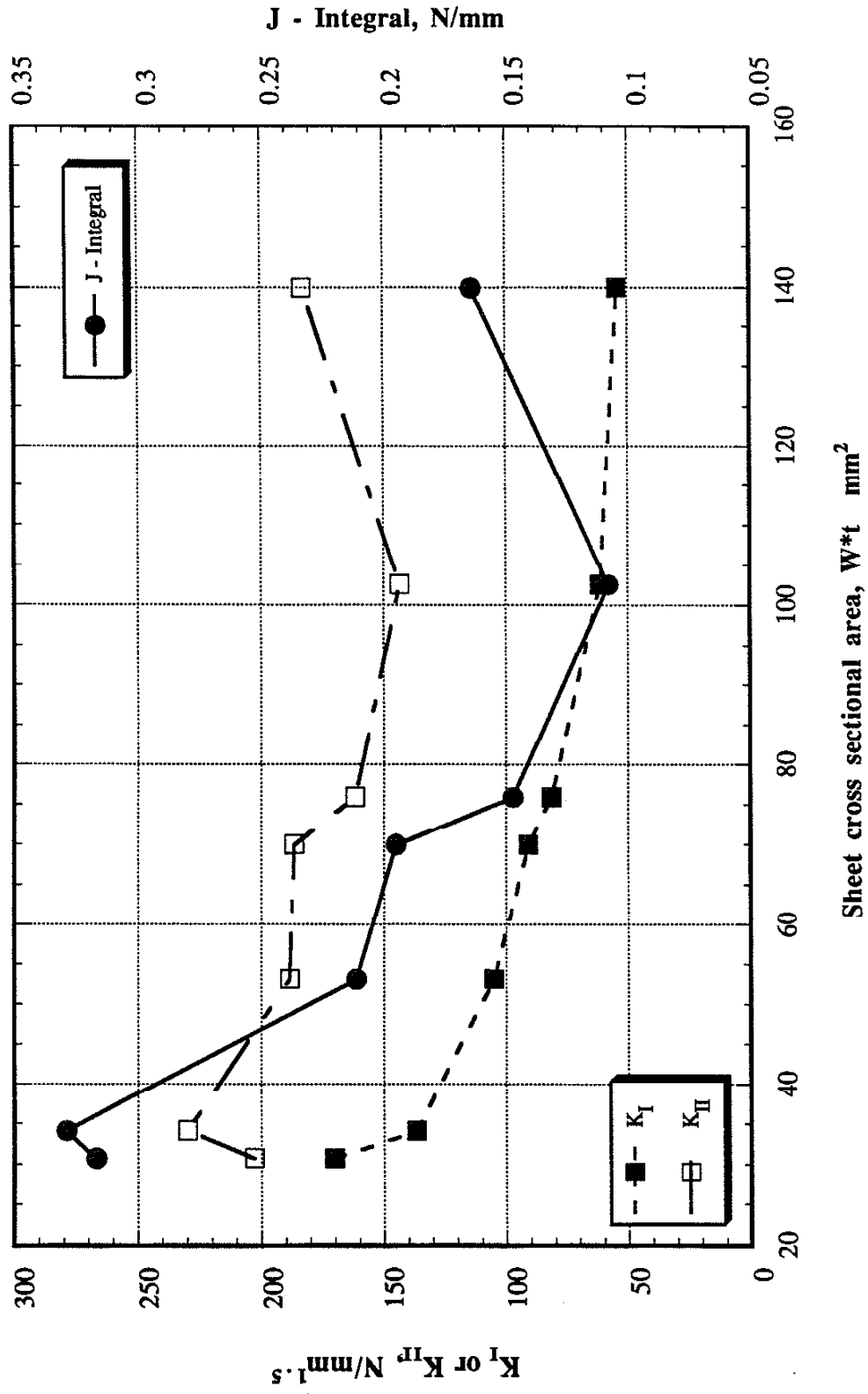


Fig. 4.7 Effect of the cross sectional area on K_I , K_{II} and J-integral.

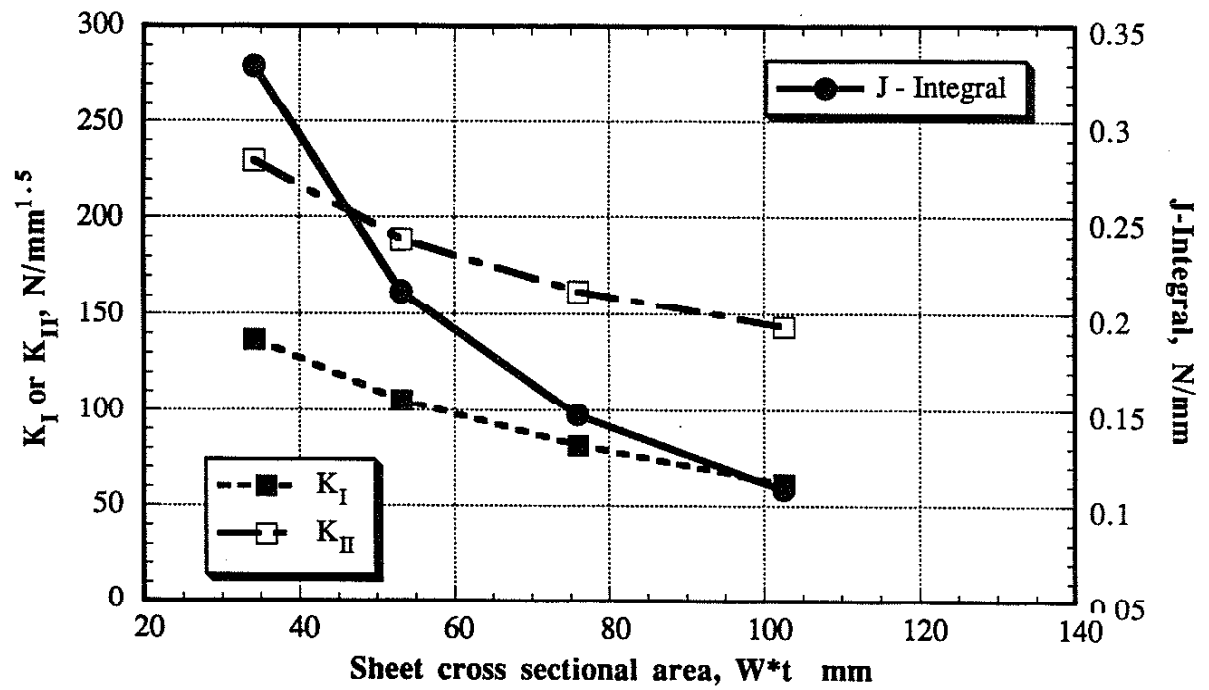


Fig. 4.8 Effect of the cross sectional area on K_I , K_{II} , and J-integral for $W = 38$ mm and variable t

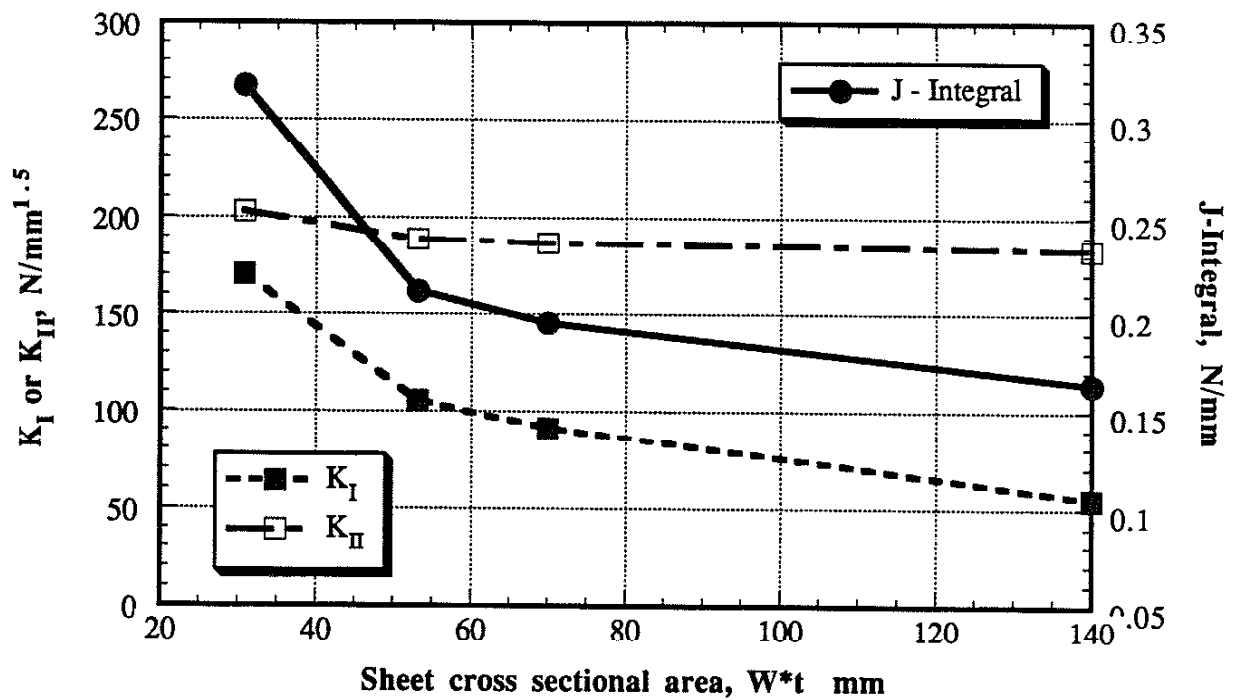


Fig. 4.9 Effect of the cross sectional area on K_I , K_{II} , and J-integral for $t = 1.4$ mm and variable W

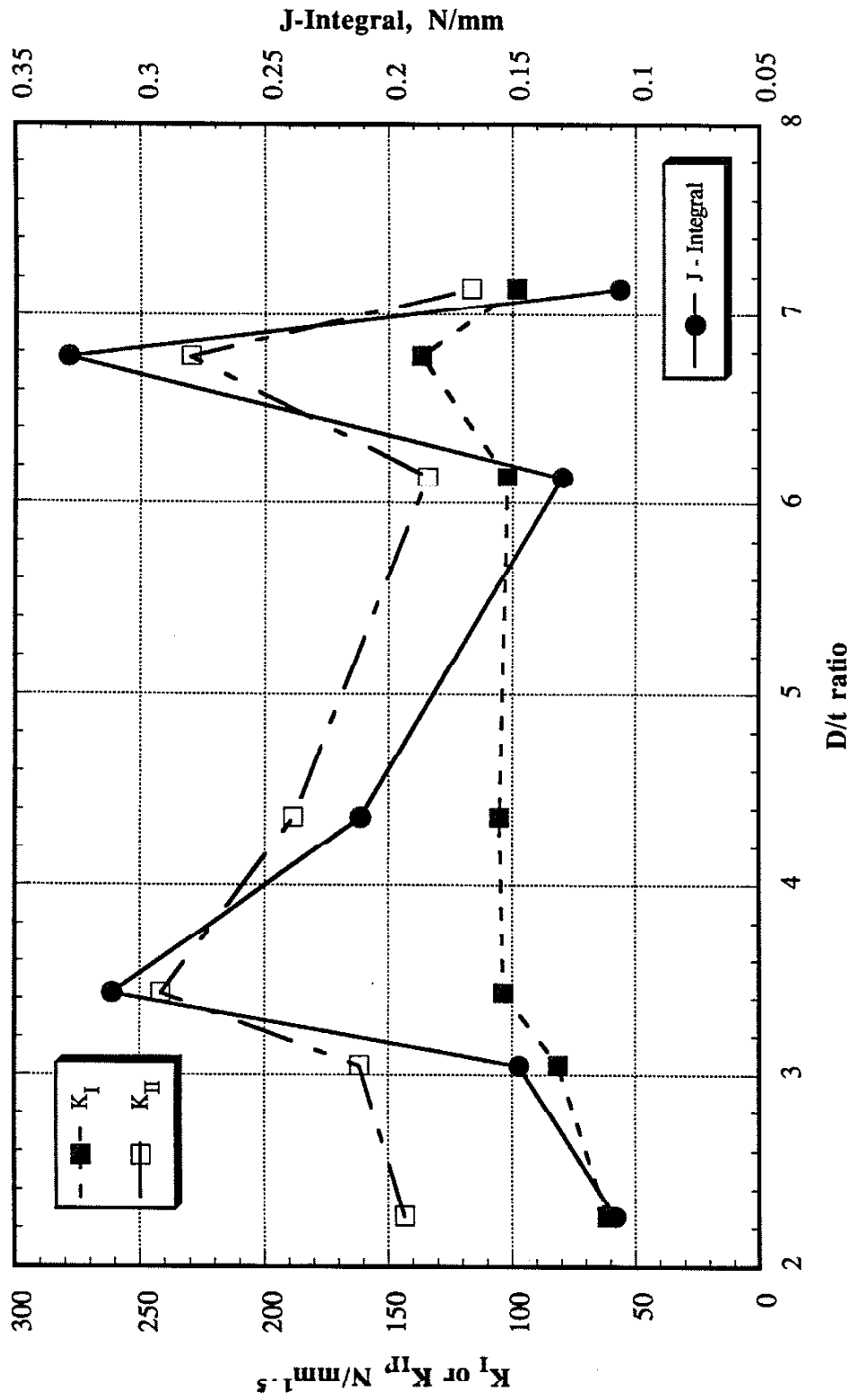


Fig. 4.10 Effect of the D/t ratio on K_I , K_{II} , and J-integral.

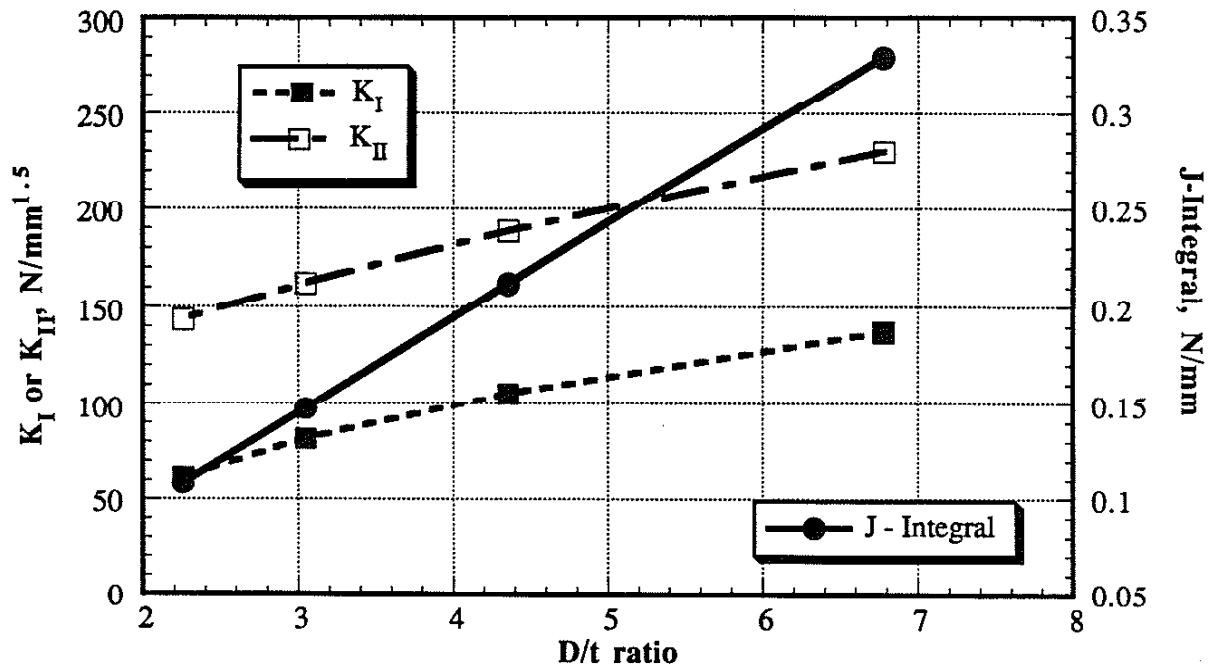


Fig. 4.11 Effect of the D/t ratio on K_I , K_{II} , and J-integral for $D = 6.1$ mm and variable t

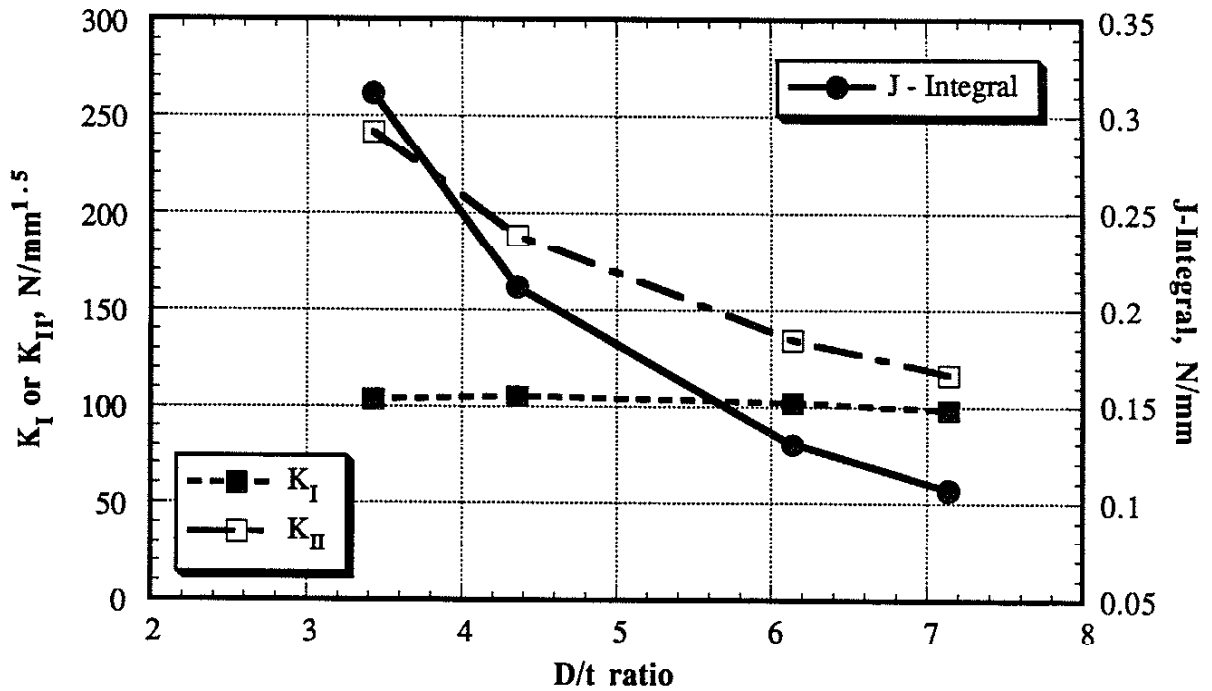


Fig. 4.12 Effect of the D/t ratio on K_I , K_{II} , and J-integral for $t = 1.4$ mm while varying D

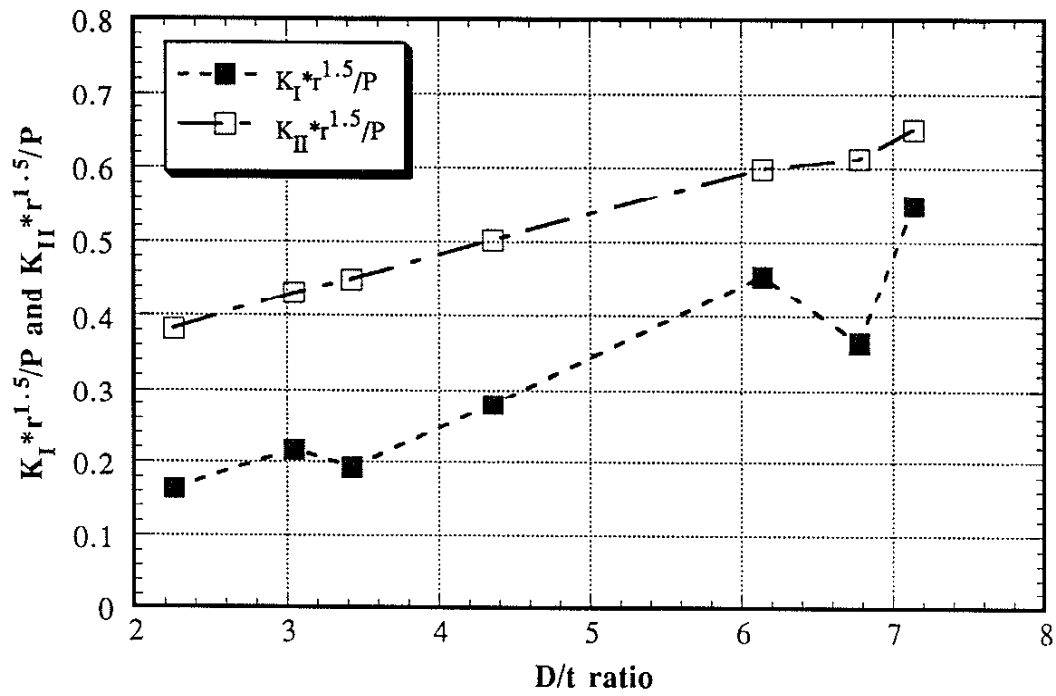


Fig. 4.13 $K_I * r^{1.5}/P$ and $K_{II} * r^{1.5}/P$ versus D/t

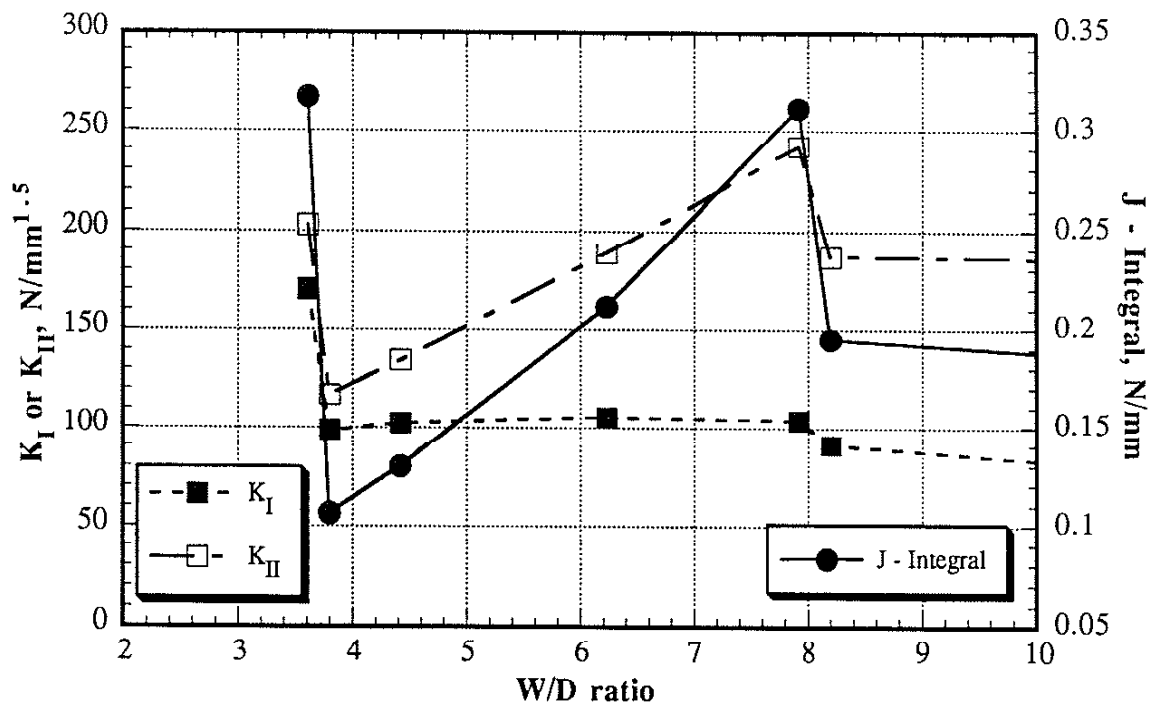


Fig. 4.14 Effect of the W/D ratio on K_I , K_{II} , and J -integral.

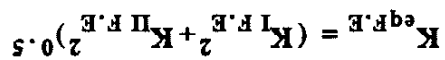


Fig. 4.15 $K_{eq.FE}$ and load-life Presentation of total fatigue life data for low carbon tensile-shear specimens, $R = 0$

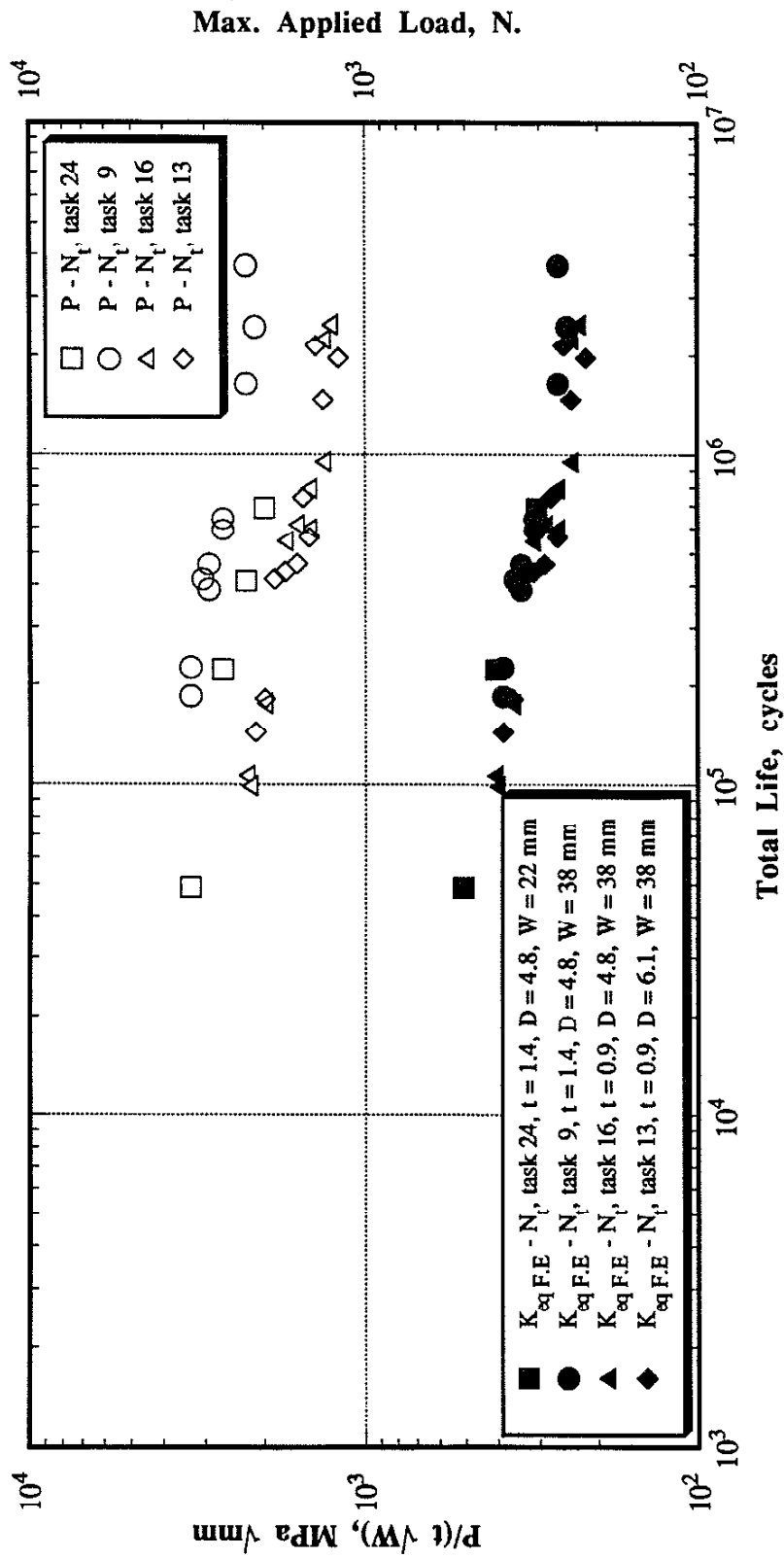


Fig. 5.1 $P/(t\sqrt{W})$ and load-life Presentation of total fatigue life data for low carbon tensile-shear specimens, $R = 0$

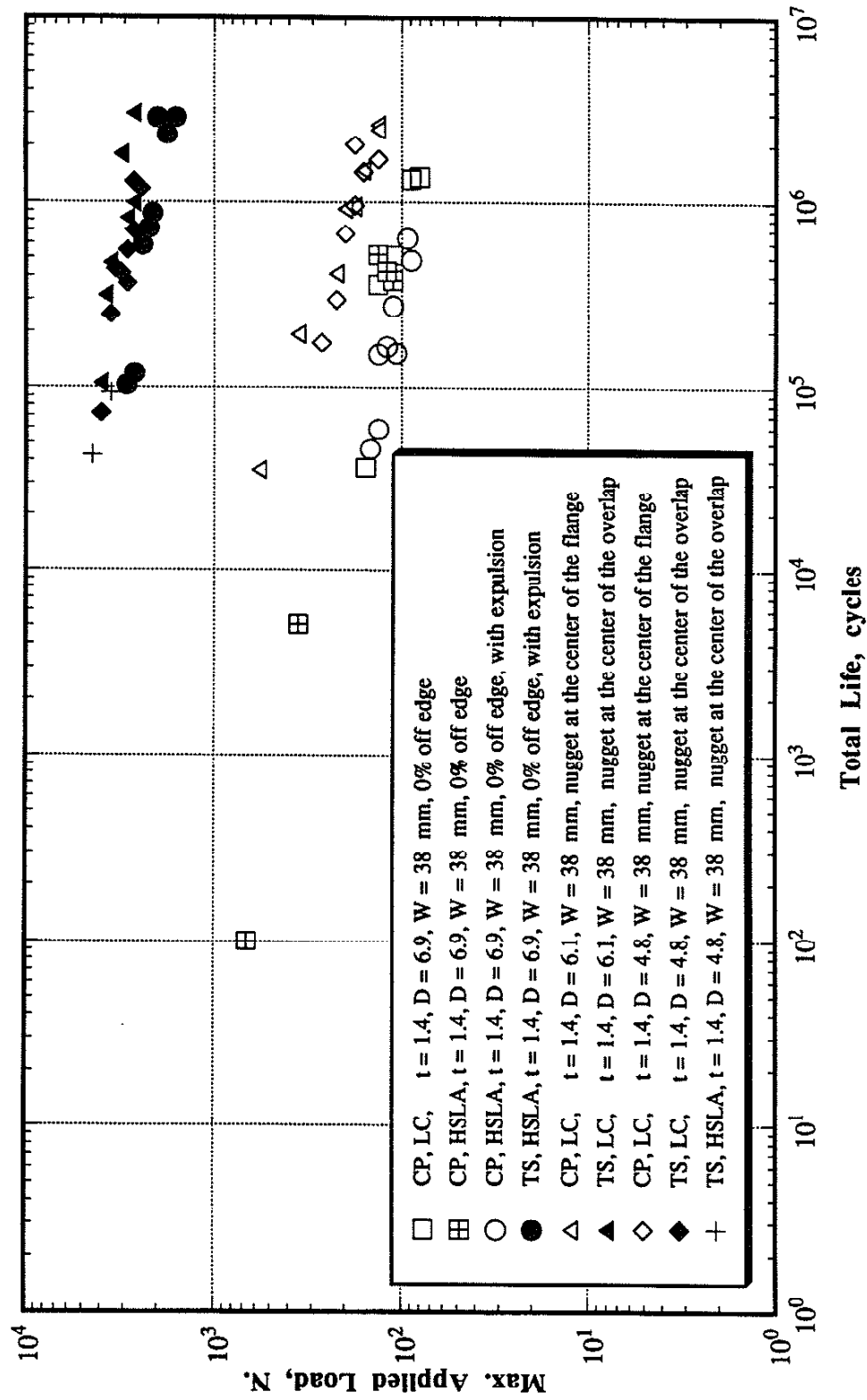


Fig. 5.2 Maximum applied load vs. total life for different tensile-shear and coach-peel specimens [81]

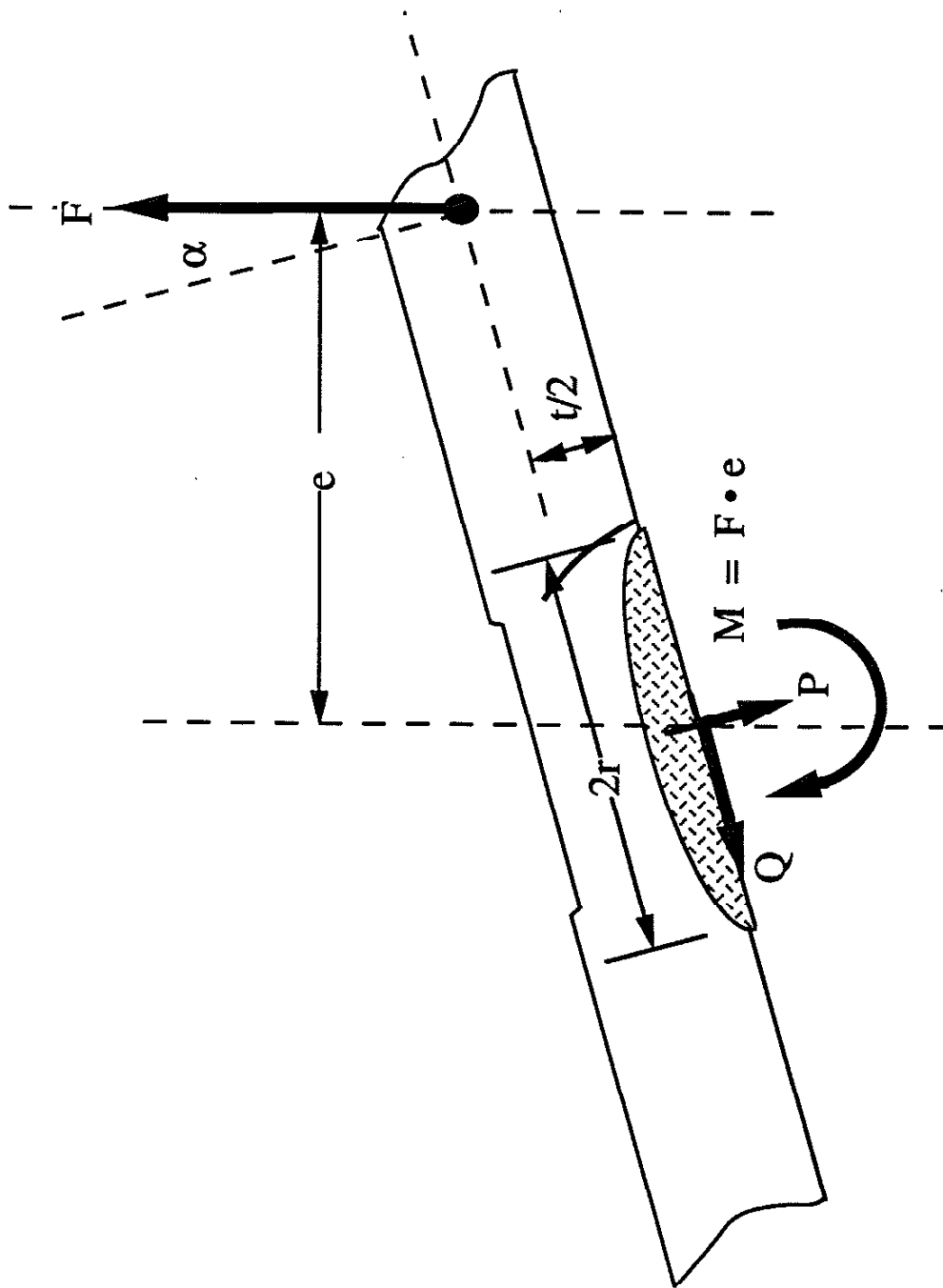


Fig. 5.3 Resolved components P , Q and M at the nugget for a general applied load F

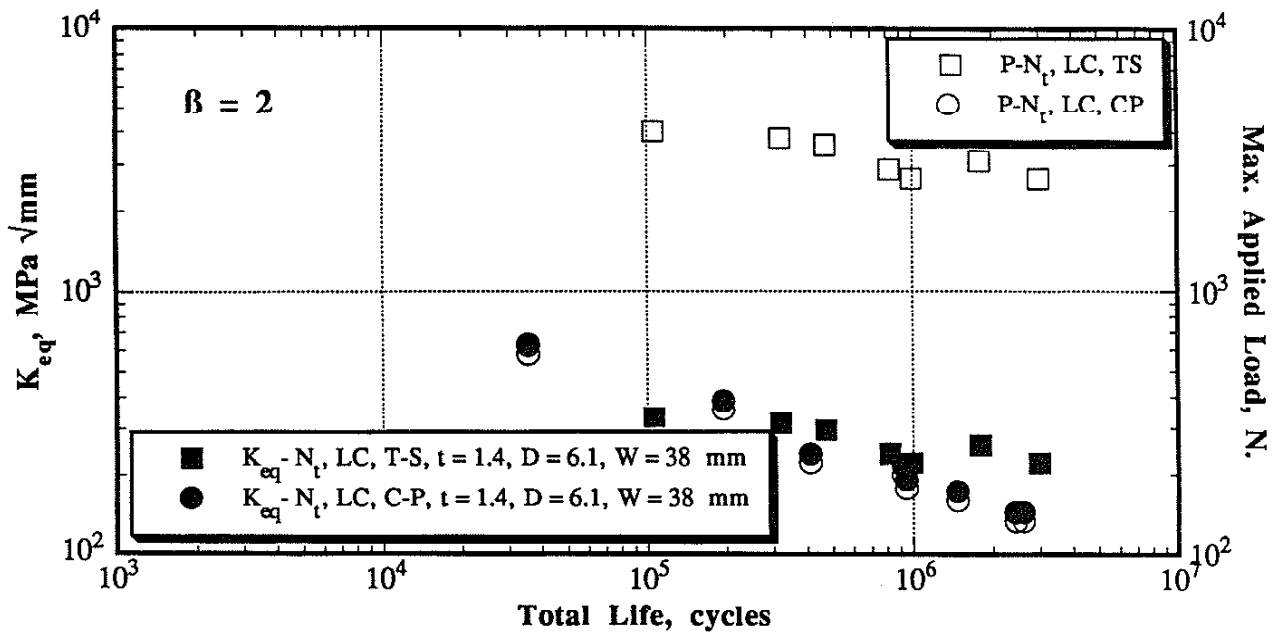


Fig. 5.4 K_{eq} and Load - Life presentation of total fatigue life data for tensile-shear and coach-peel [81] low carbon ($\beta = 2$) specimens

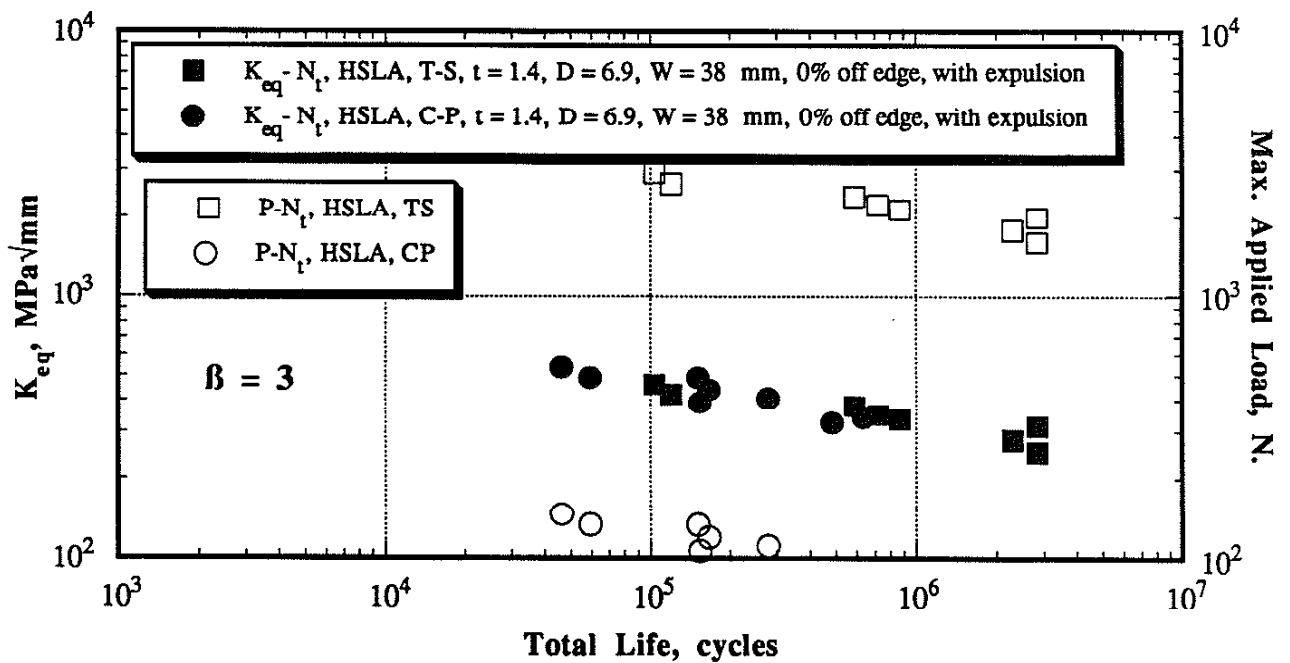


Fig. 5.5 K_{eq} and Load - Life presentation of total fatigue life data for tensile-shear and coach-peel [81] HSLA ($\beta = 3$) specimens

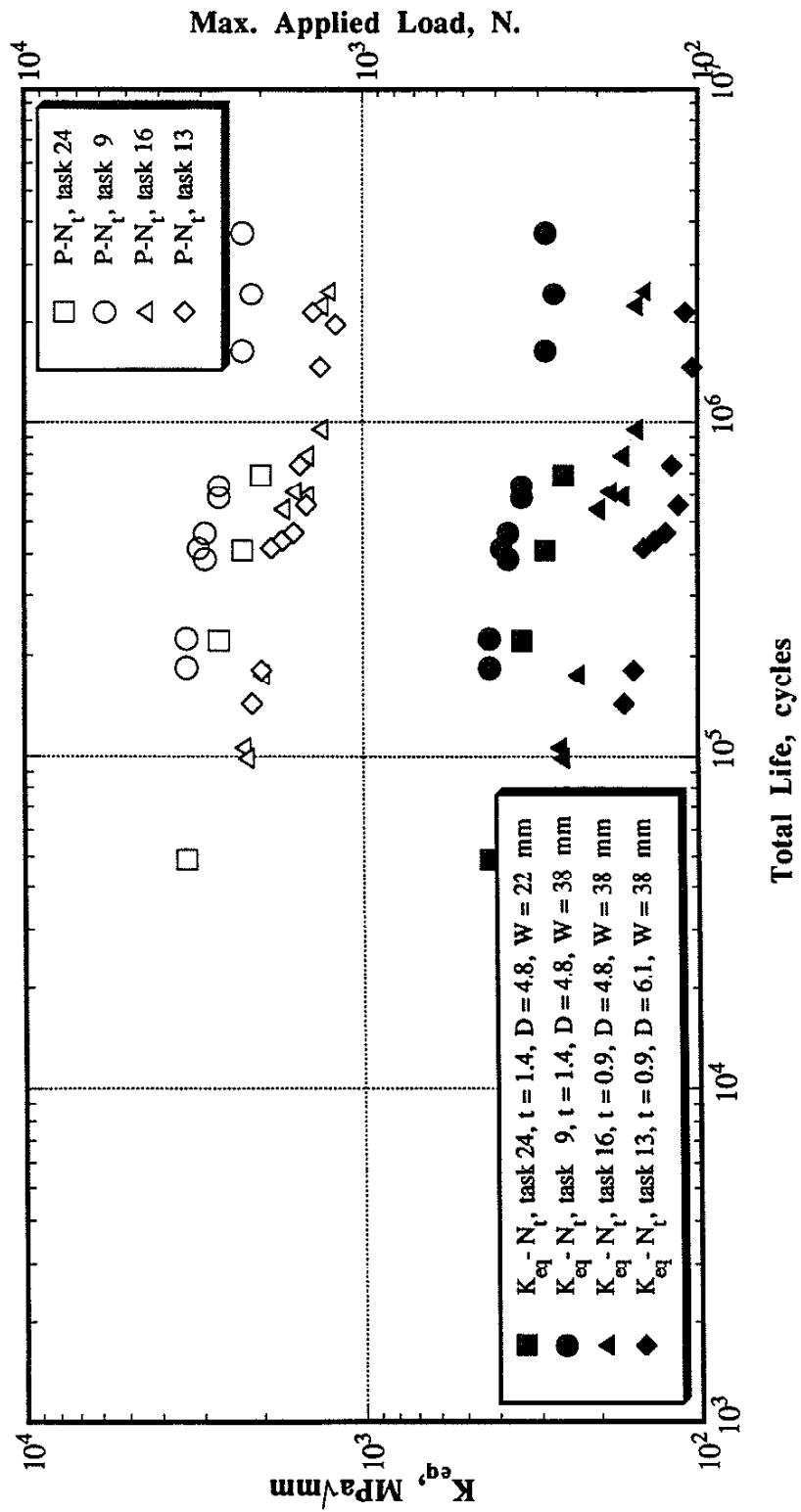


Fig. 5.6 K_{eq} and Load - Life presentation of total fatigue life data for tensile-shear low carbon specimens, $R = 0$

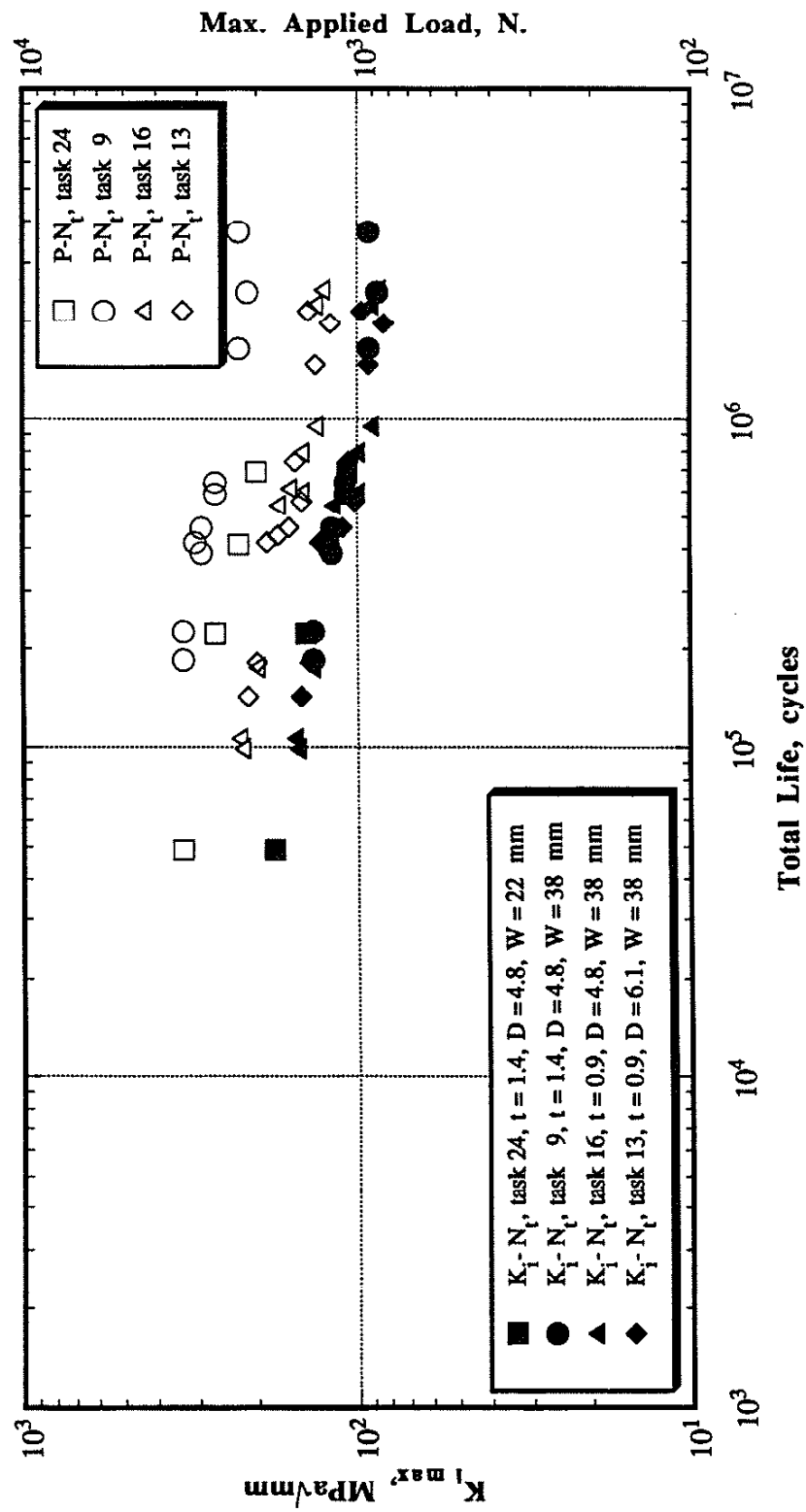


Fig. 5.7 $K_{I \max}$ and Load - Life presentation of total fatigue life data for low carbon tensile-shear specimens, $R = 0$

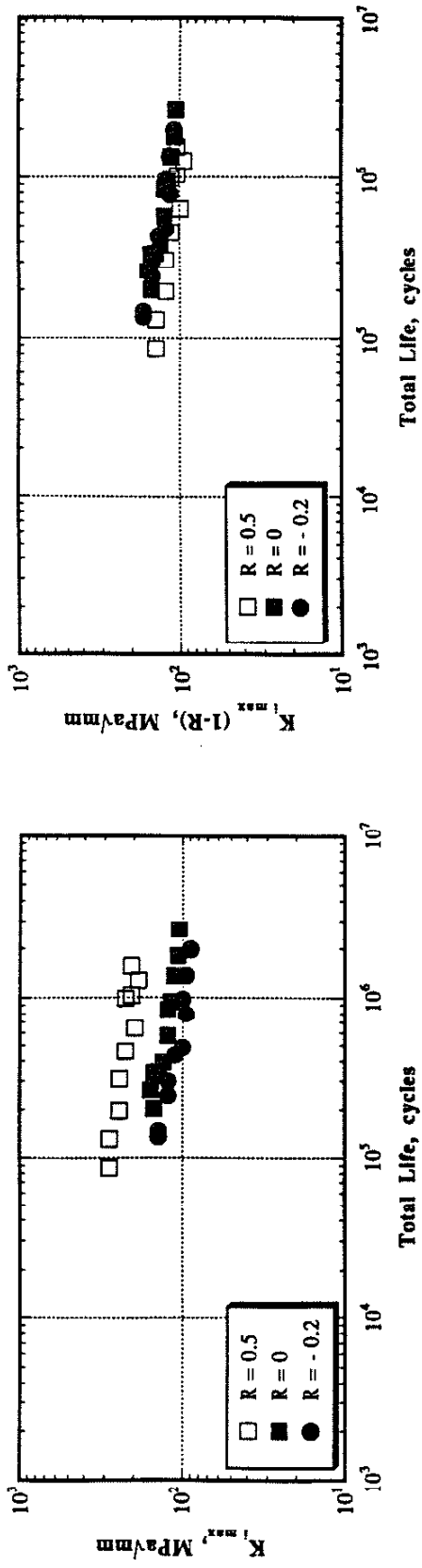


Fig. 5.8 Different Mean Stress Corrections

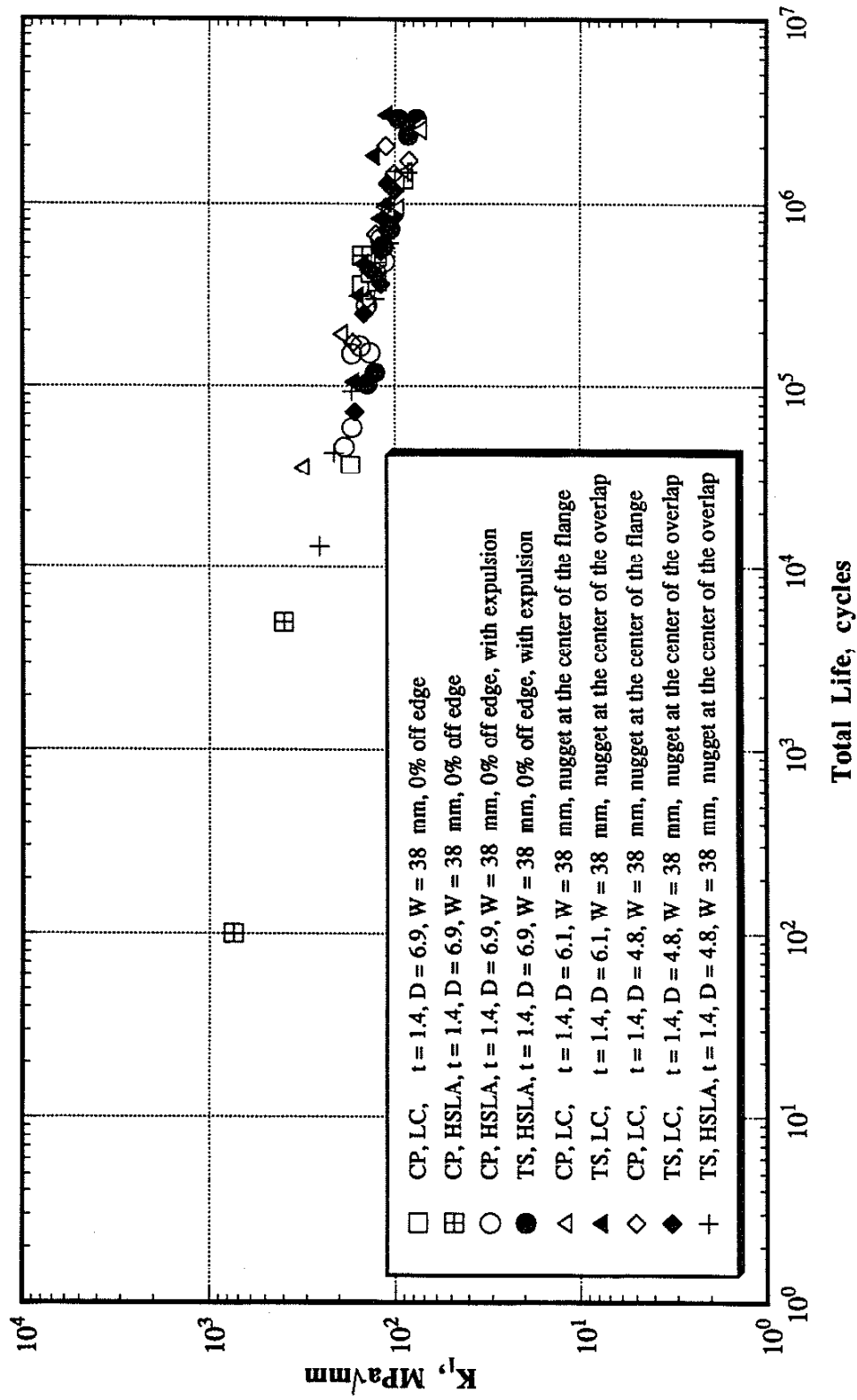


Fig. 5.9 K_I vs. total life for different tensile-shear and coach-peel specimens [81]

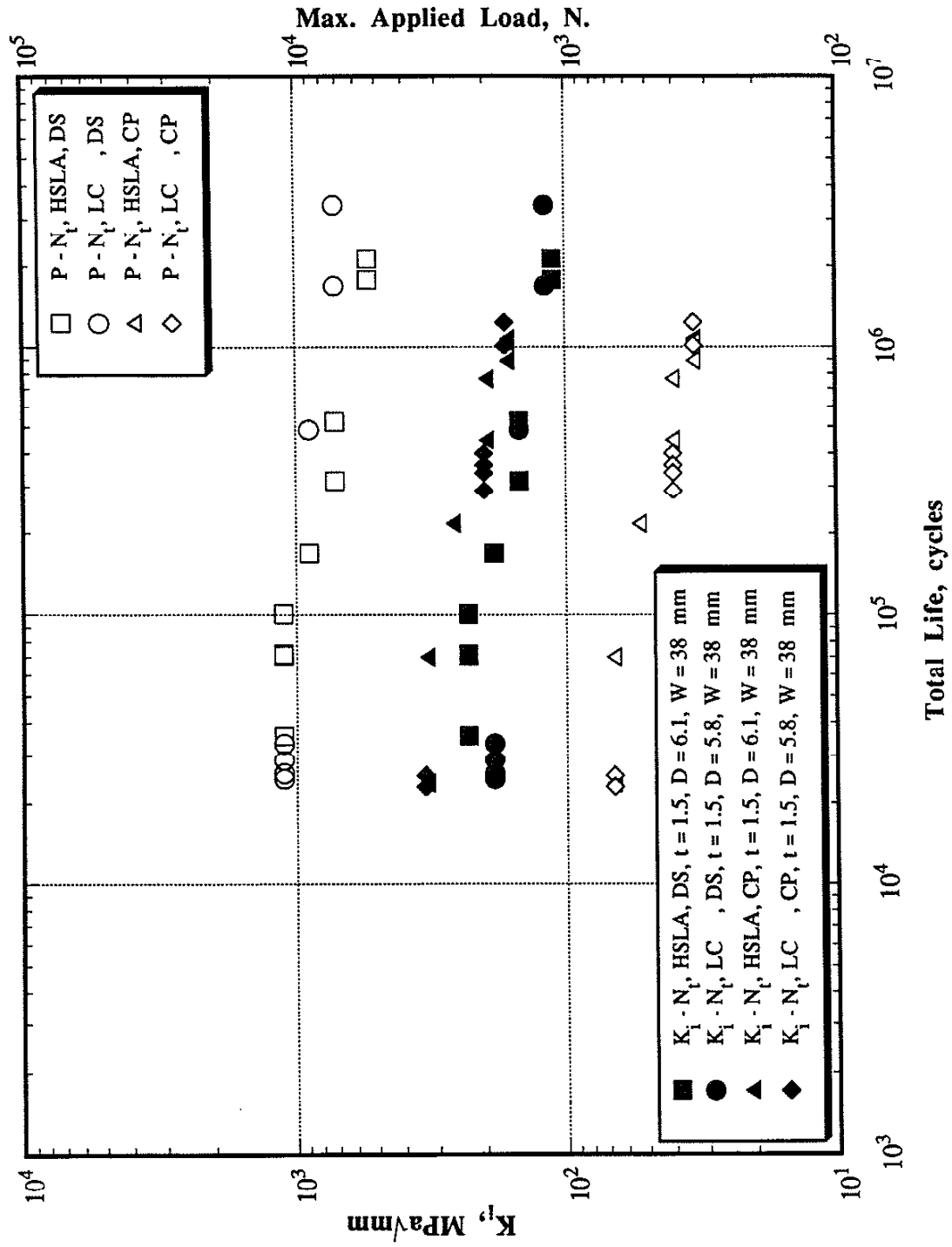


Fig. 5.10 K_I and load-life presentations of double-shear and coach-peel specimens [25]

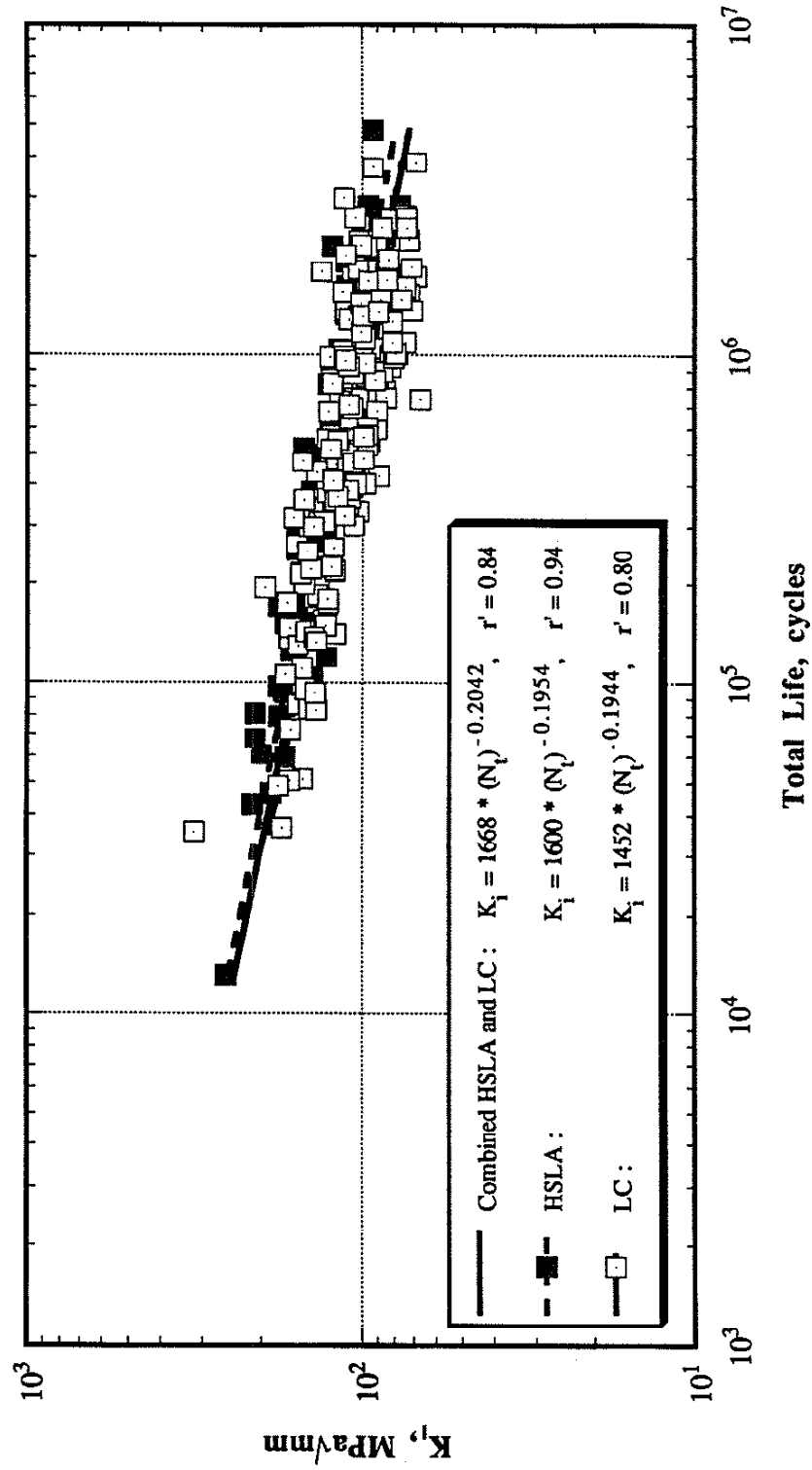


Fig. 5.11 K_I vs. total life fatigue data for HSLA and low carbon tensile-shear and coach-peel specimens

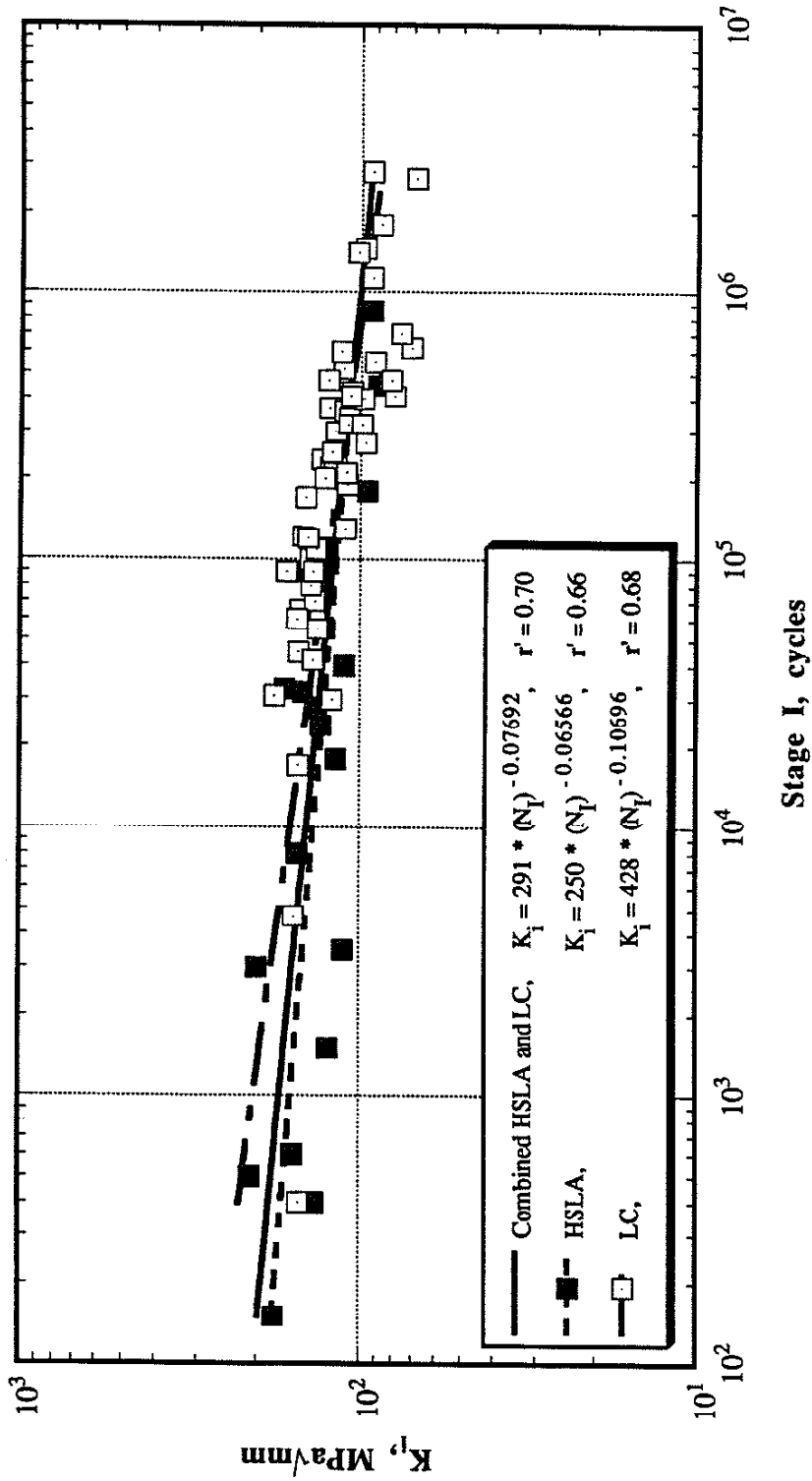


Fig. 5.12 K_I vs. Stage I fatigue data for HSLA and low carbon tensile-shear specimens

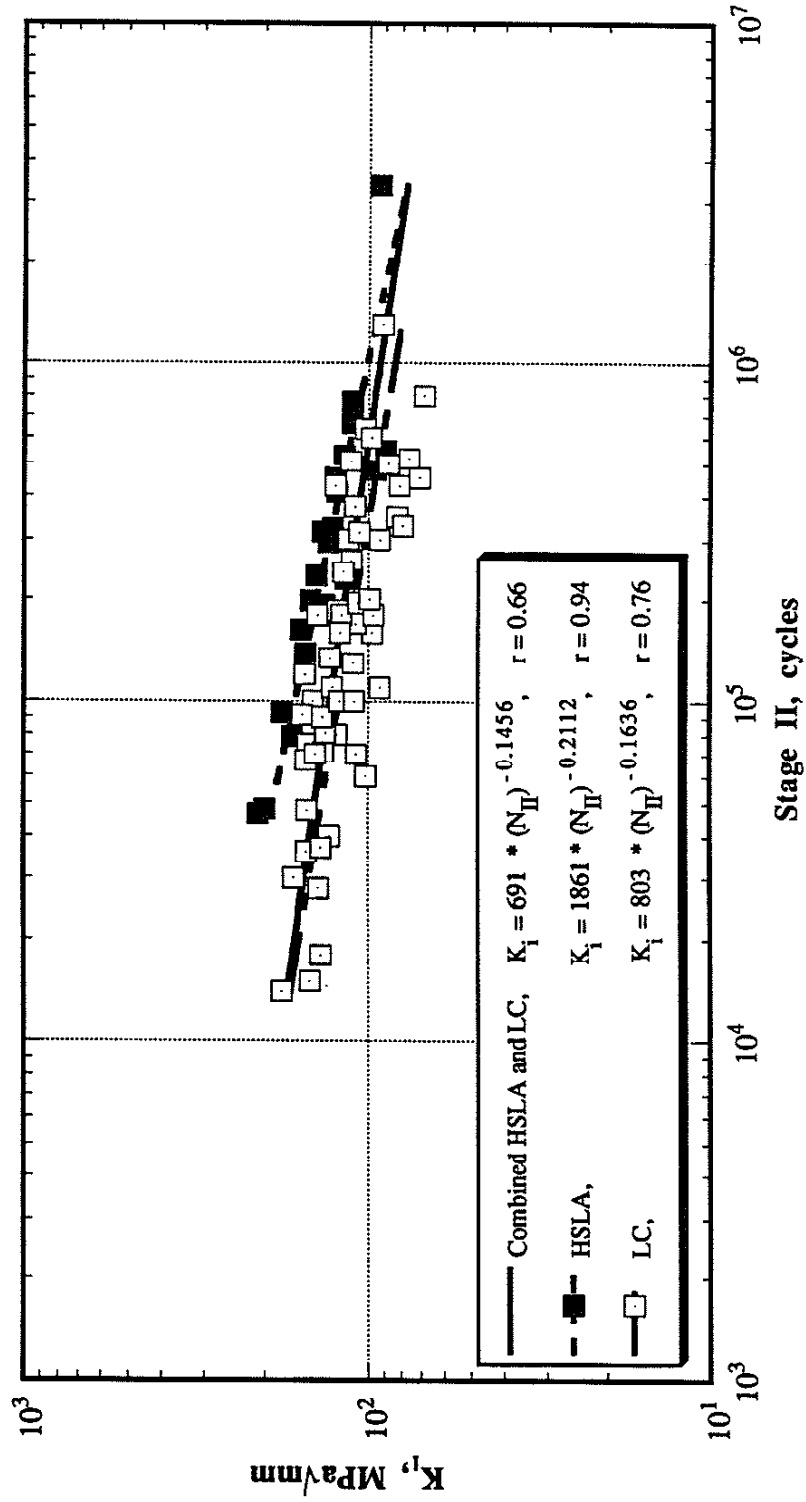


Fig. 5.13 K_I vs. Stage II fatigue data for HSLA and low carbon tensile-shear specimens

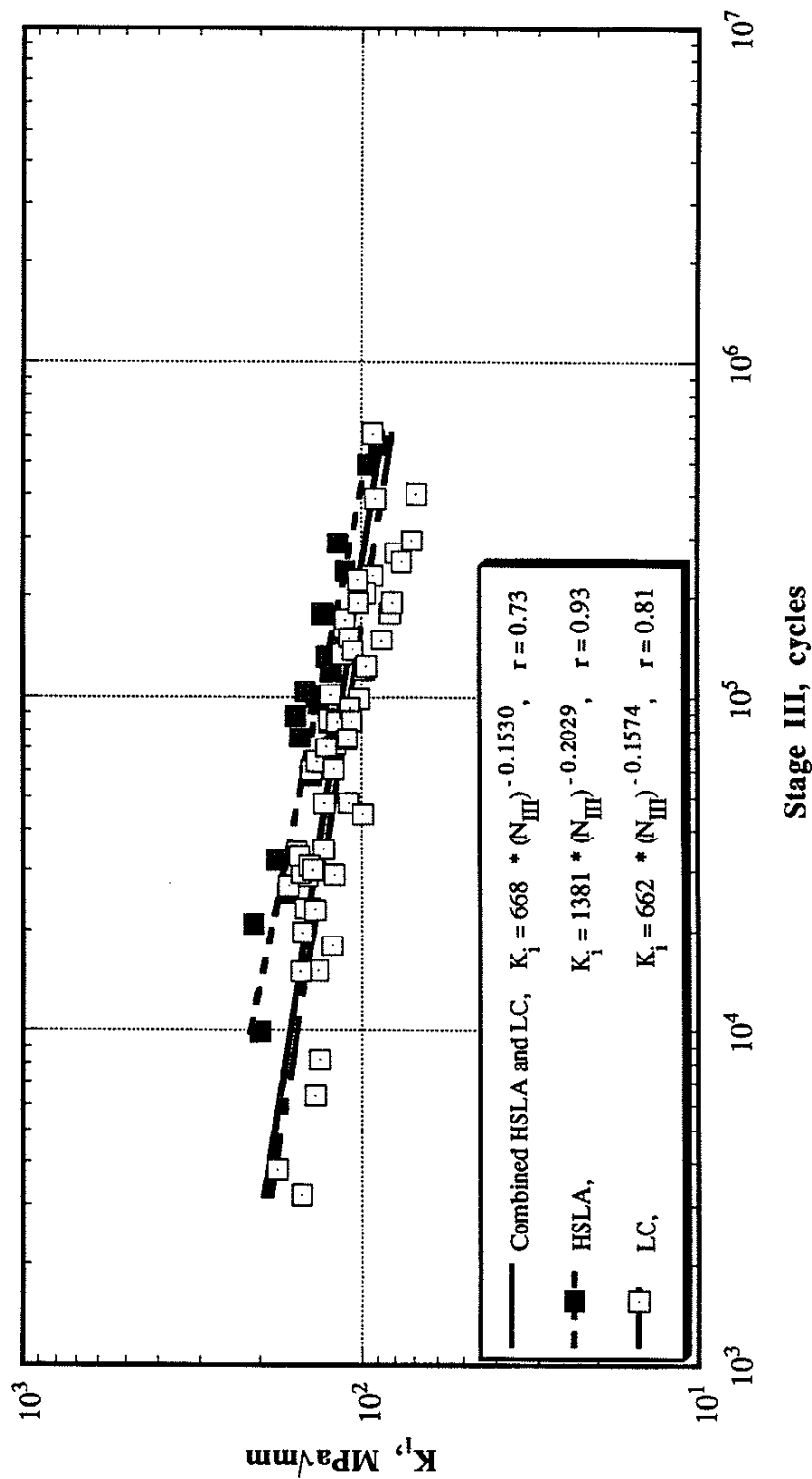


Fig. 5.14 K_I vs. Stage III fatigue data for HSLA and low carbon tensile-shear specimens

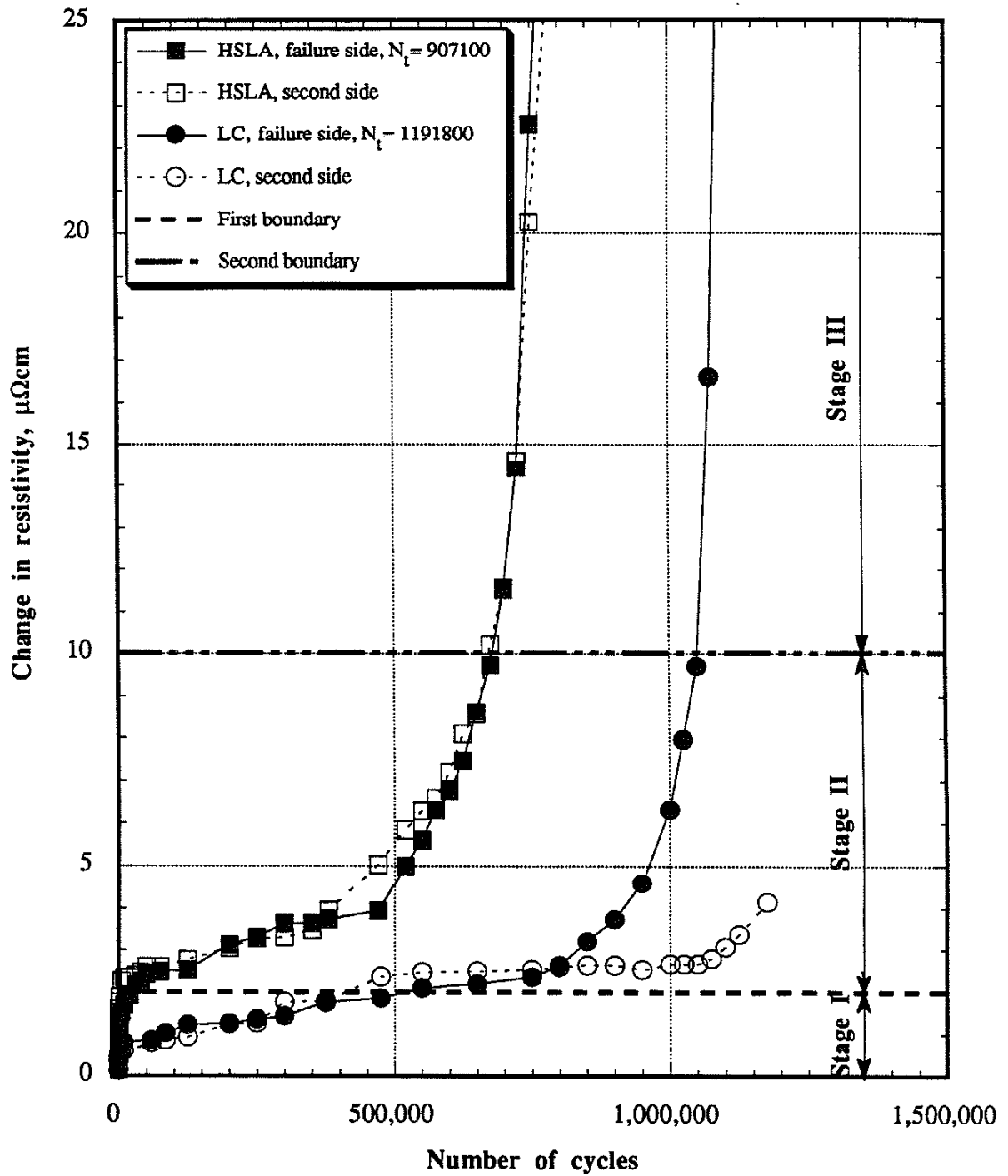


Fig. 6.1 Change in resistivity vs. number of cycles for HSLA and low carbon tensile-shear specimens $t = 1.4$, $D = 6.1$, $W = 38$ mm

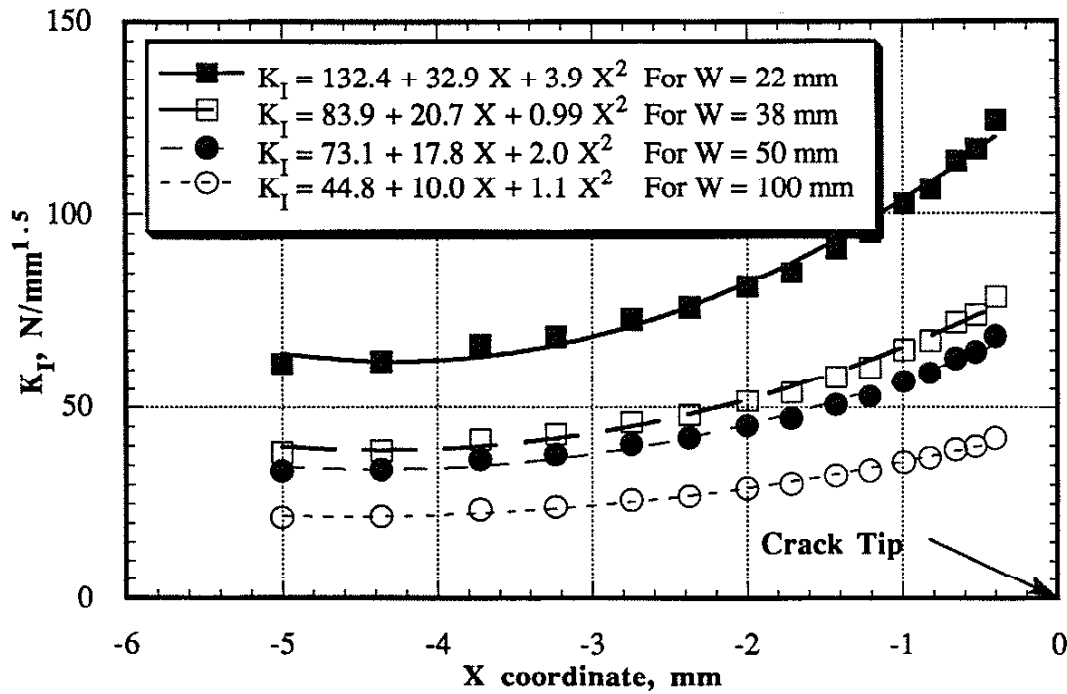


Fig. 6.2 K_I as calculated from Dieter's formulae along the longitudinal axis.

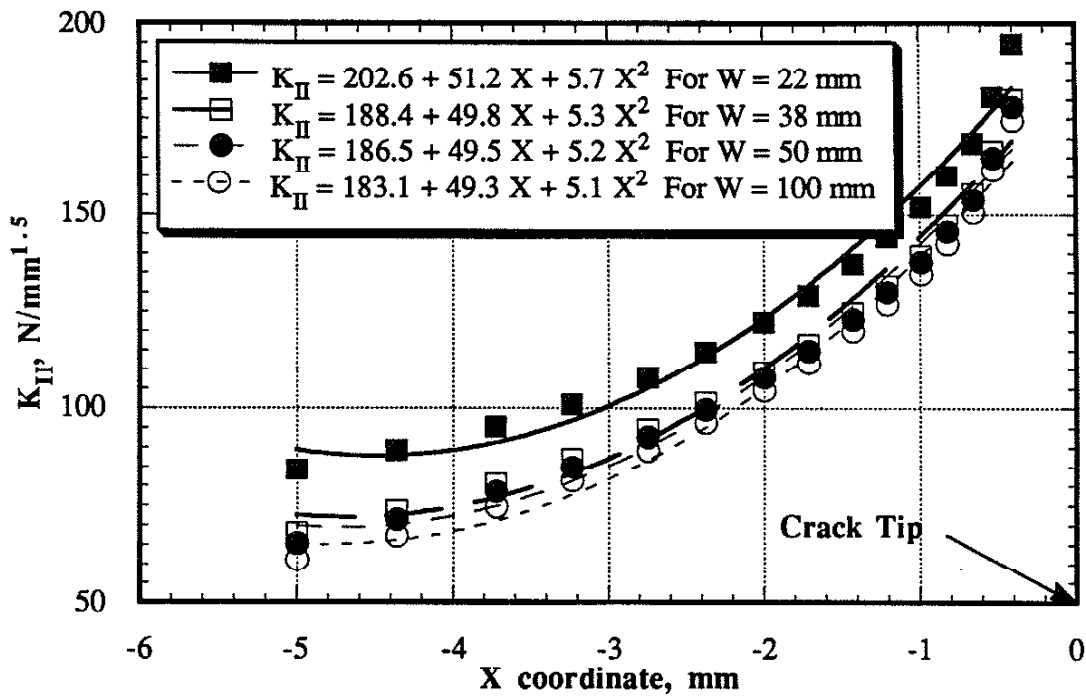


Fig. 6.3 K_{II} as calculated from Dieter's formulae along the longitudinal axis.

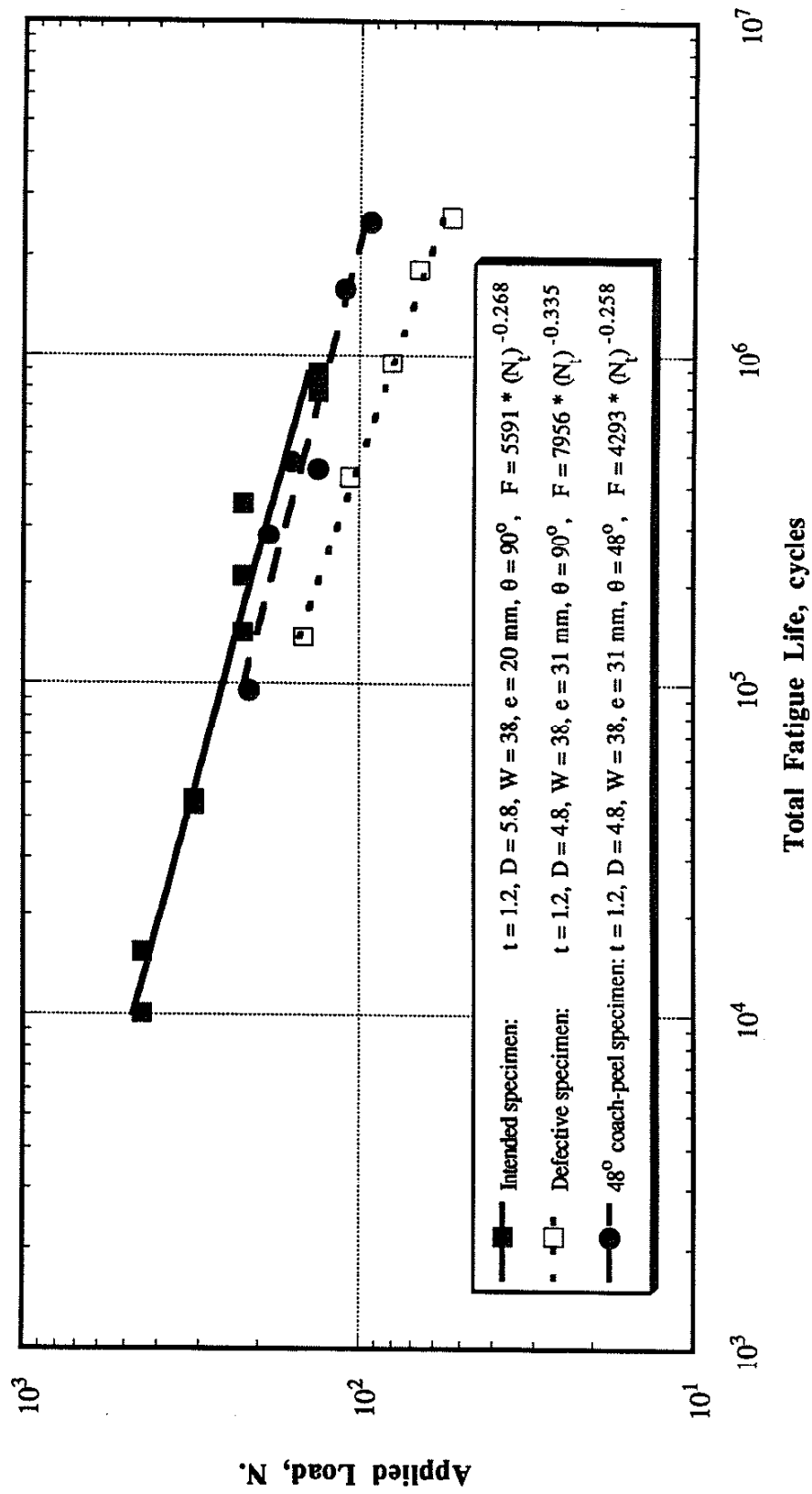


Fig. 6.4 Load-life presentation for the intended, the defective and the 48° coach-peel specimens.

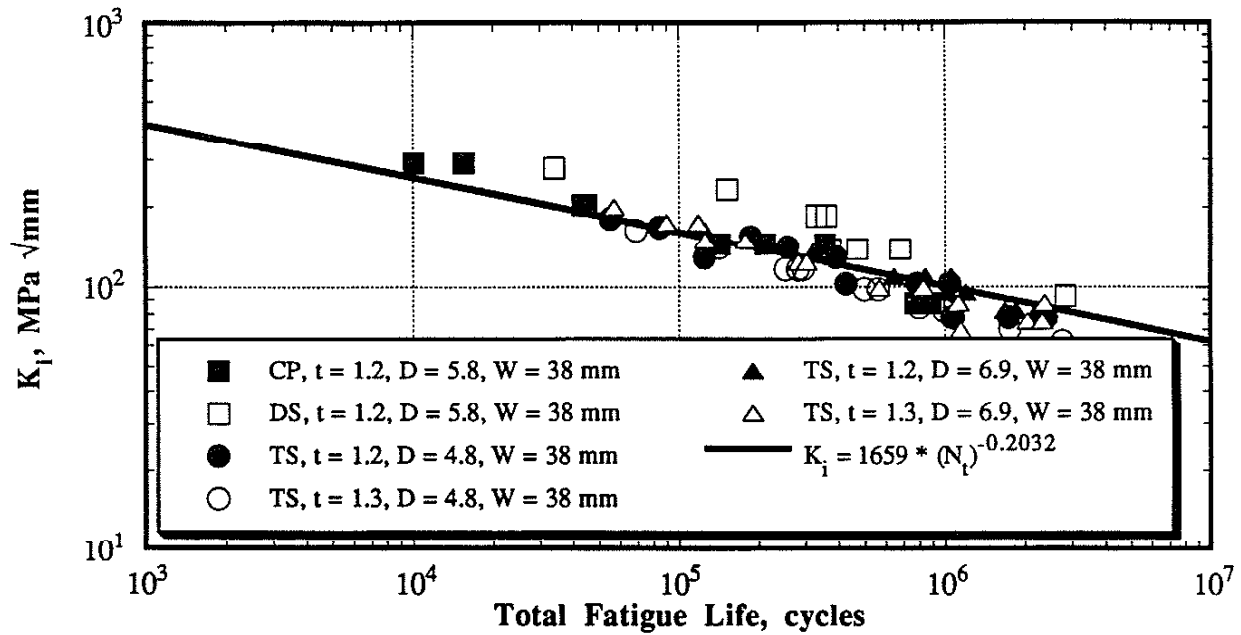


Fig. 6.5 K_I vs. total fatigue life for galvanized ($t = 1.2$ mm) and Bare ($t = 1.3$ mm) HSLA coach-peel, double-shear and tensile-shear specimens [85]

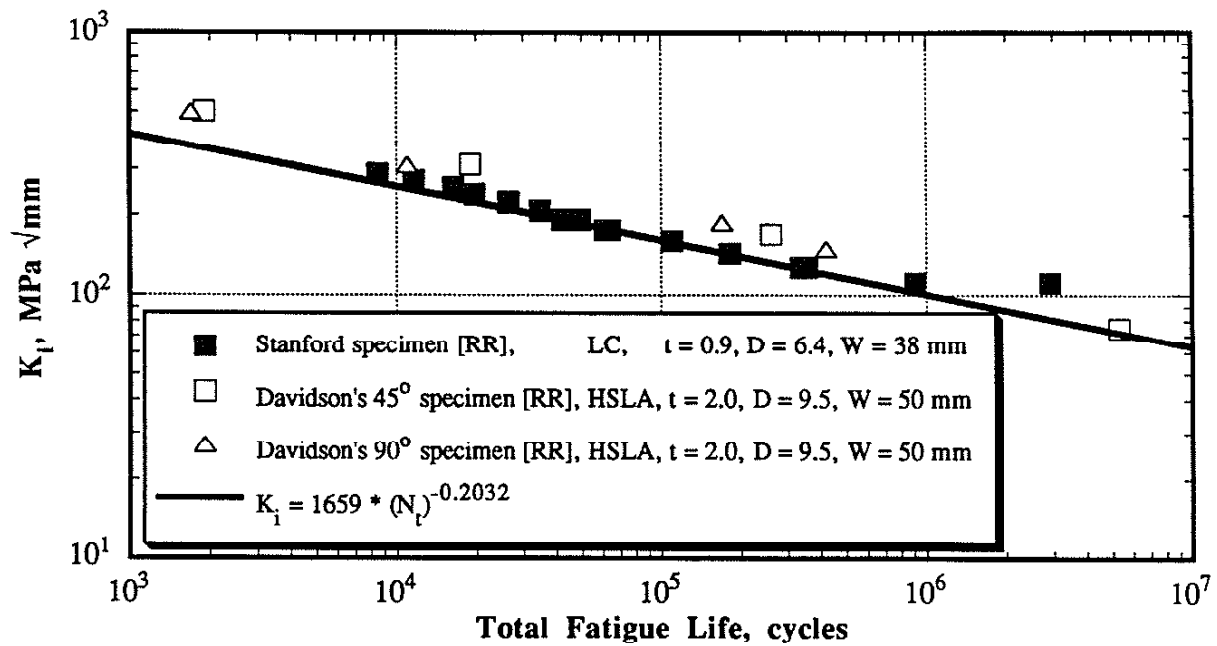


Fig. 6.6 K_I vs total fatigue life for Stanford's [86] sheet to channel specimen and Davidson's [10,11] channel to channel specimens

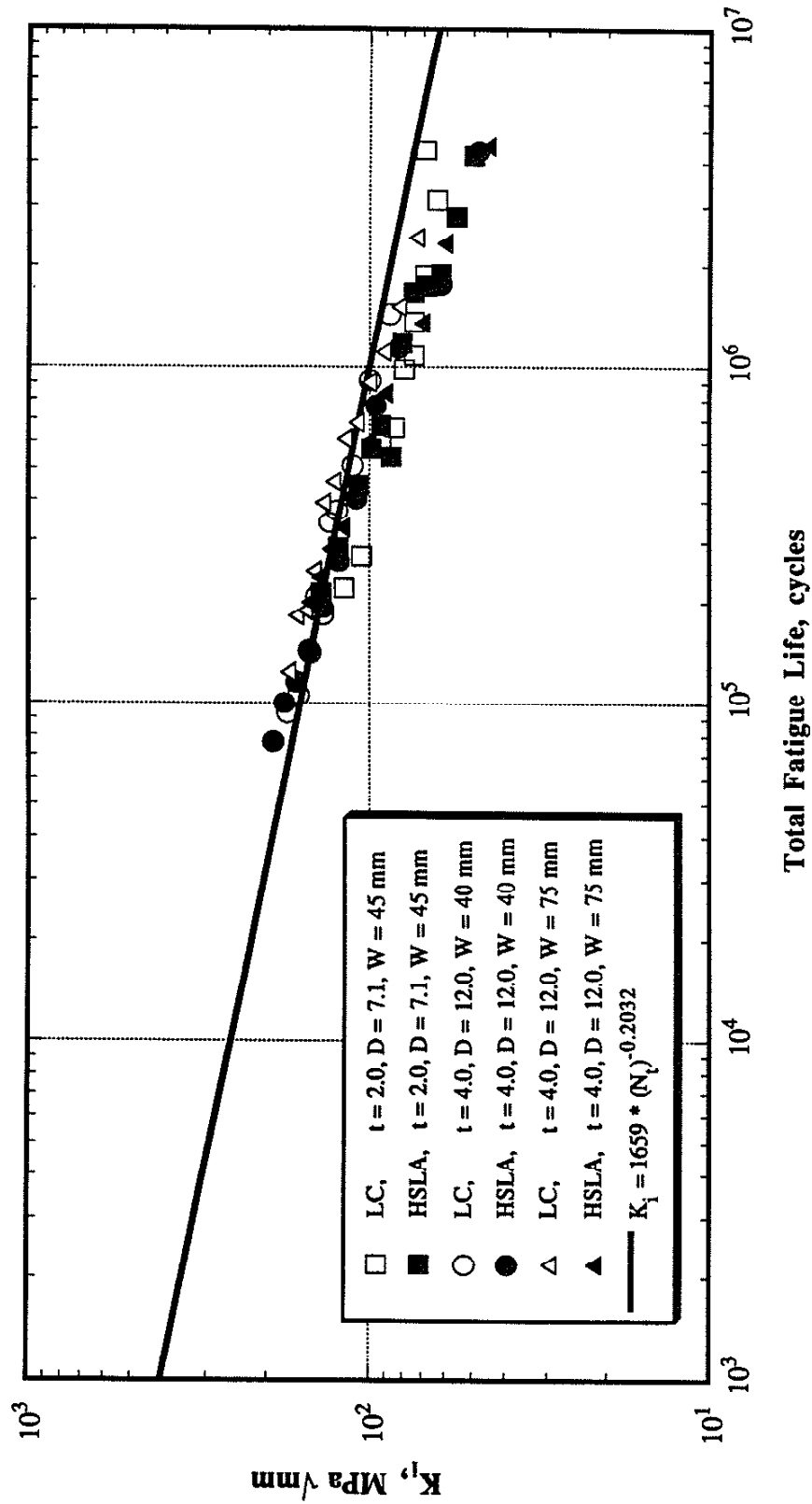


Fig. 6.7 K_I vs. total fatigue life for Rivet's [18] tensile-shear specimens

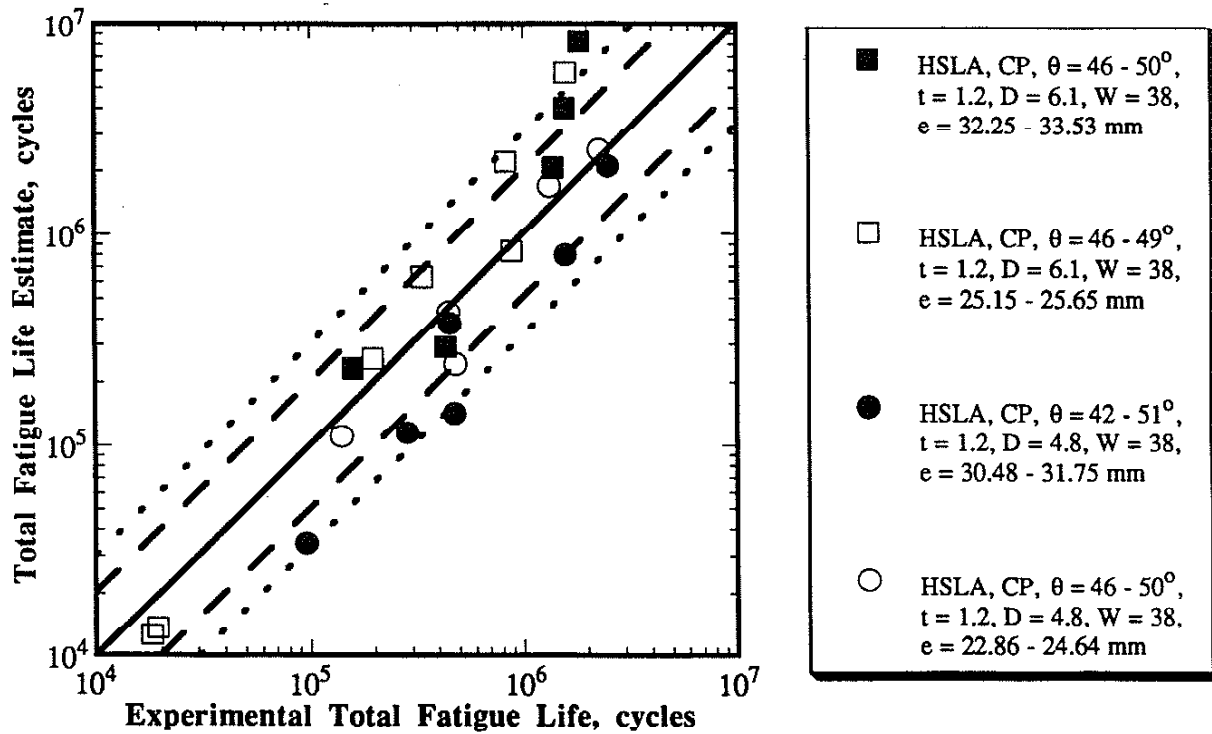


Fig. 6.8 Experimental total fatigue life vs. total fatigue life estimate for coach-peel specimens with different flange angles

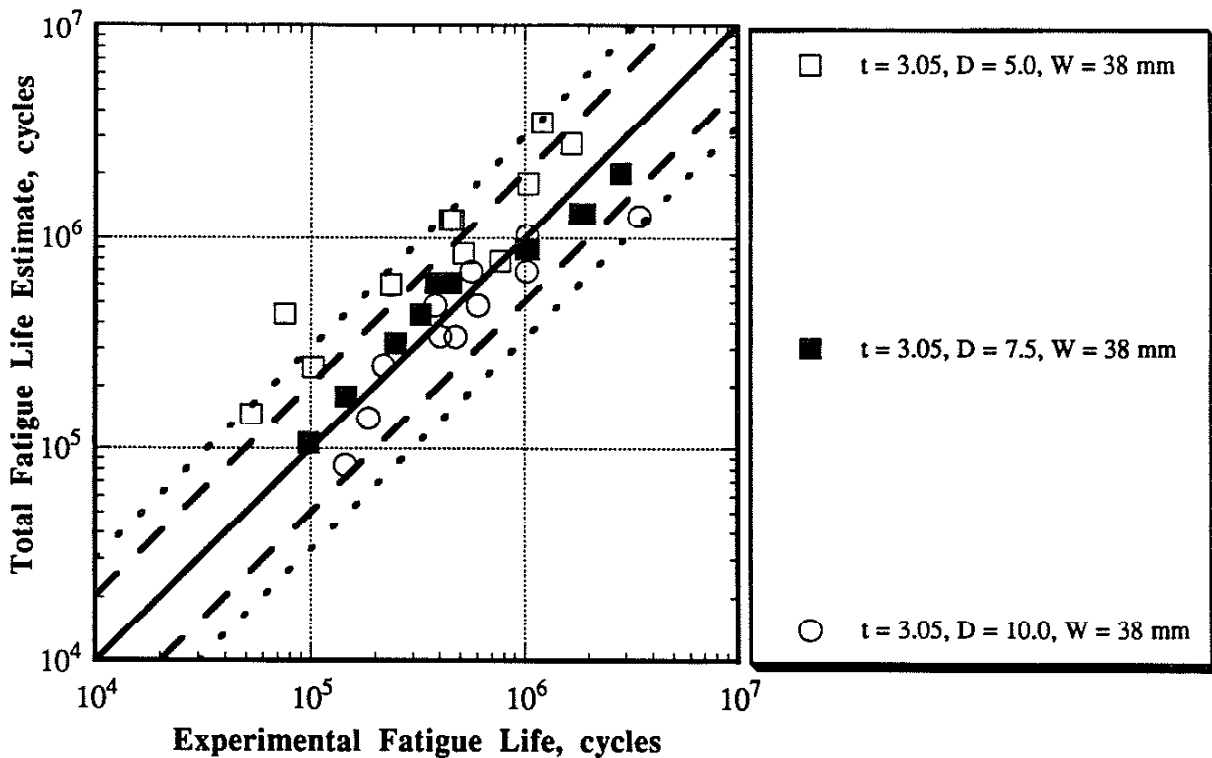


Fig. 6.9 Estimated total fatigue life vs. Experimental fatigue life for three grades of HSLA tensile-shear specimens [16]

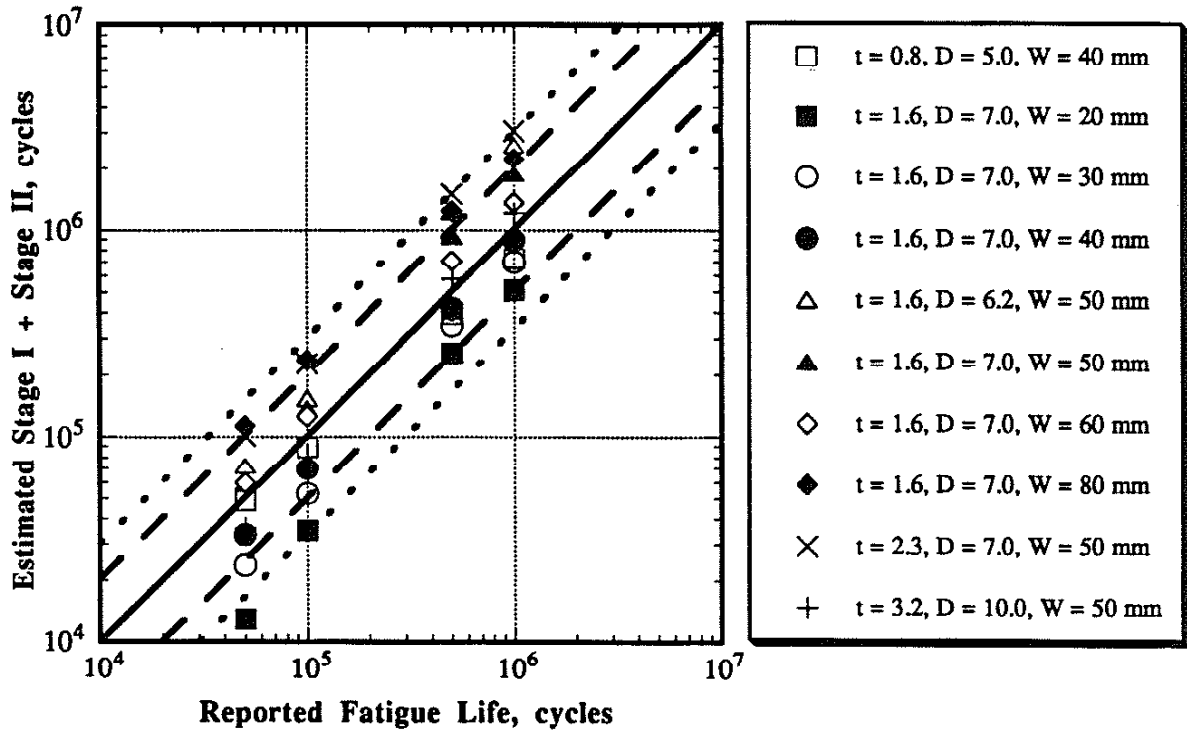


Fig. 6.10 Estimated Stage I + Stage II vs. reported life for low carbon tensile-shear specimens [14]

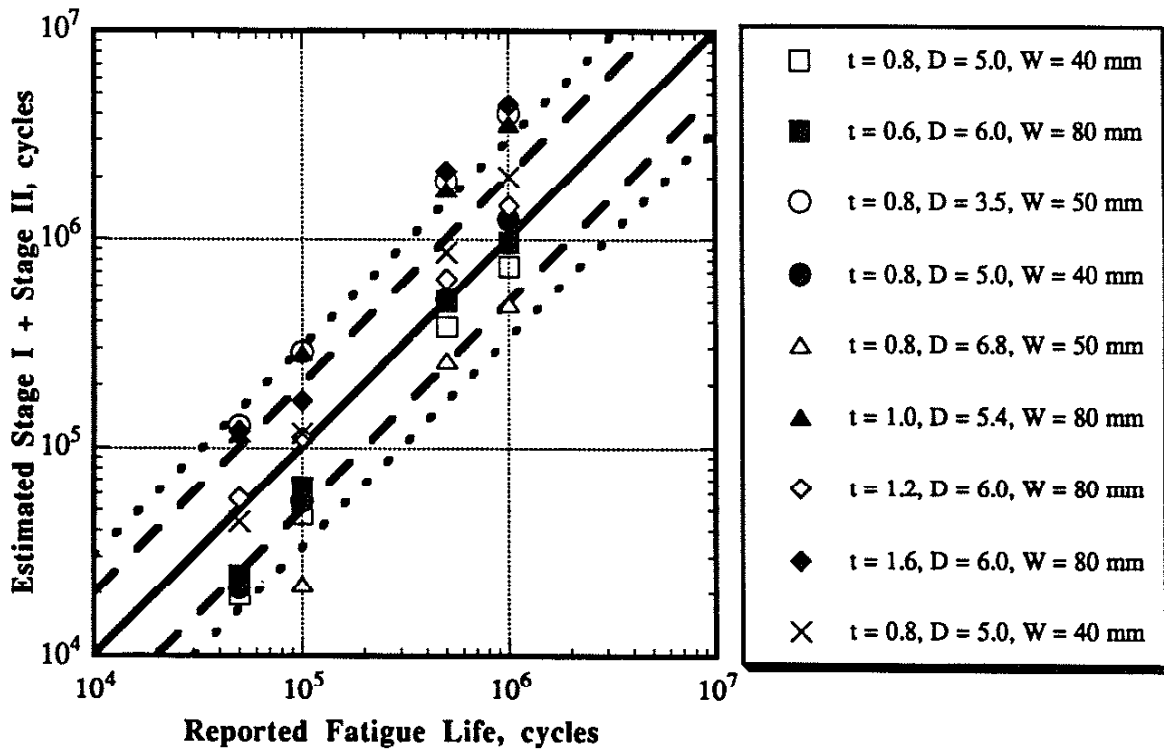


Fig. 6.11 Estimated Stage I + Stage II vs. reported fatigue life for three grades of HSLA tensile-shear specimens [14]

REFERENCES

1. Rivet, R. M. " Assessment of Resistance Spot Welds in Low Carbon and High Strength Steel Sheet - Part 1 Static Properties " The Welding Institute research report No. 193/1982.
2. Williams, N. T. and Jones, T.B. "Spot Weld Size and Fracture Mode in Low Carbon Mild Steel.", Metal Construction, vol. 11, pp541-546, 1979.
3. Smith, R. A. " Sizing of Spot Welds by Elastic / Plastic Analysis.", Fracture and Fatigue, pp49-56, 1980.
4. Cappelli, P. G., Castagna, M. and Ferrero, P., "Fatigue Strength of Spot Welded Joints of HSLA Steels", Welding of HSLA Structural Steels, Conf. Proc. ASM, pp 734-749, 1976.
5. Sperle, J. O., " Strength of Spot Welds in High Strength Steel Sheet", Metal Construction, pp200-203, April, 1983.
6. Davidson, J. A. and Imhof, E. J., "A Fracture-Mechanics and System-Stiffness Approach to Fatigue Performance of Spot-Welded Sheet Steels", SAE technical report No. 830034 Detroit, Michigan.1983.
7. Davidson, J. A. and Imhof, E. J., "The Effect of Tensile Strength on the Fatigue Life of Spot-Welded Sheet Steels", SAE technical report No. 840110. Detroit, Michigan. 1984.
8. Wang, P. C., " A Fatigue Life Prediction Method for Tensile-Shear Spot Welds.", Ph. D. dissertation, University of Illinois at Urbana-Champaign, 1984.
9. Wang, P. C. and Lawrence, F. V. "A Fatigue Life Prediction Method for Tensile-Shear Spot Welds", Fracture Control Program Report No. 113, University of Illinois, (1984).

10. Davidson, J. A., "A Review of the Fatigue Properties of Spot- Welded Sheet Steels.", SAE technical report No. 830033 Detroit, Michigan.1983.
11. Davidson, J. A. " Design-Related Methodology to Determine the Fatigue Life and related Failure Mode of Spot Welded Sheet Steels." ASM Int. Conf. on Technology and Applications of HSLA Steels in Philadelphia 1983.
12. Overbeeke, J. L. and Draisma, J., " Fatigue Characteristic of Heavy Duty Spot Welded Lap Joint.", Metal Construction and British Welding J., pp 213-219, 1974.
13. Iwasaki, T., Tanaka, J., Kabawasa, M. and Nagae, M., "Fatigue Strength of Base Metal and Spot Welded Joints in HSLA Steels for Automotive Applications", Nippon Kokan Technical Report, Overseas No. 34, 1982.
14. Hiroshi, A., Shigenori, K. and Tsugihiko, S., " Empirical Formula for Fatigue Strength of Single-Spot-Welded Joint Specimens under Tensile-Shear Repeated Load." SAE technical report No. 860606, Detroit, Michigan 1986.
15. Defourny, J., D'Haeyer, and Brayard, A., " Spot Welding of High Strength Steel Sheets for Deep Drawing. ", IIW Doc. No. III, 1980.
16. Lawrence, F.V. and Banas, G. Fatigue Resistance of Tensile-Shear Automotive Spot Weldments", Technical Report to the Chevrolet-Pontiac-Canada Group, General Motors Corporation, Warren Michigan, 1989.
17. Orts, D. H., " Fatigue Strength of Spot Welded Joints in HSLA Steel. ", SAE technical report No. 810355, Detroit, Michigan 1981.
18. Rivet, R. M. " Assessment of Single Resistance Spot Welds in Low Carbon and High Strength Steel Sheet - Part 2 Fatigue and Impact Properties " The Welding Institute research report No. 212/1983.
19. Rivet, R. M. " Assessment of Resistance Spot Welds in Low Carbon and High Strength Steel Sheet." SAE technical report No. 830126, Detroit, Michigan 1983.
20. Burk, J. D., " Effect of Residual Stresses on Weld Fatigue Life", Ph. D. dissertation, University of Illinois at Urbana-Champaign, 1978.

21. Welter, G. and Choquet, A., "Internal Stress Distribution of Single Spotwelds in Relation to their Fatigue Life ", Welding Journal, 38 (4), Research Suppl., pp145-158, 1959.
22. Chandel, R.S. and Garber, S., " Mechanical Aspects of Spot-Welded Joints in Heat Treated Low-Carbon Mild-Steel Sheets ", Metals Technology, pp 37-44, 1977.
23. Balasubramanian, S. Sundersan, S. and Vasudevan, R., " Improneement of Resistance Spot Weld Characteristics. ", Welding Research Abroad, pp. 45-63, Nov. 1978.
24. Choquet, A., Krivobok, V. N. and Welter, G. "Effect of Prestressing on Fatigue Strength of Spot welded Stainless Steel. ", Welding Journal, 33 (10), research suppl. pp 509-523, 1954.
25. Lawrence, F. V., Wang, P. C., Ho, N. J. and Corten, H. T., " The Fatigue Resistance of Thin Gauge Automotive Weldments. ", Technical Reports to General Motors Corporation, 1984.
26. McMahon, J. C., " Fatigue Crack Initiation and Early Growth in Tensile-Shear Spot Weldments.", Ph.D. dissertation, University of Illinois at Urbana-Champaign, 1986.
27. Pook, L. P., "Approximate Stress Intensity Factors for Spot and Similar Welds", National Engineering Laboratory, Report No. 588, England, (1975).
28. Pook, L. P., " Fracture Mechanics Analysis of the Fatigue Behavior of Spot Welds. ", Int. Journ. of Fracture, v. 11, pp. 173-176, 1975.
29. Chang, D. J. and Muki, R. "Stress Distribution in a Lap Joint Under Tension-Shear.", Int. J. Solids Struct. vol. 10, pp. 503-517, 1974.
30. Kassir, M.K. and Sih, G.C., " External Elliptical Crack in Elastic Solid. ", Int. Journ. of Fracture Mech., v.4, 347-356, 1968.

31. Paris, P.C. and Sih, G.C., " Stress Analysis of Cracks. ", Symp. on Fracture Toughness Testing and its Application. ASTM STP 381, pp. 30-83, 1965.
32. Sih, G.C. and Erdogan, F., " On the Crack Extension in Plates Under Plane Loading and Transverse Shear.", Trans. of ASME, J. of Basic Engineering, pp. 519-527, 1963.
33. Cooper, J. F., " Fatigue of Spot Welds", Ph.D. dissertation, Cambridge University, 1986.
34. Cooper, J. F. and Smith, R. A. , "Fatigue Crack Propagation At Spot Welds", Metal Construction, 1986, pp. 383-386.
35. Lawrence, F. V., Wang, P. C., and Corten, H. T., "An Empirical Method for Estimating the Fatigue Resistance of Tensile-Shear Spot Welds", SAE Int. Congress and Exposition. Detroit, Michigan. Paper No. 830035 (1983).
36. Basquin, O. H., " The Exponential Law of Endurance Tests ", ASTM Proc. 10:625, 1910.
37. Lawrence, F.V., Mattos, R.J., Higashida, Y., and Burk, J. D., " Estimation of Fatigue Crack Initiation Life of Weld.", ASTM STP 648, 1978.
38. Peterson, R. E., "Analytical Approach to Stress Concentration Effect in Fatigue of Aircraft Materials." WADC technical report 59-507, 1959.
39. Peterson, R. E., " Notch Sensitivity ", Metal Fatigue, Chap. 13, Editors : Sines and Waisman, McGraw-Hill, New York, 1959.
40. Topper, T. H., Wetzel, R. M. and Morrow, J., " Neuber's Rule Applied to Fatigue Notched Specimens", J. of Materials, Vol. 4, 1969.
41. Mattos, R. J., " Estimation of Fatigue Crack Initiation Life of Weld.", Ph. D dissertation, University of Illinois at Urbana-Champaign, 1973.

42. Smith G. A. and Lawrence, F. V., "Fatigue Crack Development in Tensile-Shear Spot Weldments", Fracture Control Program Report No. 108, University of Illinois, (1984).
43. McMahon, J. C., Smith, G. A., and Lawrence, F. V., "Fatigue Crack Initiation and Growth in Tensile-Shear Spot Weldments", Fatigue and Fracture Testing of Weldments, ASTM STP 1058, H. I. McHenry and J. M. Potter, Eds, (1990), pp. 47-77.
44. McMahon, J. C. and Lawrence, F. V., "Fatigue Crack Initiation and Early Growth in Tensile-Shear Spot Weldments", Fracture Control Program Report No. 131, University of Illinois, (1985).
45. Doucet, J. P., "Evaluation of the Fatigue Strength of Spot Welded Joints with a View to Establishing Design Rules", Institute de Soudure Tech. Report 12 704, Welding Institute Translation 638, (1983), pp. 2-7.
46. Recho, N. and Bramat, M., "Study of Fatigue Strength of Spot-Welded Joints", IIW Doc. XIII-1161-85 (1985), Welding Institute Translation No. 711, (1986).
47. Tada, H., Paris, P. and Irwin, G., "The Stress Analysis of Cracks Handbook", Del Research Corporation, 1985.
48. Yuuki, R., Nakatsukasa, H. and Ohira, T., " Fracture Mechanics Analysis of Fatigue Strength of Spot Welded Joints ", International Symposium on Resistance Welding and Related Welding Procedures, Osaka, Japan, 1986.
49. Radaj, D. " Stress Singularity, Notch Stresses and Structural Stresses at Spot-Welded Joints.", Eng. Fracture Mechanics, vol. 34, No. 2, pp495-506, 1989.
50. Radaj, D. " Structural Stress, Notch Stresse and Stress Intensity Factor Approach for Assessment of Fatigue Strength of Spot Welded Joints.", IIW-Doc./XIII-1263-89
51. Radaj, D. and Zhang, S. " Stress Intensity Factors for Spot Welds Between Plates of Unequal Thickness.", IIW-Doc. XIII-1368-90.

52. Mizui, M., Sekine, T., Tsuzimura, A., Takashima, T. and Shimazaki, Y., "An Evaluation of Fatigue Strength for Various Kinds of Spot-Welded Test Specimens", SAE Int. Congress and Exposition. Detroit, Michigan. Paper No. 880375, (1988).
53. Wang, P. C. and Ewing, K. W., "A J-Integral Approach to Fatigue Resistance of a Tensile-Shear Spot Weld", SAE Int. Congress and Exposition. Detroit, Michigan. Paper No. 880373, (1988).
54. Swellam, M. H., Kurath, P. and Lawrence, F.V., Jr. , " Electric-Potential-Drop Studies of Fatigue Crack Development in Tensile-Shear Spot Welds ". Accepted for publication in the ASTM STP 1122, 1991.
55. Swellam, M. H., and Lawrence, F.V., Jr.," Potential Drop Measurements on Spot Welds ". Final report to General Motors Corporation, Technical Center and the Chevorlet-Pontiac-Canada group, 1990.
56. Krempl, E. "The Influence of State of Stress on Low-Cycle Fatigue of Structural Materials: A Literature Survey and Interpretive Report", ASTM Special Technical Publication 549, (1974).
57. Garud, Y. S., "Multiaxial Fatigue: A Survey of the State of the Art", J. of Testing and Evaluation, American Society for Testing and Materials, Vol. 9, #3, (1981) pp. 165-178.
58. Ellyin, F. and Valaire, B., "Development of Fatigue Failure Theories for Multiaxial High Strain Conditions", SM Archives 10 pp. 45-85, Martinus Nijhoff Publishers, Dordrecht, Netherlands, (1985).
59. Guest, J. J., " Recent Research on Combined Stress ", Proceedings, Institution of Automobile Engineers, Vol. 35, pp.33-72, 1940.
60. Findely, W. N., "A Theory for the Effect of Mean Stress on Fatigue of Metals Under Combined Torsion and Axial Loading or Bending", Journal of Engineering for Industry, (1959), pp. 301-306.

61. Stulon, F. B. and Cummings, H. N., " A Failure Criterion for Multiaxial Fatigue Stresses ", American Society for Testing Materials Proceedings Vol. 54, pp.822-835, 1954.
62. Sines, G., ' Failure of Materials under Combined Repeated Stresses with Superimposed Static Stresses ", Technical Note 3495, National Advisory Council for Aeronautics, Washington, D. C. 1955.
63. Miller, K. J. and Brown, M. W., " A Theory for Fatigue Failure Under Multiaxial Stress-Strain Conditions", Proc. Instn. Mech. Engrs, Vol 187 65/73 (1973), pp. 745-755.
64. Miller, K. J., "Fatigue Under Complex Stress", Metal Science, (1977), pp. 432-438.
65. Miller, K. J. and Brown, M. W., "Initiation and Growth of Cracks in Biaxial Fatigue", Fatigue of Engineering Materials and Structures (1979), Vol. 1, pp. 231-246.
66. Lohr, R. D. and Ellison, E. G., "A Simple Theory for Low Cycle Multiaxial Fatigue", Fatigue of Engineering Materials and Structures (1980), Vol. 3, pp. 1-17.
67. Socie, D. F. and Kurath, P., "The Relationship Between Observed Fatigue Damage and Life Estimation Models", NASA Contractor Report No. 182191, (1988).
68. Socie, D. F. and Bannantine, J. A., "Bulk Deformation Fatigue Damage Models", Materials Science and Engineering, A103, (1988).
69. Socie, D. F. and Bannantine, J. A., "Observations of Cracking Behavior in Tension and Torsion Low Cycle Fatigue", Low Cycle Fatigue, ASTM STP 942, (1988), pp. 899-921.
70. Socie, D. F., Waill, D. F. and Dittmer, D. F., "Biaxial Fatigue of Inconel 718 Including Mean Stress Effects", Multiaxial Fatigue, ASTM STP 853, (1985), pp. 463-481.

71. Hoshide, T. and Tanaka, K., "Stress Ratio Effect of Fatigue Crack Propagation in a Biaxial Stress Field", *Fatigue of Engineering Materials and Structures*, (1981), Vol. 4, pp. 355-366.
72. Sih, G. C., "Some Basic Problems in Fracture Mechanics and New Concepts", *Engineering Fracture Mechanics* (1973) Vol. 5, pp. 365-377.
73. Wilson, W. K., "On Combined Mode Fracture Mechanics", Westinghouse Research Labs, Report No. 69_1E7_FMECH_R1. (1969).
74. Broek, D., *Elementary Engineering Fracture Mechanics*, Fourth Edition. 1984.
75. Tanaka, K., "Fatigue Crack Propagation from a Crack Inclined to the Cyclic Tensile Axis", *Engineering Fracture Mechanics*, (1974) Vol. 6, pp. 493-507.
76. Barsoum, R.S., "On the Use of Isoparametric Finite Elements in Linear Fracture Mechanics", *International Journal for Numerical Methods in Engineering*, Vol. 10 25-37, (1976)
77. Banks-Sills, L. and Bortman, Y., "Reappraisal of the Quarter- Point Quadrilateral Element in Linear Elastic Fracture Mechanics ", *Int. Journ. of Fracture*, Vol.25, pp. 169-180, 1984.
78. Shih, C.F., DeLorenzi, H.G. and German, M.D. " Crack Extension Modelling with Singular Quadratic Isoparametric Elements ", *International Journal of Fracture*, Vol. 12, (1976).
79. Personal communication with Prof. Robert H. Dodds, Civil Engineering Department, University of Illinois, Illinois.
80. Pu, S. L., Hussain, M. A. and Lorensen, W.E., " The Collapsed Cubic Isoparametric Element as a Singular Element for Crack Problems ", *Int. Journ. for numerical Methods in Engineering*, Vol. 12, pp.1727-1742, 1978.

81. Khan, Z., Banas, G. and Lawrence, F.V., "Fatigue Resistance of Thin Gauge Automotive Weldments", Phase VII Technical Report to the Technical Center of General Motors Corporation, 1988.
82. McMahon, J. C. and Lawrence, F. V., " Predicting Fatigue Properties Through Hardness Measurements ", Fracture Control Program Report No. 105, University of Illinois, (1984).
83. Sheppard, S., Schoepfel, A. and Strange, M., " Enhanced Fatigue Performance of Resistance Spot Welds ", Proceedings of Sheet Metal Welding Conference IV, Detroit, Michigan, 1990.
84. Kan, Y., " Fatigue Resistance of Spotwelds, An Analytical Study ", Metals Engineering Quarterly, 1976.
85. Cieszkiewicz, A., Banas, G. and Lawrence, F. V., " Improvement of Steel Spot Weld Fatigue Resistance ", Final Report to the American Iron and Steel Institute, 1991.
86. Personal communication with Prof. Sherri Sheppard, Mechanical Engineering Department, Stanford University, California.

APPENDICES

APPENDIX - A: POOK'S MODEL FOR THE TENSILE-SHEAR
STRESS INTENSITY FACTORS

Pook expressed the solutions for the spot welds K_I and K_{II} stress intensity factors in terms of the average shear stresses (τ) and direct stresses (σ) across the connection. He obtained his solution for the tensile-shear specimen through several levels of analogy and dimensional analysis. He compared the solutions of the elliptical [30] and the lap [29] connections between half spaces which were given by:

For the elliptical connection at points A and C (see Fig. A-1)

$K_I = \frac{\sigma}{2} \sqrt{\pi r}$ at point A, for the load P along the Z-axis and passing through the center of the specimen. A-1

$K_I = \frac{\sigma}{2} \sqrt{\pi c}$ at point C for the load P along the Z-axis and passing through the center of the specimen. A-2

$K_{II} = \frac{\tau}{2} \sqrt{\pi r}$ at point A for the load Q along the X-axis and passing through the center of the specimen. A-3

$K_{III} = \frac{\tau}{2} \sqrt{\pi c}$ at point C for the load R along the Y-axis and passing through the center of the specimen. A-4

For the lap connection (overlap = 2 b)

$K_I = \frac{2\sigma}{\pi} \sqrt{\pi b}$ for the load P per unit thickness perpendicular to the connection and passing through the center of the specimen. A-5

$K_{II} = \frac{2\tau}{\pi} \sqrt{\pi b}$ for the load Q per unit thickness across the connection and passing through the center of the specimen. A-6

$$K_{III} = \frac{2\tau}{\pi} \sqrt{\pi b} \quad \text{for the load } R \text{ per unit thickness parallel to the connection and passing through the center of the specimen.} \quad A-7$$

Pook obtained a solution for the lap connection between two sheets of finite thickness by fitting Chang's data [29]. The solutions for a lap connection between two sheets for a shear load Q per unit thickness across the connection and passing through the center of the specimen were on the form:

$$K_I = \frac{\tau}{2} \sqrt{\pi b} \left(0.77 \left(\frac{2b}{t} \right)^{0.397} \right) \quad A-8$$

$$K_{II} = \frac{\tau}{2} \sqrt{\pi b} \left(\frac{2}{\pi} + 0.365 \left(\frac{2b}{t} \right)^{0.71} \right) \quad A-9$$

Pook assumed that the difference between the solution for the lap connection of the two sheets and that of a corresponding elliptical connection would be the same $\pi/4$ factor which is the difference between the half space solutions; compare Eqs. A-1 to A-4 and A-5 to A-7. Subsequently, he substituted r for b in Eqs. A-8 and A-9 and multiplied by $\pi/4$ to obtain a solution for an elliptical connection between two sheets for a shear load Q per unit thickness across the connection and passing through the center of the specimen. The solution was on the form:

$$K_I = \frac{\tau}{2} \sqrt{\pi r} \left(0.605 \left(\frac{2r}{t} \right)^{0.397} \right) \quad \text{at point A.} \quad A-10$$

$$K_{II} = \frac{\tau}{2} \sqrt{\pi r} \left(0.5 + 0.287 \left(\frac{2r}{t} \right)^{0.71} \right) \quad \text{at point A.} \quad A-11$$

$$K_{III} = \frac{\tau}{2} \sqrt{\pi c} \left(0.5 + 0.287 \left(\frac{2r}{t} \right)^{0.71} \right) F\left(\frac{r}{W}\right) \quad \text{at point C.} \quad A-12$$

The K_{III} solution was obtained after assuming that the ratio between K_{II} at point A and K_{III} at point C (Eqs. A-3 and A-4) for an elliptical connection between half spaces also applies to connection between sheets and that the width correction, $F(r/W)$, for a series of straight connections [31] between half spaces also applies for an elliptical connection between two sheets.

Pook has also presented a solution for the circular connection between half spaces subjected to a shear Q parallel to the Y-axis and displaced a distance "e" along the positive Z-axis. The solution was on the form:

$$K_I = \frac{3 e \tau}{2 r} \sqrt{\pi r} \quad \text{at point A} \quad \text{A-13}$$

$$K_I = -\frac{3 e \tau}{2 r} \sqrt{\pi r} \quad \text{at point A'} \quad \text{A-14}$$

$$K_{II} = \frac{\tau}{2} \sqrt{\pi r} \quad \text{at points A and A'} \quad \text{A-15}$$

$$K_{III} = \frac{\tau}{2} \sqrt{\pi r} \quad \text{at points C and C'} \quad \text{A-16}$$

Where points A, A', C and C' are shown in Fig. A-1. Pook explained the negative K_I at point A' in terms of the movement of the crack faces; the negative K_I means that the crack faces are moving towards each other. This type of motion can only be assumed if a gap initially existed between the crack faces.

Pook combined equations A-10 and A-11 with A-13 to A-15 and obtained a solution for a circular connection between two sheets subjected to a shear load Q parallel to the Y-axis and displaced a distance " $t/2$ " along the positive Z-axis. The solution was on the form:

$$K_I = \frac{\tau}{2} \sqrt{\pi r} \left(0.605 \left(\frac{2r}{t} \right)^{0.397} + \left(\frac{3t}{4r} \right) \right) \quad \text{at point A.} \quad \text{A-17}$$

$$K_I = \frac{\tau}{2} \sqrt{\pi r} \left(0.605 \left(\frac{2r}{t} \right)^{0.397} - \left(\frac{3t}{4r} \right) \right) \quad \text{at point A'.} \quad \text{A-18}$$

$$K_{II} = \frac{\tau}{2} \sqrt{\pi r} \left(0.5 + 0.287 \left(\frac{2r}{t} \right)^{0.71} \right) \quad \text{at point A and A'.} \quad \text{A-19}$$

Several researchers have considered Eqs A-10 and A-11 as the K_I and K_{II} solutions for the tensile-shear specimen. However, it appears to the author that Eqs. A-17 to A-19 represents the loading of the tensile-shear specimen more than Eqs. A-10 and A-11 which do not represent the load eccentricity ($t/2$).

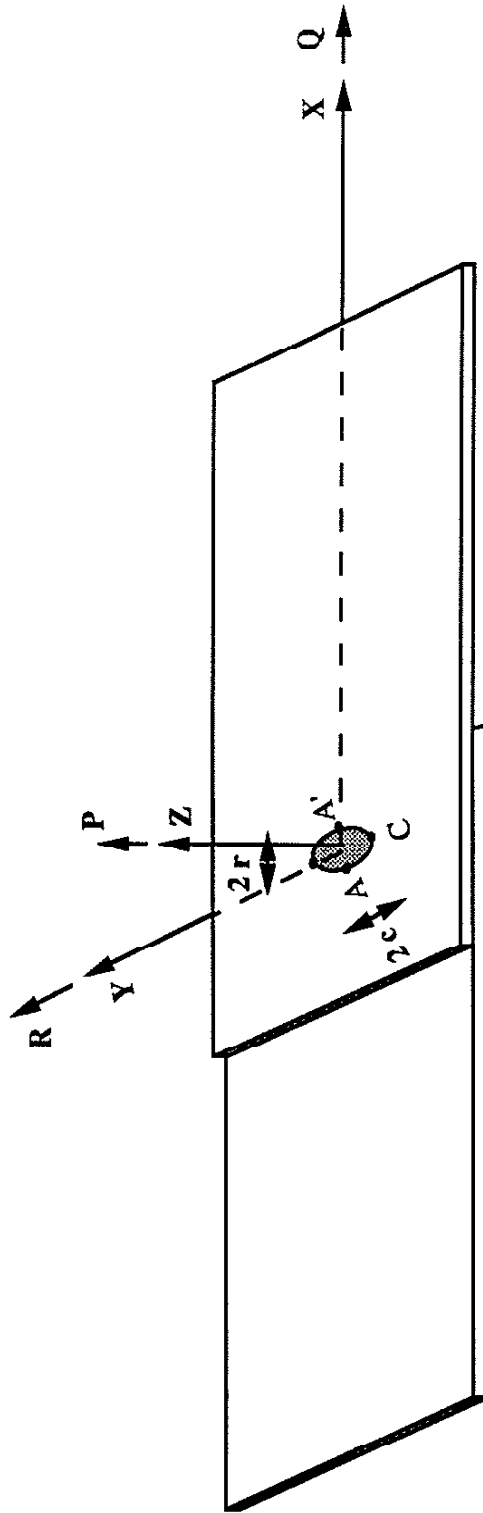


Fig. A-1 Coordinate system and main loading directions for a tensile-shear specimen with an elliptical weld nugget

APPENDIX - B : INITIATION - PROPAGATION (I-P) MODEL

Wang and Lawrence [35] divided the total fatigue life into three stages; initiation and early crack growth (Stage I), crack propagation through the thickness (Stage II), and crack propagation through the width (Stage III). They considered the total fatigue life to be the sum of N_I , N_{II} and N_{III} (the number of cycles devoted to stages I , II and III).

Wang and Lawrence combined Basquin equation [36] and the linear damage summation rule [37] to estimate the fatigue life devoted to Stage I (N_I) from:

$$\int_1^{N_I} \left[\left(\frac{\sigma_f}{\Delta\sigma/2} \right) \left(1 - \frac{\sigma_o (N)^k}{\sigma_f} \right) \right]^{\frac{1}{b}} = 1 \quad \text{B-1}$$

where $\Delta\sigma$ = local stress amplitude at the notch tip.
 σ_f = fatigue strength coefficient.
 b = fatigue strength exponent.
 σ_o = local initial mean stress.
 k = mean stress relaxation exponent.

Wang and Lawrence used Pook's solutions (Eqs. A-10 and A-11) for the stress intensity factors to calculate the maximum tangential stress (σ_t) around the sharp notch which they considered as a blunt crack tip. Subsequently, they determined the stress concentration factor (K_t) by dividing the maximum tangential stress (σ_t) by the applied nominal stress (S) as follows:

$$K_t = \frac{W t}{(\pi \rho)^{0.5} D^{1.5}} \left[1.61 \left(\frac{D}{t} \right)^{0.397} + 0.593 + 0.34 \left(\frac{D}{t} \right)^{0.710} \right] \quad \text{B-2}$$

where W = specimen width.
 t = sheet thickness.
 D = nugget diameter.
 ρ = notch root radius.

They then used Peterson's equation [38,39] to calculate K_{fmax} which was used together with Neuber's formula [40] and a set up cycle analysis [41] to calculate the local strain ($\Delta\epsilon$) and local stress ($\Delta\sigma$) (necessary for Eq. B-1) as follows:

$$\Delta\sigma \Delta\epsilon = \frac{(K_{fmax} \Delta S)^2}{E} \quad B-3$$

$$K_f = 1 + \frac{(K_t - 1)}{(1 + \frac{\gamma}{\rho})} \quad B-4$$

$$K_{fmax} = K_f \text{ when } \gamma = \rho \quad B-5$$

where ρ = notch root radius.

γ = Peterson's material constant.

Substituting Eq. B-2 into Eq. B-4 and invoking the condition given by Eq. B-5 after expressing the Peterson's constant in terms of the ultimate strength (S_u), Wang provided the following expression for K_{fmax} :

$$K_{fmax} = 1 + 2.41 * 10^{-3} \frac{W * S_u * t^{0.5}}{D} f(\frac{t}{D}) \quad B-6$$

$$f(\frac{t}{D}) = 0.569 * (\frac{t}{D})^{0.103} + 0.209 * (\frac{t}{D})^5 + 0.12 * (\frac{t}{D})^{-0.21} \quad B-7$$

As for Stage II, Wang and Lawrence calculated the number of cycles (N_{II}) devoted to that stage by integrating the Paris law; they adopted the values 5 and 1.0×10^{-13} for m and C respectively and used a value of 0.08 mm for a_i . During that stage they used the expression of the stress intensity factor of an elliptical crack which is given by:

$$\Delta K = Y \Delta S \sqrt{\pi a} \quad B-8$$

where Y = geometry correction factor [9,35].

They also computed the number of cycles (N_{III}) devoted to Stage III by integrating the Paris law. They obtained a solution for the stress intensity factor at that stage by superposing the axial and bending components [9]. They also used the nugget diameter as an initial crack length while the end of the fatigue life was determined by the separation of the specimen.

Finally the total fatigue life was given by:

$$N_t = N_I + N_{II} + N_{III} \quad B-9$$

APPENDIX-C : RADAJ'S STRUCTURAL STRESS MODEL FOR THE STRESS INTENSITY FACTORS OF SPOT WELDED SPECIMENS

Radaj [49,50,51] has formulated the stress intensity factors for spot welds in terms of the sheet thickness and the local structural stresses. He splitted the structural stresses into symmetrical and antisymmetrical portions in order to simplify the calculation of the stress intensity factors which are subsequently given by:

$$K_I = (0.58 \sigma_b^{++} + 2.23 \tau_{\perp}^{+-}) \sqrt{t} \quad (C-1)$$

$$K_{II} = (0.50 \sigma^{+-} + 0.5 \sigma_b^{+-} + 0.55 \tau_{\perp}^{++}) \sqrt{t} \quad (C-2)$$

$$K_{III} = 1.41 \tau_{//}^{+-} \sqrt{t} \quad (C-3)$$

where

$$\sigma_u = 0.5 (\sigma_{ui} + \sigma_{uo})$$

$$\sigma_l = 0.5 (\sigma_{li} + \sigma_{lo})$$

$$\sigma^{++} = 0.5 (\sigma_u + \sigma_l) = 0.25 (\sigma_{ui} + \sigma_{uo} + \sigma_{li} + \sigma_{lo})$$

$$\sigma^{+-} = 0.5 (\sigma_u - \sigma_l) = 0.25 (\sigma_{ui} + \sigma_{uo} - \sigma_{li} - \sigma_{lo})$$

$$\sigma_{bu} = 0.5 (\sigma_{ui} - \sigma_{uo})$$

$$\sigma_{bl} = 0.5 (\sigma_{li} - \sigma_{lo})$$

$$\sigma_b^{++} = 0.5 (\sigma_{bu} + \sigma_{bl}) = 0.25 (\sigma_{ui} - \sigma_{uo} + \sigma_{li} - \sigma_{lo})$$

$$\sigma_b^{+-} = 0.5 (\sigma_{bu} - \sigma_{bl}) = 0.25 (\sigma_{ui} - \sigma_{uo} - \sigma_{li} + \sigma_{lo})$$

$$\tau_{\perp}^{++} = 0.5 (\tau_{\perp u} + \tau_{\perp l})$$

$$\tau_{\perp}^{+-} = 0.5 (\tau_{\perp u} - \tau_{\perp l})$$

$$\tau_{//}^{++} = 0.5 (\tau_{ui} + \tau_{li})$$

$$\tau_{//}^{+-} = 0.5 (\tau_{ui} - \tau_{li})$$

σ = Radial stress normal to the edge of the spot weld.

σ_b = Bending radial stress normal to the edge of the spot weld.

τ_{\perp} = Mean transverse shear stress.

$\tau_{//}$ = Longitudinal shear stress in the direction of the edge of the spot weld.

The indices u and l designate the upper and lower plate while the indices i and o indicates the inner and outer sides of the plate. The superscripts (+ +) and (+ -) designate the symmetrical and antisymmetrical portions of the stresses respectively.

The above equations provide the solution for the stress intensity factors in terms of the local structural stresses at the inside and the outside of the joint sheets. Radaj emphasized that the necessary stresses can be determined either numerically or experimentally. It should be noted that although in practical situations the magnitude of the transverse shear stress may be negligible compared to the bending stresses, the transverse shear stress contribution to the K_I and K_{II} can not be neglected in all cases. However, in cases where the contribution of the transverse shear stresses is negligible, the stress intensity factors can be expressed as follows:

$$K_I = \kappa_1 \sigma_{sb} \sqrt{t} \quad (C-4)$$

$$K_{II} = \kappa_2 \sigma_s \sqrt{t} \quad (C-5)$$

$$K_{III} = \kappa_3 \tau_s \sqrt{t} \quad (C-6)$$

where

σ_{sb}	=	Structural bending stress normal to the edge.
σ_s	=	Structural bending and membrane stresses normal to the edge.
τ_s	=	Structural shear stress in the direction of the edge.
t	=	Sheet thickness.
κ_1, κ_2 and κ_3	=	Geometry correction factors.

It should be also noted that the above stress intensity factor solutions imply the sole dependance of the stress intensity factors on the structural stresses for specified sheet thickness and welded geometry. The solutions also imply that specimens (of the same geometry) with larger sheet thicknesses yield larger stress intensity factors provided that the structural stresses are the same.

APPENDIX-D : MULTIAXIAL FATIGUE

Most of the review papers on multiaxial fatigue [56-58] indicate that the early multiaxial fatigue failure criteria and their damage parameters were based on extensions of static yield theories (Rankine, Tresca and Von Mises). The stress-based parameters were limited to high-cycle fatigue while the strain-based parameters were recommended for the low-cycle regime. Table D-1 presents some of these early criteria.

Guest [59], Findely [60] Stulon and Cummings [61] all realized that fatigue failures initially started on the planes of maximum shear and thus they included a term in their damage parameters to account for maximum shear. They also included a term to account for the normal stress component on the plane of maximum shear. The normal stress component was multiplied by a material constant which indicates that the normal stress contribution to the fatigue damage differs from one material to another. Findely reported a good correlation of the fatigue data in terms of his damage parameter $(\tau + k\sigma)$. Sines [62] also included the shear effect as well as the hydrostatic stress which was again multiplied by a material constant.

Later in the sixties, the interest in low cycle fatigue grew and several strain-based criteria were developed for that regime. Miller et al. [63-65] introduced the concept of the Γ -plane which is the plane subjected to maximum shear strain. They generated constant life contours on plots of maximum shear strain (γ_{\max}) and the normal strain (ϵ_n) on the plane of maximum shear strain. The shape of the contours was dependent upon the life for which they were generated. Miller et al suggested a general form:

$$\gamma_{\max} = f(\epsilon_n) \quad (D-1)$$

Lohr and Ellison [66] later argued that for failure to occur, a fatigue crack must be propagated through the material thickness. Therefore, they proposed that it was more correct to consider the shear strains (γ^*) that assisted in progressing the crack in this critical direction. They plotted similar contours to those of Miller et al but for their critical shear strain (γ^*). They specified their failure criterion as follows:

$$\gamma^* + k\epsilon_n^* > C \quad (D-2)$$

Where γ^* = Shear strain that assists in progressing the crack in the critical direction.

$$\begin{aligned} \epsilon_n^* &= \text{Normal strain on the plane of } \gamma^* \\ k \text{ and } C &= \text{Material constants.} \end{aligned}$$

Socie et al [67-70] introduced the concept of the damage maps. They divided the fatigue life into three regions based upon the loading mode, strain amplitude and material type. Each region was characterized by a specific type of cracking which was primarily caused either by shear strain or principal strain according to the material type. Hence, Socie et al presented two damage parameters, one for each type of cracking, and recommended that one must first determine the dominant type of cracking in order to achieve a reasonable fatigue life prediction. Such a recommendation explains the different conclusions of Miller [65] and Hoshide [71]. Miller tested an aluminum alloy cruciform specimens where cracks were subjected to remote axial stress states with different combinations (uniaxial, equibiaxial and shear). He found that the shear case yielded the highest growth rate while the equibiaxial yielded the least. Hoshide and Tanaka [71] performed similar tests on a structural low carbon steel. In their tests, they observed a different behavior; the uniaxial case yielded the highest growth rate while the shear yielded the least.

Table D-1
Failure Criteria For High Cycle Multiaxial Fatigue

Reference	Damage Parameter and Failure Criterion	Notation and Remarks
Gough 1935 - 1951	$\left(\frac{T}{t}\right)^2 + \left(\frac{b}{t} - 1\right) * \left(\frac{B}{b}\right)^2 + \left(2 - \frac{b}{t}\right) * \left(\frac{B}{b}\right) > 1$ $\left(\frac{T}{t}\right)^2 + \left(\frac{B}{b}\right)^2 > 1$	B and T : Bending and torsional stress amplitudes respectively. b and t : Reversed bending and torsional endurance limits respectively. For combined in-phase bending and torsion tests. The two criteria are for brittle and ductile materials respectively .
Guest 1937 - 1940	$(X-Y) + m * (X+Y) > C$	X and Y : Maximum and minimum principle stresses. m and C : Material constants. For combined in-phase completely reversed loadings.
Findely 1953	$\tau_c + k * \sigma_c > f$	τ_c and σ_c : Shear and normal stresses on the plain of maximum shear. f and k : Material constants. For combinations of torsion and axial or bending stresses.
Cummings and Stulen 1954	$X - m' * Y > C'$	X and Y : As above m' and C' : Material constants. For in-phase fully reversed sinusoidal biaxial loading.
Sines 1955	$\frac{1}{2\sqrt{2}} \{(\Delta X - \Delta Y)^2 + (\Delta Y - \Delta Z)^2 + (\Delta Z - \Delta X)^2\}^{\frac{1}{2}} + \alpha (X+Y+Z) > C''$	$\Delta X, \Delta Y$ and ΔZ : Ranges of alternating principal stresses. X, Y, and Z : Average orthogonal static stresses over a cycle. α and C'' : Material constants. Originally for cases of loading where principal axes are fixed, but latter it has been modified to handle other cases also.

APPENDIX-E : MIXED MODE FRACTURE MECHANICS

Sih and Erdogan [72] showed that a fracture criterion in terms of stress intensity factors can be written as:

$$\frac{1}{\pi}(a_{11}K_I^2 + 2a_{12}K_IK_{II} + a_{22}K_{II}^2) = S \quad (E-1)$$

Where the constant S is the strain energy density factor and a_{ij} are material dependent constants. They also reported experimental results that confirm the elliptical shape of (E-1) and so did Willson [73] and Broek [74] who suggested the form:

$$\left(\frac{K_I}{K_{IC}}\right)^2 + \left(\frac{K_{II}}{K_{IIC}}\right)^2 = 1 \quad (E-2)$$

Which for $K_{IIC} \approx 0.75K_{IC}$ yields

$$K_I^2 + 1.78K_{II}^2 = K_{IC}^2 \quad (E-3)$$

Tanaka [75] showed that threshold values also relate through the elliptical form:

$$A_{11}K_{I\text{th}}^2 + 2A_{12}K_{I\text{th}}K_{II\text{th}} + A_{22}K_{II\text{th}}^2 = 1 \quad (E-4)$$

Where A_{11} , A_{12} and A_{22} are material constants (obtained experimentally) which reflects the material response to mixed mode loadings and notch sensitivity. For the material he tested the equation was:

$$0.0262K_{I\text{th}}^2 + 0.008K_{I\text{th}}K_{II\text{th}} + 0.0381K_{II\text{th}}^2 = 1 \quad (E-5)$$

Tanaka also reported that an equivalent stress intensity for a crack under mixed mode (K_I , K_{II}) can be given by:

$$K_{eq} = (K_I^4 + 4K_{II}^4)^{1/4} \quad (E-6)$$

This K_{eq} correlated the crack growth rate data and showed good life estimates when used in conjunction with Paris Law.

APPENDIX-F : RESISTIVITY RECORDS

Table F-1
 Resistivity Measurements For
 Galvanized HSLA
 $t = 1.4 \text{ mm}$, $D = 6.1 \text{ mm}$, $W = 38 \text{ mm}$
 $R = 0.0$, Max. Load = 2,935 N (660 lbs)
 Total Life = 334,100
 As-Welded Conditions
 Task # 1 Specimen #1

Number of Cycles	Change in Resistivity ($\mu\Omega\cdot\text{cm}$)	
	Side A	Side B
150	0.40	0.20
300	0.70	0.47
500	0.64	0.90
700	0.57	1.03
1,000	0.77	1.00
1,500	0.80	0.93
2,200	0.87	0.97
3,000	0.87	1.13
4,000	1.07	1.37
5,500	0.80	1.20
7,500	0.70	1.23
10,000	0.70	1.20
15,000	1.10	1.67
25,000	1.24	1.87
35,000	1.67	2.03
50,000	1.87	2.23
65,000	2.04	2.53
80,000	2.10	2.63
100,000	2.10	2.73
125,000	2.20	3.13
150,000	2.34	3.27
175,000	2.40	4.47
200,000	2.60	7.30
225,000	2.90	9.00
250,000	3.54	16.10
265,000	4.67	29.47
280,000	6.00	37.70
295,000	7.20	47.83
310,000	10.04	59.93
325,000	24.34	80.67

Table F-2
 Resistivity Measurements For
 Galvanized HSLA
 $t = 1.4$ mm, $D = 6.1$ mm, $W = 38$ mm
 $R = 0.0$, Max. Load = 3,560 N (800 lbs)
 Total Life = 125,300
 As-Welded Conditions
 Task # 1 Specimen # 2

Number of Cycles	Change in Resistivity ($\mu\Omega\cdot\text{cm}$)	
	Side A	Side B
1	0.24	0.24
100	1.84	1.57
200	2.30	2.10
500	2.37	2.34
1,000	2.47	2.40
2,000	2.60	2.50
5,000	2.70	2.64
10,000	2.90	2.70
15,000	2.97	2.90
20,000	3.07	3.00
25,000	3.10	3.17
35,000	3.27	3.23
45,000	3.34	3.50
60,000	3.37	4.24
75,000	3.64	5.54
80,000	3.64	6.54
85,000	4.20	7.70
90,000	4.80	9.24
95,000	5.90	11.10
100,000	8.37	15.77
105,000	10.54	35.67
110,000	23.60	45.54
115,000	30.40	54.27
120,000	45.40	64.14
125,000	59.04	76.60

Table F-3
 Resistivity Measurements For
 Galvanized HSLA
 $t = 1.4$ mm, $D = 6.1$ mm, $W = 38$ mm
 $R = 0.0$, Max. Load = 2,225 N (500 lbs)
 Total Life = 907,100
 As-Welded Conditions
 Task # 1 Specimen # 3

Number of Cycles	Change in Resistivity ($\mu\Omega\cdot\text{cm}$)	
	Side A	Side B
1	0.27	0.16
100	0.74	0.50
200	1.27	0.90
500	1.60	1.06
1,000	1.77	1.10
2,000	1.90	1.40
5,000	2.27	1.53
10,000	2.34	1.70
20,000	2.34	1.93
30,000	2.40	2.16
40,000	2.47	2.26
50,000	2.60	2.43
75,000	2.60	2.49
125,000	2.77	2.53
200,000	3.04	3.13
250,000	3.27	3.30
350,000	3.47	3.63
380,000	3.94	3.73
420,000	4.44	5.86
470,000	5.04	3.93
520,000	5.84	5.00
550,000	6.27	5.60
575,000	6.60	6.30
600,000	7.20	6.76
625,000	8.10	7.46
650,000	8.57	8.63
675,000	10.20	9.73
700,000	11.57	11.53
725,000	14.60	14.40
750,000	20.27	22.56
800,000	29.20	35.23
812,000	32.54	38.46
850,000	40.54	50.36
900,000	58.84	88.33

Table F-4
 Resistivity Measurements For
 Galvanized HSLA
 $t = 1.4 \text{ mm}$, $D = 6.1 \text{ mm}$, $W = 38 \text{ mm}$
 $R = 0.0$, Max. Load = 2,670 N (600 lbs)
 Total Life = 316,200
 As-Welded Conditions
 Task # 1 Specimen # 4

Number of Cycles	Change in Resistivity ($\mu\Omega\text{.cm}$)	
	Side A	Side B
1	0.23	0.07
100	0.47	0.10
200	0.97	0.37
500	1.10	0.47
1,000	1.33	0.50
2,000	1.40	0.57
5,000	1.50	0.60
10,000	1.57	0.64
20,000	1.90	0.77
30,000	2.03	0.84
40,000	1.83	1.07
50,000	1.90	1.17
60,000	1.93	1.37
80,000	2.03	1.27
100,000	2.07	1.44
150,000	2.87	2.40
200,000	7.93	6.50
225,000	11.83	10.60
250,000	24.80	23.27
275,000	32.73	37.07
300,000	41.57	57.10

Table F-5
 Resistivity Measurements For
 Galvanized HSLA
 $t = 1.4 \text{ mm}$, $D = 6.1 \text{ mm}$, $W = 38 \text{ mm}$
 $R = -0.2$, Max. Load = 2,670 N (600 lbs)
 Total Life = 252,000
 As-Welded Conditions
 Task # 2 Specimen # 1

Number of Cycles	Change in Resistivity ($\mu\Omega\cdot\text{cm}$)	
	Side A	Side B
1	0.03	0.13
100	0.40	0.87
200	0.27	1.57
500	0.47	1.97
1,000	0.57	2.27
2,000	0.63	2.30
5,000	0.67	2.37
10,000	0.70	2.44
20,000	1.33	2.60
30,000	1.37	2.90
40,000	1.40	2.94
60,000	1.37	3.17
70,000	1.47	3.37
90,000	1.47	3.94
100,000	1.50	4.14
140,000	3.00	7.24
150,000	3.13	8.64
160,000	3.47	9.40
165,000	3.47	10.27
170,000	3.50	11.14
175,000	3.50	12.17
180,000	3.84	20.37
190,000	4.34	24.14
195,000	4.57	25.60
200,000	4.70	27.60
205,000	5.17	30.50
210,000	5.60	33.87
215,000	6.10	38.04
220,000	6.50	41.47
225,000	6.87	52.30
230,000	7.80	63.47
235,000	8.57	68.97
240,000	9.77	75.30
245,000	11.57	84.47

Table F-6
 Resistivity Measurements For
 Galvanized HSLA
 $t = 1.4 \text{ mm}$, $D = 6.1 \text{ mm}$, $W = 38 \text{ mm}$
 $R = -0.2$, Max. Load = 2,000 N (450 lbs)
 Total Life = 831,860
 As-Welded Conditions
 Task # 2 Specimen # 2

Number of Cycles	Change in Resistivity ($\mu\Omega\cdot\text{cm}$)	
	Side A	Side B
100	0.04	0.50
200	0.04	0.70
500	0.17	1.20
1,000	0.24	1.44
2,000	0.34	1.50
5,000	0.34	1.70
10,000	0.37	1.77
20,000	0.50	2.17
30,000	0.60	2.17
80,000	0.67	2.24
150,000	0.80	2.40
200,000	0.77	2.74
250,000	0.84	2.97
325,000	0.97	4.20
375,000	0.87	5.27
400,000	0.87	6.04
415,000	0.90	6.40
430,000	0.94	6.90
440,000	0.90	7.00
450,000	1.00	7.14
460,000	1.14	7.54
475,000	1.10	7.60
500,000	1.10	8.17
525,000	1.14	9.07
550,000	1.17	10.37
575,000	1.30	11.60
600,000	1.24	13.30
625,000	1.34	19.70
650,000	1.70	31.97
675,000	2.57	40.30
700,000	3.60	45.90
775,000	3.90	66.49
800,000	5.18	73.24
825,000	6.30	87.10

Table F-7
 Resistivity Measurements For
 Galvanized HSLA
 $t = 1.4$ mm, $D = 6.1$ mm, $W = 38$ mm
 $R = -0.2$, Max. Load = 3,560 N (800 lbs)
 Total Life = 67,900
 As-Welded Conditions
 Task # 2 Specimen # 3

Number of Cycles	Change in Resistivity ($\mu\Omega\cdot\text{cm}$)	
	Side A	Side B
1	0.37	0.20
100	1.03	0.63
200	0.70	1.43
500	2.00	0.80
1,000	2.07	0.93
2,000	2.17	1.53
5,000	2.70	2.00
10,000	2.80	2.27
15,000	3.07	2.27
20,000	3.33	2.33
30,000	3.47	2.60
40,000	4.03	4.57
45,000	4.97	7.67
50,000	6.87	18.44
55,000	10.40	42.73
57,000	21.20	48.17
59,000	25.47	52.47
62,000	29.80	60.07
65,000	36.43	68.40

Table F-8
 Resistivity Measurements For
 Galvanized HSLA
 $t = 1.4 \text{ mm}$, $D = 6.1 \text{ mm}$, $W = 38 \text{ mm}$
 $R = -0.2$, Max. Load = 2,225 N (500 lbs)
 Total Life = 498,500
 As-Welded Conditions
 Task # 2 Specimen # 4

Number of Cycles	Change in Resistivity ($\mu\Omega\cdot\text{cm}$)	
	Side A	Side B
1	0.24	0.10
200	0.47	0.60
500	0.64	1.00
1,000	0.64	1.26
2,000	0.97	1.70
5,000	1.14	1.73
10,000	1.30	1.90
30,000	1.40	2.06
50,000	1.64	2.16
125,000	1.80	2.63
200,000	1.87	4.40
235,000	2.14	5.23
270,000	2.20	6.76
285,000	2.20	7.53
300,000	2.20	8.80
310,000	2.40	9.16
320,000	2.47	10.00
330,000	2.27	10.43
340,000	2.37	11.63
365,000	2.80	16.63
400,000	4.70	44.96
430,000	7.20	55.56
460,000	11.27	67.16

Table F-9
 Resistivity Measurements For
 Galvanized HSLA
 $t = 1.4$ mm, $D = 6.1$ mm, $W = 38$ mm
 $R = 0.5$, Max. Load = 4,005 N (900 lbs)
 Total Life = 953,700
 As-Welded Conditions
 Task # 3 Specimen # 1

Number of Cycles	Change in Resistivity ($\mu\Omega\cdot\text{cm}$)	
	Side A	Side B
1	0.17	0.16
100	0.37	0.36
200	0.37	0.66
500	0.67	0.90
1,000	1.00	1.16
2,000	1.30	1.26
5,000	1.40	1.36
10,000	1.70	1.46
20,000	1.87	1.50
30,000	1.97	1.76
50,000	2.14	1.76
125,000	2.20	1.83
200,000	2.27	2.00
250,000	2.27	2.03
300,000	2.30	2.06
350,000	2.34	2.23
425,000	2.47	2.40
500,000	2.74	2.66
550,000	2.74	2.93
600,000	2.84	3.66
700,000	3.10	4.76
800,000	5.20	9.00
825,000	5.67	11.33
850,000	6.77	18.00
875,000	16.14	22.23
900,000	24.67	27.40
950,000	49.97	56.50

Table F-10
 Resistivity Measurements For
 Galvanized HSLA
 $t = 1.4 \text{ mm}$, $D = 6.1 \text{ mm}$, $W = 38 \text{ mm}$
 $R = 0.5$, Max. Load = 4,450 N (1,000 lbs)
 Total Life = 534,700
 As-Welded Conditions
 Task # 3 Specimen # 2

Number of Cycles	Change in Resistivity ($\mu\Omega\cdot\text{cm}$)	
	Side A	Side B
1	0.53	0.84
100	0.63	1.14
200	1.00	1.30
500	0.76	1.70
1,000	0.87	1.90
2,000	0.93	2.44
5,000	1.63	2.80
10,000	1.96	2.84
20,000	2.33	2.97
50,000	2.93	3.30
125,000	3.26	3.34
200,000	3.83	3.77
300,000	4.03	4.50
400,000	5.43	7.90
425,000	6.56	10.50
450,000	8.73	15.40
500,000	26.43	31.40

Table F-11
 Resistivity Measurements For
 Galvanized HSLA
 $t = 1.4 \text{ mm}$, $D = 6.1 \text{ mm}$, $W = 38 \text{ mm}$
 $R = 0.5$, Max. Load = 4,895 N (1,100 lbs)
 Total Life = 417,800
 As-Welded Conditions
 Task # 3 Specimen # 3

Number of Cycles	Change in Resistivity ($\mu\Omega\cdot\text{cm}$)	
	Side A	Side B
1	0.54	0.94
100	1.20	1.20
200	1.37	1.37
500	1.47	2.04
1,000	1.87	2.50
2,000	2.04	2.60
5,000	2.34	2.77
10,000	2.30	2.90
20,000	2.50	2.94
50,000	2.90	2.84
100,000	3.04	3.80
150,000	3.27	4.04
200,000	3.80	4.67
270,000	5.37	7.07
300,000	6.44	8.90
325,000	8.57	10.54
375,000	20.90	24.77

Table F-12
 Resistivity Measurements For
 Galvanized HSLA
 $t = 1.4 \text{ mm}$, $D = 6.1 \text{ mm}$, $W = 38 \text{ mm}$
 $R = 0.5$, Max. Load = 3,335 N (750 lbs)
 Total Life = 4,817,800
 As-Welded Conditions
 Task # 3 Specimen # 4

Number of Cycles	Change in Resistivity ($\mu\Omega\cdot\text{cm}$)	
	Side A	Side B
1	0.24	0.36
100	0.30	0.36
200	0.34	0.43
500	0.40	0.43
1,000	0.44	0.43
2,000	0.57	0.43
5,000	0.57	0.46
10,000	0.60	0.43
50,000	1.14	0.46
75,000	1.17	0.50
150,000	1.60	0.63
225,000	1.67	0.66
300,000	1.67	1.20
500,000	1.70	1.46
600,000	1.70	1.56
700,000	1.87	1.66
900,000	1.94	2.13
1,200,000	2.00	2.23
1,400,000	2.34	2.26
1,500,000	2.37	2.33
1,600,000	2.47	2.66
1,750,000	2.47	2.50
1,900,000	2.44	2.79
2,300,000	2.77	2.96
2,500,000	3.10	3.06
2,800,000	3.10	3.06
3,400,000	3.47	3.26
4,000,000	4.90	3.96
4,500,000	17.47	12.43
4,550,000	22.47	17.00
4,600,000	26.80	23.03
4,650,000	30.90	27.33
4,700,000	34.04	31.80
4,800,000	50.60	61.76

Table F-13
 Resistivity Measurements For
 Galvanized Low Carbon
 $t = 1.4 \text{ mm}$, $D = 6.1 \text{ mm}$, $W = 38 \text{ mm}$
 $R = 0.0$, Max. Load = 3,335 N (750 lbs)
 Total Life = 340,100
 As-Welded Conditions
 Task # 4 Specimen # 1

Number of Cycles	Change in Resistivity ($\mu\Omega\cdot\text{cm}$)	
	Side A	Side B
1	0.30	0.13
100	0.33	0.33
200	0.53	0.40
500	0.77	0.50
1,000	1.00	0.73
5,000	1.13	1.03
10,000	1.30	1.23
15,000	1.33	1.30
25,000	1.53	1.40
35,000	1.57	1.43
50,000	1.60	1.50
65,000	1.83	1.47
80,000	1.87	1.53
100,000	2.00	1.53
125,000	2.07	1.80
175,000	2.20	1.87
225,000	2.27	3.03
275,000	2.33	7.93
300,000	2.80	36.33

Table F-14
 Resistivity Measurements For
 Galvanized Low Carbon
 $t = 1.4 \text{ mm}$, $D = 6.1 \text{ mm}$, $W = 38 \text{ mm}$
 $R = 0.0$, Max. Load = 2,670 N (600 lbs)
 Total Life = 1,191,800
 As-Welded Conditions
 Task # 4 Specimen # 2

Number of Cycles	Change in Resistivity ($\mu\Omega\cdot\text{cm}$)	
	Side A	Side B
1	0.34	0.13
100	0.37	0.33
200	0.44	0.36
500	0.47	0.43
1,000	0.50	0.46
2,000	0.54	0.53
5,000	0.57	0.73
10,000	0.60	0.80
60,000	0.77	0.86
85,000	0.87	1.03
125,000	0.94	1.23
200,000	1.24	1.26
250,000	1.27	1.36
300,000	1.77	1.43
375,000	1.80	1.76
475,000	1.87	1.86
550,000	2.47	2.10
650,000	2.50	2.20
750,000	2.54	2.36
800,000	2.60	2.63
850,000	2.64	3.20
900,000	2.64	3.73
950,000	2.54	4.60
1,000,000	2.67	6.30
1,025,000	2.67	7.96
1,050,000	2.67	10.70
1,075,000	2.80	16.60
1,100,000	3.07	34.20
1,125,000	3.37	42.56
1,175,000	4.14	62.86

Table F-15
 Resistivity Measurements For
 Galvanized Low Carbon
 $t = 1.4 \text{ mm}$, $D = 6.1 \text{ mm}$, $W = 38 \text{ mm}$
 $R = 0.0$, Max. Load = 2,935 N (660 lbs)
 Total Life = 551,900
 As-Welded Conditions
 Task # 4 Specimen # 3

Number of Cycles	Change in Resistivity ($\mu\Omega\cdot\text{cm}$)	
	Side A	Side B
1	0.30	0.03
100	0.30	0.30
200	0.33	0.30
500	0.33	0.33
1,000	0.40	0.40
2,000	0.43	0.46
5,000	0.50	0.53
10,000	0.63	0.63
30,000	0.73	0.66
80,000	0.80	0.73
130,000	0.80	0.76
180,000	0.90	0.90
250,000	1.16	1.06
330,000	1.16	1.46
400,000	1.40	4.30
450,000	1.63	18.45
500,000	2.00	46.43
550,000	4.56	83.80

Table F-16
 Resistivity Measurements For
 Galvanized Low Carbon
 $t = 1.4 \text{ mm}$, $D = 6.1 \text{ mm}$, $W = 38 \text{ mm}$
 $R = 0.0$, Max. Load = 3,560 N (800 lbs)
 Total Life = 159,700
 As-Welded Conditions
 Task # 4 Specimen # 4

Number of Cycles	Change in Resistivity ($\mu\Omega\cdot\text{cm}$)	
	Side A	Side B
1	0.23	0.33
100	0.03	0.43
200	0.23	0.53
500	0.27	0.60
1,000	0.50	0.36
2,000	0.60	0.93
5,000	0.60	0.66
10,000	0.80	0.80
15,000	1.10	0.80
20,000	1.13	0.83
35,000	1.37	1.03
60,000	1.47	1.33
85,000	1.80	2.60
110,000	2.10	6.06

Table F-17
 Resistivity Measurements For
 Galvanized Low Carbon
 $t = 1.4 \text{ mm}$, $D = 6.1 \text{ mm}$, $W = 38 \text{ mm}$
 $R = -0.2$, Max. Load = 3,335 N (750 lbs)
 Total Life = 147,100
 As-Welded Conditions
 Task # 5 Specimen # 1

Number of Cycles	Change in Resistivity ($\mu\Omega\cdot\text{cm}$)	
	Side A	Side B
1	0.03	0.06
100	0.16	0.26
200	0.23	0.30
1,000	0.33	0.33
5,000	0.60	0.56
10,000	0.77	0.70
25,000	1.00	0.83
50,000	0.83	1.13
75,000	0.93	1.73
100,000	1.63	2.50
110,000	2.93	4.10
120,000	6.53	10.70
125,000	19.03	22.93
130,000	28.03	30.20
135,000	35.03	36.13
140,000	40.17	42.46

Table F-18
 Resistivity Measurements For
 Galvanized Low Carbon
 $t = 1.4 \text{ mm}$, $D = 6.1 \text{ mm}$, $W = 38 \text{ mm}$
 $R = -0.2$, Max. Load = 2,935 N (660 lbs)
 Total Life = 298,900
 As-Welded Conditions
 Task # 5 Specimen # 2

Number of Cycles	Change in Resistivity ($\mu\Omega\cdot\text{cm}$)	
	Side A	Side B
1	0.03	0.07
200	0.20	0.67
1,000	0.40	0.67
2,000	0.37	0.34
5,000	0.70	0.87
10,000	1.03	0.87
25,000	1.20	0.97
50,000	1.40	1.27
75,000	1.43	1.37
100,000	1.57	1.54
150,000	1.80	1.74
200,000	1.87	2.30
225,000	2.10	4.14
240,000	3.13	6.64
255,000	5.27	27.37
270,000	9.90	41.40
275,000	23.27	44.97
280,000	28.07	48.40
290,000	38.07	59.70

Table F-19
 Resistivity Measurements For
 Galvanized Low Carbon
 $t = 1.4 \text{ mm}$, $D = 6.1 \text{ mm}$, $W = 38 \text{ mm}$
 $R = -0.2$, Max. Load = 2,400 N (540 lbs)
 Total Life = 483,500
 As-Welded Conditions
 Task # 5 Specimen # 3

Number of Cycles	Change in Resistivity ($\mu\Omega\cdot\text{cm}$)	
	Side A	Side B
1	0.06	0.03
100	0.13	0.03
200	0.23	0.10
1,000	0.23	0.23
2,000	0.30	0.33
5,000	0.26	0.33
20,000	0.43	0.43
70,000	0.93	0.80
100,000	1.23	0.77
150,000	1.43	0.73
250,000	1.46	0.83
300,000	1.70	2.13
310,000	1.73	2.37
320,000	1.73	2.97
330,000	1.76	3.43
340,000	1.80	3.93
350,000	1.83	4.57
360,000	1.86	5.17
370,000	2.10	6.40
380,000	2.10	7.60
390,000	2.10	8.93
400,000	2.10	10.13
410,000	2.40	23.73
435,000	2.56	43.67
450,000	3.20	49.73
475,000	6.66	71.03

Table F-20
 Resistivity Measurements For
 Galvanized Low Carbon
 $t = 1.4$ mm, $D = 6.1$ mm, $W = 38$ mm
 $R = -0.2$, Max. Load = 2,270 N (510 lbs)
 Total Life = 791,400
 As-Welded Conditions
 Task # 5 Specimen # 4

Number of Cycles	Change in Resistivity ($\mu\Omega\cdot\text{cm}$)	
	Side A	Side B
1	0.01	0.24
100	0.06	0.34
200	0.06	0.30
1,000	0.13	0.47
2,000	0.13	0.47
5,000	0.40	0.50
10,000	0.50	0.74
40,000	1.13	1.00
100,000	1.30	0.97
200,000	1.70	1.00
300,000	1.83	1.07
400,000	2.16	1.27
450,000	2.23	1.94
500,000	2.33	2.64
550,000	2.30	4.30
575,000	2.40	5.34
600,000	2.30	6.57
625,000	2.36	10.07
650,000	2.30	10.30
675,000	2.30	19.90
725,000	2.70	42.54
750,000	3.16	52.80

Table F-21
 Resistivity Measurements For
 Galvanized Low Carbon
 $t = 1.4 \text{ mm}$, $D = 6.1 \text{ mm}$, $W = 38 \text{ mm}$
 $R = 0.5$, Max. Load = 5,340 N (1,200 lbs)
 Total Life = 986,100
 As-Welded Conditions
 Task # 6 Specimen # 1

Number of Cycles	Change in Resistivity ($\mu\Omega\cdot\text{cm}$)	
	Side A	Side B
1	0.17	0.60
100	0.47	0.70
500	0.70	0.87
1,000	0.74	0.94
5,000	0.84	0.97
10,000	1.00	0.97
20,000	1.04	1.14
50,000	1.14	1.20
75,000	1.34	1.27
100,000	1.37	1.24
150,000	1.34	1.27
200,000	1.37	1.30
250,000	1.40	1.60
300,000	1.44	1.67
325,000	1.37	1.74
360,000	1.37	1.77
380,000	1.40	1.80
400,000	1.37	1.74
430,000	1.47	1.80
460,000	1.47	1.84
500,000	1.54	2.04
540,000	1.64	2.01
580,000	1.64	1.97
630,000	1.67	2.02
700,000	1.80	2.10
750,000	1.80	2.80
770,000	1.80	3.24
790,000	1.80	3.77
810,000	1.77	4.30
850,000	1.80	6.00
875,000	1.84	7.27
900,000	1.94	9.87
925,000	2.17	10.10
950,000	2.54	14.57

Table F-22
 Resistivity Measurements For
 Galvanized Low Carbon
 $t = 1.4$ mm, $D = 6.1$ mm, $W = 38$ mm
 $R = 0.5$, Max. Load = 6,670 N (1,500 lbs)
 Total Life = 130,100
 As-Welded Conditions
 Task # 6 Specimen # 2

Number of Cycles	Change in Resistivity ($\mu\Omega\cdot\text{cm}$)	
	Side A	Side B
1	0.26	0.40
100	0.23	0.70
500	0.86	1.27
1,000	0.96	1.47
2,000	1.16	1.74
3,000	1.16	1.70
5,000	1.63	2.04
7,000	1.56	2.24
10,000	1.70	2.24
15,000	1.76	2.34
25,000	1.90	2.44
40,000	2.03	2.94
55,000	2.06	3.24
65,000	2.06	4.20
75,000	2.36	5.24
85,000	2.36	7.07
93,000	2.60	8.34
100,000	2.63	10.20
108,000	2.56	12.40
115,000	2.76	23.84
125,000	3.46	27.90

Table F-23
 Resistivity Measurements For
 Galvanized Low Carbon
 $t = 1.4 \text{ mm}$, $D = 6.1 \text{ mm}$, $W = 38 \text{ mm}$
 $R = 0.5$, Max. Load = 4,895 N (1,100 lbs)
 Total Life = 1,034,300
 As-Welded Conditions
 Task # 6 Specimen # 3

Number of Cycles	Change in Resistivity ($\mu\Omega\cdot\text{cm}$)	
	Side A	Side B
1	0.04	0.10
100	0.04	0.24
500	0.04	0.47
1,000	0.04	0.80
5,000	0.20	1.07
10,000	0.20	1.40
30,000	0.64	1.47
50,000	0.90	1.50
100,000	1.20	1.57
200,000	1.84	1.84
300,000	1.77	1.77
350,000	1.90	1.80
400,000	1.90	1.87
500,000	1.94	1.90
650,000	1.87	2.34
700,000	1.87	2.67
750,000	1.87	3.64
775,000	1.90	4.27
800,000	1.80	4.84
825,000	2.20	5.90
850,000	2.24	7.24
875,000	2.54	7.94
900,000	2.54	9.84
925,000	2.54	10.87
975,000	3.34	24.84
1,025,000	7.20	36.44

Table F-24
 Resistivity Measurements For
 Galvanized Low Carbon
 $t = 1.4 \text{ mm}$, $D = 6.1 \text{ mm}$, $W = 38 \text{ mm}$
 $R = 0.5$, Max. Load = 5,780 N (1,300 lbs)
 Total Life = 195,100
 As-Welded Conditions
 Task # 6 Specimen # 4

Number of Cycles	Change in Resistivity ($\mu\Omega\cdot\text{cm}$)	
	Side A	Side B
1	0.36	0.46
100	0.46	1.03
500	0.50	1.16
1,000	0.86	1.10
5,000	0.86	1.16
10,000	0.86	1.16
30,000	1.06	1.30
50,000	1.16	1.26
75,000	1.40	1.50
125,000	1.66	2.06
140,000	1.66	3.83
155,000	1.96	5.13
160,000	1.96	5.56
170,000	2.33	6.46
180,000	2.66	10.10
185,000	3.50	12.53
190,000	5.16	18.16
195,000	8.73	28.83

Table F-25
 Resistivity Measurements For
 Galvanized Low Carbon
 $t = 1.4$ mm, $D = 4.8$ mm, $W = 38$ mm
 $R = 0.0$, Max. Load = 2,670 N (600 lbs)
 Total Life = 640,900
 As-Welded Conditions
 Task # 7 Specimen # 1

Number of Cycles	Change in Resistivity ($\mu\Omega\cdot\text{cm}$)	
	Side A	Side B
1	0.1	0.03
100	0.24	0.23
500	0.20	0.53
1,000	0.24	0.73
5,000	0.64	1.10
10,000	0.87	1.33
30,000	1.10	1.37
60,000	1.10	1.27
100,000	1.34	1.37
175,000	1.74	1.57
250,000	1.87	1.93
375,000	1.80	2.83
425,000	1.80	5.03
450,000	1.90	6.47
475,000	1.97	8.43
485,000	2.00	9.30
493,000	2.00	10.33
500,000	2.00	13.73
525,000	2.00	27.73
550,000	2.37	38.63
575,000	2.67	46.23

Table F-26
 Resistivity Measurements For
 Galvanized Low Carbon
 $t = 1.4 \text{ mm}$, $D = 4.8 \text{ mm}$, $W = 38 \text{ mm}$
 $R = 0.0$, Max. Load = 2,270 N (510 lbs)
 Total Life = 3,711,200
 As-Welded Conditions
 Task # 7 Specimen # 2

Number of Cycles	Change in Resistivity ($\mu\Omega\cdot\text{cm}$)	
	Side A	Side B
1	0.04	0.10
100	0.24	0.34
500	0.20	0.44
1,000	0.34	0.44
5,000	0.67	0.64
10,000	0.67	0.87
50,000	1.27	0.97
100,000	1.40	1.10
200,000	1.40	1.20
400,000	1.44	1.20
500,000	1.67	1.47
600,000	1.74	1.44
700,000	1.80	1.64
775,000	1.80	1.57
900,000	1.80	1.54
1,000,000	1.80	1.50
1,200,000	1.80	1.44
1,300,000	1.84	1.47
1,400,000	1.87	1.50
1,500,000	1.87	1.47
1,600,000	1.90	1.67
1,700,000	1.94	1.77
1,900,000	1.97	1.50
2,000,000	1.94	1.47
2,100,000	1.90	1.50
2,500,000	1.77	1.50
3,000,000	2.09	7.67
3,500,000	1.97	19.40
3,550,000	2.10	34.70
3,600,000	2.17	45.14

Table F-27
 Resistivity Measurements For
 Galvanized Low Carbon
 $t = 1.4 \text{ mm}$, $D = 4.8 \text{ mm}$, $W = 38 \text{ mm}$
 $R = 0.0$, Max. Load = 2,935 N (660 lbs)
 Total Life = 461,600
 As-Welded Conditions
 Task # 7 Specimen # 3

Number of Cycles	Change in Resistivity ($\mu\Omega\cdot\text{cm}$)	
	Side A	Side B
1	0.04	0.06
100	0.24	0.23
500	0.60	0.26
1,000	0.97	0.46
5,000	1.30	1.00
10,000	1.44	0.93
40,000	1.50	1.40
70,000	1.47	1.43
100,000	1.50	1.46
150,000	1.57	1.53
200,000	1.64	1.46
300,000	2.54	1.96
325,000	3.57	2.70
350,000	5.24	3.70
375,000	7.27	5.86
385,000	8.70	7.70
390,000	9.80	9.23
400,000	11.90	11.50
425,000	29.64	34.43
450,000	44.17	46.83

Table F-28
 Resistivity Measurements For
 Galvanized Low Carbon
 $t = 1.4 \text{ mm}$, $D = 4.8 \text{ mm}$, $W = 38 \text{ mm}$
 $R = 0.0$, Max. Load = 3,335 N (750 lbs)
 Total Life = 223,800
 As-Welded Conditions
 Task # 7 Specimen # 4

Number of Cycles	Change in Resistivity ($\mu\Omega\cdot\text{cm}$)	
	Side A	Side B
1	0.07	0.03
100	0.13	0.57
500	0.23	1.07
1,000	0.37	1.30
5,000	0.67	1.63
10,000	0.87	1.60
30,000	1.30	1.60
50,000	1.30	1.90
75,000	1.30	2.30
100,000	1.50	2.60
125,000	1.47	4.00
140,000	1.47	5.47
150,000	1.53	7.73
160,000	1.70	9.60
170,000	2.10	23.4
180,000	2.13	32.00
200,000	2.50	42.57

Table F-29
 Resistivity Measurements For
 Galvanized Low Carbon
 $t = 1.4 \text{ mm}$, $D = 4.8 \text{ mm}$, $W = 38 \text{ mm}$
 $R = -0.2$, Max. Load = 3,205 N (720 lbs)
 Total Life = 213,100
 As-Welded Conditions
 Task # 8 Specimen # 1

Number of Cycles	Change in Resistivity ($\mu\Omega\cdot\text{cm}$)	
	Side A	Side B
1	0.13	0.07
100	0.30	0.07
500	0.30	0.44
1,000	0.50	0.44
5,000	1.03	1.04
10,000	1.46	1.24
30,000	1.63	1.44
50,000	1.93	1.97
70,000	2.13	2.17
100,000	2.36	2.17
120,000	2.36	2.80
140,000	2.46	3.37
160,000	2.53	6.17
170,000	2.63	8.34
180,000	3.40	10.04
190,000	5.40	36.04
200,000	22.23	46.40

Table F-30
 Resistivity Measurements For
 Galvanized Low Carbon
 $t = 1.4 \text{ mm}$, $D = 4.8 \text{ mm}$, $W = 38 \text{ mm}$
 $R = -0.2$, Max. Load = 2,225 N (500 lbs)
 Total Life = 878,100
 As-Welded Conditions
 Task # 8 Specimen # 2

Number of Cycles	Change in Resistivity ($\mu\Omega\cdot\text{cm}$)	
	Side A	Side B
1	0.17	0.04
100	0.14	0.27
500	0.20	0.60
1,000	0.30	0.94
5,000	0.40	1.50
10,000	0.47	1.60
30,000	0.57	1.57
50,000	0.80	1.67
100,000	0.94	1.80
150,000	1.04	1.80
225,000	1.14	1.80
350,000	1.14	1.84
400,000	1.24	1.97
450,000	1.24	2.02
500,000	1.20	2.00
575,000	1.20	2.54
600,000	1.27	2.74
625,000	1.30	3.20
650,000	1.24	3.87
675,000	1.20	4.87
700,000	1.20	6.50
715,000	1.27	7.24
725,000	1.20	8.30
735,000	1.34	9.37
745,000	1.20	10.54
760,000	1.27	22.90
785,000	1.37	35.84
800,000	1.54	41.27

Table F-31
 Resistivity Measurements For
 Galvanized Low Carbon
 $t = 1.4 \text{ mm}$, $D = 4.8 \text{ mm}$, $W = 38 \text{ mm}$
 $R = -0.2$, Max. Load = 2,670 N (600 lbs)
 Total Life = 380,600
 As-Welded Conditions
 Task # 8 Specimen # 3

Number of Cycles	Change in Resistivity ($\mu\Omega\cdot\text{cm}$)	
	Side A	Side B
1	0.03	0.13
100	0.07	0.36
500	0.07	0.50
1,000	0.27	0.86
5,000	0.77	0.83
10,000	1.27	0.93
30,000	1.30	1.03
50,000	1.63	1.23
100,000	1.87	1.23
150,000	1.83	1.30
250,000	1.89	2.23
275,000	2.10	3.96
290,000	2.13	5.43
300,000	2.30	6.43
310,000	2.27	7.90
320,000	2.23	10.40
335,000	2.53	30.46
350,000	3.90	40.53
365,000	6.67	50.23
380,000	30.63	74.83

Table F-32
 Resistivity Measurements For
 Galvanized Low Carbon
 $t = 1.4 \text{ mm}$, $D = 4.8 \text{ mm}$, $W = 38 \text{ mm}$
 $R = -0.2$, Max. Load = 2,135 N (480 lbs)
 Total Life = 2,231,400
 As-Welded Conditions
 Task # 8 Specimen # 4

Number of Cycles	Change in Resistivity ($\mu\Omega\cdot\text{cm}$)	
	Side A	Side B
1	0.03	0.06
100	0.01	0.06
500	0.03	0.07
1,000	0.03	0.07
5,000	0.67	0.26
10,000	0.90	0.40
30,000	1.07	1.06
50,000	1.17	1.33
100,000	1.23	1.56
200,000	1.53	1.70
300,000	1.63	1.90
400,000	1.77	1.93
500,000	1.73	1.86
600,000	1.77	1.86
800,000	1.73	1.90
1,100,000	1.77	1.93
1,300,000	1.83	1.93
1,400,000	1.80	1.93
1,900,000	1.80	3.80
1,925,000	1.83	4.76
1,940,000	1.87	5.16
1,975,000	1.83	6.36
1,985,000	1.80	6.83
1,995,000	1.73	7.06
2,011,000	1.80	8.10
2,019,000	1.80	8.56
2,027,000	1.77	8.93
2,035,000	1.73	9.70
2,040,000	1.83	10.13
2,045,000	1.83	10.60
2,050,000	1.97	11.20
2,075,000	1.80	22.43
2,100,000	1.97	29.26

Table F-33
 Resistivity Measurements For
 Galvanized Low Carbon
 $t = 1.4 \text{ mm}$, $D = 4.8 \text{ mm}$, $W = 38 \text{ mm}$
 $R = 0.5$, Max. Load = 4,335 N (975 lbs)
 Total Life = 1,121,200
 As-Welded Conditions
 Task # 9 Specimen # 1

Number of Cycles	Change in Resistivity ($\mu\Omega\cdot\text{cm}$)	
	Side A	Side B
1	0.01	0.10
100	0.01	0.07
500	0.23	0.34
1,000	0.20	0.44
5,000	0.80	1.07
10,000	1.00	1.34
30,000	1.00	1.50
100,000	1.36	1.80
300,000	1.63	1.94
350,000	1.73	1.94
400,000	1.80	1.96
450,000	1.70	2.14
500,000	1.66	2.00
600,000	1.90	2.17
650,000	1.90	2.20
800,000	2.23	2.67
825,000	2.10	3.04
875,000	2.20	3.27
925,000	2.70	3.97
950,000	2.73	4.84
975,000	3.56	5.50
1,000,000	4.56	8.74
1,025,000	5.63	10.74
1,050,000	6.70	13.70
1,075,000	8.46	17.17
1,100,000	11.26	24.64

Table F-34
 Resistivity Measurements For
 Galvanized Low Carbon
 $t = 1.4 \text{ mm}$, $D = 4.8 \text{ mm}$, $W = 38 \text{ mm}$
 $R = 0.5$, Max. Load = 5,340 N (1,200 lbs)
 Total Life = 219,100
 As-Welded Conditions
 Task # 9 Specimen # 2

Number of Cycles	Change in Resistivity ($\mu\Omega\cdot\text{cm}$)	
	Side A	Side B
1	0.40	0.17
100	0.63	0.30
500	0.90	0.80
1,000	1.16	0.97
5,000	1.50	1.40
10,000	1.43	1.44
25,000	1.63	1.77
50,000	1.76	2.17
75,000	1.76	2.17
100,000	1.80	2.37
150,000	2.06	3.50
175,000	2.50	6.37
190,000	3.63	9.54
200,000	4.86	11.40
210,000	6.93	13.44

Table F-35
 Resistivity Measurements For
 Galvanized Low Carbon
 $t = 1.4 \text{ mm}$, $D = 4.8 \text{ mm}$, $W = 38 \text{ mm}$
 $R = 0.5$, Max. Load = 6,670 N (1,500 lbs)
 Total Life = 51,200
 As-Welded Conditions
 Task # 9 Specimen # 3

Number of Cycles	Change in Resistivity ($\mu\Omega\cdot\text{cm}$)	
	Side A	Side B
1	0.54	1.04
100	0.74	1.70
500	1.24	2.10
1,000	1.47	2.14
5,000	2.27	2.50
10,000	2.67	2.87
20,000	3.20	3.17
30,000	4.30	3.60
40,000	4.30	4.34
50,000	10.07	13.27

Table F-36
 Resistivity Measurements For
 Galvanized Low Carbon
 $t = 1.4 \text{ mm}$, $D = 4.8 \text{ mm}$, $W = 38 \text{ mm}$
 $R = 0.5$, Max. Load = 4,895 N (1,100 lbs)
 Total Life = 334,500
 As-Welded Conditions
 Task # 9 Specimen # 4

Number of Cycles	Change in Resistivity ($\mu\Omega\cdot\text{cm}$)	
	Side A	Side B
1	0.10	0.14
100	0.10	0.17
500	0.37	0.24
1,000	0.27	0.37
5,000	0.54	0.87
10,000	0.80	0.87
50,000	0.97	0.87
100,000	1.17	1.47
150,000	1.34	2.54
175,000	1.34	3.97
200,000	1.37	4.97
220,000	1.67	5.97
235,000	1.70	6.87
250,000	1.70	8.20
260,000	1.80	9.27
270,000	1.80	10.54
285,000	1.97	19.54
300,000	2.60	23.60
315,000	3.60	26.00
330,000	6.77	32.04

Table F-37
 Resistivity Measurements For
 Galvanized HSLA
 $t = 1.4 \text{ mm}$, $D = 4.8 \text{ mm}$, $W = 38 \text{ mm}$
 $R = 0.0$, Max. Load = 3,205 N (720 lbs)
 Total Life = 215,600
 As-Welded Conditions
 Task # 10 Specimen # 1

Number of Cycles	Change in Resistivity ($\mu\Omega\cdot\text{cm}$)	
	Side A	Side B
1	0.57	0.70
100	0.77	0.93
200	0.93	1.00
500	1.13	1.23
1,000	1.23	1.20
2,000	1.20	1.50
5,000	1.47	1.67
10,000	1.70	2.03
20,000	1.93	3.00
30,000	2.10	3.20
50,000	2.73	3.60
75,000	3.23	4.10
100,000	3.33	5.27
120,000	3.37	7.17
130,000	3.47	8.23
140,000	4.07	9.50
150,000	4.13	11.03
162,000	5.10	13.83

Table F-38
 Resistivity Measurements For
 Galvanized HSLA
 $t = 1.4$ mm, $D = 4.8$ mm, $W = 38$ mm
 $R = 0.0$, Max. Load = 2,670 N (600 lbs)
 Total Life = 511,800
 As-Welded Conditions
 Task # 10 Specimen # 2

Number of Cycles	Change in Resistivity ($\mu\Omega\cdot\text{cm}$)	
	Side A	Side B
1	0.23	0.50
100	0.27	0.57
200	0.30	0.64
500	0.47	0.74
1,000	0.57	0.94
2,000	0.60	0.84
5,000	0.60	0.84
10,000	0.70	1.20
40,000	0.83	1.84
70,000	1.00	2.40
100,000	1.03	2.54
150,000	1.27	2.57
200,000	1.43	3.37
240,000	1.57	3.67
280,000	1.70	5.30
300,000	1.83	5.64
320,000	1.83	6.04
340,000	1.93	7.14
350,000	2.00	8.07
360,000	2.10	8.60
370,000	2.20	9.97
380,000	2.37	11.00
400,000	2.63	15.70

Table F-39
 Resistivity Measurements For
 Galvanized HSLA
 $t = 1.4 \text{ mm}$, $D = 4.8 \text{ mm}$, $W = 38 \text{ mm}$
 $R = 0.0$, Max. Load = 2,000 N (450 lbs)
 Total Life = 1,150,200
 As-Welded Conditions
 Task # 10 Specimen # 3

Number of Cycles	Change in Resistivity ($\mu\Omega\cdot\text{cm}$)	
	Side A	Side B
1	0.03	0.07
100	0.30	0.34
200	0.10	0.77
500	0.26	1.00
1,000	0.33	1.20
5,000	0.60	1.17
10,000	1.10	1.14
40,000	1.03	1.24
150,000	1.50	1.40
200,000	1.50	2.10
250,000	1.86	2.20
300,000	1.86	2.70
400,000	1.93	3.70
500,000	1.96	5.70
550,000	1.96	7.00
580,000	2.03	7.77
600,000	2.03	8.27
630,000	2.10	9.44
650,000	2.10	9.90
675,000	2.20	10.64
700,000	2.56	11.47
750,000	2.73	16.77

Table F-40
 Resistivity Measurements For
 Galvanized HSLA
 $t = 1.4$ mm, $D = 4.8$ mm, $W = 38$ mm
 $R = 0.0$, Max. Load = 1,870 N (420 lbs)
 Total Life = 1,562,400
 As-Welded Conditions
 Task # 10 Specimen # 4

Number of Cycles	Change in Resistivity ($\mu\Omega\cdot\text{cm}$)	
	Side A	Side B
1	0.13	0.87
100	0.16	1.14
500	0.16	1.17
1,000	0.10	1.10
5,000	0.16	1.14
10,000	0.16	1.07
50,000	0.40	1.20
100,000	0.43	1.27
350,000	0.60	1.57
450,000	0.76	2.00
500,000	0.86	2.30
550,000	1.00	2.47
600,000	1.26	3.04
800,000	1.40	5.24
850,000	1.43	6.40
880,000	1.56	6.90
900,000	1.66	7.44
950,000	1.83	8.60
1,000,000	1.80	10.00
1,050,000	2.46	12.00
1,100,000	2.63	18.87

Table F-41
 Resistivity Measurements For
 Galvanized Low Carbon
 $t = 0.9 \text{ mm}$, $D = 6.1 \text{ mm}$, $W = 38 \text{ mm}$
 $R = 0.0$, Max. Load = 1,870 N (420 lbs)
 Total Life = 417,900
 As-Welded Conditions
 Task # 13 Specimen # 1

Number of Cycles	Change in Resistivity ($\mu\Omega\cdot\text{cm}$)	
	Side A	Side B
1	0.10	0.04
100	0.10	0.04
500	0.14	0.07
1,000	0.10	0.17
5,000	0.30	0.30
10,000	0.37	0.47
30,000	0.40	0.40
60,000	0.50	0.67
80,000	0.57	0.77
100,000	0.57	0.87
140,000	0.60	0.87
170,000	0.57	1.04
200,000	0.74	1.17
220,000	0.74	1.17
250,000	0.87	1.27
275,000	0.77	1.34
300,000	0.80	1.30
320,000	0.80	1.70
340,000	0.97	2.77
360,000	1.00	4.40
380,000	1.24	8.77
400,000	2.17	18.64

Table F-42
 Resistivity Measurements For
 Galvanized Low Carbon
 $t = 0.9$ mm, $D = 6.1$ mm, $W = 38$ mm
 $R = 0.0$, Max. Load = 2,135 N (480 lbs)
 Total Life = 160,300
 As-Welded Conditions
 Task # 13 Specimen # 2

Number of Cycles	Change in Resistivity ($\mu\Omega\cdot\text{cm}$)	
	Side A	Side B
1	0.03	0.03
100	0.10	0.10
500	0.13	0.13
1,000	0.17	0.20
5,000	0.30	0.23
30,000	0.33	0.33
50,000	0.47	0.30
75,000	0.53	0.40
100,000	0.70	0.53
110,000	0.73	0.66
120,000	0.70	1.10
130,000	0.67	2.06
135,000	0.63	3.66
140,000	0.70	11.03
145,000	0.87	16.86

Table F-43
 Resistivity Measurements For
 Galvanized Low Carbon
 $t = 0.9$ mm, $D = 6.1$ mm, $W = 38$ mm
 $R = 0.0$, Max. Load = 1,470 N (330 lbs)
 Total Life = 559,100
 As-Welded Conditions
 Task # 13 Specimen # 3

Number of Cycles	Change in Resistivity ($\mu\Omega\cdot\text{cm}$)	
	Side A	Side B
1	0.04	0.10
1,000	0.17	0.13
5,000	0.30	0.16
10,000	0.30	0.13
50,000	0.37	0.33
200,000	0.54	0.66
380,000	0.74	0.86
450,000	0.77	4.60
480,000	0.77	21.76
500,000	0.74	26.86

Table F-44
 Resistivity Measurements For
 Galvanized Low Carbon
 $t = 0.9 \text{ mm}$, $D = 6.1 \text{ mm}$, $W = 38 \text{ mm}$
 $R = 0.0$, Max. Load = 1,335 N (300 lbs)
 Total Life = 1,465,700
 As-Welded Conditions
 Task # 13 Specimen # 4

Number of Cycles	Change in Resistivity ($\mu\Omega\cdot\text{cm}$)	
	Side A	Side B
1	0.09	0.03
1,000	0.13	0.06
5,000	0.13	0.07
10,000	0.13	0.07
50,000	0.13	0.10
100,000	0.16	0.10
200,000	0.20	0.13
300,000	0.20	0.16
500,000	0.17	0.16
600,000	0.16	0.20
800,000	0.20	0.20
1,000,000	0.16	0.30
1,100,000	0.16	0.66
1,200,000	0.19	3.20
1,225,000	0.26	4.60
1,250,000	0.26	12.70
1,300,000	0.30	24.86

Table F-45
 Resistivity Measurements For
 Galvanized Low Carbon
 $t = 0.9$ mm, $D = 6.1$ mm, $W = 38$ mm
 $R = -0.2$, Max. Load = 1,870 N (420 lbs)
 Total Life = 110,600
 As-Welded Conditions
 Task # 14 Specimen # 1

Number of Cycles	Change in Resistivity ($\mu\Omega\cdot\text{cm}$)	
	Side A	Side B
100	0.37	0.05
200	0.33	0.07
500	0.37	0.13
1,000	0.40	0.10
2,000	0.43	0.20
5,000	0.53	0.27
10,000	0.80	0.50
20,000	1.03	0.50
30,000	1.20	0.97
40,000	1.20	1.00
50,000	1.23	1.24
70,000	1.33	1.74
80,000	1.67	4.27
84,000	1.70	10.57
86,000	1.80	15.87
88,000	1.77	18.54
90,000	1.80	20.24

Table F-46
 Resistivity Measurements For
 Galvanized Low Carbon
 $t = 0.9 \text{ mm}$, $D = 6.1 \text{ mm}$, $W = 38 \text{ mm}$
 $R = -0.2$, Max. Load = 1,200 N (270 lbs)
 Total Life = 1,814,400
 As-Welded Conditions
 Task # 14 Specimen # 2

Number of Cycles	Change in Resistivity ($\mu\Omega\cdot\text{cm}$)	
	Side A	Side B
1	0.04	0.03
100	0.14	0.03
500	0.07	0.07
1,000	0.10	0.03
100,000	0.57	0.23
190,000	0.87	0.37
350,000	1.00	0.57
500,000	1.07	0.53
650,000	1.07	0.53
800,000	1.07	0.50
1,000,000	1.07	0.53
1,250,000	1.17	0.57
1,350,000	1.07	0.53
1,600,000	1.10	4.43
1,650,000	1.20	25.20

Table F-47
 Resistivity Measurements For
 Galvanized Low Carbon
 $t = 0.9 \text{ mm}$, $D = 6.1 \text{ mm}$, $W = 38 \text{ mm}$
 $R = -0.2$, Max. Load = 1,600 N (360 lbs)
 Total Life = 309,600
 As-Welded Conditions
 Task # 14 Specimen # 3

Number of Cycles	Change in Resistivity ($\mu\Omega\cdot\text{cm}$)	
	Side A	Side B
100	0.04	0.07
500	0.04	0.10
1,000	0.04	0.30
5,000	0.07	0.40
10,000	0.20	0.50
50,000	0.67	0.77
80,000	0.67	0.77
130,000	1.00	1.07
160,000	1.04	1.07
200,000	1.04	1.04
270,000	1.30	3.34
300,000	21.29	28.44

Table F-48
 Resistivity Measurements For
 Galvanized Low Carbon
 $t = 0.9$ mm, $D = 6.1$ mm, $W = 38$ mm
 $R = -0.2$, Max. Load = 1,335 N (300 lbs)
 Total Life = 503,200
 As-Welded Conditions
 Task # 14 Specimen # 4

Number of Cycles	Change in Resistivity ($\mu\Omega\cdot\text{cm}$)	
	Side A	Side B
1	0.10	0.07
100	0.13	0.10
500	0.17	0.07
1,000	0.10	0.07
5,000	0.13	0.17
10,000	0.20	0.20
50,000	0.30	0.73
100,000	0.27	0.70
200,000	0.37	0.77
300,000	0.47	0.90
400,000	0.47	4.70
425,000	0.53	23.29

Table F-49
 Resistivity Measurements For
 Galvanized Low Carbon
 $t = 0.9$ mm, $D = 6.1$ mm, $W = 38$ mm
 $R = 0.5$, Max. Load = 3,470 N (780 lbs)
 Total Life = 144,200
 As-Welded Conditions
 Task # 15 Specimen # 1

Number of Cycles	Change in Resistivity ($\mu\Omega\cdot\text{cm}$)	
	Side A	Side B
1	0.33	0.07
100	0.47	0.14
500	0.50	0.40
1,000	0.77	0.50
5,000	0.80	0.87
10,000	0.93	0.90
20,000	0.97	1.10
40,000	1.10	1.07
60,000	1.23	1.10
70,000	1.33	1.14
80,000	1.40	1.17
100,000	1.50	1.37
110,000	1.50	1.44
120,000	1.53	1.47
130,000	1.90	2.54
135,000	2.33	3.74
140,000	9.63	13.30

Table F-50
 Resistivity Measurements For
 Galvanized Low Carbon
 $t = 0.9$ mm, $D = 6.1$ mm, $W = 38$ mm
 $R = 0.5$, Max. Load = 2,270 N (510 lbs)
 Total Life = 2,448,600
 As-Welded Conditions
 Task # 15 Specimen # 2

Number of Cycles	Change in Resistivity ($\mu\Omega\cdot\text{cm}$)	
	Side A	Side B
1	0.03	0.03
100	0.07	0.07
500	0.10	0.07
1,000	0.07	0.10
10,000	0.13	0.17
50,000	0.13	0.37
100,000	0.20	0.37
200,000	0.30	0.33
300,000	0.30	0.30
475,000	0.30	0.30
600,000	0.33	0.33
800,000	0.37	0.53
1,000,000	0.30	0.57
1,200,000	0.33	0.47
1,500,000	0.33	0.63
2,000,000	0.37	1.93
2,025,000	0.37	2.30
2,075,000	0.33	2.70
2,150,000	0.50	3.00
2,250,000	0.60	3.83
2,400,000	0.53	20.79

Table F-51
 Resistivity Measurements For
 Galvanized Low Carbon
 $t = 0.9 \text{ mm}$, $D = 6.1 \text{ mm}$, $W = 38 \text{ mm}$
 $R = 0.5$, Max. Load = 2,670 N (600 lbs)
 Total Life = 1,823,100
 As-Welded Conditions
 Task # 15 Specimen # 3

Number of Cycles	Change in Resistivity ($\mu\Omega\cdot\text{cm}$)	
	Side A	Side B
1	0.04	0.03
100	0.04	0.37
500	0.04	0.50
1,000	0.24	0.57
5,000	0.77	0.60
10,000	0.77	0.63
50,000	0.97	0.97
100,000	1.00	1.10
175,000	1.04	1.07
250,000	1.03	1.03
450,000	1.07	1.07
600,000	1.17	1.10
850,000	1.17	1.13
1,000,000	1.17	1.17
1,300,000	1.20	1.17
1,500,000	1.27	2.87
1,600,000	2.07	6.30
1,700,000	2.60	26.29

Table F-52
 Resistivity Measurements For
 Galvanized Low Carbon
 $t = 0.9 \text{ mm}$, $D = 6.1 \text{ mm}$, $W = 38 \text{ mm}$
 $R = 0.5$, Max. Load = 3,205 N (720 lbs)
 Total Life = 423,000
 As-Welded Conditions
 Task # 15 Specimen # 4

Number of Cycles	Change in Resistivity ($\mu\Omega\cdot\text{cm}$)	
	Side A	Side B
1	0.03	0.03
100	0.13	0.06
500	0.13	0.06
1,000	0.20	0.20
5,000	0.50	0.30
10,000	0.43	0.56
50,000	0.73	1.00
75,000	0.73	1.06
100,000	0.83	1.13
150,000	0.90	1.17
200,000	0.93	1.17
260,000	1.16	1.63
340,000	1.36	1.73
400,000	2.16	3.96
420,000	25.73	26.73

Table F-53
 Resistivity Measurements For
 Galvanized Low Carbon
 $t = 0.9$ mm, $D = 4.8$ mm, $W = 38$ mm
 $R = 0.0$, Max. Load = 1,335 N (300 lbs)
 Total Life = 2,240,700
 As-Welded Conditions
 Task # 16 Specimen # 1

Number of Cycles	Change in Resistivity ($\mu\Omega\cdot\text{cm}$)	
	Side A	Side B
1	0.03	0.03
100	0.03	0.03
1,000	0.03	0.03
5,000	0.10	0.30
10,000	0.26	0.30
50,000	0.43	0.33
100,000	0.80	0.63
200,000	0.96	0.86
300,000	0.96	1.00
400,000	1.00	1.03
500,000	1.10	1.06
600,000	1.40	1.16
675,000	1.43	1.16
750,000	1.43	1.16
850,000	1.53	1.23
925,000	1.56	1.23
1,000,000	1.56	1.23
1,200,000	1.60	1.26
1,300,000	1.63	1.33
1,500,000	1.63	1.33
2,000,000	1.63	8.83
2,050,000	1.86	18.53
2,100,000	2.00	31.66
2,150,000	2.00	40.23
2,200,000	2.06	48.83

Table F-54
 Resistivity Measurements For
 Galvanized Low Carbon
 $t = 0.9$ mm, $D = 4.8$ mm, $W = 38$ mm
 $R = 0.0$, Max. Load = 1,735 N (390 lbs)
 Total Life = 544,700
 As-Welded Conditions
 Task # 16 Specimen # 2

Number of Cycles	Change in Resistivity ($\mu\Omega\cdot\text{cm}$)	
	Side A	Side B
100	0.07	0.10
500	0.10	0.13
1,000	0.13	0.20
10,000	0.40	0.27
50,000	0.80	0.57
100,000	1.07	0.60
150,000	1.10	0.67
200,000	1.13	0.83
250,000	1.50	0.97
350,000	1.60	1.17
400,000	1.57	1.43
450,000	1.77	1.77
475,000	1.97	16.50
500,000	2.10	27.73

Table F-55
 Resistivity Measurements For
 Galvanized Low Carbon
 $t = 0.9$ mm, $D = 4.8$ mm, $W = 38$ mm
 $R = 0.0$, Max. Load = 1,600 N (360 lbs)
 Total Life = 613,000
 As-Welded Conditions
 Task # 16 Specimen # 3

Number of Cycles	Change in Resistivity ($\mu\Omega\cdot\text{cm}$)	
	Side A	Side B
100	0.03	0.03
1,000	0.33	0.06
10,000	0.33	0.26
100,000	0.70	1.10
200,000	1.26	1.26
250,000	1.36	1.33
300,000	1.40	1.60
350,000	1.36	1.70
400,000	1.46	1.73
450,000	1.53	1.73
500,000	1.56	2.40
550,000	2.40	3.66
575,000	3.50	9.00
600,000	18.20	21.40

Table F-56
 Resistivity Measurements For
 Galvanized Low Carbon
 $t = 0.9 \text{ mm}$, $D = 4.8 \text{ mm}$, $W = 38 \text{ mm}$
 $R = 0.0$, Max. Load = 2,225 N (500 lbs)
 Total Life = 99,000
 As-Welded Conditions
 Task # 16 Specimen # 4

Number of Cycles	Change in Resistivity ($\mu\Omega\cdot\text{cm}$)	
	Side A	Side B
1	0.17	0.07
100	0.17	0.07
500	0.40	0.17
1,000	0.47	0.24
5,000	0.70	0.54
10,000	0.97	1.00
20,000	1.14	1.47
30,000	1.50	1.50
40,000	1.54	1.54
50,000	1.60	1.57
60,000	1.77	1.70
70,000	1.80	2.44
80,000	1.84	3.97
85,000	2.14	6.24
90,000	2.24	14.64
95,000	3.94	20.44

Table F-57
 Resistivity Measurements For
 Galvanized Low Carbon
 $t = 2.7$ mm, $D = 8.6$ mm, $W = 38$ mm
 $R = 0.0$, Max. Load = 6,670 N (1,500 lbs)
 Total Life = 83,000
 As-Welded Conditions
 Task # 17 Specimen # 1

Number of Cycles	Change in Resistivity ($\mu\Omega\cdot\text{cm}$)	
	Side A	Side B
1,000	0.16	0.67
5,000	0.50	0.70
10,000	0.43	0.67
30,000	0.46	0.73
50,000	2.13	2.30
75,000	21.76	36.87

TableF-58
 Resistivity Measurements For
 Galvanized Low Carbon
 $t = 2.7$ mm, $D = 8.6$ mm, $W = 38$ mm
 $R = 0.0$, Max. Load = 5,340 N (1,200 lbs)
 Total Life = 385,200
 As-Welded Conditions
 Task # 17 Specimen # 2

Number of Cycles	Change in Resistivity ($\mu\Omega\cdot\text{cm}$)	
	Side A	Side B
1,000	0.23	0.03
5,000	0.27	0.07
10,000	0.33	0.03
50,000	0.43	0.17
100,000	0.67	0.43
125,000	0.67	0.57
175,000	0.87	1.30
185,000	0.90	1.53
200,000	0.90	1.53
240,000	1.17	3.17
260,000	2.13	4.30
300,000	4.43	7.77
320,000	6.60	10.90
330,000	8.43	12.87
350,000	12.70	29.93

Table F-59
 Resistivity Measurements For
 Galvanized Low Carbon
 $t = 2.7 \text{ mm}$, $D = 8.6 \text{ mm}$, $W = 38 \text{ mm}$
 $R = 0.0$, Max. Load = 3,335 N (750 lbs)
 Total Life = 3,853,200
 As-Welded Conditions
 Task # 17 Specimen # 3

Number of Cycles	Change in Resistivity ($\mu\Omega\cdot\text{cm}$)	
	Side A	Side B
1,000	0.10	0.03
5,000	0.17	0.13
10,000	0.30	0.16
50,000	0.37	0.20
100,000	0.60	0.21
200,000	0.43	0.26
500,000	0.43	0.23
600,000	0.53	0.23
800,000	0.63	0.20
900,000	0.63	0.26
1,100,000	0.67	0.23
1,300,000	0.57	0.26
1,500,000	0.73	0.30
1,600,000	0.43	0.33
1,700,000	0.37	0.30
2,000,000	0.50	0.43
2,500,000	0.50	1.26
2,600,000	0.47	1.46
2,700,000	0.47	1.80
3,000,000	0.97	4.50
3,250,000	2.03	7.36
3,300,000	2.53	8.56
3,400,000	2.97	8.93
3,550,000	4.40	14.83
3,700,000	7.40	42.16

Table F-60
 Resistivity Measurements For
 Galvanized Low Carbon
 $t = 2.7$ mm, $D = 8.6$ mm, $W = 38$ mm
 $R = 0.0$, Max. Load = 4,005 N (900 lbs)
 Total Life = 994,400
 As-Welded Conditions
 Task # 17 Specimen # 4

Number of Cycles	Change in Resistivity ($\mu\Omega\cdot\text{cm}$)	
	Side A	Side B
1,000	0.04	0.23
5,000	0.04	0.13
10,000	0.04	0.17
50,000	0.04	0.17
100,000	0.07	0.30
150,000	0.07	0.33
300,000	0.20	0.53
450,000	0.47	1.20
600,000	1.57	2.60
750,000	4.30	7.27
825,000	5.30	10.63
900,000	13.97	26.27

Table F-61
 Resistivity Measurements For
 Galvanized Low Carbon
 $t = 2.7 \text{ mm}$, $D = 8.6 \text{ mm}$, $W = 38 \text{ mm}$
 $R = -0.2$, Max. Load = 3,290 N (740 lbs)
 Total Life = 1,009,200
 As-Welded Conditions
 Task # 18 Specimen # 1

Number of Cycles	Change in Resistivity ($\mu\Omega\cdot\text{cm}$)	
	Side A	Side B
1,000	0.04	0.03
5,000	0.07	0.03
10,000	0.24	0.03
50,000	0.27	0.03
100,000	0.20	0.10
250,000	0.34	0.70
400,000	0.54	1.53
500,000	0.57	3.10
650,000	0.54	6.80
750,000	1.94	11.06
810,000	3.10	18.86

Table F-62
 Resistivity Measurements For
 Galvanized Low Carbon
 $t = 2.7 \text{ mm}$, $D = 8.6 \text{ mm}$, $W = 38 \text{ mm}$
 $R = -0.2$, Max. Load = 4,005 N (900 lbs)
 Total Life = 573,900
 As-Welded Conditions
 Task # 18 Specimen # 2

Number of Cycles	Change in Resistivity ($\mu\Omega\cdot\text{cm}$)	
	Side A	Side B
1,000	0.10	0.03
5,000	0.30	0.13
10,000	0.34	0.10
50,000	0.50	0.16
130,000	0.84	0.20
210,000	0.97	0.63
300,000	1.67	2.03
400,000	3.97	7.13
450,000	5.74	9.86
460,000	6.77	11.66

Table F-63
 Resistivity Measurements For
 Galvanized Low Carbon
 $t = 2.7 \text{ mm}$, $D = 8.6 \text{ mm}$, $W = 38 \text{ mm}$
 $R = -0.2$, Max. Load = 2,935 N (660 lbs)
 Total Life = 1,367,900
 As-Welded Conditions
 Task # 18 Specimen # 3

Number of Cycles	Change in Resistivity ($\mu\Omega\cdot\text{cm}$)	
	Side A	Side B
1,000	0.03	0.04
5,000	0.03	0.17
10,000	0.03	0.17
50,000	0.03	0.24
200,000	0.27	0.30
370,000	0.60	0.54
500,000	0.80	1.20
700,000	1.67	2.24
900,000	4.23	4.64
950,000	5.07	5.70
1,050,000	8.07	8.17
1,100,000	9.47	10.24
1,150,000	11.67	12.00

Table F-64
 Resistivity Measurements For
 Galvanized Low Carbon
 $t = 2.7 \text{ mm}$, $D = 8.6 \text{ mm}$, $W = 38 \text{ mm}$
 $R = -0.2$, Max. Load = 5,780 N (1,300 lbs)
 Total Life = 138,100
 As-Welded Conditions
 Task # 18 Specimen # 4

Number of Cycles	Change in Resistivity ($\mu\Omega\cdot\text{cm}$)	
	Side A	Side B
1,000	0.53	0.06
5,000	0.70	0.30
10,000	0.93	0.33
20,000	0.93	0.40
50,000	1.03	0.86
60,000	1.10	0.93
80,000	1.43	1.60
90,000	1.40	2.90
100,000	1.96	5.76
110,000	2.70	10.46

Table F-65
 Resistivity Measurements For
 Galvanized Low Carbon
 $t = 2.7 \text{ mm}$, $D = 8.6 \text{ mm}$, $W = 38 \text{ mm}$
 $R = 0.5$, Max. Load = 12,010 N (2,700 lbs)
 Total Life = 133,400
 As-Welded Conditions
 Task # 19 Specimen # 1

Number of Cycles	Change in Resistivity ($\mu\Omega\cdot\text{cm}$)	
	Side A	Side B
1,000	0.43	0.20
5,000	0.57	0.24
10,000	0.57	0.17
30,000	0.77	0.30
50,000	0.73	0.64
75,000	1.17	0.74
85,000	1.40	1.30
90,000	1.67	1.40
95,000	2.00	1.50
110,000	2.83	2.97
125,000	5.63	5.94
130,000	14.80	15.47

Table F-66
 Resistivity Measurements For
 Galvanized Low Carbon
 $t = 2.7 \text{ mm}$, $D = 8.6 \text{ mm}$, $W = 38 \text{ mm}$
 $R = 0.5$, Max. Load = 6,670 N (1,500 lbs)
 Total Life = 1,473,200
 As-Welded Conditions
 Task # 19 Specimen # 2

Number of Cycles	Change in Resistivity ($\mu\Omega\cdot\text{cm}$)	
	Side A	Side B
1,000	0.13	0.03
5,000	0.17	0.07
10,000	0.13	0.20
50,000	0.03	0.37
100,000	0.23	0.30
200,000	0.20	0.23
300,000	0.43	0.33
500,000	0.50	0.50
700,000	1.17	1.67
900,000	2.70	3.13
1,000,000	4.23	5.10
1,200,000	7.17	8.60
1,300,000	8.63	15.60
1,450,000	30.93	36.70

Table F-67
 Resistivity Measurements For
 Galvanized Low Carbon
 $t = 2.7 \text{ mm}$, $D = 8.6 \text{ mm}$, $W = 38 \text{ mm}$
 $R = 0.5$, Max. Load = 7,115 N (1,600 lbs)
 Total Life = 1,091,900
 As-Welded Conditions
 Task # 19 Specimen # 3

Number of Cycles	Change in Resistivity ($\mu\Omega\cdot\text{cm}$)	
	Side A	Side B
1,000	0.20	0.20
5,000	0.30	0.46
10,000	0.27	0.50
50,000	0.30	0.46
100,000	0.27	0.50
150,000	0.24	0.53
250,000	0.27	1.53
470,000	0.90	1.63
600,000	2.17	3.56
700,000	3.80	4.56
800,000	5.70	6.43
900,000	8.20	9.16
950,000	11.20	12.63

Table F-68
 Resistivity Measurements For
 Galvanized Low Carbon
 $t = 2.7 \text{ mm}$, $D = 8.6 \text{ mm}$, $W = 38 \text{ mm}$
 $R = 0.5$, Max. Load = 8,675 N (1,950 lbs)
 Total Life = 564,400
 As-Welded Conditions
 Task # 19 Specimen # 4

Number of Cycles	Change in Resistivity ($\mu\Omega\cdot\text{cm}$)	
	Side A	Side B
1,000	0.09	0.03
5,000	0.33	0.13
10,000	0.29	0.27
50,000	0.26	0.30
80,000	0.33	0.27
150,000	0.46	0.33
220,000	0.73	0.43
300,000	1.43	1.40
400,000	3.49	3.30
500,000	8.23	8.33
510,000	8.86	8.60
520,000	10.09	10.07
530,000	10.53	11.70

Table F-69
 Resistivity Measurements For
 Galvanized HSLA
 $t = 1.4$ mm, $D = 4.8$ mm, $W = 22$ mm
 $R = 0.0$, Max. Load = 2,270 N (510 lbs)
 Total Life = 382,000
 As-Welded Conditions
 Task # 23 Specimen # 1

Number of Cycles	Change in Resistivity ($\mu\Omega\cdot\text{cm}$)	
	Side A	Side B
20,000	0.76	1.20
50,000	1.50	1.24
100,000	2.53	1.97
150,000	2.76	2.17
250,000	5.16	4.50
300,000	7.83	6.90
330,000	10.33	9.64
340,000	11.56	11.74
350,000	13.53	20.70
365,000	25.23	31.14

Table F-70
 Resistivity Measurements For
 Galvanized HSLA
 $t = 1.4 \text{ mm}$, $D = 4.8 \text{ mm}$, $W = 22 \text{ mm}$
 $R = 0.0$, Max. Load = 1,870 N (420 lbs)
 Total Life = 511,800
 As-Welded Conditions
 Task # 23 Specimen # 2

Number of Cycles	Change in Resistivity ($\mu\Omega\cdot\text{cm}$)	
	Side A	Side B
50,000	1.70	0.57
80,000	1.73	0.63
110,000	1.77	0.90
140,000	1.83	1.07
150,000	1.87	1.30
170,000	1.90	1.50
190,000	1.97	1.53
200,000	2.00	1.57
300,000	2.77	3.43
350,000	4.07	3.53
400,000	5.93	6.70
450,000	8.37	13.03
500,000	22.27	40.97

Table F-71
 Resistivity Measurements For
 Galvanized HSLA
 $t = 1.4$ mm, $D = 4.8$ mm, $W = 22$ mm
 $R = 0.0$, Max. Load = 2,000 N (450 lbs)
 Total Life = 649,500
 As-Welded Conditions
 Task # 23 Specimen # 3

Number of Cycles	Change in Resistivity ($\mu\Omega\cdot\text{cm}$)	
	Side A	Side B
30,000	0.87	0.87
60,000	1.94	1.57
90,000	1.47	1.77
120,000	1.50	2.14
170,000	1.80	2.20
220,000	2.30	2.27
270,000	2.74	2.77
320,000	3.10	3.17
370,000	3.17	3.94
420,000	3.47	5.04
470,000	3.97	6.14
520,000	5.00	7.74
530,000	5.20	8.10
550,000	5.60	9.04
570,000	5.97	10.04
590,000	6.90	11.67
610,000	7.97	14.00

Table F-72
 Resistivity Measurements For
 Galvanized HSLA
 $t = 1.4$ mm, $D = 4.8$ mm, $W = 22$ mm
 $R = 0.0$, Max. Load = 3,205 N (720 lbs)
 Total Life = 60,900
 As-Welded Conditions
 Task # 23 Specimen # 4

Number of Cycles	Change in Resistivity ($\mu\Omega\cdot\text{cm}$)	
	Side A	Side B
2,000	1.97	1.70
5,000	2.20	2.07
50,000	7.00	8.97
55,000	11.64	20.17

Table F-73
 Resistivity Measurements For
 Galvanized HSLA
 $t = 1.4$ mm, $D = 4.8$ mm, $W = 22$ mm
 $R = 0.0$, Max. Load = 2,670 N (600 lbs)
 Total Life = 137,800
 As-Welded Conditions
 Task # 23 Specimen # 5

Number of Cycles	Change in Resistivity ($\mu\Omega\cdot\text{cm}$)	
	Side A	Side B
5,000	1.14	0.44
7,000	1.60	0.64
10,000	1.67	0.74
20,000	1.84	1.00
40,000	2.20	1.47
100,000	6.00	5.74
130,000	16.54	18.10

Table F-74
 Resistivity Measurements For
 Galvanized Low Carbon
 $t = 1.4 \text{ mm}$, $D = 4.8 \text{ mm}$, $W = 22 \text{ mm}$
 $R = 0.0$, Max. Load = 2,670 N (600 lbs)
 Total Life = 221,000
 As-Welded Conditions
 Task # 24 Specimen # 1

Number of Cycles	Change in Resistivity ($\mu\Omega\cdot\text{cm}$)	
	Side A	Side B
1,000	0.60	0.77
5,000	0.80	1.37
10,000	0.90	1.40
40,000	1.23	1.47
100,000	1.43	1.93
150,000	1.43	4.20
160,000	1.53	5.30
180,000	1.70	7.73
200,000	1.83	12.67

Table F-75
 Resistivity Measurements For
 Galvanized Low Carbon
 $t = 1.4 \text{ mm}$, $D = 4.8 \text{ mm}$, $W = 22 \text{ mm}$
 $R = 0.0$, Max. Load = 2,270 N (510 lbs)
 Total Life = 410,700
 As-Welded Conditions
 Task # 24 Specimen # 2

Number of Cycles	Change in Resistivity ($\mu\Omega\cdot\text{cm}$)	
	Side A	Side B
1,000	0.67	0.97
5,000	1.00	1.07
10,000	1.20	1.10
40,000	1.47	1.10
100,000	1.50	1.33
200,000	1.50	1.77
250,000	1.67	1.87
300,000	1.74	5.27
350,000	2.00	10.47
375,000	2.30	25.93

Table F-76
 Resistivity Measurements For
 Galvanized Low Carbon
 $t = 1.4 \text{ mm}$, $D = 4.8 \text{ mm}$, $W = 22 \text{ mm}$
 $R = 0.0$, Max. Load = 2,000 N (450 lbs)
 Total Life = 690,200
 As-Welded Conditions
 Task # 24 Specimen # 3

Number of Cycles	Change in Resistivity ($\mu\Omega\cdot\text{cm}$)	
	Side A	Side B
5,000	0.40	0.77
10,000	0.63	0.93
20,000	0.77	1.13
100,000	1.43	1.30
190,000	1.50	1.33
250,000	1.67	1.50
300,000	1.67	1.60
350,000	1.77	1.60
400,000	1.83	1.73
425,000	1.80	2.20
475,000	1.70	3.27
550,000	1.77	5.47
625,000	1.77	11.20

Table F-77
 Resistivity Measurements For
 Galvanized Low Carbon
 $t = 1.4 \text{ mm}$, $D = 4.8 \text{ mm}$, $W = 22 \text{ mm}$
 $R = 0.0$, Max. Load = 3,335 N (750 lbs)
 Total Life = 48,800
 As-Welded Conditions
 Task # 24 Specimen # 4

Number of Cycles	Change in Resistivity ($\mu\Omega\cdot\text{cm}$)	
	Side A	Side B
100	0.33	0.17
1,000	0.90	0.94
3,000	1.10	1.17
5,000	1.13	1.20
10,000	1.17	1.47
15,000	1.40	1.60
20,000	1.37	1.50
30,000	1.50	1.87
40,000	2.90	4.74
450,000	6.70	9.44
460,000	8.07	16.54

Table F-78
 Resistivity Measurements For
 Galvanized HSLA
 $t = 1.4 \text{ mm}$, $D = 6.1 \text{ mm}$, $W = 38 \text{ mm}$
 $R = 0.0$, Max. Load = 4,450 N (1,000 lbs)
 Total Life = 248,900
 Initial Tensile Overload = 9,075 N (2,040 lbs)
 Task # 25 Specimen # 1

Number of Cycles	Change in Resistivity ($\mu\Omega\cdot\text{cm}$)	
	Side A	Side B
1,000	1.03	0.53
5,000	1.26	0.70
10,000	1.36	0.90
30,000	1.43	0.86
80,000	1.46	0.90
130,000	1.83	1.33
160,000	1.86	1.76
170,000	1.83	2.53
175,000	1.86	2.80
180,000	1.86	3.10
190,000	2.33	4.10
200,000	2.56	5.80
210,000	3.30	7.76
220,000	4.53	10.36
225,000	5.20	19.90

Table F-79
 Resistivity Measurements For
 Galvanized HSLA
 $t = 1.4 \text{ mm}$, $D = 6.1 \text{ mm}$, $W = 38 \text{ mm}$
 $R = 0.0$, Max. Load = 3,870 N (870 lbs)
 Total Life = 1,067,700
 Initial Tensile Overload = 9,075 N (2,040 lbs)
 Task # 25 Specimen # 2

Number of Cycles	Change in Resistivity ($\mu\Omega\cdot\text{cm}$)	
	Side A	Side B
2,000	0.46	0.80
5,000	0.80	1.10
10,000	0.86	1.13
250,000	0.96	1.37
300,000	1.06	1.67
430,000	1.06	1.97
500,000	1.20	1.97
570,000	1.26	2.07
650,000	1.16	2.40
750,000	1.13	3.03
850,000	1.10	4.43
1,000,000	1.36	17.07

Table F-80
 Resistivity Measurements For
 Galvanized HSLA
 $t = 1.4$ mm, $D = 6.1$ mm, $W = 38$ mm
 $R = 0.0$, Max. Load = 3,605 N (810 lbs)
 Total Life = 1,148,300
 Initial Tensile Overload = 9,075 N (2,040 lbs)
 Task # 25 Specimen # 3

Number of Cycles	Change in Resistivity ($\mu\Omega\cdot\text{cm}$)	
	Side A	Side B
5,000	0.64	0.47
10,000	0.60	0.47
50,000	0.64	0.47
400,000	0.77	0.40
500,000	0.60	0.43
600,000	0.74	0.50
740,000	0.84	0.73
820,000	0.90	1.13
900,000	0.97	2.43
960,000	1.04	3.93
1,000,000	0.80	6.13
1,050,000	1.14	14.10

APPENDIX-G : TOTAL FATIGUE LIFE DATA

Table G-1
 Total Fatigue Life
 For Galvanized HSLA Tensile-Shear Spot Welds
 $t = 1.4 \text{ mm}$, $D = 6.1 \text{ mm}$, $W = 38 \text{ mm}$
 $R = 0.0$
 As-Welded Conditions
 Task # 1

Load (N)	Total Life
2,670	234,697
2,225	1,625,427
2,000	2,247,733
2,445	2,151,899
2,445	483,194
2,225	669,558
2,670	457,187
2,000	1,249,190
3,560	97,616
3,560	170,960
2,445	940,836
1,780	2,228,952
2,225	907,100
2,670	316,200
2,000	1,062,320

Table G-2
 Total Fatigue Life
 For Galvanized HSLA Tensile-Shear Spot Welds
 $t = 1.4 \text{ mm}$, $D = 6.1 \text{ mm}$, $W = 38 \text{ mm}$
 $R = -0.2$
 As-Welded Conditions
 Task # 2

Load (N)	Total Life
3,560	80,900
2,670	299,253
2,000	1,039,900
1,780	626,723
2,225	377,400
1,555	3,000,000
2,670	252,300
1,780	999,800
1,670	1,055,600
1,555	3,000,000
2,000	834,860
3,560	67,900
2,225	498,500

Table G-3
 Total Fatigue Life
 For Galvanized HSLA Tensile-Shear Spot Welds
 $t = 1.4$ mm, $D = 6.1$ mm, $W = 38$ mm
 $R = 0.5$
 As-Welded Conditions
 Task # 3

Load (N)	Total Life
6,225	94,902
5,780	132,501
4,895	344,561
4,450	470,299
4,005	565,795
3,335	1,579,971
3,115	1,994,182
4,005	953,700
4,450	534,700
4,895	417,800
3,335	4,817,800

Table G-4
 Total Fatigue Life
 For Galvanized Low Carbon Tensile-Shear Spot Welds
 $t = 1.4$ mm, $D = 6.1$ mm, $W = 38$ mm
 $R = 0.0$
 As-Welded Conditions
 Task # 4

Load (N)	Total Life
2,670	1,353,200
3,115	388,200
3,735	262,300
3,335	340,100
2,535	1,801,100
2,400	3,000,000
2,935	570,700
3,560	201,300
2,490	2,622,700
2,800	944,100
2,935	844,400
3,560	335,000

Table G-5
 Total Fatigue Life
 For Galvanized Low Carbon Tensile-Shear Spot Welds
 $t = 1.4$ mm, $D = 6.1$ mm, $W = 38$ mm
 $R = -0.2$
 As-Welded Conditions
 Task # 5

Load (N)	Total Life
2,400	976,200
2,135	1,978,200
2,270	1,366,100
2,670	434,300
2,935	244,000
3,335	136,300
3,335	147,100
2,935	298,800
2,400	483,500
2,270	791,400

Table G-6
 Total Fatigue Life
 For Galvanized Low Carbon Tensile-Shear Spot Welds
 $t = 1.4$ mm, $D = 6.1$ mm, $W = 38$ mm
 $R = 0.5$
 As-Welded Conditions
 Task # 6

Load (N)	Total Life
5,340	456,100
4,450	1,274,200
5,780	308,800
6,670	86,300
4,895	1,553,600
4,670	636,700
4,895	1,034,300
4,450	3,000,000
5,340	986,100
6,670	130,100
5,780	195,100

Table G-7
 Total Fatigue Life
 For Galvanized Low Carbon Tensile-Shear Spot Welds
 $t = 1.4 \text{ mm}$, $D = 4.8 \text{ mm}$, $W = 38 \text{ mm}$
 $R = 0.0$
 As-Welded Conditions
 Task # 7

Load (N)	Total Life
2,670	589,900
2,270	1,637,600
2,935	388,300
2,135	2,444,300
2,000	3,000,000
3,070	416,800
3,335	184,500
2,670	640,900
2,270	3,711,200
2,935	461,600
3,335	223,800

Table G-8
 Total Fatigue Life
 For Galvanized Low Carbon Tensile-Shear Spot Welds
 $t = 1.4 \text{ mm}$, $D = 4.8 \text{ mm}$, $W = 38 \text{ mm}$
 $R = -0.2$
 As-Welded Conditions
 Task # 8

Load (N)	Total Life
2,225	717,800
1,780	3,000,000
2,000	1,676,800
2,670	558,700
3,115	198,900
2,000	3,000,000
2,445	726,600
3,205	213,100
2,225	878,100
2,670	380,600
2,090	1,053,000
2,135	2,231,400

Table G-9
 Total Fatigue Life
 For Galvanized Low Carbon Tensile-Shear Spot Welds
 $t = 1.4 \text{ mm}$, $D = 4.8 \text{ mm}$, $W = 38 \text{ mm}$
 $R = 0.5$
 As-Welded Conditions
 Task # 9

Load (N)	Total Life
4,005	3,000,000
4,450	2,167,600
4,450	737,940
5,340	358,400
5,340	217,900
5,780	155,650
4,895	469,500
4,335	1,121,200
5,340	219,200
6,670	51,200
4,895	334,500

Table G-10
 Total Fatigue Life
 For Galvanized HSLA Tensile-Shear Spot Welds
 $t = 1.4 \text{ mm}$, $D = 4.8 \text{ mm}$, $W = 38 \text{ mm}$
 $R = 0.0$
 As-Welded Conditions
 Task # 10

Load (N)	Total Life
2,270	1,290,900
2,400	500,600
2,670	417,800
3,070	196,600
3,070	180,800
2,000	1,730,800
2,135	985,100
2,000	1,386,900
3,205	215,600
2,670	511,800
2,000	1,150,200
1,870	1,562,400

Table G-11
 Total Fatigue Life
 For Galvanized HSLA Tensile-Shear Spot Welds
 $t = 1.4 \text{ mm}$, $D = 4.8 \text{ mm}$, $W = 38 \text{ mm}$
 $R = -0.2$
 As-Welded Conditions
 Task # 11

Load (N)	Total Life
2,225	567,000
1,780	910,200
1,555	2,269,900
2,670	142,100
1,335	3,000,000
2,000	1,330,600
1,780	1,089,800
2,935	124,800
3,205	79,500
2,000	1,917,900
2,135	903,300
2,270	816,200

Table G-12
 Total Fatigue Life
 For Galvanized HSLA Tensile-Shear Spot Welds
 $t = 1.4 \text{ mm}$, $D = 4.8 \text{ mm}$, $W = 38 \text{ mm}$
 $R = 0.5$
 As-Welded Conditions
 Task # 12

Load (N)	Total Life
4,450	566,200
4,895	267,500
4,270	716,000
4,005	882,900
3,805	1,104,400
3,605	1,991,300
5,340	197,400
6,005	97,000
3,870	634,200
3,605	1,277,900
3,380	2,601,200

Table G-13
 Total Fatigue Life
 For Galvanized Low Carbon Tensile-Shear Spot Welds
 $t = 0.9$ mm, $D = 6.1$ mm, $W = 38$ mm
 $R = 0.0$
 As-Welded Conditions
 Task # 13

Load (N)	Total Life
1,200	1,965,400
1,535	743,100
1,400	2,142,700
1,735	439,200
2,000	181,500
1,600	463,600
1,870	417,900
2,135	143,400
1,475	559,100
1,335	1,465,700

Table G-14
 Total Fatigue Life
 For Galvanized Low Carbon Tensile-Shear Spot Welds
 $t = 0.9$ mm, $D = 6.1$ mm, $W = 38$ mm
 $R = -0.2$
 As-Welded Conditions
 Task # 14

Load (N)	Total Life
1,600	232,800
1,870	99,600
1,200	861,400
1,135	1,050,100
1,065	1,382,500
1,335	600,300
1,870	110,600
1,600	309,600
1,335	503,200
1,200	1,814,400

Table G-15
 Total Fatigue Life
 For Galvanized Low Carbon Tensile-Shear Spot Welds
 $t = 0.9$ mm, $D = 6.1$ mm, $W = 38$ mm
 $R = 0.5$
 As-Welded Conditions
 Task # 15

Load (N)	Total Life
2,670	1,313,200
2,670	333,100
2,225	784,000
2,000	3,000,000
2,135	2,592,300
3,070	551,500
3,335	171,400
3,470	144,200
2,270	2,448,600
2,670	1,823,100
3,205	423,000

Table G-16
 Total Fatigue Life
 For Galvanized Low Carbon Tensile-Shear Spot Welds
 $t = 0.9$ mm, $D = 4.8$ mm, $W = 38$ mm
 $R = 0.0$
 As-Welded Conditions
 Task # 16

Load (N)	Total Life
2,000	175,300
1,270	2,488,400
1,475	596,900
1,475	792,200
1,335	952,000
2,270	106,200
1,335	2,240,700
1,735	544,700
2,225	99,000
1,600	613,000

Table G-17
 Total Fatigue Life
 For Galvanized Low Carbon Tensile-Shear Spot Welds
 $t = 2.7 \text{ mm}$, $D = 8.6 \text{ mm}$, $W = 38 \text{ mm}$
 $R = 0.0$
 As-Welded Conditions
 Task # 17

Load (N)	Total Life
6,005	224,700
8,005	50,600
5,070	402,700
4,670	601,300
4,005	919,700
3,605	1,384,700
6,670	83,000
5,340	385,200
3,335	3,853,200
4,005	994,400

Table G-18
 Total Fatigue Life
 For Galvanized Low Carbon Tensile-Shear Spot Welds
 $t = 2.7 \text{ mm}$, $D = 8.6 \text{ mm}$, $W = 38 \text{ mm}$
 $R = -0.2$
 As-Welded Conditions
 Task # 18

Load (N)	Total Life
3,605	890,500
3,335	982,200
3,070	1,606,200
4,005	528,700
5,340	149,500
5,740	93,400
3,290	1,009,200
4,005	573,900
2,935	1,367,900
5,780	138,100

Table G-19
 Total Fatigue Life
 For Galvanized Low Carbon Tensile-Shear Spot Welds
 $t = 2.7$ mm, $D = 8.6$ mm, $W = 38$ mm
 $R = 0.5$
 As-Welded Conditions
 Task # 19

Load (N)	Total Life
9,340	467,300
10,675	258,000
12,010	133,400
7,115	1,266,700
8,005	840,500
6,670	1,473,200
7,115	1,091,900
6,225	1,850,000
8,675	480,200
8,675	564,400

Table G-20
 Total Fatigue Life
 For Galvanized Low Carbon Tensile-Shear Spot Welds
 $t = 2.7$ mm, $D = 7.6$ mm, $W = 38$ mm
 $R = 0.0$
 As-Welded Conditions
 Task # 20

Load (N)	Total Life
3,560	1,755,700
4,005	1,320,000
4,670	548,000
4,405	777,100
5,340	366,200
6,225	174,700
7,115	83,300
3,380	1728,600
4,450	595,700
3,290	735,900

Table G-21
 Total Fatigue Life
 For Galvanized Low Carbon Tensile-Shear Spot Welds
 $t = 2.7 \text{ mm}$, $D = 7.6 \text{ mm}$, $W = 38 \text{ mm}$
 $R = -0.2$
 As-Welded Conditions
 Task # 21

Load (N)	Total Life
3,290	1,005,900
3,115	1,092,300
4,450	302,000
3,735	426,200
5,340	179,700
6,225	95,700
3,560	743,600
2,935	3,000,000
3,115	2,648,200

Table G-22
 Total Fatigue Life
 For Galvanized Low Carbon Tensile-Shear Spot Welds
 $t = 2.7 \text{ mm}$, $D = 7.6 \text{ mm}$, $W = 38 \text{ mm}$
 $R = 0.5$
 As-Welded Conditions
 Task # 22

Load (N)	Total Life
8,005	678,200
9,340	441,700
7,115	983,000
6,670	1,537,200
10,010	323,100
10,675	141,500
6,405	2,246,200
11,340	56,000
8,675	404,800
6,405	1,523,900

Appendix-H : Fatigue Life Data for Stages I, II and III

Table H-1
 Fatigue Life Partitioning
 For Galvanized HSLA Tensile-Shear Spot Welds
 $t = 1.4 \text{ mm}$, $D = 6.1 \text{ mm}$, $W = 38 \text{ mm}$
 $R = 0.0$
 As-Welded Conditions
 Task # 1

Load (N)	Stage I	Stage II	Stage III	Total Fatigue Life
2,935	32,000	198,000	104,100	334,100
3,560	150	93,000	32,150	125,300
2,225	3,500	666,500	237,100	907,100
2,670	28,000	192,000	96,200	316,200

Table H-2
 Fatigue Life Partitioning
 For Galvanized HSLA Tensile-Shear Spot Welds
 $t = 1.4 \text{ mm}$, $D = 6.1 \text{ mm}$, $W = 38 \text{ mm}$
 $R = -0.2$
 As-Welded Conditions
 Task # 2

Load (N)	Stage I	Stage II	Stage III	Total Fatigue Life
2,670	600	163,400	88,000	252,000
2,000	18,000	530,000	286,860	834,860
3,560	500	46,500	20,900	67,900
2,225	24,000	296,000	178,500	498,500

Table H-3
 Fatigue Life Partitioning
 For Galvanized HSLA Tensile-Shear Spot Welds
 $t = 1.4 \text{ mm}$, $D = 6.1 \text{ mm}$, $W = 38 \text{ mm}$
 $R = 0.5$
 As-Welded Conditions
 Task # 3

Load (N)	Stage I	Stage II	Stage III	Total Fatigue Life
4,005	40,000	770,000	143,700	953,700
4,450	1,500	413,500	119,700	534,700
4,895	400	316,600	100,800	417,800
3,335	850,000	3,350,000	617,800	4,817,800

Table H-4
 Fatigue Life Partitioning
 For Galvanized Low Carbon Tensile-Shear Spot Welds
 $t = 1.4 \text{ mm}$, $D = 6.1 \text{ mm}$, $W = 38 \text{ mm}$
 $R = 0.0$
 As-Welded Conditions
 Task # 4

Load (N)	Stage I	Stage II	Stage III	Total Fatigue Life
3335	100,000	180,000	60,100	340,100
2670	520,000	510,000	161,800	1,191,800
2935	370,000	80,000	101,900	551,900
3560	65,000	75,000	19,700	159,700

Table H-5
 Fatigue Life Partitioning
 For Galvanized Low Carbon Tensile-Shear Spot Welds
 $t = 1.4 \text{ mm}$, $D = 6.1 \text{ mm}$, $W = 38 \text{ mm}$
 $R = -0.2$
 As-Welded Conditions
 Task # 5

Load (N)	Stage I	Stage II	Stage III	Total Fatigue Life
3335	90,000	30,000	27,100	147,100
2935	170,000	100,000	28,900	298,900
2400	300,000	100,000	83,500	483,500
2270	360,000	260,000	171,400	791,400

Table H-6
 Fatigue Life Partitioning
 For Galvanized Low Carbon Tensile-Shear Spot Welds
 $t = 1.4 \text{ mm}$, $D = 6.1 \text{ mm}$, $W = 38 \text{ mm}$
 $R = 0.5$
 As-Welded Conditions
 Task # 6

Load (N)	Stage I	Stage II	Stage III	Total Fatigue Life
5,340	470,000	430,000	86,100	986,100
6,670	4,700	91,300	34,100	130,100
4,895	600,000	300,000	134,300	1,034,300
5,780	109,000	71,000	15,100	195,100

Table H-7
 Fatigue Life Partitioning
 For Galvanized Low Carbon Tensile-Shear Spot Welds
 $t = 1.4 \text{ mm}$, $D = 4.8 \text{ mm}$, $W = 38 \text{ mm}$
 $R = 0.0$
 As-Welded Conditions
 Task # 7

Load (N)	Stage I	Stage II	Stage III	Total Fatigue Life
2,670	320,000	170,000	150,900	640,900
2,270	2,800,000	300,000	611,200	3,711,200
2,935	210,000	180,000	71,600	461,600
3,335	70,000	90,000	63,800	223,820

Table H-8
 Fatigue Life Partitioning
 For Galvanized Low Carbon Tensile-Shear Spot Welds
 $t = 1.4 \text{ mm}$, $D = 4.8 \text{ mm}$, $W = 38 \text{ mm}$
 $R = -0.2$
 As-Welded Conditions
 Task # 8

Load (N)	Stage I	Stage II	Stage III	Total Fatigue Life
3,205	60,000	120,000	33,100	213,100
2,225	425,000	315,000	138,100	878,100
2,670	200,000	110,000	70,600	380,600
2,135	1,400,000	640,000	191,400	2,231,400

Table H-9
 Fatigue Life Partitioning
 For Galvanized Low Carbon Tensile-Shear Spot Welds
 $t = 1.4 \text{ mm}$, $D = 4.8 \text{ mm}$, $W = 38 \text{ mm}$
 $R = 0.5$
 As-Welded Conditions
 Task # 9

Load (N)	Stage I	Stage II	Stage III	Total Fatigue Life
4,335	400,000	600,000	121,200	1,121,200
5,340	30,000	160,000	29,100	219,100
6,670	400	47,600	3,200	51,200
4,895	130,000	130,000	74,500	334,500

Table H-10
 Fatigue Life Partitioning
 For Galvanized HSLA Tensile-Shear Spot Welds
 $t = 1.4 \text{ mm}$, $D = 4.8 \text{ mm}$, $W = 38 \text{ mm}$
 $R = 0.0$
 As-Welded Conditions
 Task # 10

Load (N)	Stage I	Stage II	Stage III	Total Fatigue Life
3,205	8,000	140,000	75,600	215,600
2,670	55,000	325,000	131,800	511,800
2,000	180,000	480,000	490,200	1,150,200
1,870	450,000	550,000	562,400	1,562,400

Table H-11
 Fatigue Life Partitioning
 For Galvanized Low Carbon Tensile-Shear Spot Welds
 $t = 0.9$ mm, $D = 6.1$ mm, $W = 38$ mm
 $R = 0.0$
 As-Welded Conditions
 Task # 13

Load (N)	Stage I	Stage II	Stage III	Total Fatigue Life
1,870	235,000	135,000	47,900	417,900
2,135	122,000	15,000	23,300	160,300
1,475	400,000	60,000	99,100	559,100
1,335	1,125,000	110,000	230,000	1,465,700

Table H-12
 Fatigue Life Partitioning
 For Galvanized Low Carbon Tensile-Shear Spot Welds
 $t = 0.9$ mm, $D = 6.1$ mm, $W = 38$ mm
 $R = -0.2$
 As-Welded Conditions
 Task # 14

Load (N)	Stage I	Stage II	Stage III	Total Fatigue Life
1,870	45,000	36,000	29,600	110,600
1,200	1,450,000	160,000	204,400	1,814,400
1,600	235,000	40,000	34,600	309,600
1,335	340,000	70,000	93,200	503,200

Table H-13
 Fatigue Life Partitioning
 For Galvanized Low Carbon Tensile-Shear Spot Welds
 $t = 0.9$ mm, $D = 6.1$ mm, $W = 38$ mm
 $R = 0.5$
 As-Welded Conditions
 Task # 15

Load (N)	Stage I	Stage II	Stage III	Total Fatigue Life
3,470	55,000	81,000	8,200	144,200
2,270	1,800,000	500,000	148,600	2,448,600
2,670	1,400,000	200,000	223,100	1,823,100
3,205	220,000	185,000	18,000	423,000

Table H-14
 Fatigue Life Partitioning
 For Galvanized Low Carbon Tensile-Shear Spot Welds
 $t = 0.9$ mm, $D = 4.8$ mm, $W = 38$ mm
 $R = 0.0$
 As-Welded Conditions
 Task # 16

Load (N)	Stage I	Stage II	Stage III	Total Fatigue Life
1,335	550,000	1,300,000	390,700	2,240,700
1,735	220,000	240,000	84,700	544,700
1,600	190,000	375,000	48,000	613,000
2,225	17,000	67,000	15,000	99,000

Table H-15
 Fatigue Life Partitioning
 For Galvanized Low Carbon Tensile-Shear Spot Welds
 $t = 2.7 \text{ mm}$, $D = 8.6 \text{ mm}$, $W = 38 \text{ mm}$
 $R = 0.0$
 As-Welded Conditions
 Task # 17

Load (N)	Stage I	Stage II	Stage III	Total Fatigue Life
6,670	42,000	18,000	23,000	83,000
5,340	210,000	100,000	75,200	385,200
3,335	2,650,000	800,000	403,200	3,853,200
4,005	465,000	350,000	179,400	994,400

Table H-16
 Fatigue Life Partitioning
 For Galvanized Low Carbon Tensile-Shear Spot Welds
 $t = 2.7 \text{ mm}$, $D = 8.6 \text{ mm}$, $W = 38 \text{ mm}$
 $R = -0.2$
 As-Welded Conditions
 Task # 18

Load (N)	Stage I	Stage II	Stage III	Total Fatigue Life
3,290	410,000	330,000	269,200	1,009,200
4,005	270,000	180,000	123,900	573,900
2,935	620,000	455,000	292,900	1,367,900
5,780	80,000	28,000	30,100	138,100

Table H-17
 Fatigue Life Partitioning
 For Galvanized Low Carbon Tensile-Shear Spot Welds
 $t = 2.7 \text{ mm}$, $D = 8.6 \text{ mm}$, $W = 38 \text{ mm}$
 $R = 0.5$
 As-Welded Conditions
 Task # 19

Load (N)	Stage I	Stage II	Stage III	Total Fatigue Life
12,010	90,000	37,000	6,400	133,400
6,670	700,000	520,000	253,200	1,473,200
7,115	470,000	430,000	91,900	1,091,900
8,675	320,000	200,000	44,400	564,400

Table H-18
 Fatigue Life Partitioning
 For Galvanized HSLA Tensile-Shear Spot Welds
 $t = 1.4 \text{ mm}$, $D = 4.8 \text{ mm}$, $W = 22 \text{ mm}$
 $R = 0.0$
 As-Welded Conditions
 Task # 23

Load (N)	Stage I	Stage II	Stage III	Total Fatigue Life
2,270	90,000	234,000	58,000	382,000
1,870	205,000	230,000	76,800	511,800
2,000	110,000	455,000	84,500	649,500
3,205	3,000	48,000	9,900	60,900
2,670	33,000	79,000	25,800	137,800

Table H-19
 Fatigue Life Partitioning
 For Galvanized Low Carbon Tensile-Shear Spot Welds
 $t = 1.4 \text{ mm}$, $D = 4.8 \text{ mm}$, $W = 22 \text{ mm}$
 $R = 0.0$
 As-Welded Conditions
 Task # 24

Load (N)	Stage I	Stage II	Stage III	Total Fatigue Life
2,670	120,000	70,000	31,000	221,000
2,270	250,000	100,000	60,700	410,700
3,335	31,000	14,000	3,800	68,800
2,000	410,000	195,000	85,200	690,200

Table H-20
 Fatigue Life Partitioning
 For Galvanized HSLA Tensile-Shear Spot Welds
 $t = 1.4 \text{ mm}$, $D = 6.1 \text{ mm}$, $W = 38 \text{ mm}$
 $R = 0.0$
 Overloaded: 9,073.9 N
 Task # 25

Load (N)	Stage I	Stage II	Stage III	Total Fatigue Life
4,450	165,000	50,000	33,900	248,900
3,870	530,000	400,000	137,700	1,067,700
3,605	870,000	155,000	123,300	1,148,300

APPENDIX-I : CRACK TIP ELEMENTS

The quarter-point node elements have been first introduced by Barsoum [RR]; the use of such elements generate the $\sqrt{\frac{1}{r}}$ singularity at the crack tip. The quarter-point-node elements is created by collapsing the nodes on one of the faces of a regular 20-node-brick element to the line of the crack front and subsequently moving the midside nodes to the quarter point positions as shown in **Fig. I-1**. Hence, clusters of independent nodes will be formed along the crack front. The nodes at each cluster are either tied together or free to move independently; the elastic solution of the crack problem is insensitive to these two kinematic conditions. The formulation and generation of the $\sqrt{\frac{1}{r}}$ singularity through the use of the quarter-point node elements will be clarified hereafter.

Figure I-1a shows a regular 20-node brick element, its parametric axis (ξ , η and ω) and nodes before being collapsed. The shape functions (h_i) for the nodes 1, 9, 2, 5, 13 and 6 are given by [RR]:

$$h_1 = \frac{(1+\xi)(1+\eta)(1+\omega)}{8} [-2+\eta+\xi+\omega] \quad (I-1)$$

$$h_9 = \frac{(1+\xi)(1-\eta^2)(1+\omega)}{4} \quad (I-2)$$

$$h_2 = \frac{(1+\xi)(1-\eta)(1+\omega)}{8} [-2-\eta+\xi+\omega] \quad (I-3)$$

$$h_5 = \frac{(1+\xi)(1+\eta)(1-\omega)}{8} [-2+\eta+\xi-\omega] \quad (I-4)$$

$$h_{13} = \frac{(1+\xi)(1-\eta^2)(1-\omega)}{4} \quad (I-5)$$

$$h_6 = \frac{(1+\xi)(1-\eta)(1-\omega)}{8} [-2-\eta+\xi-\omega] \quad (I-6)$$

Subsequently, the value of any function along the edges 1-9-2 ($\omega = 1$ and $\xi = 1$) and 5-13-6 ($\omega = -1$ and $\xi = 1$) can be expressed as:

$$F = \sum h_i F_i = f(\eta) \quad (I-7)$$

where F_i is the value of the function at the nodes along the considered edge of the element.

After collapsing the nodes, nodes 2, 6 and 18; 10 and 14; and 3,7 and 19 form clusters of independent nodes at three locations as shown in Fig. I-1b. Later, nodes 9,13,11 and 15 are moved to the quarter point positions between the vertex and the base of the triangular cross section of the collapsed element. Thus considering the origin of the X-Y-Z frame to be at the vertex and substituting for the corresponding values of x_i in Eq. I-7, we can express η in terms of x along either 1-9-2 or 5-13-6 as follows:

$$\eta = 2 \sqrt{\frac{x}{L}} - 1 \quad (\text{I-8})$$

where L is the length of the element in the x -direction.

Substituting into Eq. I-7 with Eqs. I-1 to I-6 and expressing η in terms of x , we may express the displacements u and w along the edges 1-9-2 and 5-13-6 as follows:

$$u_{1-9-2} = (2 u_1 - 4 u_9 + 2 u_2) \frac{x}{L} + (4 u_9 - u_1 - 3 u_2) \sqrt{\frac{x}{L}} + u_2 \quad (\text{I-9})$$

$$w_{1-9-2} = (2 w_1 - 4 w_9 + 2 w_2) \frac{x}{L} + (4 w_9 - w_1 - 3 w_2) \sqrt{\frac{x}{L}} + w_2 \quad (\text{I-10})$$

$$u_{5-13-6} = (2 u_5 - 4 u_{13} + 2 u_6) \frac{x}{L} + (4 u_{13} - u_5 - 3 u_6) \sqrt{\frac{x}{L}} + u_6 \quad (\text{I-11})$$

$$w_{5-13-6} = (2 w_5 - 4 w_{13} + 2 w_6) \frac{x}{L} + (4 w_{13} - w_5 - 3 w_6) \sqrt{\frac{x}{L}} + w_6 \quad (\text{I-12})$$

It should be noted that the $\sqrt{\frac{x}{L}}$ terms are those which generate the $\sqrt{\frac{1}{r}}$ singularity at the crack tip.

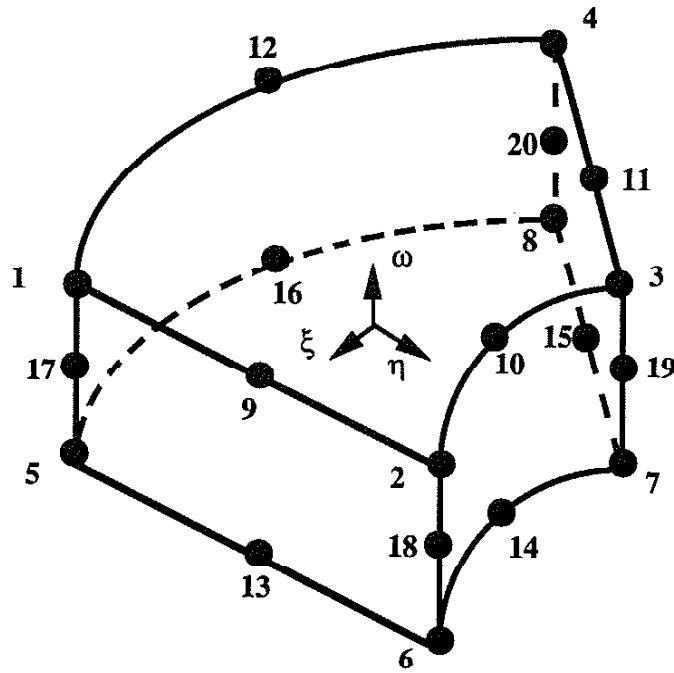


Fig. I-1a The 20-node brick element

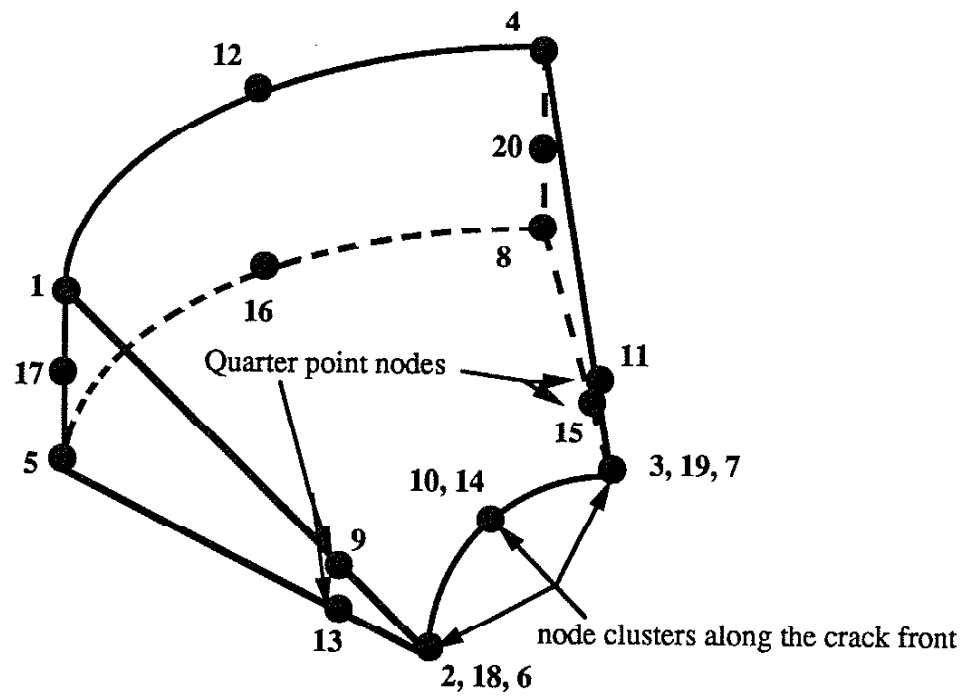


Fig. I-1b The 20-node brick element after collapsing face 2-6-7-3